Multi-Scale Diagnosis of Lithium-Ion Batteries Using Correlative Dilatometric, Acoustic and X-ray Imaging Techniques

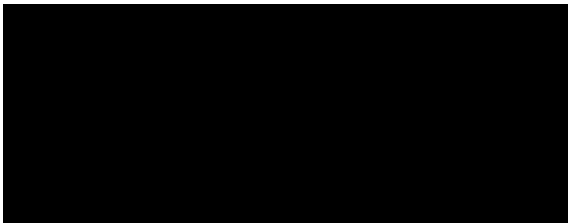Harry Michael

INTENTIONALLY BLANK

Declaration

I, Harry Michael confirm that the work presented in this thesis is my own. Where information has been derived from other sources, I confirm that this has been indicated in the thesis.

Signature

April 2022

INTENTIONALLY BLANK

Abstract

There are growing concerns over the environmental, climate and health impacts associated with the use of non-renewable fossil fuels. Therefore, affordable, renewable energy storage devices are becoming increasingly critical as a necessary route to transition to a clean energy ecosystem. In particular, lithium-ion batteries (LiBs) as a storage solution would enable renewable energy generation to be stored until required. To overcome the limitations of LiBs in performance, capacity, power and lifetime, it is important to understand the degradation mechanism of LiB electrodes. For example, during battery operation, electrodes undergo bulk volume changes that can exacerbate electrode strain and particle cracking, which in turn contribute to the electrode's cumulative degradation. Hence, understanding how electrodes dilate can be of critical value in improving the durability of these energy storage devices.

In this thesis, *in-situ* electrochemical dilatometry (ECD) will be carried out in combination with microscopy techniques, such as scanning emission microscopy (SEM) and X-ray computed tomography (X-ray CT), to investigate bulk volume changes of LiB electrodes. X-ray CT will be carried out across multiple length-scales to allow visual interpretation of the entire cell architecture and electrode morphology. Image-based modelling and quantification of X-ray images will be carried out to reveal physical parameters of electrodes such as porosity and surface area. Finally, acoustic measurements will reveal the physical changes undergone by LiBs during operation.

The experiments reported in this work successfully demonstrate a multi-scale approach to assessing the degradation mechanisms undergone by LiBs during operation, from an electrode to whole cell assemblies. Insights from ECD and acoustic measurements can be used to inform electrode design in future generation LiBs.

INTENTIONALLY BLANK

Impact Statement

The lithium-ion industry is an ever-growing industry with a market size projected to reach $182.53 billion (USD) by 2030. As such, there is a growing consensus on the need to optimise the performance and longevity of lithium-ion batteries. This thesis investigates the use of emerging diagnostic techniques to examine physical changes undergone by lithium-ion batteries during cycling, focusing on aspects that limit battery lifetime. The author presents significant findings using correlative dilatometry, acoustic and X-ray imaging techniques across multiple lengths and time scales. Furthermore, this thesis describes novel research methodologies and analyses which have been disseminated in the form of international conference talks, journal publications, journal covers and public engagement activities. The findings discussed in this work can assist in the development of next-generation materials, the implications of which will be seen from battery manufacture to operation. In addition, this work can inform apparatus design for effective diagnosis of physical changes in a battery. The impact of this work is not limited solely to academia but could also extend into commercial sectors. From a commercial perspective, dilatometry and acoustic spectroscopy are nascent diagnostic tools that can add value across the battery energy value chain, from cell manufacturing to pack integration, vehicle integration, recycling, and second-life use. These results may influence further fundamental research by encouraging the use of the same investigative techniques to inspect batteries of different configurations. The author has collaborated with researchers from a number of UK universities including the University of Cambridge and the University of Oxford and international institutions such as the Faraday Institution (Didcot, UK), NASA, the National American Space Agency, (Houston, USA), WMG (Coventry, UK) and The Diamond Synchrotron Facility (Oxford, UK). The author has actively committed to community engagement activities throughout his PhD, in the form of events attended by members of the public from a variety of backgrounds and ages.

Discussing battery technologies at such events improves public perception of these technologies and encourages involvement. Discussing how academic work can be translated into real-world applications effectively promulgates the importance of this research and the specific challenges that current lithium-ion battery technologies need to overcome to enable further commercial adoption. This study has incorporated rich national and international collaborations, effectively drawing on a range of different scientific and engineering disciplines. The work has been communicated through a variety of channels. Beyond peer-reviewed journals, it has been the subject of teaching and public events. This ensures effective promulgation to a range of different audiences, encouraging interest in the future as well as in the present.

UCL Research Paper Declaration Forms: referencing the doctoral candidate's own published work(s)

Please use this form to declare if parts of your thesis are already available in another format, e.g. if data, text, or figures:

- have been uploaded to a preprint server;
- are in submission to a peer-reviewed publication;
- have been published in a peer-reviewed publication, e.g. journal, textbook.

This form should be completed as many times as necessary. For instance, if you have seven thesis chapters, two of which containing material that has already been published, you would complete this form twice.

1. For a research manuscript that has already been published (if not yet published, please skip to section 2)**:**	
a) Where was the work published? (e.g. journal name)	Journal of the Electrochemical Society
b) Who published the work? (e.g. Elsevier/Oxford University Press):	Elsevier
c) When was the work published?	07/01/2021
d) Was the work subject to academic peer review?	Yes
e) Have you retained the copyright for the work?	Yes

[If no, please seek permission from the relevant publisher and check the box next to the below statement]:

☐ *I acknowledge permission of the publisher named under 1b to include in this thesis portions of the publication named as included in 1a.*

2. For a research manuscript prepared for publication but that has not yet been published (if already published, please skip to section 3)**:**		
a) Has the manuscript been uploaded to a preprint server? (e.g. medRxiv):	Please select.	**If yes, which server?** Click or tap here to enter text.
b) Where is the work intended to be published? (e.g. names of journals that you are planning to submit to)	Click or tap here to enter text.	
c) List the manuscript's authors in the intended authorship order:	Click or tap here to enter text.	
d) Stage of publication	Please select.	

3. For multi-authored work, please give a statement of contribution covering all authors (if single-author, please skip to section 4**):**	

H. Michael: Conceptualization, Methodology, Investigation, Formal analysis. **F. Iacovello:** Investigation, Software, Visualization, Formal analysis. **T.M.M. Heenan:** Investigation, Formal analysis. **A. Llewellyn:** Sample preparation and analysis. **J. S. Weaving:** Methodology, Investigation. **R. Jervis:** Methodology, Formal analysis, Supervision, Funding acquisition. **D.J.L. Brett:** Conceptualization, Supervision, Funding acquisition. **P.R. Shearing:** Conceptualization, Methodology, Supervision, Funding acquisition.

4. In which chapter(s) of your thesis can this material be found?

Chapters 3 and 4

5. e-Signatures confirming that the information above is accurate (this form should be co-signed by the supervisor/ senior author unless this is not appropriate, e.g. if the paper was a single-author work):

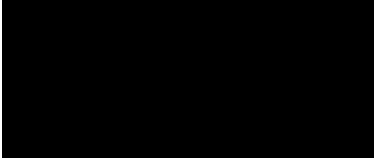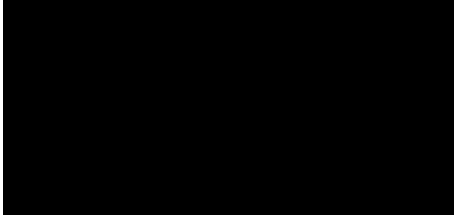| **Candidate:**	▮▮▮▮▮▮▮▮▮▮ Harry Michael	**Date:**	07/08/2022
Supervisor/ Senior Author (where appropriate)**:**	▮▮▮▮▮▮▮▮▮▮ P. R Shearing	**Date:**	1/8/22

UCL Research Paper Declaration Form: referencing the doctoral candidate's own published work(s)

Please use this form to declare if parts of your thesis are already available in another format, e.g. if data, text, or figures:

- have been uploaded to a preprint server;
- are in submission to a peer-reviewed publication;
- have been published in a peer-reviewed publication, e.g. journal, textbook.

This form should be completed as many times as necessary. For instance, if you have seven thesis chapters, two of which containing material that has already been published, you would complete this form twice.

1. For a research manuscript that has already been published (if not yet published, please skip to section 2)**:**			
a) Where was the work published? (e.g. journal name)	Batteries and Supercaps		
b) Who published the work? (e.g. Elsevier/Oxford University Press):	Elsevier		
c) When was the work published?	09/04/2021		
d) Was the work subject to academic peer review?			
e) Have you retained the copyright for the work?			
[If no, please seek permission from the relevant publisher and check the box next to the below statement]: *I acknowledge permission of the publisher named under 1b to include in this thesis portions of the publication named as included in 1a.*			
2. For a research manuscript prepared for publication but that has not yet been published (if already published, please skip to section 3)**:**			
a) Has the manuscript been uploaded to a preprint server? (e.g. medRxiv):	Please select.	**If yes, which server?** Click or tap here to enter text.	
b) Where is the work intended to be published? (e.g. names of journals that you are planning to submit to)	Click or tap here to enter text.		
c) List the manuscript's authors in the intended authorship order:	Click or tap here to enter text.		
d) Stage of publication	Please select.		
3. For multi-authored work, please give a statement of contribution covering all authors (if single-author, please skip to section 4)**:**			

H. Michael: Conceptualization, Methodology, Formal analysis and review. **R. Jervis:** Methodology, Formal analysis, Supervision, Funding acquisition. **D.J.L. Brett:** Conceptualization, Supervision, Funding acquisition. **P.R. Shearing:** Conceptualization, Methodology, Supervision, Funding acquisition.

4. In which chapter(s) of your thesis can this material be found?			
Chapters 2 and 3			

5. e-Signatures confirming that the information above is accurate (this form should be co-signed by the supervisor/ senior author unless this is not appropriate, e.g. if the paper was a single-author work):			
Candidate:	Harry Michael	**Date:**	07/08/2022
Supervisor/ Senior Author (where appropriate)**:**	P. R Shearing	**Date:**	01/08/2022

UCL Research Paper Declaration Form: referencing the doctoral candidate's own published work(s)

Please use this form to declare if parts of your thesis are already available in another format, e.g. if data, text, or figures:

- have been uploaded to a preprint server;
- are in submission to a peer-reviewed publication;
- have been published in a peer-reviewed publication, e.g. journal, textbook.

This form should be completed as many times as necessary. For instance, if you have seven thesis chapters, two of which containing material that has already been published, you would complete this form twice.
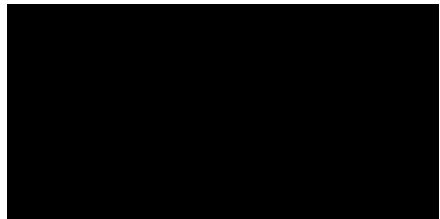
6. **For a research manuscript that has already been published** (if not yet published, please skip to section 2)**:**	
f) **Where was the work published?** (e.g. journal name)	Journal of Power Sources
g) **Who published the work?** (e.g. Elsevier/Oxford University Press):	Elsevier
h) **When was the work published?**	15/09/2022
i) **Was the work subject to academic peer review?**	
j) **Have you retained the copyright for the work?**	
[If no, please seek permission from the relevant publisher and check the box next to the below statement]: *I acknowledge permission of the publisher named under 1b to include in this thesis portions of the publication named as included in 1a.*	

7. **For a research manuscript prepared for publication but that has not yet been published** (if already published, please skip to section 3)**:**		
e) **Has the manuscript been uploaded to a preprint server?** (e.g. medRxiv):	Please select.	**If yes, which server?** Click or tap here to enter text.
f) **Where is the work intended to be published?** (e.g. names of journals that you are planning to submit to)	Click or tap here to enter text.	
g) **List the manuscript's authors in the intended authorship order:**	Click or tap here to enter text.	
h) **Stage of publication**	Please select.	

8. **For multi-authored work, please give a statement of contribution covering all authors** (if single-author, please skip to section 4)**:**
H. Michael: Conceptualization, Methodology, Investigation, Formal analysis. **R.E. Owen:** Investigation, Software, Visualization, Formal analysis. **J.B. Robinson:** Methodology, Formal analysis. **T.M.M. Heenan:** Investigation, Formal analysis. **C. Tan:** Sample procurement and preparation. **A.J. Wade:** Investigation. **R. Jervis:** Methodology, Formal analysis, Supervision,

Funding acquisition. **D.J.L. Brett:** Conceptualization, Supervision, Funding acquisition. **P.R. Shearing:** Conceptualization, Methodology, Supervision, Funding acquisition.

9. In which chapter(s) of your thesis can this material be found?
Chapters 3, 6 and 7

10. e-Signatures confirming that the information above is accurate (this form should be co-signed by the supervisor/ senior author unless this is not appropriate, e.g. if the paper was a single-author work):

Candidate:	████████ Harry Michael	Date:	07/08/2022
Supervisor/ Senior Author (where appropriate)**:**	████████ P. R Shearing	Date:	01/08/2022

Acknowledgements

First and foremost, I would like to thank my supervisors Professor Paul Shearing and Professor Dan Brett for all their support and guidance during my PhD at the Electrochemical Innovation Lab at University College London. Throughout my PhD you have given me the opportunity to carry out exciting research projects, present at overseas research symposia and provided me with expert knowledge of the energy industry. You have also motivated me to pursue new territories in research that have developed my character and instilled confidence in me. I would like to extend a massive thanks to my family and friends especially my mum and girlfriend Vaishali, for always being there for me, and providing me with support and advice throughout this journey. This would not have been possible without you. The EIL is a special place, full of incredible engineers and people. I'd like to thank my colleagues and friends at the EIL. I'm grateful that I was able to collaborate with you, seek technical advice and have a drink with you after a long day at the office. I've formed some truly warm memories with you all that I'll carry with me into the future. Some of you I'll continue seeing after my PhD no doubt! Toby, I could not have asked for a better lab manager, someone always happy to help, chat and talk Arsenal with me.

INTENTIONALLY BLANK

Table of Contents

INTENTIONALLY BLANK

List of Figures

Figure 9: (a) Potential-specific capacity profile and (b) thickness change-potential profile of $Li_{1.17}Ni_{0.20}Mn_{0.53}Co_{0.10}O_2$ at 20 mA g^{-1} (C/10 rate) in the potential range of 2.5-4.6 V in 1 M $LiPF_6$ in ethylene carbonate/dimethyl carbonate solution. The potential-time and thickness change profile are shown in (c) for $Li_{1.17}Ni_{0.20}Mn_{0.53}Co_{0.10}O_2$ at 20 mA g^{-1} (C/10 rate) in the same voltage

List of Tables

INTENTIONALLY BLANK

List of Abbreviations

Abbreviation	Definition
2D	Two-dimensional
3D	Three-dimensional
BMS	Battery management system
CBD	Carbon binder domain
CC	Constant current
CCD	Charge coupled device
CE	Counter electrode
CT	Computed tomography
CV	Constant voltage
D-ECD	Differential electrochemical dilatometry
EA-ToF	Electrochemical acoustic time-of-flight spectroscopy
ECD	Electrochemical dilatometry
EDS	Energy dispersive spectroscopy
EV	Electric vehicle
FOV	Field of view
H1	Hexagonal-1
H2	Hexagonal-2
H3	Hexagonal-3
ICE	Internal combustion engine
LCO	Lithium cobalt oxide

LFP	Lithium iron phosphate
LiB	Lithium-ion battery
Li-ion	Lithium-ion
LMO	Lithium metal oxide
LTO	Lithium titanate
LVDT	Linear voltage displacement transducer
M	Monoclinic
NCA	Lithium nickel cobalt aluminium oxide
NMC	$LiNi_xMn_yCo_zO_2$
NMO	Nickel metal oxides
OCV	Open circuit voltage (V)
PC	Polycrystal
PSD	Particle size distribution
PVDF	Poly(vinylidene fluoride)
ROI	Region of interest
SC	Single crystal
SEI	Solid electrolyte interphase
SEM	Scanning electron microscopy
SoC	State of charge
SoH	State of health
ToF	Time-of-flight
TM	Transition Metal
VSSA	Volume specific surface area ($m^2\,m^{-3}$)

WE	Working electrode
X-ray µCT	X-ray micro-tomography
X-ray nCT	X-ray nano-tomography
XRD	X-ray diffraction

INTENTIONALLY BLANK

List of Nomenclature

Nomenclature	Definition
C_6	Graphite
LiC_6	Lithiated graphite
$LiPF_6$	Lithium hexafluorophosphate

List of Symbols

Symbol	Definition
Z	Acoustic impedance
Q	Capacity (Ah)
i	Current (A)
ρ	Density (kg m^3)
D^{eff}	Effective diffusivity (m^2 s^{-1})
L_{eff}	Effective path length (m)
d_{sph}	Equivalent spherical diameter (m)
C_{irr}	First cycle irreversible capacity
z	Geometric tortuosity
h	Height (m)
I_0	Initial intensity of an X-ray beam (W m^{-2})
μ_A	Linear attenuation coefficient (m^{-1})
L	Path length (m)
υ	Poisson ratio
E	Electrode potential (V)
R	Reflection coefficient
c	Speed of sound (m s^{-1})
A	Surface area (m^2)
T	Temperature (°C)

t	Thickness (m)
τ	Tortuosity factor
I	Intensity of an X-ray beam (W m^{-2})
V	Cell voltage (V)
E$_{mod}$	Young's Modulus

INTENTIONALLY BLANK

Chapter 1

Introduction

1.1. Overview

The exploitation of carbon intensive fuels has contributed to a significant rise in global air pollution and global warming. As a result, the international community has developed strategies that reduce our reliance on these fuels and explored alternative sustainable means of providing energy, evidenced recently during the UN climate change conference (COP26) in 2021 and formerly the Paris Agreement climate proposal of 2016 [1] [2]. Fossil fuels are increasingly being replaced by renewable energy sources, such as solar and wind, particularly in the electricity supply and transport sectors [3]. In fact, renewable electricity is now cheaper per unit energy than oil but still more expensive than coal [4]. A plethora of electrochemical storage devices such as fuel cells and secondary (i.e., rechargeable) batteries have been developed to transition to renewable electricity sources. These devices operate by converting energy stored as chemical potential energy into electrical energy, by reversibly reducing and oxidising chemical species [5].

Electricity often offers advantages over other non-renewable energies, such as higher energy efficiency in the final production of energy services and lower local environmental costs. For instance, in the transport sector, electric vehicles (EVs) are more efficient than vehicles with internal combustion engines (ICE). However, decades of industrial development in ICE vehicles has led to them

being produced at a far lower cost, meaning battery powered vehicles are still more expensive [4].

More technological breakthroughs and pioneering research in secondary batteries for EVs can further reduce the costs of a transition to EVs. Today, lithium-ion batteries (LiBs) are the fastest growing and most promising secondary battery chemistry in the race to solve the climate crisis [6]. As well as having significant potential for use in EVs and grid scale applications, LiBs boast high energy capacity and high-power densities, and thus are also useful for portable electronic devices such as mobile phones and laptop computers [7].

1.2. A Brief History of Lithium-Ion Batteries

In 1980, John Goodenough developed a LiB at the University of Oxford, expanding upon earlier works from M. Stanley Whittingham on batteries containing a titanium disulfide cathode and a lithium-aluminium anode. Goodenough used a composition of lithium cobalt oxide (LCO), serving as a lightweight, high energy density positive electrode against a soft carbon negative electrode [8]. In 1991, Goodenough's work was commercialized through Sony by Akira Yoshino, and Asahi Kasei who had contributed additional improvements to the battery construction [7] [9]. The commercial Li-ion cell had a voltage of 4.1 V at top of charge, and an energy density of 80 Wh kg^{-1}, which was considerably higher than what nickel-metal hydride or nickel-cadmium technologies were capable of at that time [10]. Numerous commercially available LiBs available on the market today still utilise LCO and carbonaceous materials as electrodes.

In 1999, the development of novel electrode materials for LiBs gained new momentum to improve LiB performance and overall capacity. The discovery of a high capacity, high voltage Li-ion rich electrode material known as lithium

metal oxide (LMO) and contained manganese (Li_2MnO_3) was reported by Johnson et al. [11]. Just over a decade after, in 2011, lithium nickel manganese cobalt oxides (NMC) positive electrodes, which are a form of LMOs, were developed for LiBs at Argonne National Laboratory, and manufactured commercially by BASF in Ohio [12]. Multiple commercially available compositions of NMC exist today and are widely considered to play a vital contribution to next-generation LiBs. In fact, on Battery Day 2020, TESLA Motors outlined how they plan to vary the composition of NMC electrodes in a LiB to suit different EV applications in future designs [13]. This electrode material will be examined in detail in later chapters.
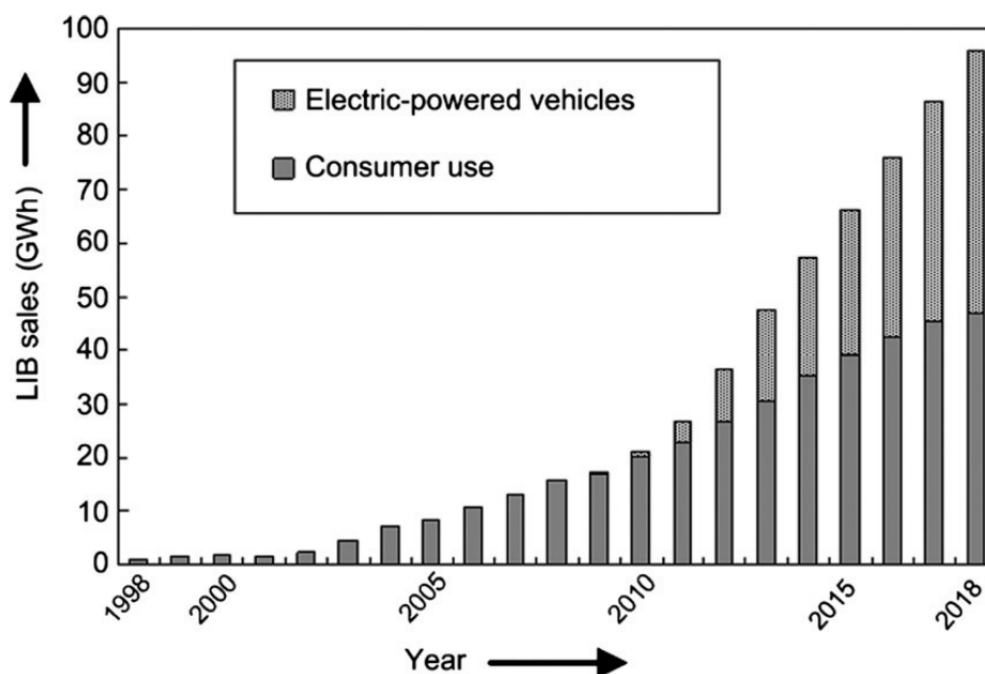
Figure 1: *The demand for LiBs in the last two decades in electric-powered vehicles and other consumer use. Reproduced from Yoshino* [8].

Numerous LiB configurations have been developed to meet market demand, including cylindrical spiral wound batteries, coin and wound prismatic designs that vary widely in capacity [8] [14] [15].

In 2019, John Goodenough, M. Stanley Whittingham and Akira Yoshino received the Nobel Prize in Chemistry for the development of LiBs [16]. In the

same year, the rechargeable battery market generated more than 600 GWh yr^{-1}. More than 160 GWh yr^{-1} of this was comprised of the LiB battery manufacturing market. As electric vehicles become more prevalent, the rechargeable battery market is set to increase to 1,500 GWh yr^{-1} by 2030 [17].

1.3. The Lithium-ion Battery

The lithium-ion battery consists of four main components: anode, cathode, separator, and electrolyte (Figure 2). During discharge, these batteries create an electron flow, which can be used to power a variety of devices. The anode and cathode are constructed of two dissimilar materials which accommodate the oxidation and reduction reactions of Li/Li$^+$ ions respectively. The battery's power is determined by the ease of electron-transfer between the anode and cathode, before flowing through the current collectors and electrical leads, enabling charge balance to complete the oxidation/reduction process [18]. The electrolyte provides a medium for Li$^+$ ions to flow between the respective electrodes. The purpose of the separator is to allow Li$^+$ ions to flow and ensure the anode and cathode do not electrically short circuit [19].

During discharge, electrons are given up by the anode and flow around the external circuit to the cathode. Meanwhile, Li$^+$ ions flow from the anode to the cathode through the electrolyte and vice versa for charging processes. During operation, the electrodes typically dilate or contract. During charge, the anode either intercalates or alloys with Li$^+$ ions (depending on the electrode composition) generally leading to a dilation, whilst the cathode deintercalates Li$^+$ ions generally causing a contraction. Oxidation/reduction and intercalation/deintercalation are two distinct chemical processes. Oxidation/reduction reactions involve the transfer of electrons between different chemical species, whereas intercalation/deintercalation involves the insertion and removal of ions or molecules between layers of a material.

Generally, alloying reactions cause more severe morphological changes than intercalation reactions and so thickness variations occur at a far larger scale in these systems (silicon, tin, germanium etc) [20]. The properties of a battery, such as its capacity, current capability, cycle life, safety, storage life, operating temperature and voltage, are determined by the materials used to construct the anode, cathode and electrolyte and its operating parameters [21].
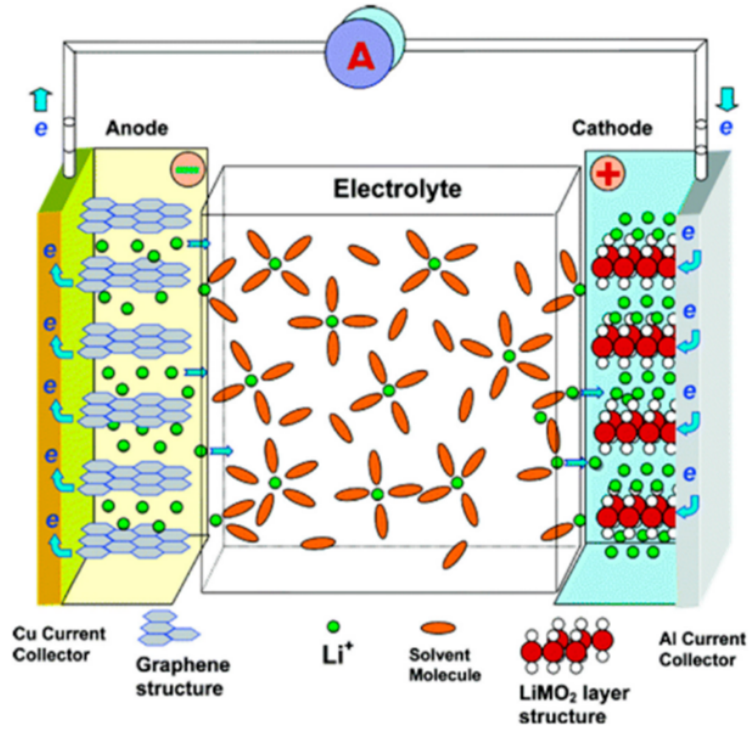
Figure 2: *A schematic representation of a LiB reproduced from Xu et al.* [22]. *The electrons are shown as 'e'.*

The cell potential (E_{Cell}) depends on the electrical conduction of the electrodes, the ionic conduction of the electrodes and electrolyte and the kinetics of the oxidation/reduction reactions. The potential difference between each electrode drives the oxidation/reduction reactions [18]. The various losses in an operating cell can be summarised as follows [23]:

$$E_{Cell} = E_0 - [(\eta_{ct})_{anode} + (\eta_{ct})_{cathode}] - [(\eta_c)_{anode} + (\eta_c)_{cathode}] - iR_i = iR \qquad (1.1)$$

Where E_0 is the standard cell potential, $\eta_{ct\ anode}$ and $\eta_{ct\ cathode}$ are charge transfer polarizations at the anode and cathode and $\eta_{c\ anode}$ and $\eta_{c\ cathode}$ are concentration polarizations at the anode and cathode, i is the operating current of the cell, R_i is the internal resistance of the cell and R is the apparent cell resistance [23].

1.4. Anode Chemistries

Graphite and silicon are the two most widely used anode materials in commercialised LiBs. Currently, graphite anodes feature in commercialised LiBs to a greater extent than silicon anodes despite the specific capacity of silicon being far greater than graphite [24]. The potential for widespread silicon anode-based LiBs is limited by silicon's ca. 300% volume expansion during operation [25]. However, recent LiB technologies have utilised graphite-silicon composite anodes, these compositions can facilitate higher capacities than standard graphite electrodes, and less detrimental volume expansion than pure silicon anodes [26].

Numerous carbon materials such as graphite, petroleum coke, carbon black, carbon fibre, mesocarbon microbeads and amorphous carbon, with a high diversity of physical and chemical features have been studied as Li$^+$ ion-intercalation electrodes [27] [28] [29] [30] [31]. However, graphite is the most widely used commercial anode material in LiBs because of its high coulombic efficiency and cycle performance. Graphite owes its popularity to having the lowest irreversible capacities (<100 mAh g^{-1} $_{Graphite}$) and reasonable reversible capacity values (372 mAh g^{-1} $_{Graphite}$) . It also has an almost constant electrode potential during charging and discharging, close to Li$^+$/Li potential (approximately 0.1-0.2 V higher, enough to prevent lithium metal deposition). Furthermore, graphite is a low-cost material compared to other anode chemistries [32].

To date, much research effort has been focused on the chemical processing and electrochemical properties of Li^+-intercalated graphite which has a capability of intercalating Li^+ ions to x = 1 in Li_xC_6, equal to a gravimetric specific capacity of 372 mAh $g^{-1}_{Graphite}$ [33] [34].

$$xLi^+ + xe^- + C_6 \rightarrow Li_xC_6 \tag{1.2}$$

In graphite, Li^+ ion occupation sites are between two adjacent C layer planes (layers), where one Li^+ ion is associated with a hexagonal C ring in the LiC_6 structure [35] [36]. A depiction of the Li^+ ion intercalation mechanism of a graphite electrode is shown in Figure 3.
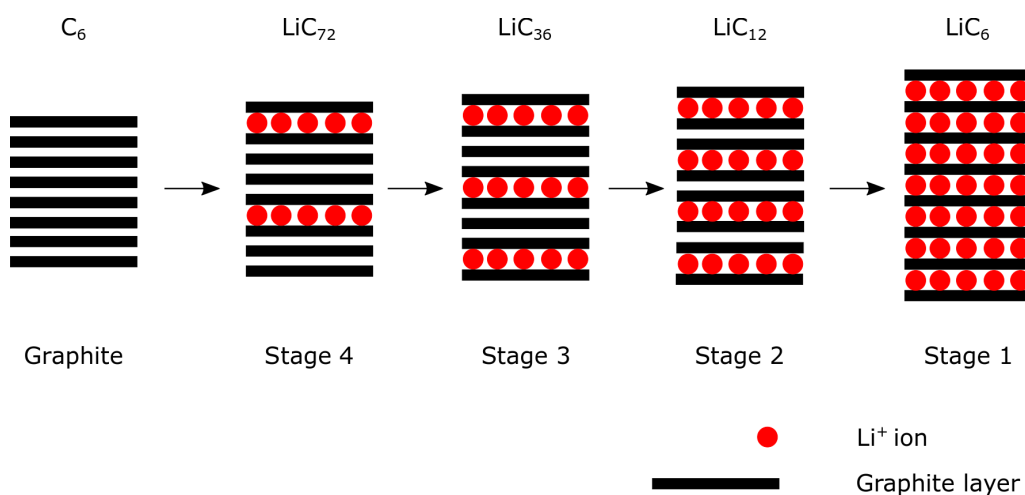
Figure 3: *Schematic illustration of the intercalation mechanism of Li⁺ ions into a graphite electrode.*

Table 1: A comparison of the various anode materials for LiBs [37].

Anode material	Specific capacity (mAh g⁻¹)	Volume change (%)	Benefits	Challenges
Lithium	3,862	None	Highest energy density; light	Unstable during fast charging, safety concerns
Silicon	3,600	~300	High energy density	Capacity fade due to irreversible volume changes
Aluminium	2,235	~600	High energy density	More severe volume changes than silicon and poorer capacity
Tin	990	~250	More stable than silicon and aluminium	Lower energy density than aluminium and silicon
Graphite	372	~10	Highly stable; Minimal volume changes, widely used	Relatively poor energy density

1.5. Cathode Chemistries

Layered materials such as nickel manganese cobalt oxide, $Li_{1-x}NiMnCoO_2$ (NMC) and nickel metal oxides, $Li_{1-x}NiMO_2$ (NMO) are widely used for electric and hybrid-electric vehicles owing to their long-range operation and fast-charging. Their layered structures enable much higher capacities (> 200 mAh g⁻¹ $_{NMC}$) and favourable rate capabilities (electronic conductivity ≈ 2.8×10^{-5} S cm⁻¹ and Li⁺ diffusivity of 10^{-8} to 10^{-9} cm² s⁻¹), compared to traditional cathode materials such as $LiCoO_2$ and $LiMn_2O_4$ spinel (Figure 4) [38] [39] [40]. However, such layered structures face three fundamental challenges: capacity fading; slow charge/discharge rates; and, voltage instability (poor cycling performance when charged to high potentials) [41].

$$LiMO_2 \rightarrow Li_{1-x}MO_2 + xLi^+ + xe^- \qquad (1.3)$$
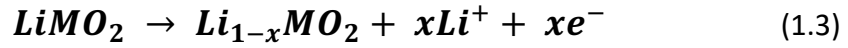
Multiple commercially available compositions of NMC exist; however, three specific variants are typically used in battery technology analysis: $LiNi_{0.33}Mn_{0.33}Co_{0.33}O_2$ (NMC111), $LiNi_{0.6}Mn_{0.2}Co_{0.2}O_2$ (NMC622) and $LiNi_{0.8}Mn_{0.1}Co_{0.1}O_2$ (NMC811) (the numbers correspond to the ratio of nickel, cobalt and manganese on a mole fraction basis) [42].
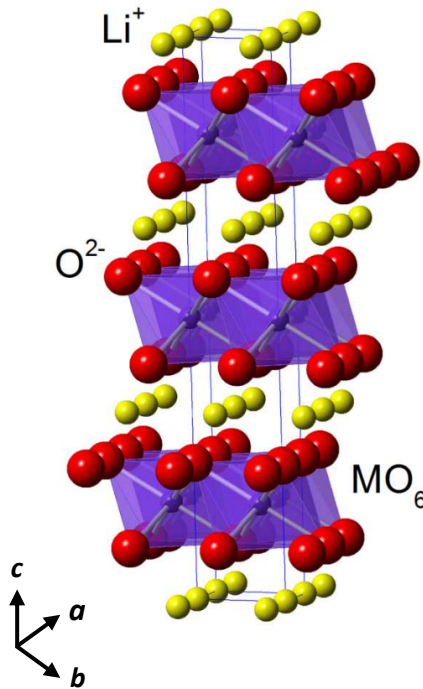
Figure 4: *The crystal structure of $Li_xNi_yCo_zMn_{(1-y-z)}O_2$ NMC cathode reproduced from Wang et al.* [43] *with the crystallographic axes of the material.*

The *a*-axis of NMC runs perpendicular to the surface of the layered crystal structure and represents the direction of highest lithium-ion mobility. It is aligned with the edges of the hexagonal crystal structure. The *c*-axis of NMC runs perpendicular to both the *a*-axis and the electrode surface and represents the direction of the crystal's symmetry. It is aligned with the crystal's basal plane, which is the plane in which the layers of transition metal and lithium ions stack on top of each other [44].

The energy content increases as the nickel content increases in the NMC class of materials whilst stability decreases [45]. Moreover, high nickel content materials also tend to lead to extra processing costs. The manganese and cobalt ions in these mixed metal electrodes has a stabilizing effect and prevent cathode corrosion that can lead to failure [46]. NMC111 is a commercially well-established composition; NMC622 has made a recent market introduction and NMC811 is favoured on the automotive roadmaps due to its higher energy content. Nonetheless, it still experiences significant capacity fade, higher safety risks and electrochemical tests from half cells and full cells show poor cycling performance when charged to potentials above 4.2 V [42] [47] [48] [49] [50].

Table 2: A comparison of the various cathode materials for LiBs [51].

Cathode material	Specific capacity (mAh g^{-1})	Benefits	Challenges
Lithium nickel cobalt aluminium oxide (NCA)	200	Highest specific energy density.	Very expensive. Medium lifetime.
Lithium nickel manganese cobalt oxide (NMC)	170	High energy density. Long lifetime.	Safer than LCO but still relatively unstable and expensive.
Lithium iron phosphate (LFP)	165	Medium-high energy density. Long lifetime. Iron is abundant and cheap.	Lower energy density than NMC. Medium cost.
Lithium cobalt oxide (LCO)	145	High energy density.	Volatile and expensive. Cobalt is toxic. Medium lifetime and cost.
Lithium manganese oxide (LMO)	120	Manganese is abundant and environmentally friendly.	Low lifetime.

1.6. Research Motivation

There are multiple degradation mechanisms at play in the ageing of a LiB. Learning about how to predict which mechanism, or combination of mechanisms, is most critical in particular conditions is vital to understanding and mitigating degradation, especially for ostensibly similar Li-ion cells [52].

Electrode and particle morphology can influence cell degradation. For instance, some particles can be more susceptible to cracking, leading to variable gas formation, particle-binder rearrangements and LiB swelling. The particle-binder rearrangements that occur in an electrode during prolonged cycling may vary according to its particle morphology. Understanding the implications of different particle morphologies on degradation mechanisms is of critical importance, as this can be used to inform future electrode designs to minimise degradation and improve overall cell durability and cycling performance.

LiB electrodes undergo thickness changes during cycling depending on their stoichiometry and structure [53] [54]. These thickness changes can cause mechanical fracture of the active materials and structural disintegration of the particle-binder matrix, leading to electrically isolated active particles causing capacity fade. These dynamic changes therefore pose an engineering and design challenge during cell design and manufacturing. Information on the rate of these thickness changes can guide battery housing/module design in next generation EVs and improve overall cell diagnostics [55].
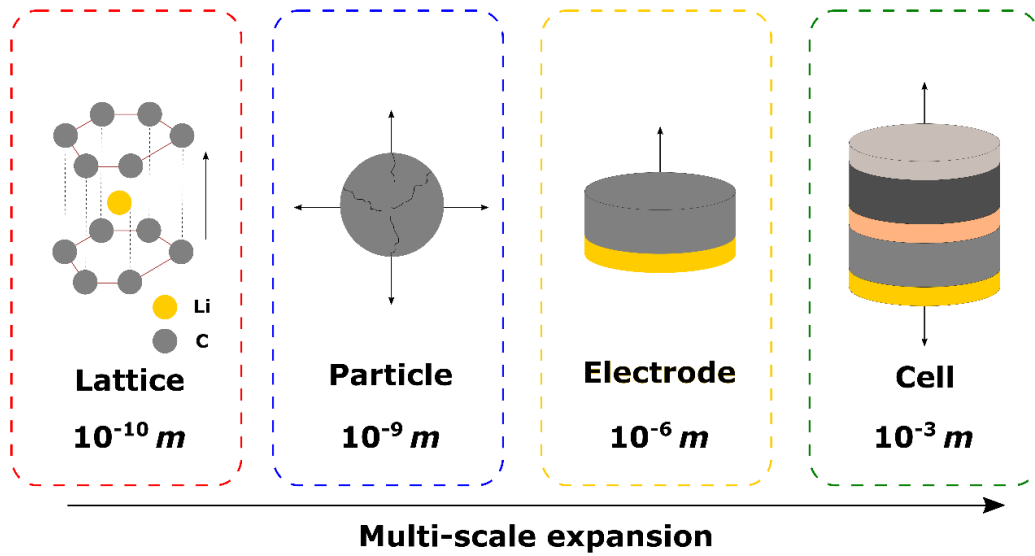
Figure 5: Illustration of the dimensional changes that occur in a LiB at different length-scales.

Figure 5 shows the volume expansion that occurs at various length-scales in LiBs which contributes to the overall cell expansion; therefore, a comprehensive approach is required to understand LiB expansion. Various experimental techniques are required to facilitate a multi-scale approach to understanding the volume expansion mechanisms at various length-scales.

1.7. Research Aims and Objectives

Through a variety of electrochemical and imaging techniques, encompassing tomography, dilatometry and acoustic spectroscopy, the aim of this thesis is to better understand the mechanisms driving the degradation of LiBs.

Specific objectives of this research are:

- To inspect electrode properties that contribute to, or are caused by, cell degradation using X-ray imaging techniques.

- To reveal vital information about spatial variations in microstructural parameters across the thickness of commercially available LiB electrodes and measure the thickness changes of electrodes during operation.

- To identify the various experimental techniques that can be combined with *in-situ* electrochemical dilatometry (ECD), which is a technique used to measure thickness changes of a sample material, in order to better elucidate the degradation of LiB electrodes.

- To evaluate how electrochemical acoustic time-of-fight (EA-ToF) spectroscopy can be used in conjunction with X-ray CT to examine the physical properties of ostensibly similar LiBs that vary only in particle morphology of the NMC811 electrode.

- To evaluate differences in physical properties within entire LiBs composed of NMC811 electrodes with different particle morphology during cycling, and to determine whether these differences correlate with changes in exterior cell temperature and cycling performance.

1.8. Thesis outline

The thesis is organised into the following chapters:

Chapter 2 details the basic principles of LiBs and provides a review of literature focusing on the 3D microstructural characterisation of degradation in LiBs. Key findings are discussed from works that use the experimental techniques that are also used in this thesis.

Chapter 3 provides fundamental theory to the various experimental techniques used throughout this body of work, namely ECD, X-ray CT and ultrasound detection studies. This chapter also discusses the procedure for electrode characterisation and battery cycling techniques.

Chapter 4 is the first of the results chapters and showcases the findings of ECD measurements of graphite electrodes during cycling. Morphological characterisation of the tested graphite electrode is carried out and compared to a pristine electrode with image-based modelling, using X-ray CT with the intention to assess electrode degradation after cycling and in turn undergoing numerous thickness changes.

Chapter 5 is the second results chapter that reports the findings from ECD measurements. This chapter showcases the dilatometric investigations of NMC811 electrodes during cycling. Similarly to chapter 4, X-ray CT is used to characterise the morphology of NMC811 electrodes to discern the health of the electrode prior to and after dilatometric testing and deduce whether cycling caused noticeable changes in electrode morphology. Differential electrochemical dilatometry (D-ECD) is also showcased in this chapter, which

was used to record the rate of thickness changes in NMC811 electrodes, revealing whether faster thickness changes occur at certain stages of charging.

Chapter 6 is the penultimate results chapter. X-ray CT instruments of various resolutions are utilised to probe the internal architecture of wounded Li-ion pouch cells containing varied cathode particle morphology. A multi-scale visual examination of the cell is reported in this chapter including cell, electrode and particle level characteristics. These experiments were incumbent to reveal electrode microstructure and particle morphology that can have implications on cell degradation and acoustic spectroscopy experiments.

Chapter 7 is the final results chapter and includes all acoustic experiments of the LiBs containing electrodes with varying particle morphology. In chapter 7, electrochemical acoustic time-of-flight (EA-ToF) spectroscopy is examined as a diagnostic tool for LiBs to determine whether it is an effective tool in measuring degradation mechanisms in wounded pouch cells that vary in particle morphology at the cathode. The physical changes of these batteries are measured using EA-ToF spectroscopy during cycling and any changes in exterior cell temperature are measured in parallel.

The final chapter (chapter 8) provides a conclusive summary of the thesis and proposes suggestions for future investigations.

INTENTIONALLY BLANK

Chapter 2

Literature Review: Microstructural Degradation of Lithium-Ion Batteries

2.1. Overview

Degradation mechanisms can occur across length-scales from nano to microscopic, and over a broad timeframe from seconds up to years. Therefore, a comprehensive understanding of the causes and effects of degradation of LiBs necessitates a synergistic investigation across these scales and time frames with numerous experimental techniques. The morphological changes in active material in the porous electrodes, is driven by their electrochemical reactions with Li$^+$ ions, which can subsequently alter the electrode microstructure. The performance of the device, specifically its capacity and charge/discharge times, is dictated by the microstructure of the electrode [56]. A detailed illustration of the various degradation mechanisms that can occur in LiBs is shown in Figure **6**.
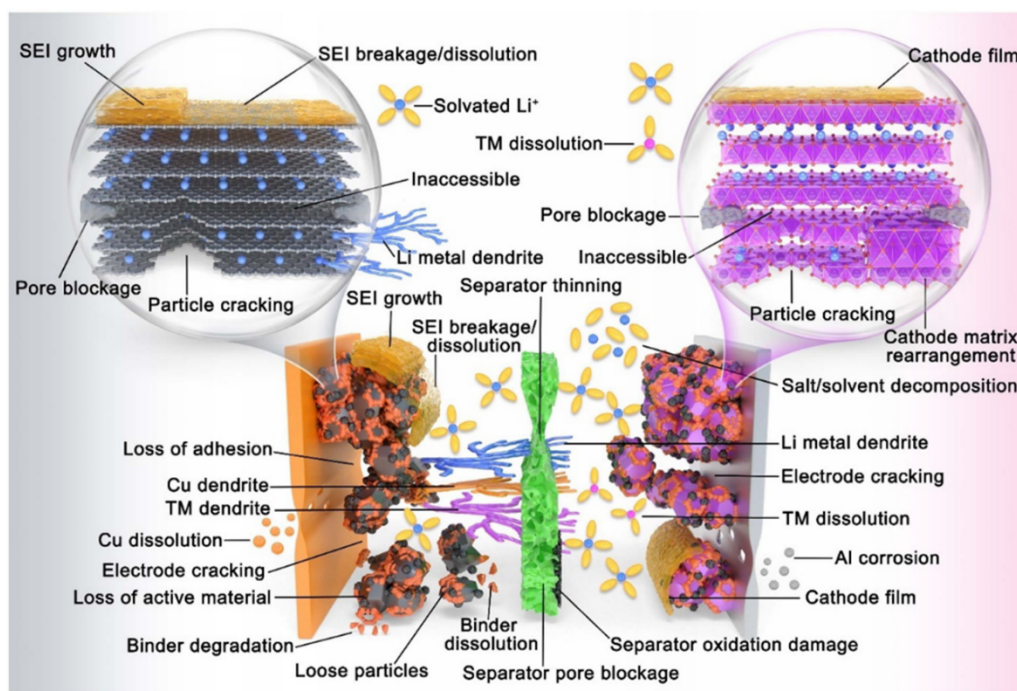
Figure 6: *An illustration of the various degradation mechanisms in a LiB highlighting the complex interplay of degradation phenomena in a cell. Reproduced from Majasan et al.* [57].

During prolonged charge/discharge cycling, reversible Li$^+$ ion transport leads to active materials in the electrode undergoing alternating volume expansion and contraction. The consequences of electrode expansion are far-reaching and can cause a propagation of microstructural defects that compromise the mechanical integrity and function of the cell resulting in capacity loss [58]. For instance, electrode expansion can reduce the flexibility of the electrode binder during prolonged cycling, which leads to active material particles cracking and pulverizing. Irreversible expansion can also reduce the cycle life of LiBs [59] [60].

Electrode fracture and loss of adhesion can lead to capacity loss when it causes the active particles to no longer be electrically connected to the current collector, each other or the carbon matrix in which they are embedded. It can also arise when the battery material undergoes volume changes during

charging and discharging [61]. Many approaches exist to overcome effects caused by changes in volume. Efforts are being concentrated on binders and electrolyte additives because a large irreversible specific charge loss occurs during the initial cycles. Charge loss is related to the high surface area of nanoparticles, and in the absence of surface passivation measurements, the overall electrode electrolyte interface increases [62].This Chapter will detail the degradation mechanisms of electrode materials that are investigated throughout this thesis. In addition, a review of studies that use experimental techniques that are also used in this thesis is provided along with their key findings.

2.2. Degradation of Graphite Electrodes

Dilation and contraction are common for crystal structures that have a layered lattice and undergo intercalation/deintercalation of guest ions. When graphite/lithium cells are discharging (applying a constant negative current), Li^+ ions intercalate between the graphene layers and the electrode increases in height (dilates). During charging (constant positive current), Li^+ ions deintercalate causing the electrode's height to decrease (contract). Note that the notation of charge and discharge here is applicable to the graphite/lithium 'half-cell' and will be different for full cells [63] [64].

Solvent molecules can intercalate between graphite with Li^+ ions because Li^+ ions are susceptible to solvation during lithium diffusion through the electrolyte. Solvated Li^+ ion intercalation can cause severe exfoliation of graphite particles resulting in their destruction, because the intermolecular forces between the graphene layers of graphite are weak and solvent molecules are often much larger than Li^+ ions [33]. In addition, significant dynamic stress or expansion of free-standing cells can arise from a high cycling load of the electrodes. Expansion of graphite can cause deformations as large

as 13% of the anode volume during full lithium intercalation [65]. Furthermore, the reduction of solvent molecules leads to gases forming which can cause the graphite particles to crack when using propylene carbonate-based electrolytes. However, ethylene carbonate-based electrolytes do not pose this risk [66]. Graphite electrode stability and reversibility depend significantly on passivation in continuous lithium intercalation/deintercalation cycling and the stress that evolves inside batteries is also related to the rate of charging [67] [68].

A solid electrolyte interphase (SEI) grows and deposits on the surface of graphite anodes due to irreversible electrochemical decomposition of the electrolyte, which competes with the faradaic half-cell reaction at the electrode surface (Figure 7). An SEI layer consists of electrolytic salts and forms at the anode because commonly used electrolytes are unstable at operating potentials of anodes during charging [69]. Electrolyte decomposition that occurs during the formation of an SEI on the electrode surface is the primary source of gas evolution in LiBs [70].

$$\boldsymbol{Li^+(Solvent)_n \; \rightarrow \; Li^+ + nSolvent} \tag{2.1}$$

$$\boldsymbol{Li^+ \; \rightarrow \; Li^+_{SEI}} \tag{2.2}$$
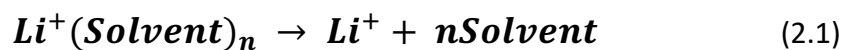
The SEI layer provides protection for the graphite electrode from co-intercalation of electrolyte solvent molecules. However, the process of forming the SEI layer consumes Li^+ ions, leading to an irreversible loss of battery capacity. The SEI layer that forms on graphite anodes is very thin ($\sim$20 Å to several hundred angstroms) [71], and therefore is unlikely to significantly affect the thickness change of a graphite anode over numerous cycles.
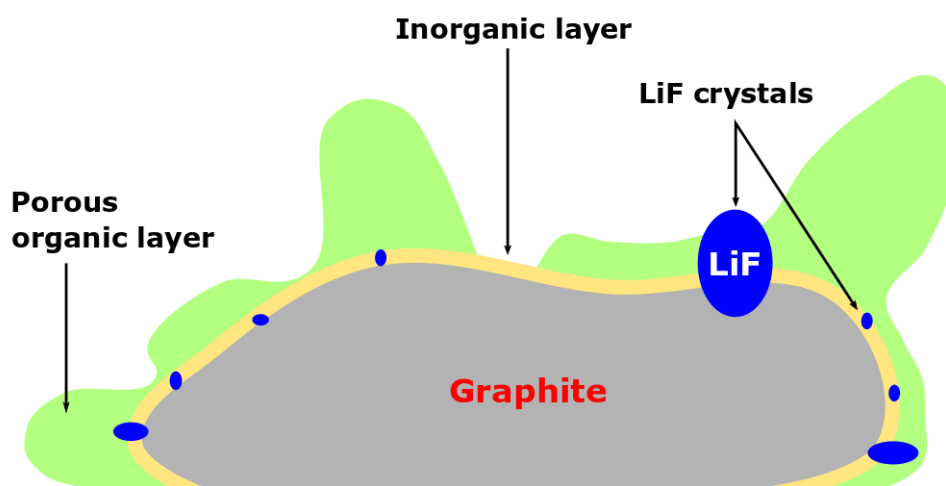
Figure 7: A schematic of the SEI layer that forms on a graphite particle. Adapted from Edstrom et al. [71].

SEI can be more easily formed by using conductive additives in the electrolyte. Conductive additives are substances that are added to the electrolyte of a LiB to improve its electrical conductivity. These additives are typically organic compounds that have good electrochemical stability and low volatility. Conductive additives can help to improve the performance of LiBs by reducing their internal resistance and increasing their energy density. They can also help to extend the lifespan of the battery by improving its stability and preventing the formation of harmful by-products [72].

Numerous compounds have been observed to deposit on the surface of graphite electrodes as part of the SEI [73] [74] [75]. The type of Li^+ ion salts in electrolytes have a direct influence on the proportion of inorganic and organic components in the SEI layer. Most electrolyte salts ($LiBF_4$, $LiPF_6$, $LiAsF_6$, etc.) cause a layer of LiFs to form on the electrode surface. Temperature and trace impurities affect the size and number of LiF crystals that are found in the SEI [71]. A higher abundance of LiF compounds can be found in graphite anodes at lower temperatures [71] [76] [77].

2.3. Degradation of NMC811 Electrodes

Layered NMC811 electrodes have the potential to be among the highest energy cathodes for next generation LiBs, however numerous degradation mechanisms play a part in NMC811's cycling performance which can be traced back to its stoichiometric ratios of nickel, manganese and cobalt. For example, there is now general consensus that decreased structural and thermal stability accompanies increasing nickel content [78] [79] [80]. The more nickel and less manganese and cobalt, the lower the onset temperature of a phase transition (from layered to spinel), which is associated with large amounts of oxygen release [81].

NMC811's high nickel content means that it is hindered by its high surface reactivity resulting in a shorter lifetime than other NMC chemistries such as NMC111 [82]. A high proportion of nickel and low proportion of manganese as a structural stabilizer can also promote side reactions such as cation mixing of the large amounts of Ni^{4+} on the surface layer of the electrode and Ni^{2+}. Consequently, severe capacity fading can occur due to the structural instabilities in nickel-rich cathode materials. Other factors innate to NMC chemistries can also contribute to the degradation of NMC811 electrodes, such as active material dissolution, oxygen release and intergranular cracking of primary particles [83]. Heenan *et al.* found that varying manganese content within NMC particles may correlate to crystallographic disordering using fluorescence and X-ray diffraction. They reported that the mobility and dissolution of manganese may have ramifications on NMC811 electrode degradation during initial cycling [84].

Cobalt plays an important role in suppressing cation (Li/Ni) mixing and enabling high rate capability [85] [86]. However, current efforts are focused on reducing or entirely removing cobalt in transition metal electrodes owing to its finite

availability, high cost and ethical concerns relating to cobalt mining. This has led to various NMC chemistries developed with incremental changes in stoichiometric ratios e.g., the NMC-111→NMC-622→NMC-521→NMC-811 and aluminium-doped NMC (sometimes referred to as NMCA) [87]. However, drawbacks from reducing cobalt content have been reported in literature, including poor rate capability and/or severely restricted compositional tuning. Furthermore, the poor rate capability that arises during cycling is owed to manganese incorporation that promotes Li/Ni mixing and is preventable with a counterbalancing ion such as cobalt [87] [88] [89].

NMC811 electrodes are also susceptible to macroscopic degradation in the form of active material delamination from the current collector and the loss of bulk mechanical integrity during high voltage operation. This mechanism is attributed to binder adhesion degradation [84].

2.4. Dilatometric Characterisation of LiBs

2.4.1. Overview

Electrochemical dilatometry (ECD) is a useful tool for monitoring thickness changes and demonstrating that irreversible dimensional changes can be reduced by, for example, reducing the loss of active material during operation. As a voltage is applied to a sample, it expands or contracts depending on its composition and its length or height changes. This change in height or length is detected by the displacement transducer, which converts the mechanical displacement of the sample into an electrical signal. The signal is then recorded by a computer, which plots the change in sample length or height as a function of voltage.

It is a tool capable of showing alterations in irreversible dilation depending on electrode design and experimental set-up and thus is a useful technique for assessing battery stability and lifetime. There are multiple different ECD set-ups, which include instruments capable of monitoring single electrode expansion and those capable of monitoring electrode stacks. However, resolution can reduce as the measured volume/sample size is increased. Also, expansion and contraction of an electrode during operation is expected to occur even in relatively healthy cells. For instance, graphite anodes in LiBs dilate during ion intercalation and contract during ion deintercalation. Therefore, these volume changes are not necessarily a reflection of any degradation mechanism.

Most ECD experiments are conducted *in-situ* to examine dimensional changes during cycling. However, ex-situ dilatometric measurements of thickness changes after cycling have also been carried out on electrochemical devices [90] [91]. A drawback of making these measurements after cycling is that it is not possible to deduce the nature of the measured dimensional changes. For instance, reversible thickness changes can be a result of particular phase transitions that can occur at certain voltages. Lee *et al*. [67] have argued that ECD experiments cannot distinguish between electrode expansion and displacement due to gas evolution, and that neutron imaging is capable of detecting these differences, if the gas accumulated is large enough due to the change in density and transmission through the tested material [67]. Modern dilatometer design can effectively manage and mitigate unwanted pressure build-up due to gas evolution.

When choosing an instrument for dilatometric studies, three main questions arise. Firstly, is the resolution sufficient? This is particularly important for studying cathode materials that undergo constant but less significant volume changes than their anode counterparts. Secondly, does the instrument provide

a suitable working temperature range? Different models are selected when studying materials at temperatures higher than 700 °C owing to limitations in push-piston dilatometers. Push rod dilatometers allow measurements to be taken between 0 °C and 1200 °C [92] [93] [94]. Thirdly, is the cell hermetically sealed? The cell has to be assembled in a way to avoid moisture or air contamination, particularly for sensitive cathode materials.

2.4.2. Graphite

Biberacher *et al*. [95] and Besenhard *et al*. [96] were among the first published studies to use dilatometry to investigate graphite's dilation during cycling [97] [98]. Hahn *et al*. [99] demonstrated that graphite electrodes undergo height changes as the stoichiometry of graphite changes with Li$^+$ ion intercalation across a time frame of 40 hours using the in-house construction described in their earlier works [99]. When graphite was fully intercalated and thus the height change was largest, the highest recorded value of expansion was also recorded by the dilatometer. They showed that stoichiometric changes that occur to an electrode material due to lithium intercalation can be evidenced using dilatometry and the results were confirmed with X-ray diffraction (XRD) studies [100]. Another example of a study that used XRD in tandem with dilatometry is Hantel *et al.* [101] who used *in-situ* XRD and *in-situ* ECD to reveal electrochemical activation of partially reduced graphite oxide to irreversibly modify the interlayer distance. The three electrode dilatometer cell used in this study was developed in-house and was the same as that used by Hahn *et al.* [102].

In LiBs, SEI formation and the electrochemically driven growth of passivation layers on graphite is a subject of dilatometric studies. ECD is sensitive to amorphous phases and SEI formation, as long as the resolution of the instrument is sufficient to detect the change in electrode thickness [103]. The irreversible formation of a stable SEI layer can be accelerated by electrolyte

additives, which contributes to electrode swelling [104]. An example of a commonly used electrolyte additive in LiBs is vinylene carbonate. Ivanov *et al.* [104] investigated how varying the concentration of vinylene carbonate in electrolytes affected the volumetric expansion of graphite composite electrodes in LiBs (Figure 8).
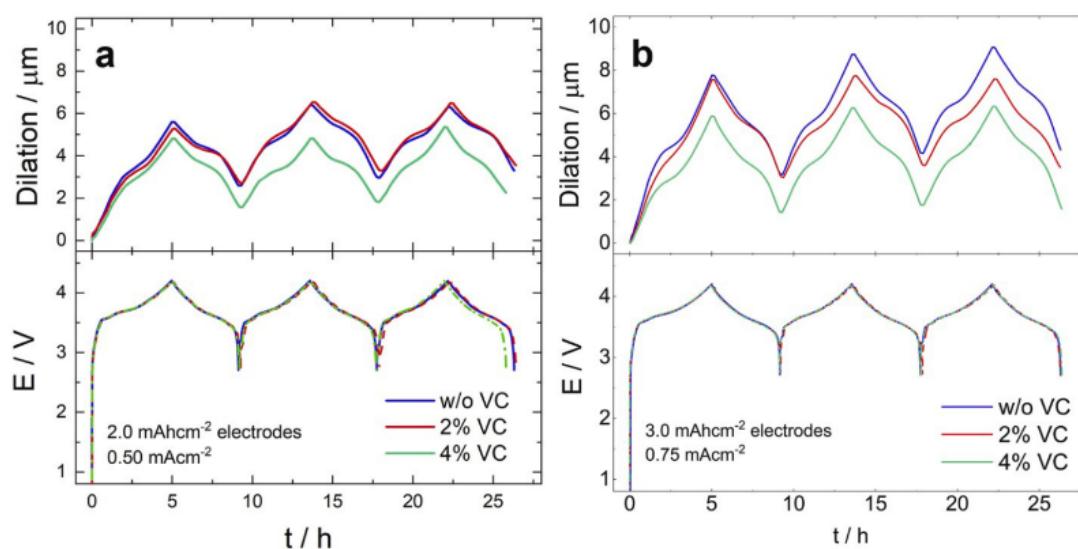
Figure 8: *Dilation-time (top) and potential-time profile (bottom) of Graphite/NMC cells for (a) 2.0 and (b) 3.0 mAh cm^{-2} nominal capacity and constant 23% porosity. ECD measurements are taken during three C/4 charge/discharge cycles. Electrolyte composition: 1 M LiPF6 in ethylene carbonate: ethyl methyl carbonate 3:7 (w: w), without vinylene carbonate - (blue), 2% vinylene carbonate - (red) and 4% vinylene carbonate - (green). Reproduced with permission from Ivanov et al.* [104].

In this study, a graphite electrode with no vinylene carbonate additive underwent a maximum of 8 μm dilation at the end of first discharge. In contrast, a graphite electrode with 4% vinylene carbonate underwent a maximum of 6 μm dilation at the end of first discharge. It was concluded that irreversible dilation is largely influenced by the vinylene carbonate concentration in the electrode. X-ray photoelectron spectroscopy measurements revealed that the

addition of additives allowed for a thicker SEI layer to be established which contributed to the irreversible dilation recorded. However, SEI layers are typically expected to be on the nanometre scale, and an overall decrease in irreversible dilation was observed when adding higher concentrations of vinylene carbonate, despite a thicker SEI layer. This was associated with differences in electrolyte decomposition and adsorption/incorporation of chemical products produced during cycling. Additional irreversible volume expansion occurred due to the incorporation of soluble decomposition products into the electrode when no additives were used [104].

Most dilatometric studies of graphite in the literature use similar variants of galvanostatic cycling parameters to record the dilation/contraction arising from continuous intercalation of Li$^+$ ions. However, Bauer et al. elected to use galvanostatic intermittent titration techniques for high-rate dilatometry experiments, focussing particularly on the relaxation phenomena that graphite/NMC pouch cells underwent after current pulses [64]. They used the ECD-1 dilatometer for single electrode experiments and an in-house developed dilatometer for whole cell dilation experiments. The ECD-1 dilatometer could detect height changes from 20 nm and the cell drift-stability was < 0.1 μm h^{-1} in an empty cell. The in-house developed dilatometer had a resolution of 1 μm. The in-house developed dilatometer was used for high-rate dilatometry experiments, and the ECD-1 dilatometer was used for low-rate dilatometry experiments. They suggested that the ECD-1 dilatometer was not suitable for fast C-rate experiments due to the large borosilicate glass separator used in the instrument, which could have contributed to diffusion limitations of Li$^+$ at high C-rates evidenced by the fast capacity fading. Furthermore, they found that the ECD-1 dilatometer has a resolution that is sufficient to detect lithium plating in graphite anode dilation data at high SOCs, whereas moderate lithium plating is difficult to discriminate during charging at mid-range SOCs. Therefore, this study suggests that there's potential for this instrument to be used in safety

tests, that evaluate the safety of LiBs such as by detecting lithium plating during overcharge and overdischarge tests.

Numerous articles report the volume changes in graphite electrodes during cycling, using *in-situ* ECD, with dimensional changes ranging between 4 to 13% owing to differences in electrode composition, electrolyte and cell configuration [64] [33] [65] [68] [105] [106] [107] [35] [108] [109] [110] [111]. Graphite particles can rearrange themselves in the particle-binder matrix as they expand and contract during cycling, which leads to severe contact stresses and fracturing of particles that are packed closely together [112]. Electrode delamination that causes the graphite particles to no longer be connected to the current collector has also been proposed as a degradation mechanism that influences ECD measurements [63]. In addition, calendering during the manufacturing process can give rise to stresses at the cell level, which cause the electrode material to fracture [113]. Calendering involves compressing dried electrodes by passing the electrode between two rollers to increase electrode density and improve its energy and power density. This process reduces electrode porosity [114]. Nonetheless, despite variation in the scale of thickness change, a consistent dilation/contraction behaviour has been recorded across numerous reports, reconciling the thickness changes that occur during phase transitions at certain voltages.

2.4.3. Cathode chemistries

Cathode dilation is often neglected in dilatometric research because thickness variations at the cathode are of a much smaller magnitude compared to the anode, and thus the consequences of cathode dilation are thought to be far less detrimental to the cycling capability of LiBs [64]. Although studies seldom report cathode material dilation in comparison to anodic dilation, Rieger *et al*. reported a thickness change of 1.8% for a $LiCoO_2$ cathode during delithiation using dilatometry [115]. They reported high overpotentials in potential curves

and argued that it was a result of the large distance (ca. 500 μm) between the reference electrode and working electrode (WE). Yu *et al*. highlighted limitations in dilatometry cell configurations, with overpotentials reported due to mass diffusion limitations [116]. In order to conduct dilatometry experiments, Rieger *et al*. assembled segments of the pouch cell battery electrode into a dilatometer; the battery selected had two single-sided cathode layers towards the top and bottom of the electrode stack, which were used for the dilatometric experiments of the cathode (symmetrical cell). For the dilatometric experiments on the graphite anode, an electrode was cut and placed inside the dilatometer from the pouch cell electrode bilayer. Although graphite was coated on both sides of the bilayer, only one side participates in the electrochemical reaction inside the dilatometer assembly. This is because the copper current collector acts as a barrier for Li^+ ions. This study demonstrates that dilatometry can be a useful tool for investigating commercially available Li-ion batteries with a pouch cell configuration. The drawback to this approach is that it destroys the pouch cell since it cannot be reassembled after measurements.

NMC is a cathode material widely used in commercial LiBs. The stoichiometry and thus structure of NMC can vary depending on the ratio of nickel, manganese and cobalt, respectively [117]. Nayak *et al*. demonstrated that dilatometry can be utilised to monitor reversible and irreversible processes of NMC in LiBs. They prepared a lithium rich $Li_{1.17}Ni_{0.20}Mn_{0.53}Co_{0.10}O_2$ cathode material using a sol-gel method and investigated the dimensional changes that occur during galvanostatic cycling (see Figure 9) [118].
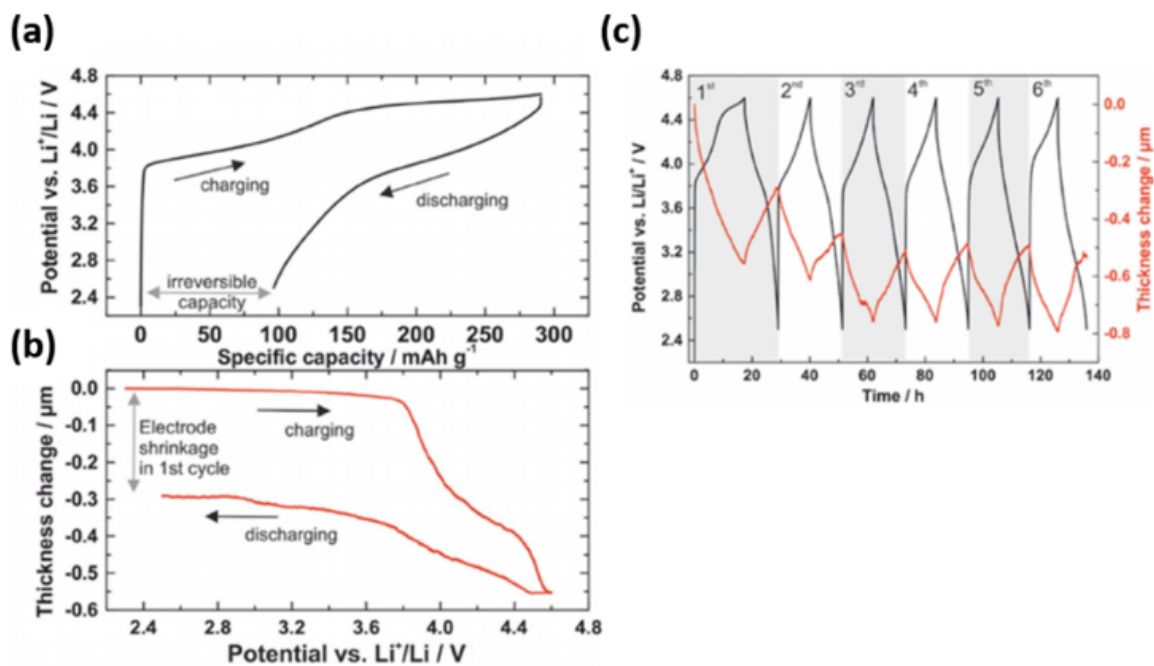
Figure 9: (a) Potential-specific capacity profile and (b) thickness change-potential profile of $Li_{1.17}Ni_{0.20}Mn_{0.53}Co_{0.10}O_2$ at 20 mA g^{-1} (C/10 rate) in the potential range of 2.5-4.6 V in 1 M $LiPF_6$ in ethylene carbonate/dimethyl carbonate solution. The potential-time and thickness change profile are shown in (c) for $Li_{1.17}Ni_{0.20}Mn_{0.53}Co_{0.10}O_2$ at 20 mA g^{-1} (C/10 rate) in the same voltage range as (a) and (b) for six consecutive cycles. These images were reproduced with permission from Nayak et al. [118].

In-situ ECD revealed an irreversible contraction/expansion during charge/discharge which correlated to irreversible capacity loss during the first cycle. A large voltage hysteresis and substantial voltage loss on first charge/discharge is thought to occur because of the formation of molecular O_2 at 4.6 V versus Li^+/Li, which becomes trapped in voids within the particles in the bulk and is thereby lost from the surface. The O_2 that forms during first charge causes the disorder of the transition metal ions associated with the loss of the honeycomb structure, which thus forms vacancy clusters that accommodate O_2 [119]. Dilatometry confirmed that reversible electrode contraction/expansion

occurred after initial cycling, quantitatively confirming the good cycling stability of this material. The absolute change in electrode thickness during cycling was about 0.27 µm during prolonged cycling. The electrode periodically "breathed" with each cycle by less than one percent compared to its total thickness. Overall, the dilatometer proved to be a very useful instrument in examining the reversible and irreversible processes in composite electrodes with thickness changes as small as 1% of the total electrode thickness. The dilatometer contained a high-resolution capacitive transducer that was able to detect dimensional changes at the WE down to a few micrometre resolution. Dilatometers with different detectors have also been used. Ariyoshi *et al*. [120] used a dilatometer with a linear voltage displacement transducer to detect the dimensional changes of LTO/LiCoMnO$_4$ LiB during galvanostatic cycling. The same model was used by Nagayama *et al*. and is an in-house fabricated assembly [121]. The dilatometer uses a pouch cell test sample and thickness changes of the cell are transmitted via a spindle to a linear voltage displacement transducer. The transducer is connected to an amplifier that converts displacement signals in micrometres to a voltage signal in mV [121].

Cathode materials also undergo volume changes during cycling which are dependent on their stoichiometry and structure. Nonetheless, the influence that cathode material dilation and contraction have on battery performance, and overall cell dilation, is often neglected as it is assumed to be an order of magnitude smaller than the anode dilation [64]. In fact, multiple studies that report dimensional changes of cathode material primarily focus on pouch cells as opposed to individual electrodes [122] [123]. It is possible that dilatometric investigations focusing entirely on cathode materials are rarer compared to their anode counterpart owing to the finer resolution required to notice small details in thickness changes of cathodes. The dilatometry instruments that currently exist may not be capable of detecting the finer details that would explain the thickness changes of the cathode which could be associated with crystallographic changes and cracking.

2.5. Visualisation of LiBs Using X-ray Computed Tomography

2.5.1. Overview

While ECD is a powerful technique to probe the dimensional changes of electrodes during cell cycling, there are degradation mechanisms such as particle cracking that cannot be detected by this technique and can influence thickness changes and contribute to capacity fading [84]. It can also be difficult to specify what is causing the thickness variations that are recorded as multiple degradation mechanisms can occur simultaneously. For instance, volume expansion that occurs due to electrode delamination can only be observed using other microscopy techniques such as X-ray computed tomography (X-ray CT) [63]. This technique is widely used to visualise and quantify the 3D evolution of electrochemical and mechanical degradation of LiBs [124] [125]. In addition, X-ray micro-computed tomography (X-ray μCT) serves a valuable purpose in visualising and characterising the evolution of LiB electrodes at a microstructural level [126] [127]. A vital advantage of employing X-ray μCT is that it enables non-destructive analysis in a range of fields [128]. Numerous X-ray CT specialised electrochemical cells have been designed to minimise hard X-ray absorption allowing an unhindered view of the electrode region of interest (ROI) [129] [130]. X-ray characterisation methods used in this work are discussed in detail in Section 3.7 along with data processing techniques.

2.5.2 Electrode microstructure characterisation

The first use of X-ray μCT to characterise graphite electrodes across various geometrical parameters of the electrode - such as porosity, tortuosity, surface area and particle size distribution (PSD) - was by Shearing *et al.* [131]. They found that the tested graphite electrode had a porosity of 15.4% with more than 95% of these pores percolating through the electrode. PSD revealed that the

particles had an average diameter of 4.78 µm and 1.26 µm for the pore diameter respectively. This method can be used to find differences in geometrical parameters after electrodes have been cycled under different conditions to evaluate the effect on its morphology.

In section 2.2, the effect that an SEI layer can have on a graphite electrode was considered as well as its general composition. Frisco et al. [132] found that the SEI layer that had formed on a graphite anode extended into the internal structure of the electrode and thus a significant reduction in internal pore diameter was recorded. The 3D X-ray images depicted a general collapse of pore structure throughout the volume of the cycled anode compared to the pristine anode. Consequently, a dramatic increase in series resistance occurred as SEI grew both on the surface and within the pore structure of the graphite anode. This is during deep cycling and not likely to occur for cells that are not cycled an excessive number of times and at a moderate C-rate such as an applied C/20 rate. Nonetheless, this work demonstrates that an SEI layer can be observed using X-ray µCT. The thickness of the SEI layer can also be quantified, to see what proportion of thickness change this layer has compared to the overall electrode when it undergoes expansion/contraction during cycling.

Zernike phase-contrast is a technique that has been implemented in X-ray CT to reduce background illumination effects, consequently enhancing the appearance of edges and interfaces within a tested material. This is achieved by inserting an annular phase ring after the sample [133] [134]. This technique will be discussed further in Chapter 3. Eastwood et al. [135] characterised the morphological properties of graphite electrodes such as tortuosity and porosity using X-ray µCT, as well as properties of five individual graphite particles namely volume specific surface area (VSSA) and sphericity using X-ray computed nano-tomography (X-ray nCT). They found that while particle volume significantly

varied, the sphericity of the particles was very similar. In addition, the VSSAs of the individual particles were significantly larger than the total VSSA of the electrode when measured using X-ray nCT compared to X-ray μCT imaging. It was suggested that this was due to the greater particle surface area visible at higher resolution using X-ray nCT. Using X-ray CT instruments with different resolution capabilities can facilitate interpretation of electrode properties at different length-scales.

Unfortunately, implementing Zernike phase-contrast during X-ray CT can produce undesired artifacts, such as "halos" and "shade-off" for low atomic number materials [136]. Taiwo *et al*. [137] took the work of Eastwood *et al*. [135] and others further by developing and applying a combined contrast approach using image absorption-contrast and Zernike phase-contrast to examine the 3D microstructure in a graphite-based electrode (

Figure 10). Enhanced X-ray image contrast was obtained by signal blending and optimization. Zernike phase-contrast imaging was found to enhance features and edges of the graphite electrode particles providing more boundary edge contrast information and exposing cracks in the graphite microstructure. However, the use of absorption-contrast allowed material density information to be obtained due to sufficient X-ray attenuation contrast between different boundaries in the absorption-contrast images. These works demonstrate the various quantifiable physical properties of an electrode that can be identified using this technique such as particle surface area, sphericity and VSSA. VSSA can provide both structural and cycling performance-related information for

LiB electrodes, as the particle-pore interface is where charge transfer reactions occur during battery cycling between the active material and the electrolyte.
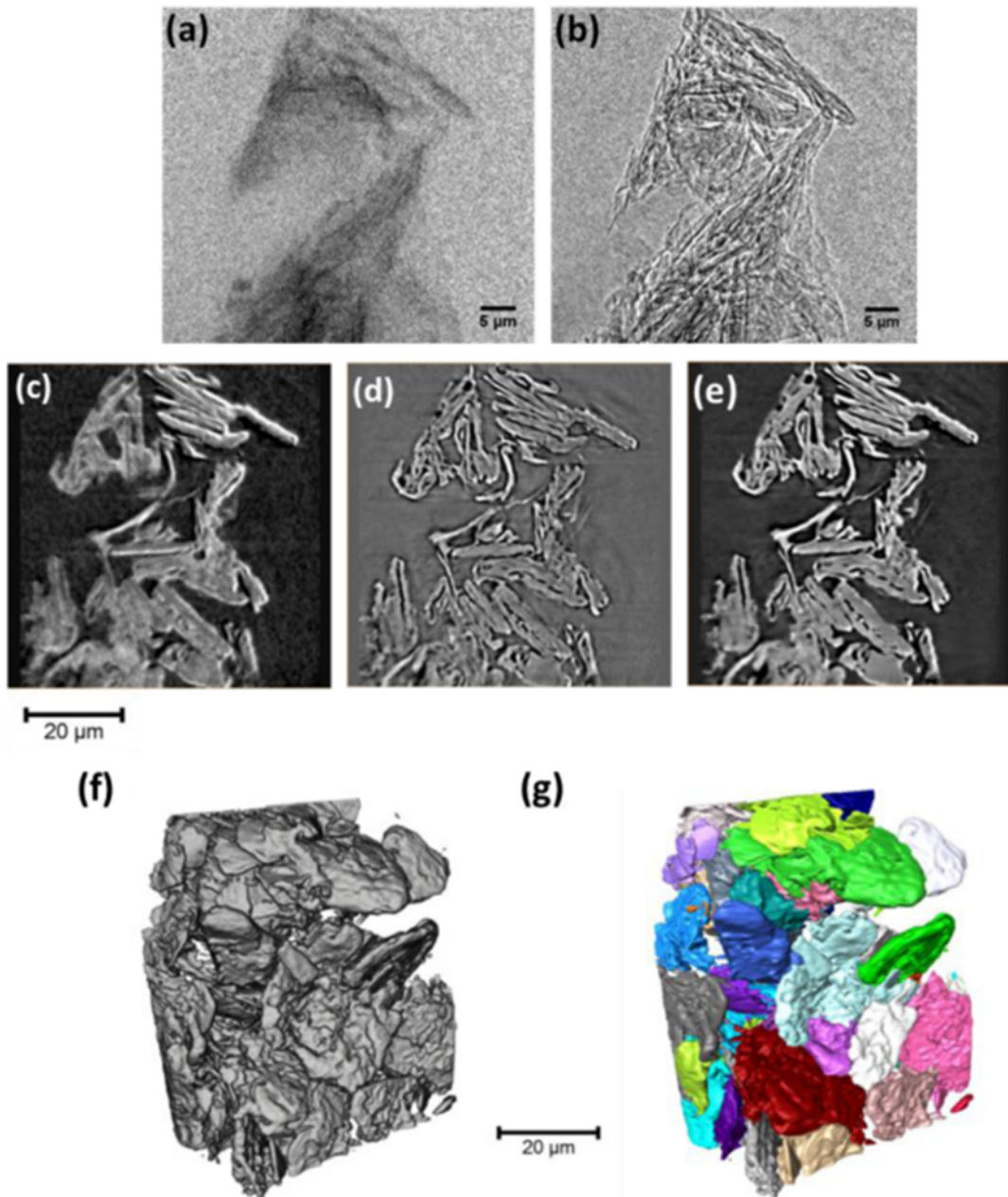
Figure 10: An X-ray image of a ROI within a graphite electrode acquired using (a) absorption-contrast X-ray nCT and (b) Zernike phase-contrast. Single reconstructed slices from X-ray nCT in (c) absorption-contrast mode, in (d) phase-contrast mode, and (e) after combined-contrast enhancement. (f) Resulting volume rendering of the graphite ROI, and (g) after algorithmic particle separation and identification. Reproduced from Taiwo et al. [127] .

Daemi *et al*. [138] evaluated the crystal dimensions of NMC111 particles in NMC111/graphite cells cycled to 4.2 V and 4.7 V to determine changes in unit cell dimensions after the electrodes had been cycled using X-ray diffraction computed tomography (XRD-CT). This correlative technique allows for visual inspection of samples by acquiring X-ray CT images, whilst quantitatively measuring changes in the crystal structure. The unit cell defines the smallest repeating unit of a crystal structure. The particles of the NMC111 cathode cycled to higher voltages underwent a greater shrinkage (0.6% of the unit cell volume) compared to NMC111 particles of the electrode cycled to a lower cut-off voltage (0.4% of the unit cell volume). Particles in NMC111 electrodes cycled to higher cut-off voltages of 4.7 V exhibited extensive particle cracking confirming that severe cycling conditions can exacerbate degradation. Particles in NMC111 electrodes cycled to 4.2 V exhibited particle cracking to a lesser degree. This work realised the potential of XRD-CT to investigate dimensional changes on the particle scale, by using the unit cell volume and analysing the expansion along the c-axis and shrinkage along the *a*-axis of NMC cathodes after extended cycling. The *a*-axis is the direction of the longest axis of the crystal structure, while the *c*-axis is the direction of the shortest axis. The lithium ions tend to move more easily along the *c*-axis than the *a*-axis [44].

ECD measurements could be corroborated with XRD-CT to elucidate which unit cell volume changes translate into measurable changes in the bulk electrode level. A holistic approach to understanding dimensional changes in LiBs can be

realised by assessing dimensional changes at various length-scales. Heenan *et al*. [40] cycled NMC811/graphite cells five times after an initial formation cycle, then disassembled them so that the cathode could be imaged using X-ray CT to
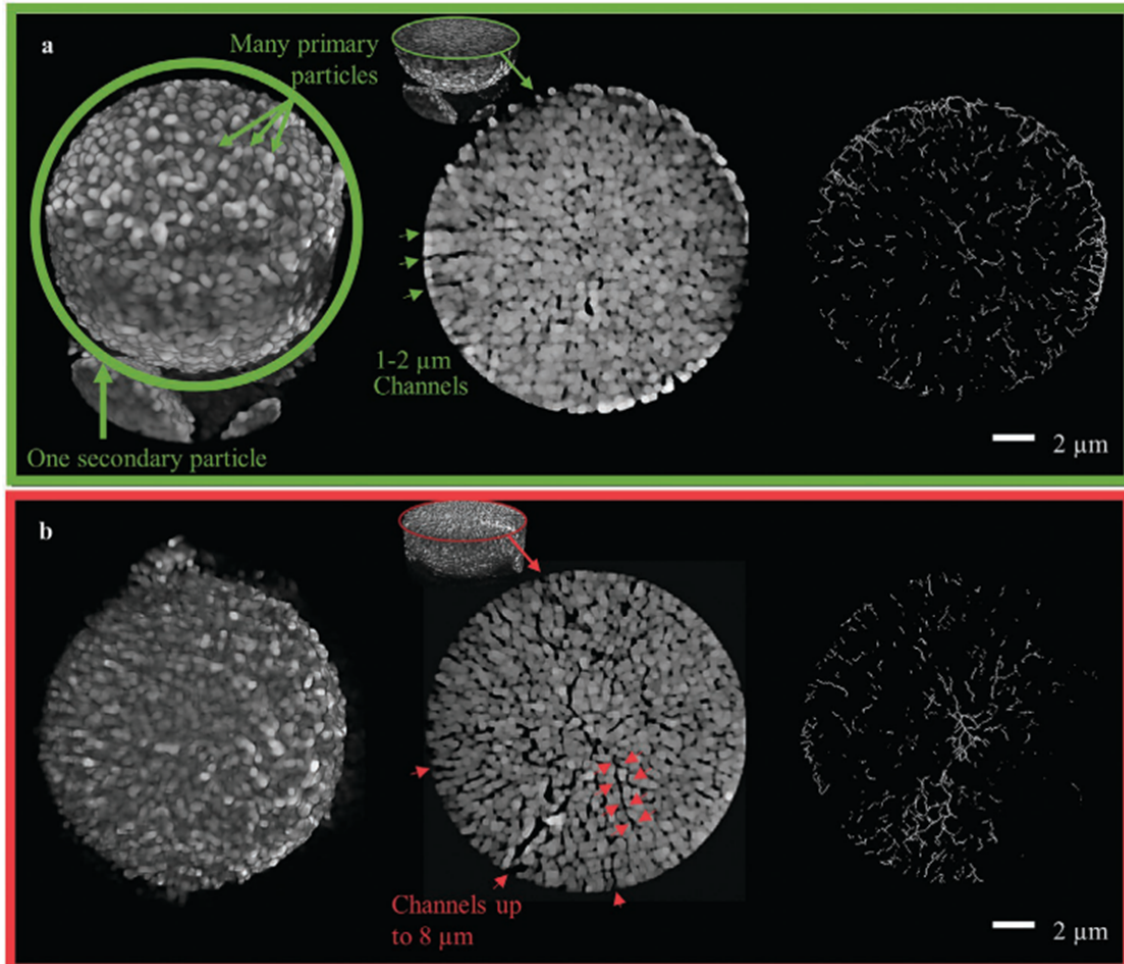
reveal   any   particle   degradation   (

Figure **11**). They found that any particles could experience cracking, and that there was no relationship between particle size and degree of cracking when cycled at low C-rates for a low number of cycles. In addition, Hexagonal-2 (H2)/Hexagonal-3 (H3) and rock-salt phases were detected in small amounts after five cycles. The H2 and H3 represent hexagonal phases of the crystal lattice structure. The H2/H3 transition is associated with a reduction in the unit cell volume [81]. This phase transition will be critically assessed in Chapter 5.

Figure 11: *A 3D volume rendering, 2D ortho-slice and pore skeleton map for (a) a pristine (uncycled) NMC811 secondary particle, and b) a cycled NMC811*

secondary particle charged to 4.5 V versus graphite five times then discharged to 3.0 V versus graphite before disassembly and imaging. Reproduced from Heenan et al. [40].

They concluded that during low cycle numbers, the crystal ordering of NMC811 cathodes is largely influenced by the manganese content of NMC cathodes and that manganese content dominates transitional metal dissolution. Furthermore, voltage-induced cracking occurred in NMC811 very similarly to what is expected of lower nickel content NMC electrodes such as NMC111 [139]. Crystallographic disordering of the NMC811 cathode may be associated with the instability of manganese in the cathode as surface clusters of NMC active particles were found to form. However, this does not correlate clearly with the secondary particle cracking in the case of early stage cycling. In this case, cracks that were detected may have primarily been caused by electrode fabrication and the disconnection/separation of neighbouring primary particles may have been caused by electrochemical expansion/contraction.

2.5.3 Visualisation of whole cell assemblies

In addition to particle scale and electrode scale characterisation, X-ray CT can be used to visually characterise whole cell assemblies (Figure 12) [140]. Whole cell characterisation is useful for discerning faults in manufacturing such as component misalignment, gas formation and bulk volume expansions [141] [142]. X-ray CT was used to diagnose the LiBs in the highly publicised Galaxy Note7 incidents when a number of consumers reported phone explosions [143], demonstrating a critical application of this tool in preventing harm to individuals. By carrying out X-ray CT of the entire cell assembly, the cause of the issue was identified as misalignment of the negative electrode. This ultimately led to direct contact between the positive tab with the negative electrode, shorting the circuit and resulting in catastrophic failure.

Yufit *et al*. [128] demonstrated how X-ray CT can be used to identify volume expansion of electrode assemblies inside post-mortem LiBs by quantifying physical distortion in individual layers of untested and failed cells. The parallel electrode assemblies (electrode and current collector) were shown to be very uniform with cell spacings below 43 μm inside pristine cells. However, the failed cell underwent significant volume expansion and the X-ray μCT data revealed major degradation of the internal architecture of the pouch cell. This work demonstrates that X-ray μCT can be used to assess the dimensional changes of LiB pouch cells by collecting images before and after cycling providing a visual representation of volume expansion and degradation.
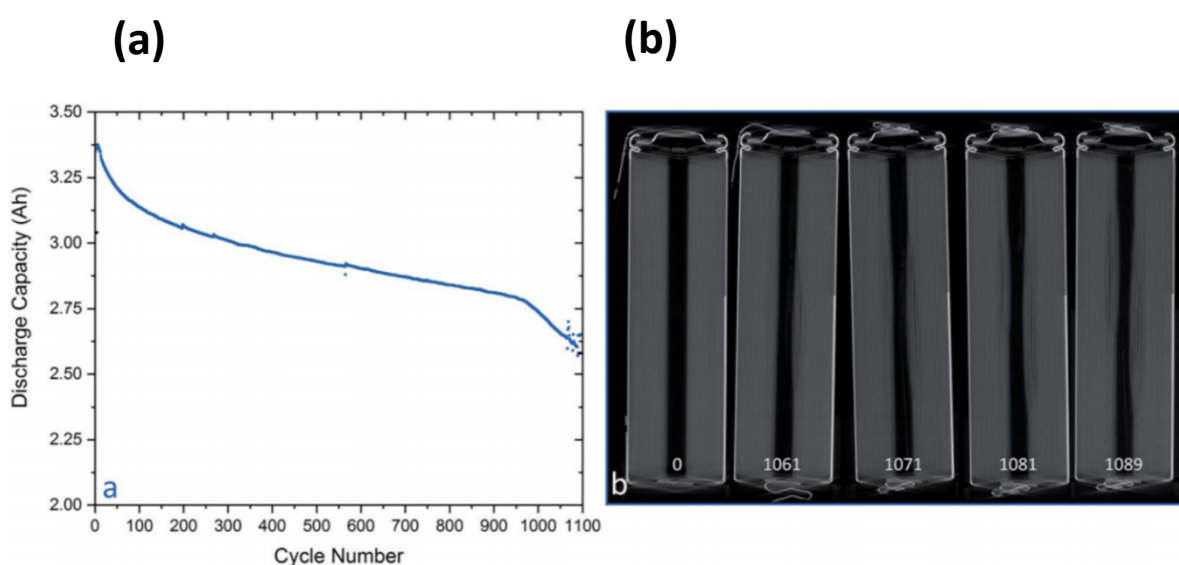
Figure 12: (a) Capacity fade of a spirally-wound LiB over 1097 cycles. (b) A series of orthogonal slices of the LiB at different cycling intervals, showing the gradual increase in the size of the large deformation on the inner portion of the jelly roll. Reproduced from Kok et al. [140].

2D/3D X-ray μCT of entire cell assembles can reveal numerous degradation mechanisms inside the LiB pouch cell during cycling. Chen *et al*. [124] found that cell expansion caused the outer anodes to curve inwards and push the multi-layered anode components together. In addition, buckling and severe wrinkling

of the electrode components were witnessed. Wrinkles resulted in cell swelling, however, the distribution and cause of the wrinkles was not concluded. This study demonstrates the impact of volume expansion on the electrode components of a LiB pouch cell. The consequences of volume expansion of individual electrodes on entire whole cell assemblies can be visualised using X-ray μCT at higher length-scales that encapsulate the entire cell.

Multi-scale X-ray CT can also be used to investigate the impact of physical changes across various length-scales. Bond *et al*. [144] investigated pouch cells that varied only in particle morphology of the NMC811 cathode. They found that cell-level degradation phenomena, such as jelly roll deformation and electrolyte depletion, occur to a greater extent in pouch cells containing NMC811 electrodes with larger particles. In addition, by increasing X-ray CT resolution, they were able to examine electrode scale degradation phenomena. Using this resolution, they were able to detect that electrodes containing larger particles underwent more drastic thickness changes. Nonetheless, they were unable to detect particle cracking at this spatial resolution. Particle cracking observation requires nano-scale X-ray CT resolution. In this section, X-ray CT has been shown to be effective in visualising numerous degradation phenomena in LiBs. The findings discussed in this section portray how physical changes of the electrode have ramifications on the entire whole-cell assembly and therefore the importance of visual interrogation of LiBs at different length-scales.

2.6. Acoustic Spectroscopy as a Diagnostic Tool for Characterising Battery Degradation

In recent years there has been a move towards the application of new characterisation techniques to batteries to better understand the degradation

processes and extend lifetime. Whilst X-ray CT is a valuable diagnostic tool for capturing images of LiBs before and after cycling, it is impractical and expensive to cycle a cell inside an X-ray CT instrument for a long period of time [145]. However, many significant findings from lab-based X-ray CT experiments have emerged in recent years related to the link between microstructure and performance, cracking and cell-level failure, amongst other phenomena [146] [147] [148] [149]. In contrast to expensive X-ray tools, acoustic spectroscopy can be low cost and performed in-operando to probe internal changes in a LiB's architecture [150] [151]. This has led to an increase in publications and research in this area, with acoustic spectroscopy being used to study energy storage electrode materials in various electrochemical devices including LiBs, [151] [152] [153] nickel-metal hydride batteries, [154] [155] [156] hydrogen-palladium batteries, [157] solid oxide fuel cells, polymer electrolyte membrane fuel cells [151] and polymer electrolyte membrane electrolysers [158] [159] [160].

Acoustic techniques have increased in popularity extremely rapidly [57], with electrochemical acoustic time-of-flight (EA-ToF) spectroscopy being used to study various degradation phenomena in LiBs such as gas formation [125], cell expansion [152], and cathode dissolution [153]. Different forms of acoustic spectroscopy such as EA-ToF and acoustic emission spectroscopy can be used non-destructively to identify a range of defects inside a LiB and probe purpose-built defects across multiple length-scales such as entire electrode assemblies missing from a pouch cell and particle-scale volume changes [153]. The experimental methodology adopted for EA-ToF spectroscopy in this work is detailed in Chapter 3.8.

In-operando EA-ToF spectroscopy of NMC/silicon-graphite composite pouch cells was conducted by Steingart *et al*. [152] to identify regions of charge/discharge cycling that were susceptible to severe gas formation. Significant gas formation occurred during the first 2/3 of initial charging and

was associated with SEI formation. Gas that formed inside the cell caused attenuation of acoustic signals, and thus an intermittent loss of acoustic data. After the initial formation cycle, significant gas formation subsided due to a stable SEI layer having been formed demonstrated by the reappearance of acoustic signals.

An advantage of acoustic spectroscopy is that it can be used whilst cycling LiBs at a large range of different C-rates, from the slower C-rates used in Steingart *et al*. [152] of C/50 and C/20; to fast C-rates of 1/2C and 1/20C reported in Pham *et al*. [125]. Pham *et al*. used correlative EA-ToF spectroscopy and X-ray imaging to reveal gas induced delamination in LiBs during thermal runaway [125]. Gas formation was identified in acoustic spectrograms as acoustic signal loss by gas attenuation. Furthermore, cell destruction e.g., separator failure and electrode delamination were recorded in spectrograms as the acoustic signals became rapidly spaced apart during cycling (Figure 13). X-ray CT confirmed that electrode delamination and separator failure occurred, demonstrating the correlation of acoustic spectroscopy in conjunction with visual characterisation techniques.
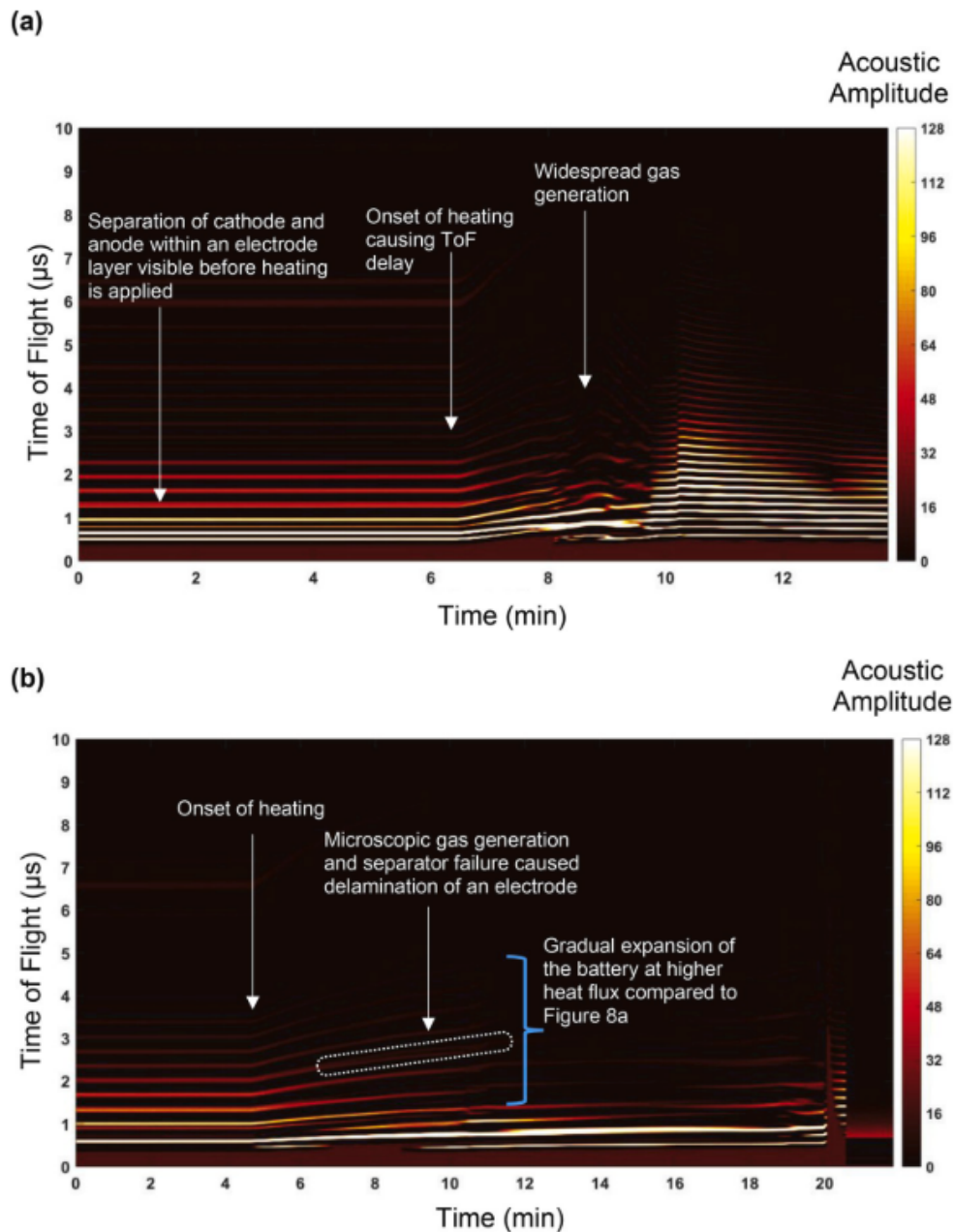
Figure 13: (a) EA-ToF spectrogram of a 210 mAh commercial pouch cell during a failure test, with highlighted regions of interest during induced thermal runaway. Onset of heating at approximately 6 min 20 s into the test. (b) EA-ToF spectrogram of another 210 mAh commercial pouch cell during the second failure test, with highlighted regions of interest during thermal runaway. Onset of thermal runaway at approximately 4 min 20 s into the test with the main features of interest identified on the spectrogram. The acoustic amplitude is displayed in arbitrary units. The 'Time of Flight (μs)' describes the distance in which the acoustic signal has travelled through the cell i.e., at 10 μs the signal has passed through the entire cell. Reproduced from Pham et al. [125].

Acoustic response can suggest changes in elastic modulus and density of the various material interfaces that form a sample [161]. Ladpli et al. [162] found that volume expansion in a closed electrochemical cell resulted in a reduction in the total mass density, and consequently sound waves travelled faster through the cell. The global stiffening and expansion of the electrodes was found to have the opposite effect on wave speeds. Therefore, acoustic spectroscopy can be used to track volume changes in a LiB during cycling. Robinson et al. [151] found that charging $LiCoO_2$/graphite batteries resulted in an expansion of both electrodes between 1.74%. Nonetheless, misinterpretation in measurements is possible as changes in electrode density can alter the acoustic impedance of electrode layers, and consequently the speed at which the sound pulse passes through the material. These misinterpretations can impact correlations made between the acoustic measurements and physical position of the electrode layers in the LiB. X-ray CT can be used in conjunction with acoustic spectroscopy to provide visual evidence of electrode expansion and discern acoustic recordings caused by physical changes in the LiB and interpretations made in acoustic measurements.

Although there are some published studies which use ECD in tandem with acoustic spectroscopy [35] [163], these works predominately use ECD to measure dimensional changes in electrodes, whilst acoustic techniques are used to detect degradation phenomena that can contribute to the dimensional changes measured. Tranchot et al. [163] used in-operando ECD in conjunction with an acoustic emission technique to track thickness changes in a Si electrode and detect morphological changes in Si particles during cycling. They suggested that using acoustic emission techniques solely to evaluate dimensional changes of silicon electrode particles is challenging because the displacement caused by silicon particle expansion is not very constrained, and therefore the acoustic activity in relation to this process is very low, in comparison to the acoustic activity that is emitted from events such as particle cracking. However, Steingart et al. [152] used acoustic spectroscopy to focus specifically on the

dimensional changes that occurred in NMC811/silicon-graphite cells during cycling without ECD. They found that NMC811/silicon-graphite pouch cells irreversibly expanded as irreversible capacity loss occurred during prolonged cycling. Acoustic spectroscopy was demonstrated to be capable of tracking silicon passivation over long-term cycling. Although, measurements were limited to entire cell thickness changes and could not be used to measure single electrode thickness changes, there are merits to using acoustic spectroscopy over other finer resolution techniques such as ECD. For instance, acoustic spectroscopy can provide vital information on LiB state of health (SoH) that can contribute to understanding why certain thickness changes either occur or are exacerbated.

2.7. Potential Research Directions

This review has examined various experimental techniques available and used extensively to monitor battery and electrode degradation across numerous length-scales. For instance, XRD studies that record stoichiometric changes have been correlated with electrode thickness changes recorded from *in-situ* ECD, showing the advantages of testing a given electrode material using various techniques [164]. According to the literature, ECD has been used in tandem with acoustic techniques in the past, with ECD providing a tool to measure dimensional changes whilst recording acoustic signals associated to degradation events such as particle cracking and electrode fracturing that can cause, or be caused by dimensional changes [138] [165] [163]. X-ray CT can also be used in conjunction with acoustic spectroscopy to reveal the internal architecture of LiBs so that internal properties identified using X-ray CT can be correlated to their acoustic signature [125] [153]. This is an appropriate approach to studying electrode degradation as these degradation mechanisms can occur simultaneously and not in isolation.

The outlook for the increased use of ECD and acoustic spectroscopy in battery research is promising. Although there is a plethora of research using these techniques, in conventional anode materials such as graphite and silicon and commonly used cathode materials such as LCO, there is scope for *in-situ* ECD and acoustic spectroscopy to be used to assess next generation anode and cathode materials. There is a growing consensus of the need to migrate from the current state-of-the-art layered NMC cathodes to stoichiometries with lower cobalt content. For instance, in October 2019, The Faraday Institution, the UK's independent institute for electrochemical energy storage science and technology, launched the FUTURECAT, NEXTRODE and CATMAT programmes to develop and deploy next generation Li-ion electrodes and the NEXTGENNA programme that looks to develop novel electrode materials for NiBs. ECD can be used to evaluate novel compositions of NMC electrodes in LiBs and innovative electrode materials in NiBs.

This review has considered and discussed a variety of published studies that use ECD, X-ray CT and acoustic spectroscopy to investigate degradation phenomena that occur during cycling, as well as the impact these changes can have on the performance of the device. Other techniques such as solid-state NMR [166], and X-ray diffraction [167] can be used in conjunction with ECD and acoustic spectroscopy to corroborate and explain the degradation mechanisms recorded; enhance understanding of the impacts of these changes; and inform mitigation to improve performance. ECD is useful for laboratory use, but less suited to real-world application since integration of an ECD instrument in a battery system is difficult and potentially destructive. Strain gauges may show more promise for real-world application given that they have been used in a laboratory setting to evaluate a matrix of LiBs on battery ageing during operation [168]. Interestingly, most dilatometric studies reviewed in this work investigate thickness variations during standard galvanostatic conditions with moderately slow C-rates; there is a lack of dilatometric studies at high C-rates, as well as studies on ageing, safety, and abusive conditions apart from lithium

plating. This may be due to limitations in design in the current state-of-the-art commercial dilatometers and challenges with in-house constructed dilatometers. Nonetheless, addressing this noticeable gap in the literature would provide valuable information about the performance of batteries under more realistic cycling and ageing regimes. Acoustic spectroscopy and X-ray CT do not have these limitations and can be used to evaluate LiB dimensional changes as well as cell failure at extreme conditions [125].

Progress in dilatometric investigations of electrode dilation/contraction in electrochemical devices can inform understanding of structural changes during electrode phase transitions and their contribution to the overall electrode dimensional changes. A greater understanding of these electrode dynamics is required to overcome limitations in current density, battery lifetime and capacity fade. The acceleration in the number of papers published on this topic is evidence of the increased focus on ECD as a diagnostic tool and the advancement of the technique in recent years. In addition, more studies are using ECD in tandem with other characterisation tools to further enhance understanding of the structural changes taking place in the materials that make up electrochemical devices. Although ECD is capable of detecting thickness changes of single electrodes at a nanometer resolution, current ECD devices are limited to two-dimensional measurements. X-ray CT allows 3D visual diagnosis of electrodes to inform morphological changes that are caused by, or impact thickness changes. However, as discussed in Section 2.8. X-ray CT is extremely expensive and impractical for long-term experiments. Therefore, cheaper methods to use in tandem with ECD should be explored. EA-ToF spectroscopy is significantly cheaper than X-ray CT measurements, making it ideal for long-term cycling. As it is a relatively new experimental technique for LiB interrogation, its broader diagnostic capabilities need to be explored, to assess its viability as a tool to measure detrimental physical changes of LiBs during long-term cycling.

INTENTIONALLY BLANK

Chapter 3

Methodology

3.1. Overview

This chapter outlines the fundamental theory and practical knowledge relating to the different experimental techniques used in this work. It begins with an overview of the different cell configurations used and goes on to cover the fundamental principles of scanning electron microscopy (SEM), X-ray imaging and acoustic techniques. The use of X-ray imaging systems as well as the techniques used in the analysis of X-ray CT data are also discussed. Methodology that is specific to experiments carried out in this work is provided in the relevant chapters.

3.2. The CR2032 Coin Cell

The coin cell is a common standard cell configuration used for electrochemically testing battery materials in laboratories because it does not require large quantities of electrode material. Typically coin cells have circular dimensions between 5-25 mm in diameter and 1-6 mm in height with the most common format being the stainless steel 2032 cell (20 mm diameter, 3.2 mm height). The 2032-type coin cell has excellent electrolyte leakage resistance characteristics.

All coin cells used in this work consist of a two-electrode configuration comprised of a WE containing a mixed metal oxide, binder and conductive additives coated on a current collector, a lithium metal counter electrode (CE) and separator soaked in lithium hexafluorophosphate ($LiPF_6$)-based electrolyte. This separator is a PP/PE/PP three layers (polypropylene-polyethylene-polypropylene) membrane. The CE also serves as a pseudo-reference electrode, providing data for the WE potential versus lithium. These two-electrode configurations are also commonly referred to as half-cells and are referred to as such throughout this thesis. The components of a typical coin cell are shown in Figure 14. Electrode materials investigated in this work include graphite and NMC811 soaked in $LiPF_6$ with 2% vinylene carbonate additive.
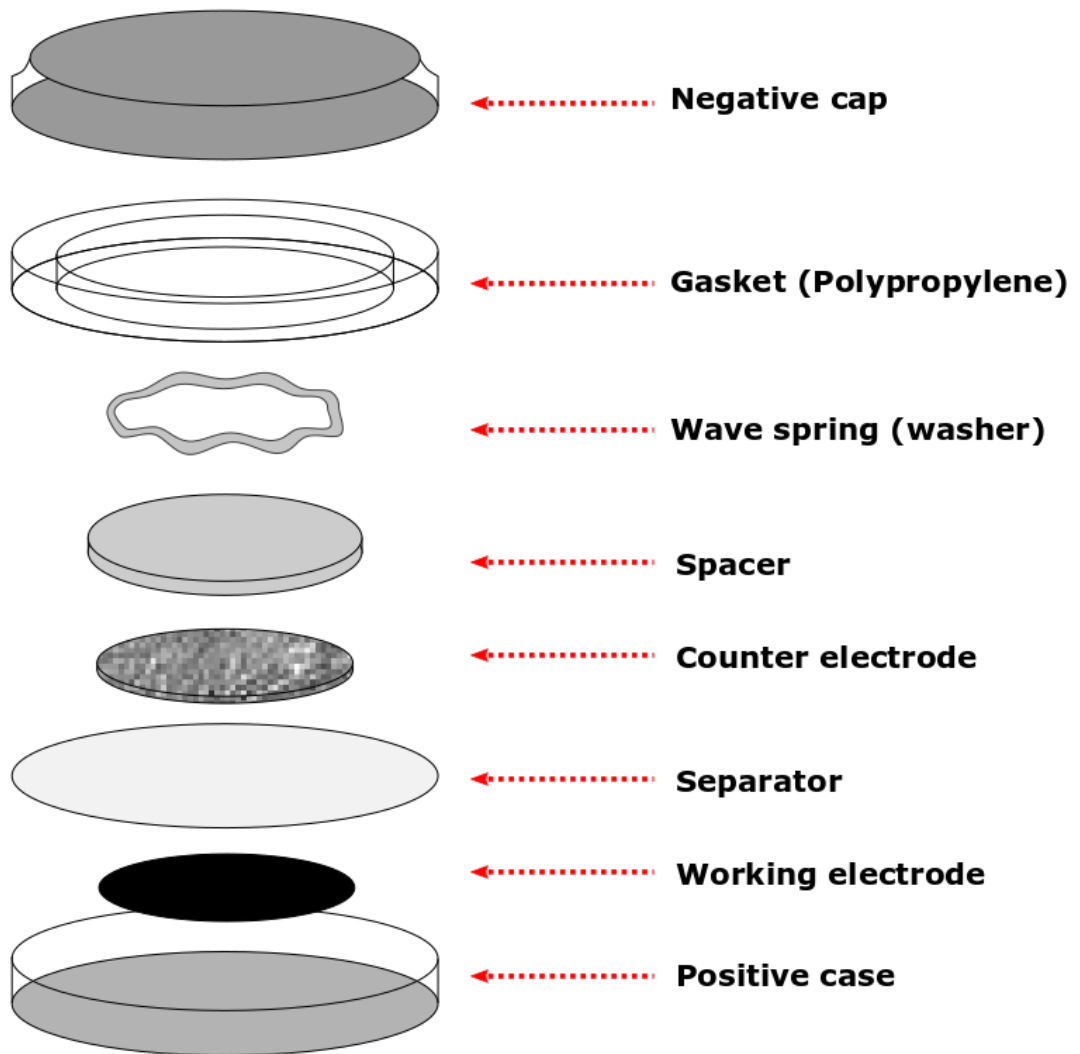
Figure 14: *A schematic of the different components of a CR2032 type coin cell.*

3.3. Electrochemical Dilatometry

3.3.1. Principles of Electrochemical Dilatometry

A dilatometer measures volume changes of a sample material caused by chemical or physical processes. Dilatometry is used to test a wide range of materials, including metals, carbonaceous materials, ceramics, glasses and polymers [169]. There are different types of dilatometers: push-piston dilatometers (Figure 18); push rod dilatometers (Figure 15a); and high resolution, laser (optical) dilatometers (Figure 15b).

Push-piston dilatometers are designed to measure either horizontal or vertical displacement at a single point in 1-dimension. A ceramic piston and cylinder set is used to provide an enclosed defined volume, and the volume changes are translated into piston movement which can be recorded by a mechanical dilatometer. Push rod dilatometers enclose the sample between the end of the measuring system and a push-rod. As the sample expands and contracts, the measuring system and sample move together. The measuring head records a signal that is the sum of these changes. An optical dilatometer is a non-contact device. A laser, illuminates the sample and some of the light is reflected by the sample and interferes with the incoming light, creating optical interference fringes. As the sample contracts or expands, there is a proportional movement of the interference fringes, which can be measured using a camera system.

(a)

(b)
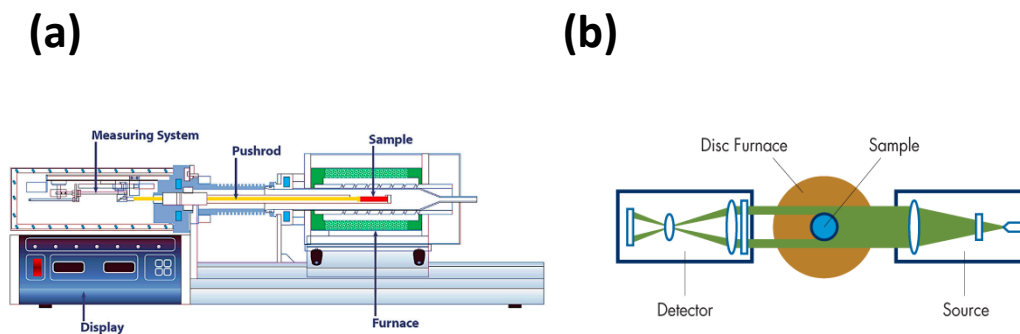
Figure 15: A schematic of a (a) push-rod dilatometer and (b) laser (optical) dilatometer [170] [171] .

This work uses a push-piston dilatometer (Figure 18), which is the most commonly selected type of dilatometer for electrochemical devices, owing to the spatial resolution of commercially available models. That said, it should be noted that in solid state batteries research, the push rod dilatometer is more common because it can operate at temperatures exceeding 1000 °C. Most commercial dilatometers cannot operate at temperatures above 100 °C and tend to be used in studies carried out at room temperature.

Push-piston dilatometers use a parallel plate capacitor, with one stationary plate, and one mobile plate. When the sample material expands or shrinks, the mobile plate moves, which alters the gap between the two plates [172] [173] [174] [175]. Push-piston dilatometers are designed to measure either horizontal or vertical displacement at a single point (~3 mm diameter) in 1-dimension.

There are various dilatometer instruments designed to measure electrochemical devices whilst sealed against ambient temperature and pressure, and dilatometer cells can be designed to allow for gas expansion from the electrode in the electrochemical device. Commercially available push-piston dilatometers are often designed in a way to allow for gas evolution to be

mitigated and thus not effect dilatometric measurements, so that the dilation recorded is indicative of structural changes in the sample material. Pressiometry can be employed to monitor pressure changes in a sample material during cycling [176] [177]. Numerous commercial pressiometry devices such as the PAT-Cell Press provided by EL-Cell group are built in a way that allows for the gas formed to be collected and transferred for subsequent gas analysis e.g., gas chromatography. This allows measurement of gases formed during certain cycling protocols of different materials.

Linear voltage displacement transducers (LVDTs) and capacitive parallel-plate displacement sensor systems are the two most commonly found in numerous dilatometer instruments. An LVDT consists of a metal rod that moves inside an electrical coil. A force applied to the metal rod results in a displacement that affects the inductance of the coil. The inductance of the coil is converted into electrical signal recordings that are proportional to the material displacement [178]. A capacitive sensor detects solid or liquid displacement without physical contact. Displacements change the capacitance between two capacitive plates in a parallel-plate configuration. The capacitance is converted into electrical signal recordings proportional to the material displacement [179].

Whilst there are multiple examples of bespoke dilatometers designed for volumetric measurements [64] [102] [180] [181] [182], of the commercially available instruments, such as the ECD model cells provided by EL-Cell group are the most widely applied. This dilatometer cell configuration is discussed further in Chapter 4.

It is also common to construct a tailored assembly to suit the purpose of the experiment. For instance, Hahn *et al.* constructed an in-house developed dilatometer that consisted of a two-electrode assembly with a paper separator (see

Figure **16**a) [102]. The lower CE was fixed into position while the upper WE had freedom to move against a constant load (20 N) applied by a spring. An inductive displacement transducer and a measuring amplifier were used to record the height changes of the cell. The transducer and measuring amplifier were mounted on top of a plunger that connected the detector to the WE. A drying agent was connected to the cell to prevent pressure increases due to gas evolution.

(a)
- displacement transducer (10)
- force adjustment screw (9)
- spring body (8)
- spring (7)
- moveable plunger (6)
- cell body, top half (5)
- distance ring (4)
- cell body, lower half (3)
- tripod (2)
- fixed plunger (1)

A   B   C

(b)
- weight (Cu)
- ferrite shells
- coil
- movable piston (PP)
- sample
- current collector (Ni)
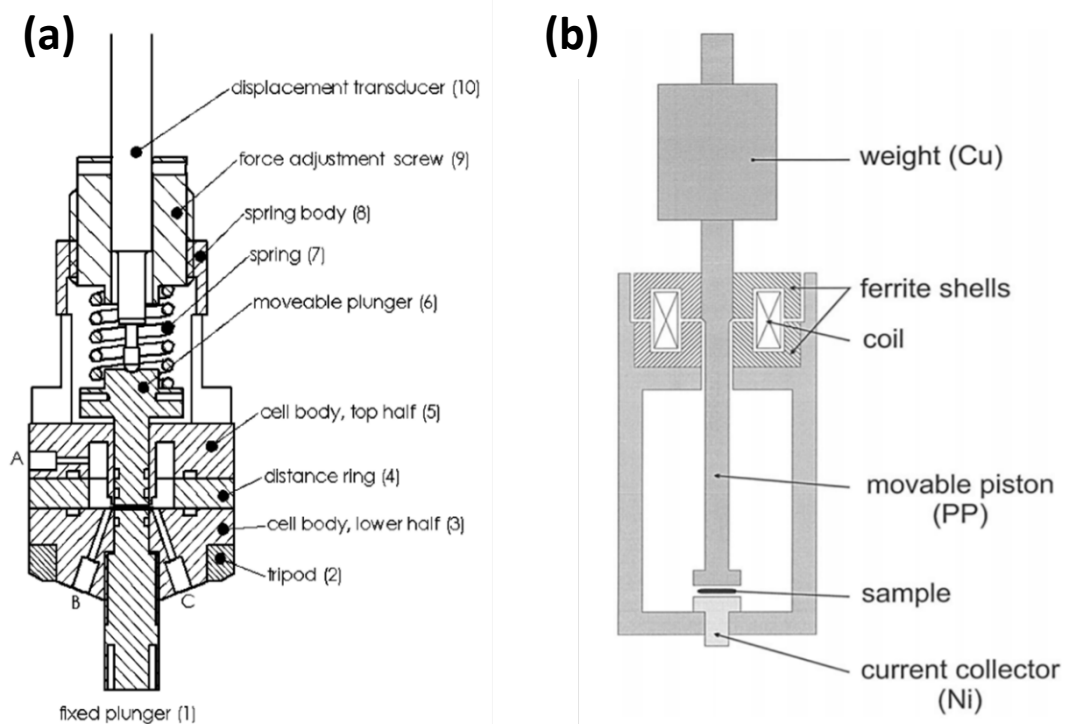
Figure 16: A schematic of the bespoke dilatometer developed and used by Hahn et al. [102] (a) and Winter et al. [180] (b). Copyright (2000) The Japan Society of Applied Physics.

Figure 16b illustrates the dilatometer developed by Winter *et al*. [180]. They used the resonance frequency shift in an oscillatory circuit that contained two ferrite shells. One of the ferrite shells was mounted so that it was mobile. The WE was placed between two pistons. Nickel was used to make the bottom piston, which

was stationery and functioned as the current collector. Polypropylene was used to make the upper piston, which was allowed to move and transmit thickness changes in the WE to the upper ferrite shell of the oscillatory circuit. Some design limitations were observed; capillary forces allowed electrolytic solution to move between the WE and piston producing false expansion measurements. In addition, electrolyte creeped between the sample and nickel current collector, disrupting electronic contact between the current collector and sample, and leading to measurements being entirely aborted. This issue of electrolyte creeping was resolved by installing a small copper weight into the dilatometer apparatus to ensure contact between the nickel current collector (bottom piston), WE (sample) and upper piston was maintained [180].

The dilatometry set-up used by Ivanov *et al*. included an electrode stack, which consisted of an anode coating on one side and a cathode on the opposite, with a separator in between (see Figure 17a). The three constituents of the electrode stack could be pressed by bracing the spring with a force adjustment screw to ensure a homogenous mechanical pressure was applied to the cell. Electrode expansion was monitored by using the displacement sensor and the macroscopic electrode stress by the load cell [104]. As a result of the increased length of the pressure spring in comparison to the displacement of the electrodes caused by swelling, force changes during measurements were negligible. In addition, the effect of gas evolution during cycling was suppressed owing to the small electrode area, the applied compression, and the non-gas tight housing. Bauer *et al*. also measured the expansion of a whole cell using an in-house developed dilatometer [64]. The height changes of the cell were transmitted via a membrane and a piston onto a LVDT. A voltage output was produced, which varied linearly according to the cell's expansion (see Figure 17b). The bespoke load system used for ECD measurements by Jeong *et al*. consisted of a sandwich-type electrode stack with a spring component [182]. A gap-sensor (resolution: 0.5 µm) was used to measure the thickness changes of the electrode stack (Figure 17c).
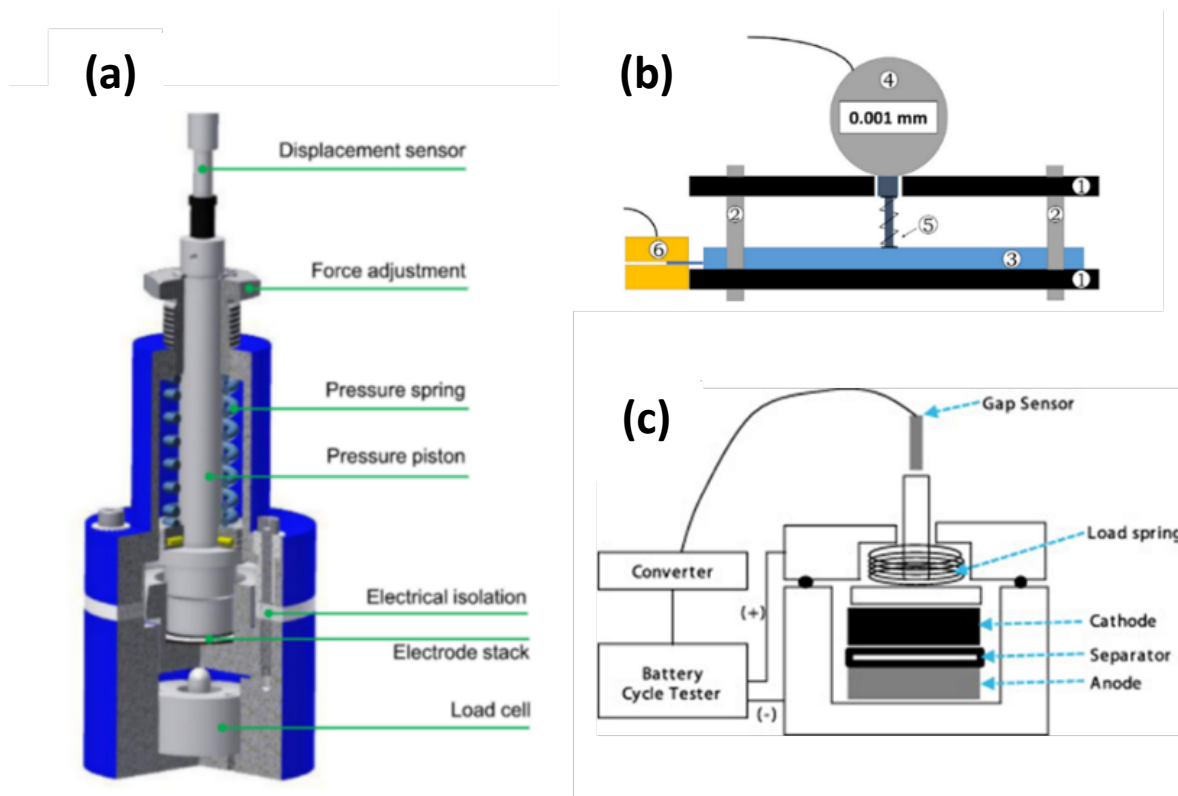
Figure 17: (a) A schematic of the bespoke dilatometer developed by Ivanov et al. Reproduced with permission from Sauerteig et al. [181]. (b) The dilatometer developed by Bauer et al. for high-rate dilatometry experiments using galvanostatic intermittent titration techniques. Reproduced with permission from Bauer et al. [64]. The dilatometer set-up consists of a (1) Aluminium- plate (2) threaded rod (3) cell (4) dial gauge (5) tip with spring and metallic plate (1 cm^2) (6) electric contact pads (gold plated). (c) The lab-generated load cell system used for dilatometric studies by Jeong et al. Reproduced with permission from Jeong et al. [182].

Numerous studies use dilatometry in tandem with other electrochemical techniques to provide more information on the electrochemical device in question. For instance, Winter *et al*. used cyclic voltammetry to assess the feasibility of electrolytic solutions with graphite in rechargeable cells that were subsequently used for ECD measurements [180]. The study set out to monitor electrolyte penetration into pores or fissures of an exfoliated sample. However, they found that combining ECD with cyclic voltammetry caused cyclic

voltammograms to be strongly affected by background currents in the dilatometer apparatus, demonstrating the limitations of combining these techniques. The dilatometer used in this work is shown in

Figure **16**b. It is common for dilatometry measurements to be constructed with the entire experimental setup in a climate chamber so that conditions can be controlled during data acquisition and dimensional changes caused by certain temperatures can be assessed.

Most bespoke dilatometer assemblies follow the same principles as those discussed in this section, with some adjustments. For example, studies by Fu *et al*. [183] and Bauer *et al*. [184] used two LVDTs because of the vertical alignment of the pouch cell in the designed fixture. One LVDT was placed on either side of the battery allowing the measurement of thickness variations at two different locations of the cell.

3.3.2. Dilatometer cell configuration

The ECD-3-nano, El-Cell GmbH is the electrochemical dilatometer used in this work. The device measures charge-induced strain (dilation and contraction) of electrodes with nanometre resolution. The test sample can consist of bound film or single crystals/grains (e.g., graphite flakes). The maximum sample size is 10 mm × 1 mm (diameter × thickness). Displacement signals below 5 nm are detected by the capacitive parallel-plate sensor systems.

At the centre of the dilatometer is the electrochemical cell which is hermetically sealed against ambient atmosphere. A stiff "T-shaped" frit made of borosilicate glass is fixed in position and acts as a separator between the working and CE. Any charge-induced thickness changes are transmitted towards the sensor/load unit from the upper WE that is sealed by means of a thin metal foil and thus the height change of the WE can be determined without any interference from the CE (see Figure 18). Dimensional changes of the WE are detected by a high-resolution capacitive displacement transducer with resolution ranging from a few nanometres up to 250 μm.
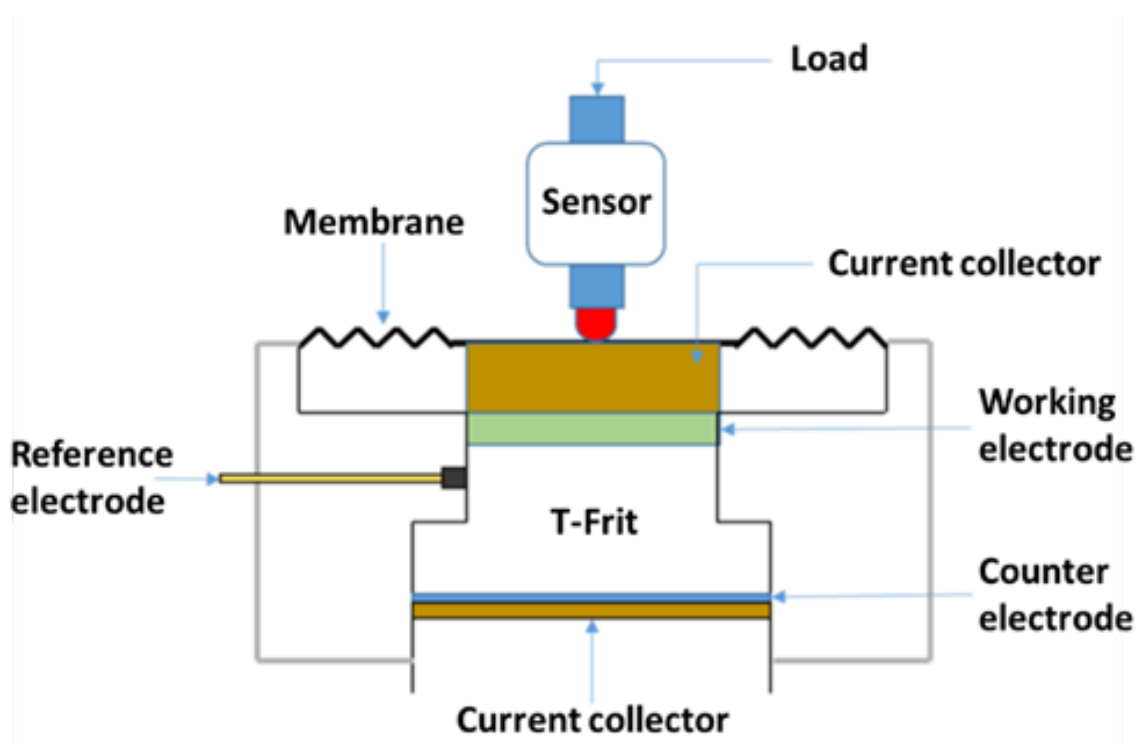
Figure 18: *A figure detailing the internal mechanism of the ECD-3-Nano Dilatometer (by EL-Cell GmbH) based on a 3-electrode geometry and an inductive sensor. Only the dilation of the WE is recorded because the glass T-frit is fixed in position.*

It is noteworthy that this commercial cell can also be used for two-electrode cell configurations by replacing the reference electrode with a plug ferrule. In addition, The ECD-3-nano can be used to measure the expansion of a whole cell

stack (instead of just the electrode on top of the frit). In this scenario, the glass frit is replaced by a stainless-steel support. The cell stack components consist of the WE, separator and CE electrode. This alternative dilatometer assembly is also suitable for solid-state batteries [185].

3.4. Battery Cyclers and Potentiostats

A variety of commercially available battery cyclers and potentiostats were used in this work. The first battery cycling system used was the BCS-805 (BioLogic, France) that has numerous independent channels for battery testing and the instrument is controlled by BT-Lab software. A single channel battery tester (Reference 600+ Potentiostat/Galvanostat/ZRA, Gamry Instruments) was also used. These potentiostats are equipped with 6-wire connections because they are tailored towards fundamental electrochemistry applications. All battery cyclers and potentiostats used in this work were capable of providing a variety of test procedures that can also be repeated as many times as desired using the loop function. Test functions that were used include, but are not limited to, open circuit, charge at constant current/voltage/power and discharge at constant current/voltage/power.

3.5. Battery Cycling Protocols

The two cycling protocols used in this thesis are constant current (CC) and constant voltage (CV) (see **Figure 19**). CC is a simple cycling protocol used to charge a cell. The cell is cycled with a CC throughout a pre-set voltage range. The CC can be set so that the cell cycles through the pre-set voltage range at different rates. The rate at which the cell charges or discharges through the pre-set voltage window is commonly referred to as C-rate (in h^{-1}) and is defined with respect to either its practical or theoretical capacity.

CV is a cycling protocol that involves holding a cell at a CV whilst cycling a cell throughout a pre-set current range. Constant current constant voltage (CCCV) is a cycling protocol that consists of a combination of CC and CV. During the CC cycling, charging limits the amount of current to a pre-set level until the cell reaches a pre-set voltage level. The current then reduces as the battery becomes fully charged. This cycling protocol allows for fast charging to be carried out without the risk of over-charging.
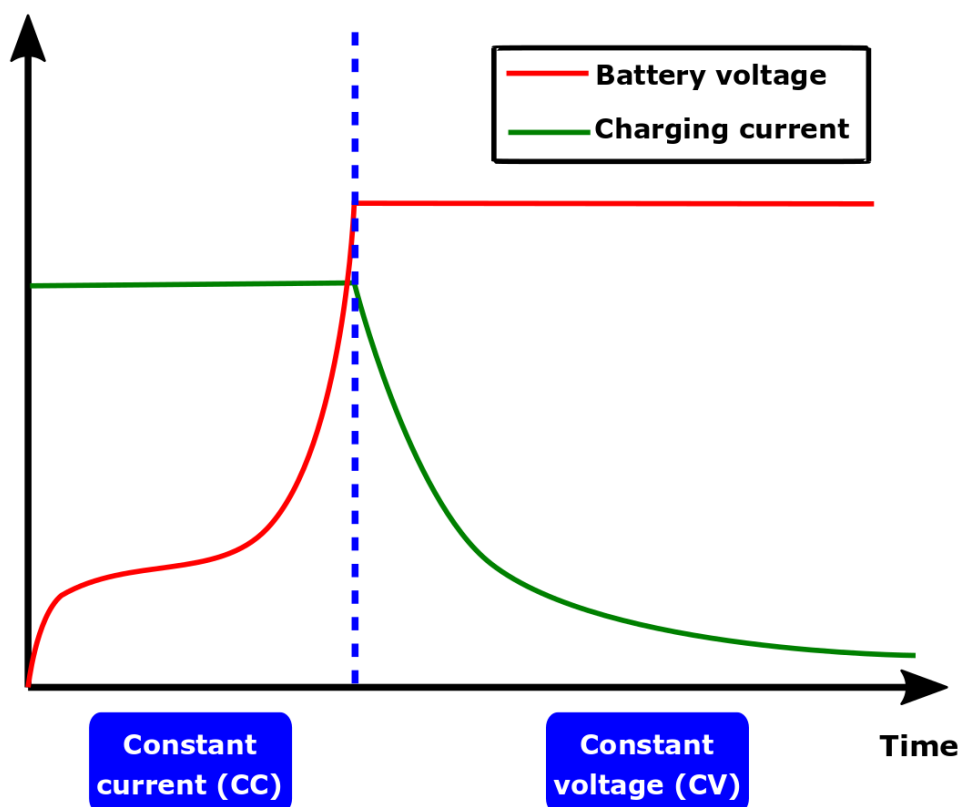
Figure 19: *A schematic illustrating characteristic behaviour during CCCV charging protocol.*

These battery cycling protocols cause oxidation/reduction reactions to occur at the electrode-electrolyte interface, where the electrode potential depends on the reaction kinetics and the mass transport of the reactants and products (as discussed in Section 1.3). The rate of these electrochemical reactions depends

on several factors, including the nature of the reactants, their concentrations, the temperature, and the electrode potential.

The electrode potential is governed by the Nernst equation, which relates the electrode potential to the concentrations of the reactants and products and the standard potential of the electrode reaction.

$$E = E^0 - \left(\frac{RT}{nF}\right) \ln{(Q)} \qquad (3.1)$$

E is the measured electrode potential, E° is the standard electrode potential (also known as the standard reduction potential) for the electrode reaction at standard conditions (1 M concentration of all species, 1 atm pressure, and 25 °C temperature), R is the gas constant (8.314 J mol^{-1} K^{-1}), T is the absolute temperature (in Kelvin), n is the number of electrons involved in the electrode reaction, F is the Faraday constant (96,485 C mol^{-1}) and Q is the reaction quotient, which is the ratio of the product concentrations to the reactant concentrations, each raised to the power of their stoichiometric coefficients.

The standard potential (E^0) is a measure of the driving force of the electrode reaction and depends on the nature of the electrode material and the reactants. In a CC cycling protocol, the electrode potential will change as a function of time until a steady state is achieved, where the rate of the electrochemical reaction is equal to the rate of the mass transport of the reactants and products. In a CV cycling protocol, the current will change as a function of time until a steady state is achieved, where the rate of the electrochemical reaction is equal to the rate of the mass transport of the reactants and products [186].

Numerous test conditions can be run on the battery including charge (at constant current, voltage, power), discharge (at constant current, voltage, power or resistance), or rest (at open circuit). Cut-off conditions before the cycler/potentiostat triggers the next step of the test sequence depends on the test protocol used, with a cut-off voltage for CC cycling, and a cut-off current for CV cycling. In some cases, when testing cells in this work, a loop was applied to the test procedure, so that test conditions could be looped for a specified number of cycles.

3.6. Scanning Electron Microscopy

SEM provides information on the surface morphology of a tested sample [187]. The instrument rasters a focused electron beam across the surface of a material. The electrons in the beam interact with electrons in the sample and this is measured by the system to create an image of the sample. Two different interactions occur between the SEM and the sample producing signals that can be detected by specialized detectors. These signals are dependent on the penetration depth of electrons. The first interactions involve elastically scattered electrons through an angle of $>90^\circ$ from the incident beam and are known as backscattered electrons. The second interaction involves secondary electrons that are emitted from the sample due to inelastic scattering as the incident electron beam excites atoms in the sample [188]. The detected signals are then amplified and displayed in a computer-generated image with variations in brightness according to the materials in the tested sample. Characteristic radiation of atomic species in a sample is produced as a result of the incident electron beam. This radiation is produced from the excitation of inner shell electrons as a result of the ejection of photoelectrons leaving vacant holes that electrons fill. The characteristic interactions that occur in an SEM are shown in Figure 20.
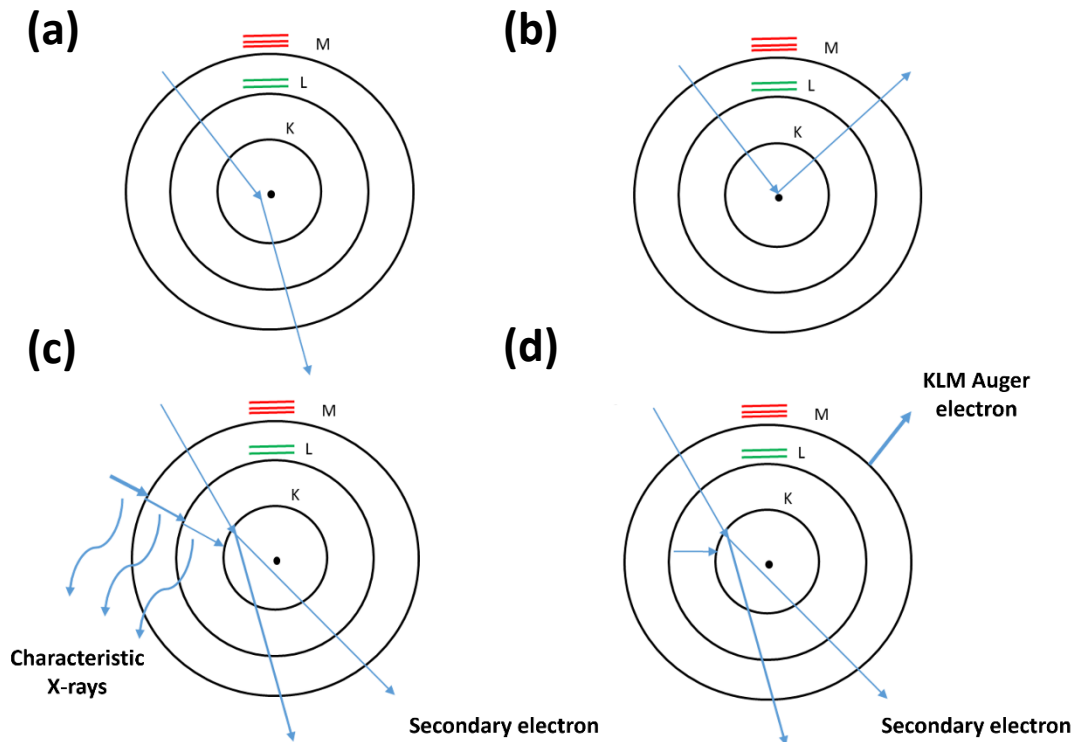
Figure 20: *The characteristic interactions that occur in a SEM are depicted in this figure. Inner electron shells of an atom are labelled with standard notation (K, L) and the outermost electron shell (M). The incident particle is shown with an arrow. (a) Low angle scattering of electrons with very little loss of energy, (b) backscattered electrons; (c) secondary electron emission and characteristic X-rays produced and (d) emission of a secondary electron and Auger electron. Adapted from Vernon-Parry et al.*[187]*.*

SEM does not offer information on the internal microstructure of the electrode; it is limited to revealing the surface or an equivalent 2D layer of the electrode material. Species present in a sample can be measured and identified from characteristic radiation. This technique is called energy dispersive spectroscopy (EDS). EDS systems are typically integrated into the SEM instrument. EDS systems contain a liquid nitrogen dewar for cooling, an X-ray detector, and specialist software to record energy spectra. The EDS detector is usually comprised of silicon (lithium) crystals and is mounted in the sample chamber.

The detector is cooled by the liquid nitrogen and is typically operated at low voltages to increase sensitivity. The EDS detector absorbs incoming X-rays emitted during sample ionization, which yields free electrons in the crystal detector. These electrons become conductive, and an electrical charge bias is produced. Individual X-rays are converted into proportionally sized electrical voltages. These voltages are proportional to the X-rays absorbed for different elements.

In the course of this work, SEM imaging and EDS were performed using an EVO MA 10 microscope (Carl Zeiss Microscopy GmbH) in order to examine morphological surface changes and elemental composition of pristine and tested electrodes. For SEM imaging experiments, electrodes were mounted onto stubs using an adhesive carbon tape. Typical SEM parameters included a working distance ~11-12 mm, accelerating voltage of 3 kV in back-scattered electrons mode and gun vacuum below 5 x 10^{-7} mbar.

3.7. X-ray Computed Tomography

3.7.1 Overview

Numerous scientific disciplines use X-ray CT, including medicine, astrophysics, archaeology, biology, geophysics, oceanography, and material Sciences. The term tomography originates from the Greek words "tomos", which means to cut or to divide, and "graphos", which is a graphic depiction. Thus, tomography is a technique aimed to obtain an image by cutting a section of a material sample [189]. X-ray CT was introduced into clinical practice in 1972 and was the first modern slice-imaging technique. Its capability to reconstruct images computationally from acquired data and display those images and archive them in digital form was a novelty then but is routinely carried out today [190]. Recent advances in modern X-ray generation sources, optics and computer power have

paved the way for absorption tomography to be widely used in battery research. Three-dimensional images can be acquired, non-destructively, for a diverse range of samples with a micrometre and sub-micrometre resolution using X-ray µCT and X-ray nCT [191].

3.7.2. X-ray generation

In a laboratory X-ray CT system, X-rays are emitted from a filament (cathode) using a micro-focus X-ray tube (Figure 21). Thermionic emission of electrons at the cathode occurs when they have sufficient energy to leave the cathode (when the temperature of the filament wire reaches ~2200 °C) [192]. A beam of electrons is then accelerated in a vacuum tube by a voltage of up to 240 kV and is sharply decelerated before collision onto a tungsten or similar heavy metal target anode (copper, molybdenum or silver) [193]. Part of the kinetic energy of the electron beam is converted into X-rays when it reaches the anode surface. The interaction between the fast-moving electrons and the metal target produces Bremsstrahlung radiation [192].
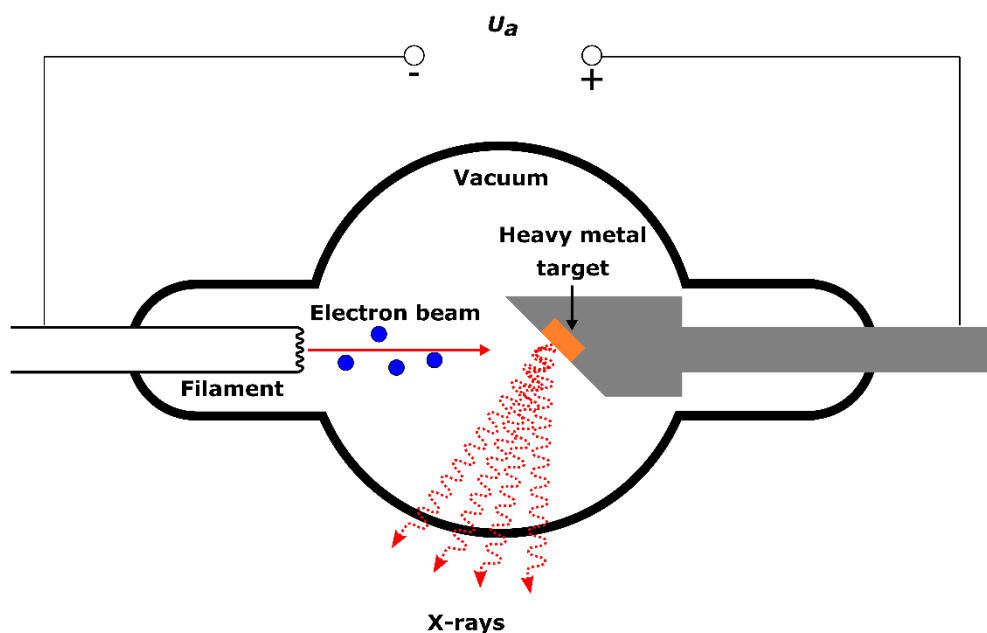
Figure 21: Schematic of a micro-focus X-ray tube, where U_a is the accelerating voltage [194].

The photon energies at which sharp peaks reside in the characteristic spectrum are caused by the particular metal used in the X-ray tube as the metal anode target. Therefore, it is fittingly referred to as "characteristic radiation" [195]. The characteristic energy spectrum of X-rays produced by a micro-focus X-ray tube is shown in Figure 22. There are two ways that X-rays are produced, one which results in a broad range of photon energies (broad peak), and the other which produces distinct photon energies (sharp peaks). Bremsstrahlung radiation is responsible for the broad range of photon energies observable on the characteristic energy spectrum. Bremsstrahlung radiation is an electromagnetic radiation produced by the deceleration of high-speed electrons by the electric field caused by atomic nuclei. When the energy of the decelerated particles increases the broad spectrum created by Bremsstrahlung radiation tends to shift toward higher frequencies and become more intense.
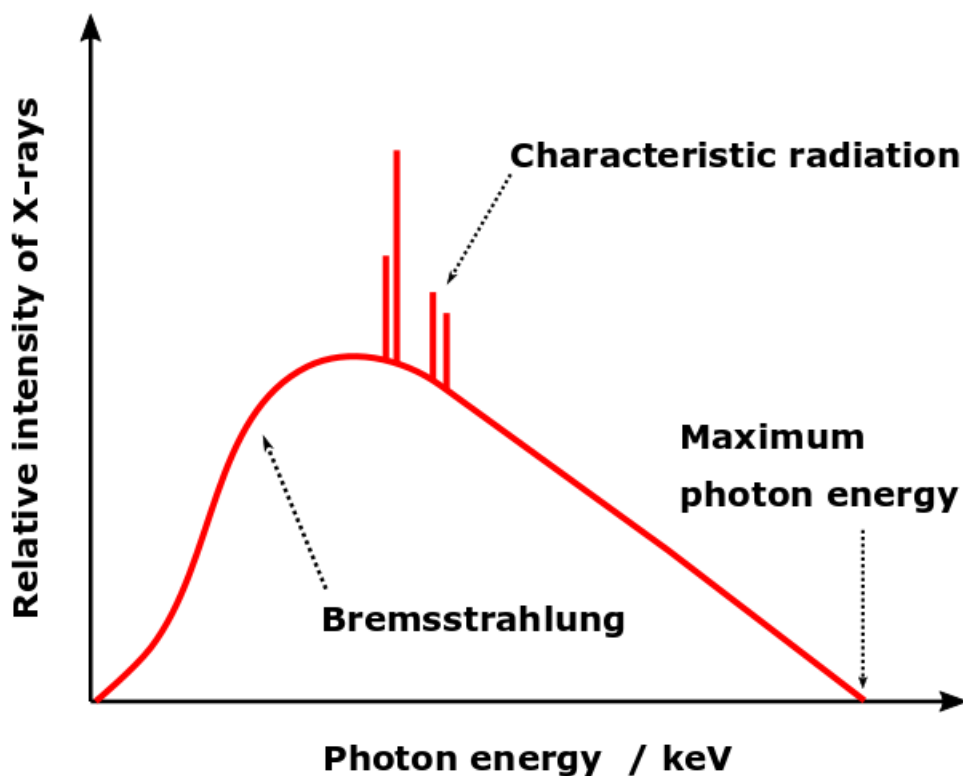
Figure 22: *Characteristic energy spectrum of Bremsstrahlung radiation produced in the X-ray tube.*

3.7.3. X-ray interaction with matter

When an X-ray beam is focused on a target material, the energy of the incident X-ray beam is absorbed by the material causing an electron that is closely located to the atomic nucleus to be emitted from either the K- or L-shell in the sample material as shown in Figure 23. Consequently, the energy of the resulting ejected electron is equal to the energy of the incident X-ray beam, and thus the binding energy of the electron. The ejection of an inner shell electron causes an electron from the outer shell to fill the resulting inner vacancy and thus move to a higher energy atomic orbital level. The migration of this electron causes the emission of a "characteristic X-ray" with an energy that is equal to the difference in the binding energies of the ejected and migrated electrons. Therefore, the energy of this characteristic X-ray is very low, in comparison to the energy of the X-ray caused by the ejection of an electron and is not absorbed by the material. Therefore, the energy of the incident X-ray beam that caused the ejection of an electron is entirely absorbed by the material and does not reach the detector. The term given to this phenomenon is "the photoelectric effect" [195].
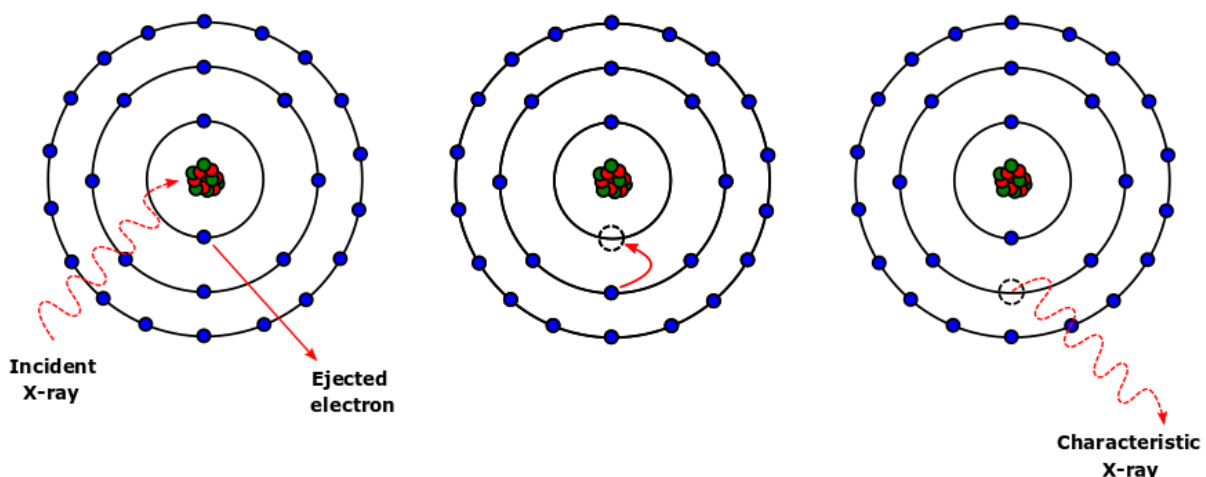
Figure 23: *Schematic showing the 3 stages of the photoelectric effect. The K-shell is the inner most shell of electrons, followed by the L-shell and M-shell.*

X-ray imaging systems detect attenuated X-ray radiation from a sample material. According to the Beer-Lambert law, the intensity of an X-ray beam (I) that passes through a homogenous material of thickness (t) is dependent on the initial intensity of an X-ray beam (I_0) and the linear attenuation coefficient (μ_A) as is shown below:

$$I(x) = I_0 e^{-\mu_A t} \qquad \text{or} \qquad -\ln\left(\frac{I}{I_0}\right) = \mu_A t \qquad (3.1)$$

A material is characterised by the linear attenuation coefficient which is dependent on the material's density [196] [197].

3.7.4. Laboratory X-ray imaging systems

Laboratory X-ray CT instruments typically use cone-beam sources with a poly-chromatic energy spectrum. The micro-focus X-ray tube produces a broad range of photon energies which are dependent on the electrical voltage applied to the X-ray tube. A thin metal filter, most commonly aluminium or copper, is used to change the shape of the spectrum, and can tailor the spectrum towards higher energy peaks. Thus, both characteristic radiation and Bremsstrahlung radiation contribute to the total energy spectrum.

Once the sample has been prepared it is mounted onto a rotation stage inside the laboratory X-ray CT instrument. X-rays are then passed through the sample as it rotates (Figure 24). For clear and accurate image acquisition, it is imperative that the sample is mechanically stable and vibration-free during the tomographic scan. If the sample deforms, undergoes structural changes, or moves slightly during scanning, the true shape of objects can appear deformed [198]. Such deformations are referred to as motion artefacts [199].
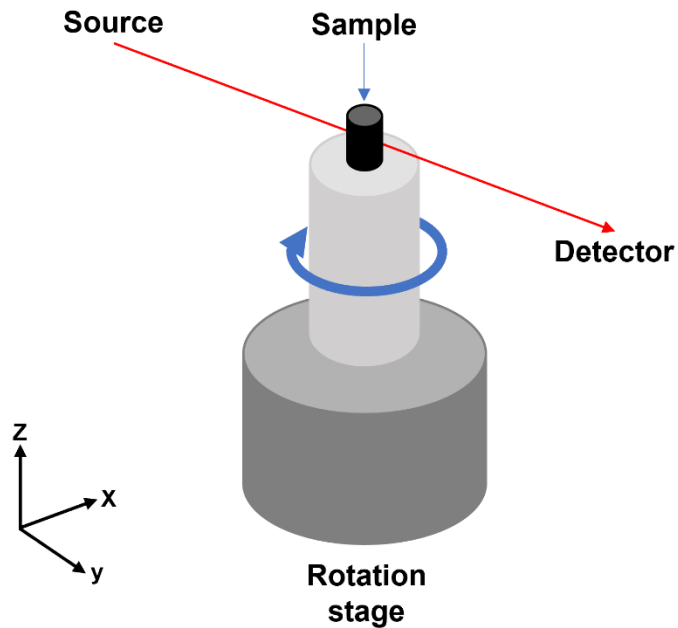
Figure 24: *Spatial orientation of the X-ray beam path (red arrow) as it passes through a sample mounted onto a rotation stage. The sample's clockwise rotation path is illustrated by the blue arrow.*

The attenuated X-ray beam is recorded and detected at the detection system. A scintillator converts the beam into visible light to generate a visible image which is projected onto a Charge-Coupled Device (CCD) chip and a digital image is shown on a computer. Using this method, numerous 2D projection images are acquired at discrete angles during a tomography scan. A back projection of these 2D cross-sectional images is computationally carried out to create a 3D visual reconstruction of the data set from every angle with filtered back-projection algorithms [200].

3.7.5. X-ray micro-computed tomography

X-ray µCT systems most commonly operate with an accelerating voltage range of 20 to 225 kV$_p$. The X-ray photons that pass through a material can be either absorbed or scattered depending on their energies. The interaction of lower energy X-rays (<50 keV) with a sample material in an X-ray µCT system generally results in attenuation (the photoelectric effect).

The focal spot size of the X-ray source and the detector pixel size determine the imaging spatial resolution of the X-ray µCT system. The focal spot size is the size of the part of the target anode that X-rays are created from. Therefore, the focal spot size limits the possible spatial resolution for large geometrical magnification. Typically, spot sizes of ca. 1 µm are used for high resolution X-ray µCT instruments that use microfocus X-ray sources. Furthermore, the detector pixel size is controlled by the optical and geometrical magnifications of the X-ray µCT system. The pixel size can be altered by varying the optical magnification between the scintillator and CCD detector sensor.

The work showcased in this thesis used two laboratory-based X-ray µCT instruments, namely ZEISS Xradia Versa 520 (Carl Zeiss Microscopy Inc., Pleasanton, USA) and the Nikon XTH 225 ST (Nikon Metrology, Leuven, Belgium). The ZEISS Xradia Versa 520 (Figure 25) can achieve 700 nm spatial resolution and the Nikon XTH 225 ST can achieve spatial resolutions down to 3 µm for sample sizes of <10 mm diameter [201]. The ZEISS Xradia Versa 520 provides four optical magnification modes: 0.4X, 4X, 20X and 40X. The Nikon XTH 225 ST does not provide optical magnification modes, the magnification of this instrument is manually varied by moving the sample stage relative to the X-ray source. The Nikon XTH 225 ST has a high resolution 2,880 × 2,880 pixels flat panel detector system. Both systems use a micrometre spot size X-ray source with a cone beam geometry. Accelerating voltage and tube current of the X-ray CT instruments were altered based on the X-ray absorption

coefficients of the sample material being tested. The ZEISS Xradia Versa 520 uses a high resolution 2048 × 2048 pixel CCD detector to acquire radiographic images of the sample mounted on the rotation stage between the source and the detector [202].
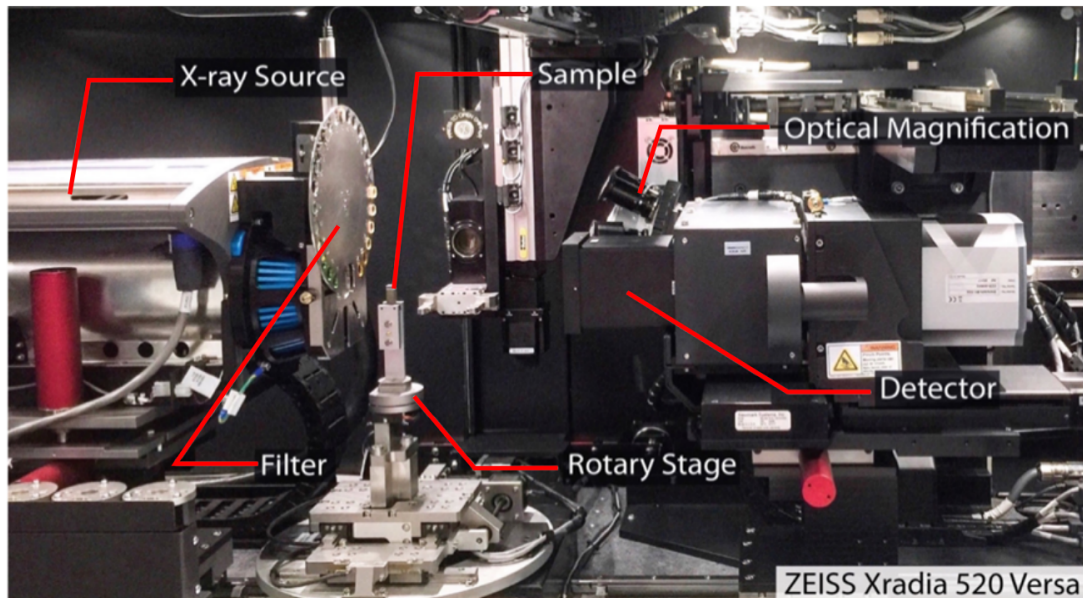
Figure 25: Interior of the ZEISS Xradia 520 Versa reproduced from Carl Zeiss Microscopy GmbH [203].

3.7.6. X-ray nano-computed tomography

In X-ray nCT instruments the sample is illuminated by a rotating anode micro-focus X-ray source. The X-ray beam is focused into a hollow cone beam geometry by a capillary condenser. The objective lens (Fresnel zone plate) collects the transmitted light to form an image in the detector plane [204]. A technique that is commonly used in X-ray nCT imaging for weakly absorbing samples is Zernike phase contrast [205]. A Zernike ring (commonly referred to as a phase ring), is positioned after a Fresnel zone plate to cause a phase shift between diffracted and undiffracted light from the sample (Figure 26).

The light that illuminates the sample material is divided into a diffracted and undiffracted portion and contains information about the sample material. A spatial separation of these two components of light is captured in the back-focal plane of the objective lens. A Zernike ring introduces a predetermined phase shift (90° for positive contrast or 270° for negative contrast) onto the undiffracted portion. The interference of the phase shifted undiffracted portion with the undisturbed diffracted portion results in a phase-contrast image by translating phase modulations of the sample into intensity modulations in the image plane [204].
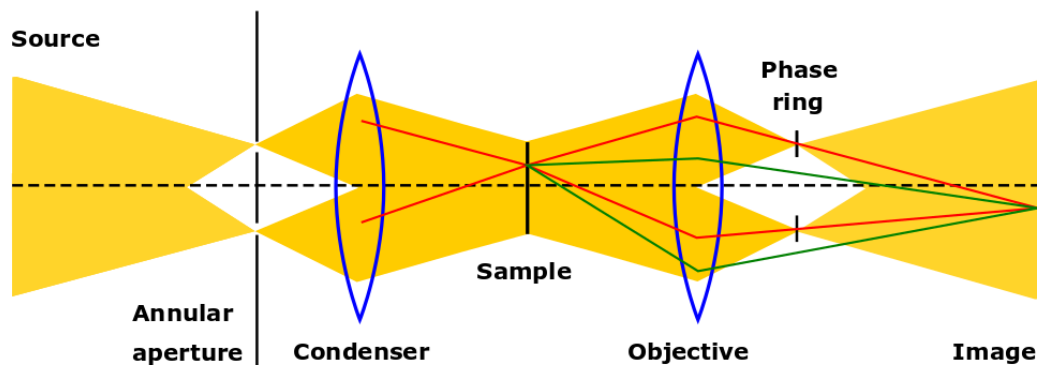
Figure 26: *Schematic of the principles of Zernike phase contrast. Undiffracted light (red) is phase shifted by the Zernike ring with the diffracted light (green), translating phase variations of the material into intensity modulations to attain a phase-contrast image.*

In this work, the ZEISS Xradia 810 Ultra (Carl Zeiss Microscopy Inc., Pleasanton, USA) was used for X-ray nCT imaging. This instrument features two imaging modes depending upon the zone plate used: large field of view and high resolution. The two imaging modes differ in resulting voxel length and field of view. It operates at 5.4 keV and can achieve non-destructive 3D imaging with spatial resolution better than 50 nm [206]. The ZEISS Xradia 810 Ultra and ZEISS Xradia Versa 520 operate with chromium and tungsten anodes respectively producing characteristic X-ray emission peaks at 5.4 and 59.3 keV. The ZEISS

Xradia 810 Ultra uses a high resolution 1024 × 1024 pixel CCD detector system with two available imaging modes: a high resolution (HRES) mode that attains a 16 nm voxel size with 50 nm spatial resolution in a 16 μm field of view, and a large field of view mode that attains a 65 μm field of view at the expense of reduced spatial resolution of 150 nm and an increased voxel size of 64 nm [207].

3.7.7. Limitations of laboratory-based X-ray imaging systems

3.7.7.1. Edge enhancements

Numerous types of noise can disrupt an image [208]. Edge enhancements can arise when deflection of X-rays occurs as they pass through a sample. Refraction of the incident X-ray beam at a sample's interface between two phases with different refractive indices causes weak perturbations of the X-rays. This gives rise to bright and dark interference fringes at different material interfaces and will appear in the tomographic reconstruction. In most X-ray absorption contrast tomography imaging, edge enhancement effects are ignored [198].

3.7.7.2. Ring artefacts

Ring artefacts can disrupt an image if the camera has defective pixels and if the scintillator is defective or dirty. Such ring constructions will be present in an image when the defective pixel has the same value in every projection [209] [210]. Beam fluctuations may also cause broader ring artefacts and are mitigated using reference images [198].

3.7.7.3. Beam hardening effects

The spectrum of a polychromatic X-ray beam changes as it is absorbed by a material. High-energy photons generally pass through a material more easily than low-energy photons. This leads to beam hardening because the average energy of the X-ray beam is increased by the low energy photons being more absorbed by the material, leaving only higher energy photons [211] [212]. Generally, a high energy X-ray beam is selected for thicker and denser materials. A variation of beam-hardening filters, mathematical models and X-ray energies can be trialled to mitigate the effect of beam hardening in the reconstruction [213].

Beam hardening is arguably the most problematic cause of artefacts such as dark bands and streaks. A filter, such as a thin aluminium, copper or iron foil or a beam-flattening filter can be applied to the path of the X-ray to narrow its energy spectrum and thus reduce the effects of beam-hardening [214]. In addition, mathematical methods based on the X-ray path length and material of the sample can be used to reduce beam hardening effects [215]. Most of these methods involve interpolation [216] [217], Poisson inpainting [218], Euler's elastica [219], and iterative reconstruction methods [220] [221].

3.7.8. Data analysis and image processing

Figure 27 shows an overview of the workflow for X-ray CT data processing and image analysis. 3D information is acquired by collecting numerous projections of the sample material at multiple angles using a tomograph. Reference images are used to correct each tomograph, and the data is combined using reconstruction algorithms to spatially resolve the information. Various reconstruction algorithms exist. However, the filtered back-projection algorithm is the most commonly used, and is the chosen reconstruction

algorithm in this work [222]. The tomographs are collated to form a reconstructed 3D dataset, also referred to as a tomogram. A tomogram consists of numerous voxels, each containing an assigned number corresponding to the X-ray attenuation coefficient at a specific point in space. The tomographs collected from X-ray μCT and X-ray nCT were reconstructed using a commercial image reconstruction software package (ZEISS XMReconstructor, Carl Zeiss X-ray Microscopy Inc., Pleasanton, USA) which employs a filtered back-projection algorithm. Reconstructed X-ray CT scans result in a stack of 2D greyscale images of a 3D sample material in .*tiff* or .*txm* format.
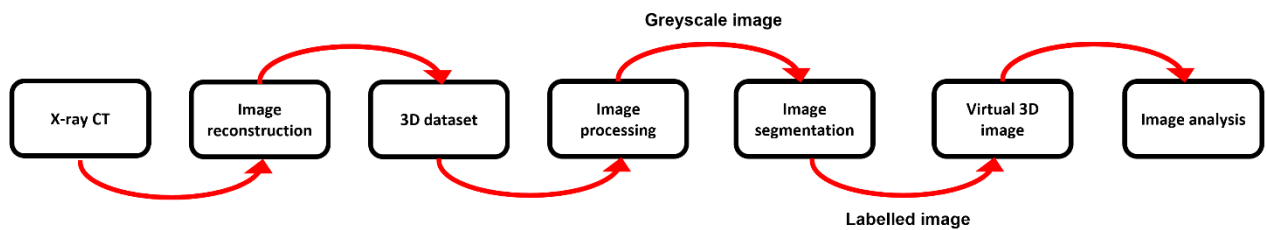
Figure 27: *Schematic representation of the workflow for X-ray CT data processing and image analysis.*

In this work, analysis of reconstructed images acquired from X-ray μCT and X-ray nCT was carried out using the proprietary software Avizo (FEI Company) and a MATLAB plugin called TauFactor [223]. These incorporate various data manipulation tools, such as volume rendering and image segmentation, to visualise particle size distribution (PSD). The 2D greyscale images had to be processed and segmented in order to extract useful information about the sample material. Image segmentation is a technique adopted to identify objects and their boundaries within an image for subsequent object separation. Segmentation is achieved by assigning labels to image voxels so that objects can be identified and separated in a 3D image. The most common approach adopted in this work for image processing included first enhancing the

greyscale image quality for subsequent image segmentation. A ROI was then chosen, that was representative of the entire 3D dataset for image processing.

Usually, image cropping is necessary to reduce the amount of data that needs to be processed. This is a useful method for dealing with large image datasets. Furthermore, digital image filters are used to remove unwanted artefacts and reduce noise and were applied to grayscale image datasets in this work. These digital image filters are available in the Avizo software and are not limited to grayscale images but can also be applied to images that have been processed and segmented.

A wide range of filters can be used to enhance image features as described below by editing image contrast, and de-noising. An X-ray CT image can appear noisy when background features have a pixel intensity similar to the features of interest. Image quality can be improved to facilitate the post processing of X-ray CT scans. Commonly used digital image filters used in image processing include median filter and non-local means filter. The median filter is a smoothing filter that defines the edges of objects. It works by calculating the median of an n × n matrix surrounding each pixel and substituting that pixel with the median value [224]. The non-local means filter is also a smoothing filter with edge-defining properties which is especially effective on noisy images [225]. Different image filters may require more memory to run and result in a larger dataset (.am file).

3.7.9. Feature separation and identification

The "Separate Objects" tool in the Avizo software identifies boundaries (lines) between objects and separates them along these boundaries using a 3D watershed algorithm on the segmented binarized image stack. The resulting

output image contains individual object separations. Subsequently, each individual object is assigned a unique label automatically (using a connected component analysis) for 3D visualization or for further analysis.

3.7.10. Volumetric particle size distribution

Volumetric particle size distribution (PSD) is a method employed using the Avizo software that involves isolating individual objects in a segmented volume rendered image and quantifying the volume of each object within its boundaries. PSD follows image processing and segmentation. In addition, the objects in an image have to be separated using the "Separate Objects" tool. Carrying out PSD on an unfiltered image would be challenging because the boundaries of individual particles would not have been identified.

The "Label Analysis" module can then be used on the image stack to extract statistical and numerical information such as the volume, surface area, mean value, number of voxels, etc., for each separated particle. The "Label Analysis" tool can thus be used to quantify object properties. In addition to particle volume, other properties such as particle sphericity and area can be quantified. Particle volume, V, can be converted to equivalent spherical diameter, d_{sph}, with the following equation [226]:

$$d_{sph} = \sqrt[3]{\frac{6}{\pi} \, V} \qquad\qquad (3.2)$$

3.7.11. Volume specific surface area

Volume specific surface area (VSSA) is the solid-electrolyte interface area of a particle with respect to its bulk volume, and thus decreases with increasing

particle size. Larger volume specific surface area can be associated with smaller electrode particle size. The 3D surface area is computed using Avizo software once the orthogonal slices of the electrode in question have been segmented and separated according to particle and pores. This process is performed using the 'Surface Area-Volume' module in Avizo, which uses the area of a triangular surface mesh approximation of the particle/pore interface. The triangular surface is applied to the image using a marching cubes algorithm [227].

The marching cube algorithm in Avizo can capture phase interfaces by generating interfaces between multiple segmented phases and using sub-voxel weights for surface smoothing. In this case, an optimal smoothing extent is used in the surface generation step and mesh refinement is done and validated against the analytical solution of model image samples. This microstructural parameter is useful for elucidating how particles are packed in a 3D electrode volume. It is imperative to be aware of the image pixel resolution for VSSA estimations as this is not a dimensionless parameter (unit-1/length).

3.7.12. Tortuosity factor

Geometric tortuosity (ζ) is a measure of the ratio between a path length from point A to B in a 3D microstructure (L_{eff}), and the path length as a straight path distance from point A to B (L).

$$\zeta = \frac{L_{eff}}{L}$$

(3.3)

The tortuosity factor is an estimate of the diffusive or conductive transport flux across one phase in a 3D microstructure, divided by the transport flux for

straight-through paths. The tortuosity factor (τ) is therefore defined as the square of the geometric tortuosity (ζ) [228].

$$\tau = \left(\frac{L_{eff}}{L}\right)^2 \approx \zeta^2 \tag{3.4}$$

Diffusive tortuosity factor (τ), defined as the TauFactor, solves the steady-state diffusion equation between two Dirichlet boundary conditions for a binarized volumetric data set [229] [230]. Only sub-volumes that statistically represent the entire electrode volume are considered, as confirmed by a representative volume element analysis. The MATLAB plugin TauFactor can be used to calculate transport parameters such as phase volume fraction, tortuosity factor (τ) and effective diffusivity (D^{eff}).

3.7.13. Phase volume fraction

In addition to the tortuosity factor (τ), phase volume fraction and directional percolation are other relevant microstructural quantities in this work. TauFactor can be used to determine the volume fraction and directional percolation of objects within an image using a 3D ".*tiff* stack" file produced on the Avizo software and imported into TauFactor. Alternatively, the "volume fraction" tool in Avizo can be used to provide phase volume fraction. The phases in question must first be separated using the image segmentation tool in Avizo for phase volume fraction to be effectively carried out.

3.8. Acoustic Spectroscopy

3.8.1. Overview

This section will begin by describing how ultrasonic waves are produced in materials to provide the necessary contextual knowledge for understanding the application of acoustic techniques and how they can reveal mechanical changes in a material sample.

3.8.2. Production of ultrasonic waves

According to Wadley, [231] acoustic emission refers to ultrasonic signals in the form of elastic waves emitted by bodies undergoing microscopic changes due to a change in stress (event source) (Figure 28). An event source precedes the release of sound energy which propagates as an elastic wave.

Surface displacement at (p_2 , t_2)

Elastic waves propagate

Interior defect causes stress change at (p_1 , t_1)
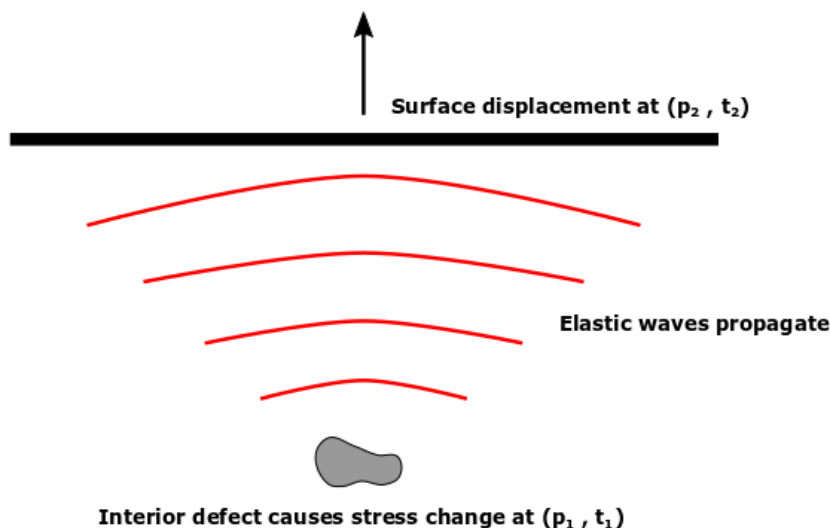
Figure 28: Schematic illustration of the acoustic emission process. An interior defect causes a stress change at position 1 (p_1) at time 1 (t_1). The resulting elastic waves propagate until they hit a material interface at position 2 (p_2) and at time 2 (t_2). Schematic is adapted from Wadley et al. [231].

According to Snell's Law of refraction, ultrasonic signals (sound energy) transmit from one material to another. A sound beam travels straight until it hits a boundary; a beam that hits a boundary at an angle will bend. Sound waves travel in numerous directions at ultrasonic frequencies [232]. It is these fundamental properties of ultrasonic sound waves that underpin acoustic studies [233].

3.8.3. Acoustic signal analysis

Acoustic signal analysis is usually used for 3 main applications: source location, a test carried out to determine the locations where a particular event occurred; material mechanical performance, the characterisation of materials over time/ during operation; and health monitoring, to monitor whether a material operates safely and its SoH [234] [235].

Acoustic wave techniques are capable of globally monitoring a component for defects, allowing large structures and devices to be examined *in-situ* non-evasively and non-destructively [153]. By using multiple transducers, acoustic signals from event sources (and hence damage) can be located in multiple locations [236]. Acoustic signals can be detected in a range of frequencies that range from under 1 kHz, to frequencies around 100 MHz. However, most ultrasonic sound waves are released within the 1 kHz to 1 MHz range [237]. A spectrum of stress waves starting from 0 Hz to several MHz can be generated from an event that rapidly releases stress waves [231].

3.8.4. Principles of electrochemical acoustic-ToF spectroscopy

Electrochemical acoustic time-of-flight (EA-ToF) spectroscopy involves passing an ultrasonic pulse (acoustic signal) through a sample and recording the reflected signal that passes though the sample's respective layers. As the pulse passes through the sample, a portion of the pulse is reflected back from the sample's internal interfaces resulting in a unique acoustic signature.

EA-ToF spectroscopy was first carried out on a battery system by Hsieh *et al.* to examine the SoH of $LiCoO_2$/graphite pouch cells [238]. The key parameter obtained from this type of acoustic experiment is the acoustic time-of-flight (ToF). ToF can be calculated using Eq. 3.5:

$$ToF = \frac{L}{c} = \frac{L}{\sqrt{\frac{E}{\rho}}} \qquad (3.5)$$

where L is the path length travelled, E is the elastic modulus, and ρ is the density of the material. The square root of E/ρ is the speed of sound, c, through a given medium [151].

In each EA-ToF measurement, an ultrasonic sound pulse is incident on the sample being tested. As the initial pulse passes through each interface of the sample material, a portion of the ultrasonic sound wave is transmitted and some is reflected, depending on the degree of mismatch in the sound speed (c) between adjacent layers and whether c increases or decreases from one layer to the next (Figure 29). The wave is also attenuated (i.e., loses energy) as it passes through the bulk region of each layer. As each interface is an opportunity for the pulse to either be transmitted or reflected, the acoustic signature of the

sample can become complicated as each new wave interacts not only with interfaces (creating even more waves) but also with each other. The complex interplay of the mismatch in sound wave speed coupled with constructive and destructive interference between the waves results in the observed reflection and transmission traces. Sound waves also dissipate as they pass through an increasing number of interfaces in the sample resulting in a dampened acoustic response at higher ToF signals. The result is an "echo chamber" effect for the longer ToF waves [151].
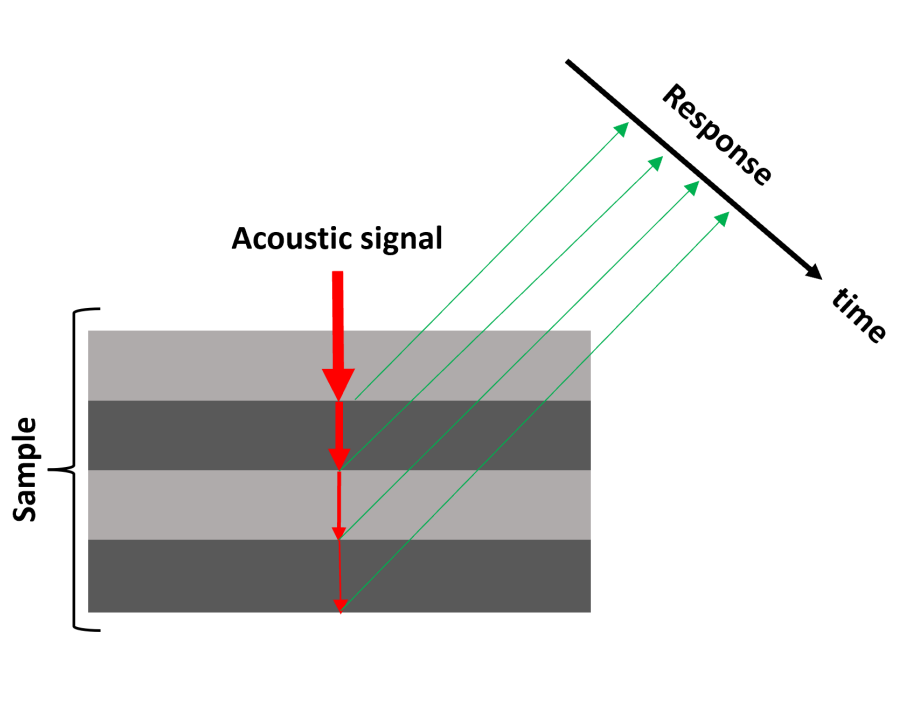
Figure 29: *An illustration of how an ultrasonic sound pulse (acoustic signal) passes through a test specimen during EA-ToF measurements. As the signal passes through each interface a portion of that signal is reflected. As the signal propagates through each interface of the sample specimen, energy is dissipated. The summation of reflected signal (i.e acoustic response) gives a unique acoustic signal.*

3.8.5. The ultrasonic transducer

Generally speaking, a transducer is a device that converts energy from one form into another. Ultrasonic transducers convert sound energy intro electrical energy and vice versa. In EA-ToF spectroscopy, transducers typically contain an active element that is made of either a composite, polymer, or piezoelectric ceramic material [239] [240]. This element vibrates through a specific spectrum of frequencies and emits sound waves when a high voltage electrical pulse is applied to it. An incoming sound wave causes the element to vibrate the transducer and in turn emit its own electrical pulse [233]. A cross section of a typical contact transducer used in EA-ToF spectroscopy is shown in Figure 30.
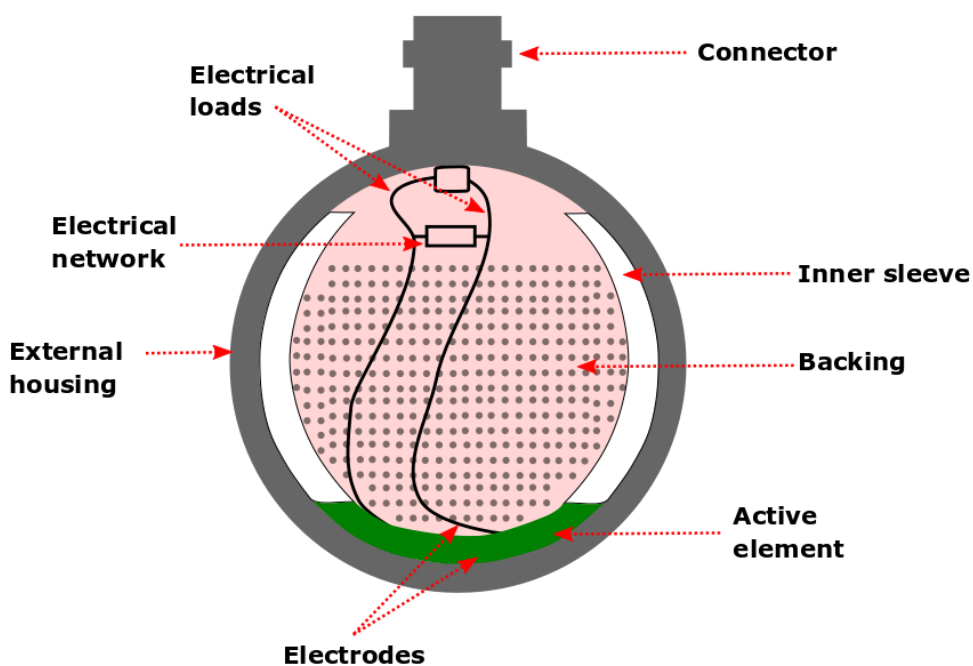
Figure 30: *Cross section of a typical contact transducer used in EA-ToF spectroscopy. A wear plate (not shown in this cross-sectional image) contacts the vibrating surface* [239].

3.8.6. Ultrasonic testing couplant

It is common for large acoustic impedance mismatches to occur between air and solids. Nearly all of the energy is reflected, and very little energy is transmitted into the test material. Therefore, a couplant is used, usually in liquid form, to displace the air medium and accommodate transmission of ultrasonic energy from the transducer into the test material [241]. Commonly used couplant agents consist of oil, glycerine, or water. The exact composition of the couplant agent elected for use in applications usually depends on the nature of the test conditions [242].

3.8.7. Ultrasonic pulse-receivers

Portable devices known as ultrasonic pulse-receivers are used to record and display echo patterns created by materials. These devices are used extensively in industry and production processes. Advanced ultrasonic pulse-receivers usually feature a waveform display for visual interpretation of the sound pulse passing through a material, an ultrasonic pulse/receiver that transmits and receives sound pulses and a data logging module. Software is usually included to capture acoustic signals for subsequent analysis. The shape and amplitude of the sound transmitted from the transducer pulse can be modified, to appropriate conditions for the test carried out. In addition, other parameters such as signal-to-noise ratios, receiver gain and bandwidth can be altered to best suit the test conditions. Further details on the specific equipment used in this work can be found in Section 7.3.

3.9. Conclusion

In this chapter, the working principles of different cell configurations is discussed as well as the electrochemical testing that can be carried out on LiBs. At present, various specialised *in-situ* cell designs are used to examine different properties of LiBs during operation such as pressure changes and thickness changes. Dilatometry can prove to be a powerful technique for measuring dimensional changes in a LiB during operation. Visual corroborative techniques such as SEM can be used in conjunction with *in-situ* dilatometry to examine surface topography and crystalline structure, thus providing a much richer explanation of the dimensional changes undergone during cell cycling.

The fundamental principles of X-ray production and X-ray interaction with matter, and how they can be utilised in X-ray CT instruments to provide useful information on battery electrodes is discussed. X-ray CT is highly suited to battery characterisation as it allows for visual inspection on various length-scales. X-ray μCT and X-ray nCT can be used in parallel to facilitate visual inspection of LiB components at different lengths.

The use of acoustic spectroscopy for LiB characterisation is still in its infancy and is being pioneered by the works of Steingart and co-workers [235] [238] [243] [152]. The experimental techniques discussed in this chapter have been used for multi-scale measurements of degradation mechanisms undergone by a LiB during operation, from particle to single electrode to whole cell level.

INTENTIONALLY BLANK

Chapter 1

A Dilatometric Investigation of Graphite Electrodes

4.1. Overview

The work in this chapter aims to evaluate the bulk volume changes undergone by graphite electrodes during cycling using *in-situ* ECD. X-ray CT is used to visualise the 3D microstructure of the electrode to inform dilatometric interpretation. This chapter describes the various experimental techniques and methods used for sample preparation, characterisation, and testing in this research. The works in this chapter form part of a publication by the author in the Journal of Electrochemical Society [63].

4.2. Introduction

The procedures adopted for cell assembly and electrochemical testing are introduced in this chapter, as well as the techniques used for electrode microstructure characterisation and visualisation. The main experimental tool adopted to measure the bulk volume changes of graphite electrodes in this chapter was *in-situ* ECD, however numerous characterisation techniques were used in conjunction with *in-situ* ECD to investigate the volume changes detected during cell cycling. This approach also provided an understanding as to which techniques best complement ECD.

In this chapter, X-ray µCT was used to reveal vital information about spatial variations in microstructural parameters across the thickness of the electrode. X-ray CT is useful for the inspection of particle cracks, particle expansion and material composition that contribute to electrode dilation/contraction [147] [244] [128]. This work used correlative *in-situ* ECD, SEM and X-ray µCT to elucidate the mechanisms driving the volume changes of graphite electrodes in LiBs, with a view to inhibiting this degradation pathway and possibly predicting its impact on capacity fade. The irreversible dilation of graphite electrodes was recorded during discharge/charge using *in-situ* ECD. During prolonged cycling, the graphite electrode did not return to its original thickness due to changes in the particle-binder matrix and severe delamination in later cycles. Severe delamination of the active material layer from the current collector was confirmed with X-ray µCT.

4.3. Experimental Methodology

4.3.1. Electrode preparation

Throughout the course of this work, the graphite electrodes that were examined were obtained as ready-made electrode sheets from commercial suppliers. Prior to cell preparation, all commercially supplied graphite electrode sheets were dried under vacuum at 120 °C for 24 hours to remove any traces of moisture. Prior to electrochemical tests, the graphite electrodes were dried at 80 °C under vacuum and inserted into an argon-filled glove box (LABStar, MBraun) with H_2O and O_2 levels kept below 0.5 ppm.

4.3.2. CR2032 Coin cell preparation

The graphite electrodes provided by NEI corporation (NANOMYTE®) were assembled as graphite/lithium half-cells. Coin cells were assembled in an argon-filled glovebox (oxygen and water levels in the glove box were both maintained at <0.5 ppm). The graphite electrodes were cut into 15 mm diameter discs and the lithium metal discs (MTI Corp.) CE had a diameter of 15.6 mm. Polypropylene film (Celgard 2400, Celgard, LLC) 19 mm diameter discs were used as the separator in each CR2032 coin cell. The electrodes and separator were soaked in electrolyte containing 1 M lithium hexafluorophosphate ($LiPF_6$) dissolved in a mixture of ethylene carbonate: ethyl methyl carbonate in the ratio 3:7 by volume and 2% vinylidene carbonate. Numerous studies of anode materials use lithium metal for both the CE and the reference electrode which is also adopted here. In the research reported here, the graphite electrode was treated as the WE with respect to the metallic lithium CE.

A manual hydraulic crimping machine (MSK-110, MTI Corp, USA) equipped with a 2032-type die at pressures of 1000-1200 psi was used to pressure seal CR2032

coin cells. The cells were not used in any form of experimental testing for at least seven hours after assembly to allow sufficient time for the electrodes to be soaked with electrolyte. The CR2032-type coin cell (CR2032, MTI Corp, USA) components were cleaned in isopropanol (≥ 99.5% purity) and dried under vacuum for 12 h at 60 °C before use to remove any traces of moisture before cell fabrication.

4.3.3. Cycling of CR2032 cells

Graphite/lithium half cells were discharged and charged under CC at an applied C/20 rate based on graphite's nominal capacity at 0.1C (365 mAh $g^{-1}_{graphite}$) for 10 cycles with a potential window of 0.01 V to 1.5 V. A BCS-805 (BioLogic) battery cycler was used for all graphite/lithium coin cell cycling experiments. Slow discharge rates were employed to ensure that a stable SEI layer was formed.

4.3.4. Dilatometer cell preparation

Assembly of the electrochemical dilatometer cell (Figure 31b) was carried out inside an argon-filled glove box (LABStar, MBraun). Firstly, the glass T-frit was inserted into a frit flange followed by a lithium metal disc (10 mm diameter) and counter piston. To ensure this stack was firmly held together, the piston was pushed in firmly, and turned clockwise. Secondly, the dead volume cover and base body of the cell were placed together with two O-rings to ensure the cell was tightly sealed against ambient temperature and pressure. The stack containing the lithium chip CE was inserted into the cell base body. A polyethylene seal was then placed on top of the T-frit together with the WE and the current collector facing upwards to ensure the WE was facing the CE. Graphite electrodes provided by NEI corporation (NANOMYTE®) were used as

the WE to assemble graphite/lithium half-cells with a dilatometer cell configuration.

The 2.3 mm gap between the WE and piston must be filled to ensure electrical contact. This was achieved by using a metal spacer disc and thin membrane. A spacer disc was placed on top of the current collector of the WE. A thin metal membrane was then placed on top of the spacer disc followed by the cover flange, and the cell body was closed. The spring load was screwed into the cell base and approx. 0.5 ml of electrolyte was sucked into the cell by a syringe to create a vacuum.

The purpose of a shut-off valve is to connect or break the cell volume and the dead volume of the dilatometer cell. During electrolyte addition, the valve must be closed to ensure the cell volume can effectively evacuate and be filled with electrolyte. Once the electrolyte is added and the experiment is running, the valve should be open. Thus, pressure build-up via gas evolution is effectively removed.

The reference electrode (in this case lithium) was mounted onto a metal pin with a blind bore at its end that pointed to the glass T-frit. It is important to ensure the reference pin is fully filled with the reference material, as incomplete filling may result in scatter/ noise of the WE potential. Once the cell was assembled and hermitically sealed, it could be removed from the glovebox. In a fully assembled dilatometer cell, 1 N in load is applied to the WE.

Outside the glovebox, the assembled cell was mounted on a bracket and the sensor unit was attached onto the cell (Figure 31). Before attaching the sensor unit, it is important to unlock the locking screw and to turn the sensor tip clockwise into its upmost position, to avoid damage to the glass T-frit,

membrane or sensor unit when attaching it to the cell. The locking screw and excenter prevent the sensor from moving when being handled and are used to protect the sensor tip.

Once the sensor unit was placed onto the cell, the sensor tip was lowered towards the cell by turning the micrometer screw. An LED bar graph indicator at the control box (Figure 31a) of the dilatometer indicates the position of the sensor. A yellow LED indicates a valid position for the sensor tip resting on top of the membrane. Finally, to prevent any possible gas evolution affecting the measured displacement, the shut off valve was opened to connect the dead volume with the cell volume. The complete experimental set-up for cell cycling is shown in Figure 31c.
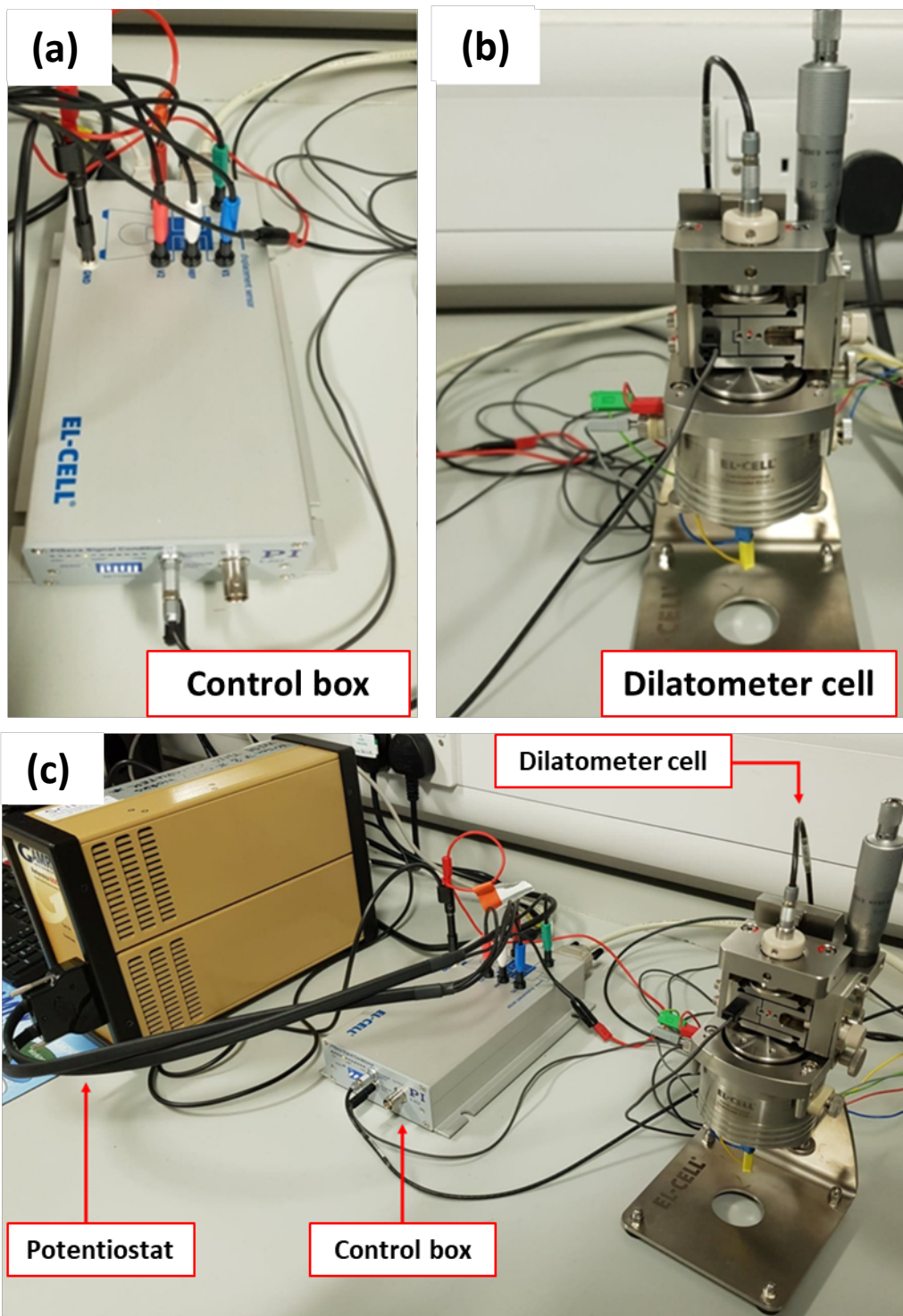
Figure 31: *(a) The control box. (b) The dilatometer. (c) The experimental set-up for galvanostatic cycling. Note, the dilatometer cell is placed inside a climate chamber during cell cycling, and is not shown in these diagrams.*

4.3.5. Dilatometer cell disassembly and cleaning

After cell testing, all cables from the dilatometer cell and the sensor unit were disconnected. The cell was removed from the climate chamber (KB 23, BINDER GmbH) and disassembled. All parts that were in contact with electrolyte were collected for subsequent cleaning. These parts were cleaned immediately after disassembly using a water bath (USC 300-TH, VWR) sonication with deionised water and isopropanol. Valves and tubing of the dilatometer may clog if not properly sonicated with water or appropriate solvent. All parts were then dried in a vacuum oven at 80 °C overnight.

4.3.6. Cycling of the dilatometer cell

A single channel battery tester (Reference 600+ Potentiostat/Galvanostat/ZRA, Gamry Instruments) was connected to the front panel of the control box. Both instruments shared a common ground potential. The potentiostat was equipped with 6-wire connections consisting of working sense, counter sense, working, counter, reference and floating ground. All current cables were connected to the dilatometer control box to account for cable impedance.

The cell was held at open circuit for several hours prior to cycling, to allow for baseline stabilization. This initial rest period helped to discern charging induced height changes from the initial electrolyte wetting of the WE. Height changes occur during charging as a result of the mechanical properties of the WE being altered and thus are not treated as artefacts of measurement.

The dilatometer "half-cell" was cycled between 0.01-1.0 V under a constant current. The current rate was selected based on the active mass of the tested material. Preliminary investigations of electrode materials used a single cycle

test procedure before following with multiple cycle testing procedures with discharge/charge cycles looped numerous times. All ECD experiments discussed in this chapter were carried out at a constant ambient temperature of 25 °C using a climate chamber.

4.3.7. Scanning electron microscopy of graphite electrodes

SEM was used to examine morphological changes of graphite electrodes prior to, and after *in-situ* ECD. Pristine electrodes were mounted onto conductive stubs without any prior washing. Tested electrodes were rinsed with dimethyl carbonate (Sigma-Aldrich) in a glovebox, dried and transferred to the SEM in a vacuum-sealed transfer vial to avoid any air or moisture contamination.

4.3.8. Electrode preparation for X-ray micro-computed tomography

Ex-situ X-ray μCT imaging of graphite electrodes was conducted prior to dilatometric experiments (in the pristine state) and following dilatometric measurements (after cell cycling).

Prior to tomographic imaging experiments, electrode samples had to be prepared in a way that maximised the quality of resulting 3D tomographic images. An A Series/ Compact Laser Micromachining System (Oxford Lasers, Oxford, UK) with an embedded Class 4, 532 nm wavelength laser was used for all samples prepared for X-ray μCT. The laser instrument functions between 0.1 and 2.4 W laser power and has a maximum pulse energy of 1 mJ. Electrodes were machined down to the appropriate geometry and dimensions for the applied field of view during X-ray imaging. This minimised the artefacts that can arise during interior tomography scans and maximised the scanned electrode volume, making full use of the lateral field of view of the detector.
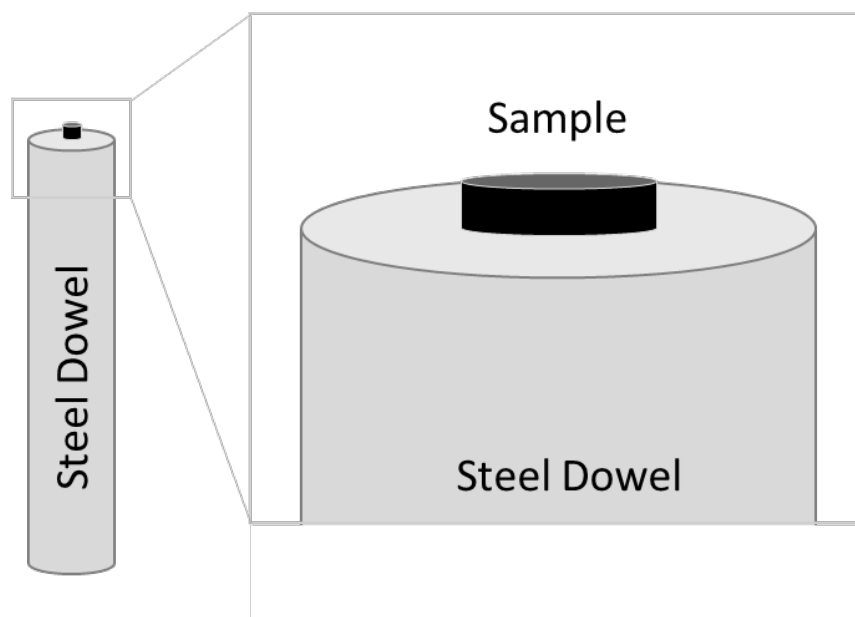
Figure 32: *An illustration of an electrode sample lasered down to the appropriate dimension for X-ray µCT and placed on the top of a steel dowel with double sided tape.*

The sample was mounted onto a steel dowel using double-sided tape or two-part quick setting epoxy (Araldite Rapid, Huntsman Advanced Materials (Switzerland) GmbH) and was placed into the sample holder of the X-ray CT instrument (see Figure 32). Despite tomography being a non-destructive tool i.e., the sample is not deliberately damaged or destroyed in order to analyse the material, damage to the sample can occur during sample preparation, for example, whilst manually moving the sample between instruments and treating the sample with the laser. Therefore, movement of the sample was kept to a minimum, and the parameters used during laser treatment of the sample were carefully chosen to reduce any thermal damage such as laser power (40%), number of passes (5-10) and laser speed (~2 m s^{-1}).

4.3.9. X-ray micro-computed tomography of graphite electrodes

X-ray μCT was performed on the graphite electrode mounted onto a stainless-steel pin with double-sided tape. Double-sided tape was chosen over the more commonly used quick setting epoxy to avoid any epoxy resin contaminating the sample and affecting the images acquired. A lab-based X-ray μCT instrument (Zeiss Xradia Versa 520, Carl Zeiss Inc.) was used, containing a polychromatic micro-focus sealed source set to an accelerating voltage of 80 kV on a tungsten target at a maximum power of 7 W.

X-ray μCT scans were carried out with an X-ray source tube voltage of 60 kVp-with an exposure time of 50 seconds per projection image. The sample was rotated through 360° with radiographs simultaneously collected at discrete angular intervals, amounting to a total of 1028 projections per scan using 40X magnification. Reconstruction of the radiographic data was achieved using a cone-beam filtered back projection algorithm, implemented in Zeiss Scout and Scan software resulting in a reconstructed voxel size (μm) of 0.203 × 0.203 × 0.203.

4.3.10. Image analysis

The pore phase and particle phase of the tested graphite electrode were separated from each other using the image segmentation tool on Avizo. The current collector tab was also separated as its own phase, as to not interfere with the particle phase analysis. This resulted in a three-phase segmentation for pristine and cycled graphite electrodes. 3D volume fractions were quantified for each phase respectively using the Label Analysis module in Avizo that performs voxel counting of the three-phase label fields. A particle phase volume fraction and pore phase volume fraction were quantified respectively.

The border kill module in Avizo was applied to the 3D volume rendering of the electrode to remove particles that were not fully contained within the volume of interest. This was to avoid partially contained graphite particle interfering with the particle size distribution analysis. The Label Analysis tool was used to isolate the particle phase volume fraction and calculate the volumes of each particle.

1.4. Results and Discussion

4.4.1. Benchmark voltage profiling of graphite electrodes

Benchmark voltage profiling was carried out to ensure that the graphite electrodes cycled as expected with capacities near to their theoretical capacities (372 mAh g^{-1} $_{graphite}$) and to discern whether any differences in capacity are incurred when using different cell configurations (see Figure **33**) [36]. It was important to test the electrodes in a coin cell (CR2032) configuration before *in-situ* ECD testing because the dilatometer cell is a specialised cell, and different cell capacities can arise due to the specific cell configuration used.
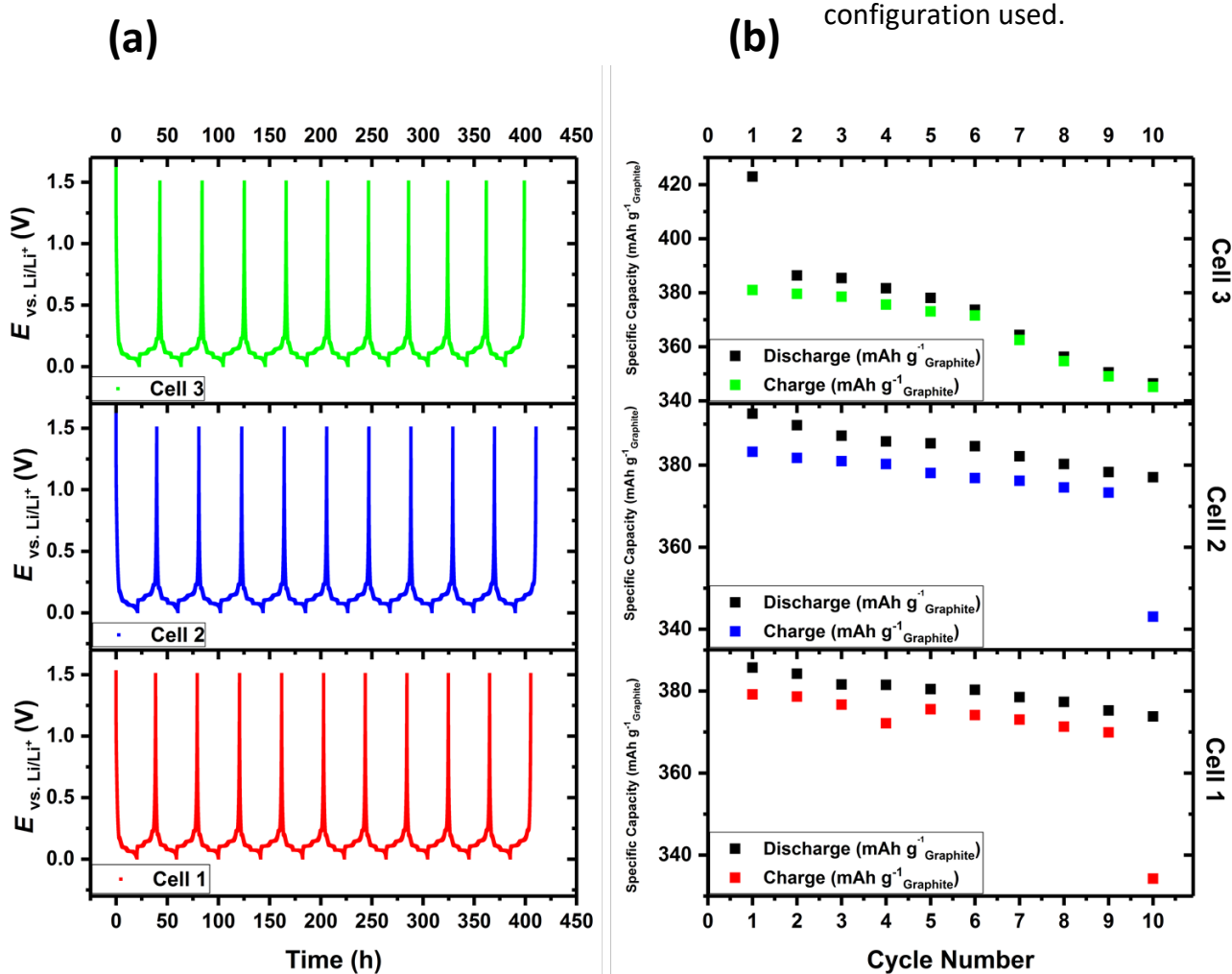
Figure 33: (a) Potential vs time profile for three Graphite/lithium CR2032 half cells and (b) specific capacity vs cycle number for the same three cells.

No significant overpotentials can be deduced from Figure **33**a, with each discharge/charge cycle lasting approximately 20 hours as expected from applying a C/20 C-rate. In addition, the specific capacity of each electrode is within range of the theoretical capacity (372 mAh g^{-1} $_{graphite}$) as is shown in Figure **33**b for each cell. The specific capacity of each cell exceeded the theoretical capacity at low cycle numbers. The reduction in capacity after the first cycle in graphite anodes is known as 'first cycle irreversible capacity' (C_{irr}) and is due to reductive electrolyte decomposition and the consumption of Li^+ ions as the charge carrier. Generally, a "stable" SEI layer is expected to form on the graphite anode surface during the first cycle, consuming ~10% to 20% of the initial capacity [36] [245] [246]. However, formation and continuous growth of the SEI layer can occur during repeated cycling, actively consuming Li^+ ions and thus, cause irreversible capacity fading [74] [246].

The specific capacity of cell 1 and cell 2 faded gradually as the cycle number increased. However, the specific capacity of cell 3 faded much faster. Cell 3 exhibited overpotentials, evidenced by the 420 mAh g^{-1} $_{graphite}$ recorded during the first cycle and a discharge capacity of 346 mAh g^{-1} $_{graphite}$ during the tenth cycle, meaning its capacity faded by 20% after only 10 cycles. Nonetheless, cell 1 and cell 2 had far higher capacity retention than cell 3. The significant capacity fading observed in cell 3 may be attributed to damages incurred on the electrode during cell preparation. It is unlikely to be attributed to an unstable SEI layer forming, given the large irreversible capacity loss observed during the first cycle, suggesting a stable SEI layer had in fact formed.

4.4.2. *In-situ* electrochemical dilatometry of graphite electrodes

4.4.2.1. Single cycle characterisation

Figure 34a shows the potential profile and the simultaneous dilation/contraction recorded of a graphite electrode during its first discharge/charge cycle. The initial potential region from OCP to approximately 0.3 V vs Li/Li$^+$ is usually associated with irreversible processes, SEI formation and possibly graphite exfoliation. The height change (Δh) is used to calculate percentage thickness change (Δt) of the electrode by using:

$$\Delta t\ (\%) = \frac{h\ (t) - h_i}{h_i}\ x\ 100 \tag{4.1}$$

where h_i is the initial thickness of the electrode and $h\ (t)$ is the thickness of the electrode measured continuously during cycling, resulting in a thickness change-time curve. The changes in electrode thickness (height) observed, are in accordance with findings reported by Hahn *et al.* [164], who also investigated the dilatometric behaviour of graphite electrodes during initial formation cycling. During discharging (applying a constant negative current) Li$^+$ ions intercalate between the graphene layers and the electrode increases in height (dilates) in graphite/lithium cells, whereas during charging (applying a constant positive current), Li$^+$ ions deintercalate causing the height of the electrode to decrease (contract) (as shown in Figure 34a). This dilation/contraction behaviour is expected to be observed for many LiB electrode materials as Li$^+$ ions intercalate/deintercalate an electrode during discharge/charge.

Li-GICs (lithium-graphite intercalation compounds) Li_xC_6 are formed upon further charging. Stages (well-defined periodicity along the c-axis consisting of lithium occupied and vacant interlayer spacings) form as a typical feature of Li-GICs. Usually, close to the equilibrium stages at low current densities, the trend in potential and its associated plateaus can be ascribed to stoichiometric domains of pure intercalation phases (stages) and the transformation of these phases into other phases [247].
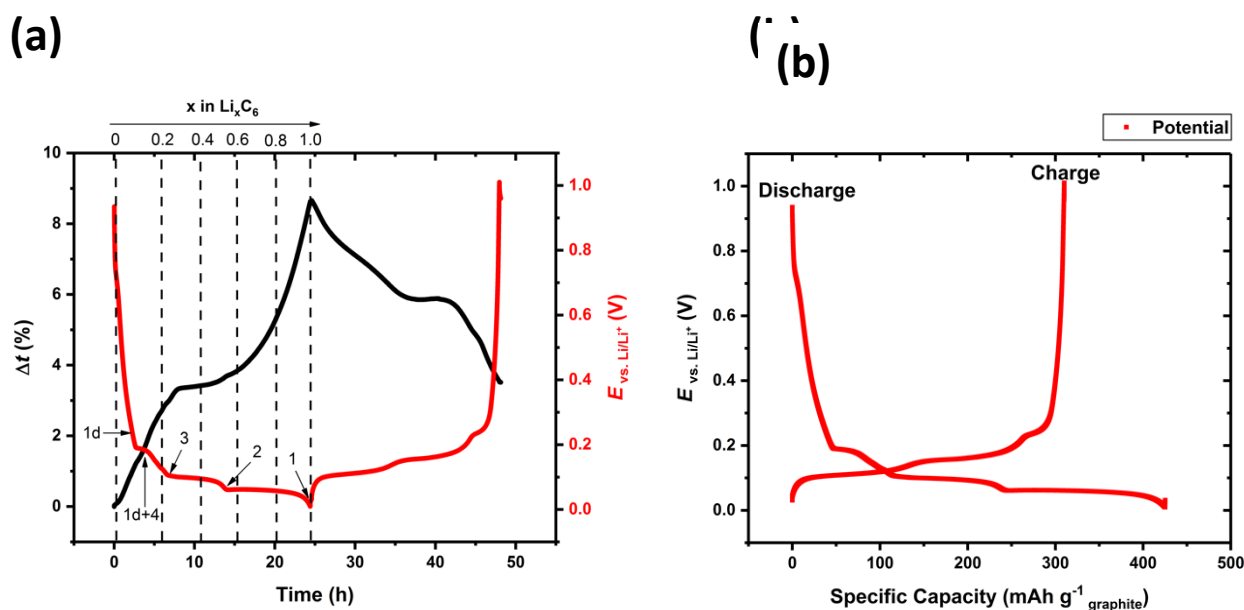
Figure 34: *(a) Potential profile and simultaneous dilation record of graphite (NEI) during first discharge/charge and (b) Potential profile and specific capacity record of graphite (NEI) during first discharge/charge at C/20.*

The formation of a diluted stage 1 (1d) occurs at potentials <0.3 V vs. Li/Li$^+$. The first potential slope is immediately followed by a plateau attributed to transformation of diluted stage 1 (LiC$_6$) into stage 4 as LiC$_{72}$ (1d+4). Stage 3 (LiC$_{36}$), 2 (LiC$_{12}$) and 1 are subsequently formed. Volume changes of the electrode are minimal between x = 0.2 and 0.6 and is in agreement with XRD that detects small changes in volume between these phase transitions [164] [248] [249] [250] [251].

According to the detailed view in Figure 34a, the expansion of the electrode starts positive to 0.18 V vs. Li/Li$^+$, in the region of SEI formation, and before the actual intercalation of unsolvated Li$^+$ ions is observed. There is significant SEI formation after the single cycle, evident by the approximate 3.5% increase in electrode thickness recorded. Electrolyte reduction products depositing on the surface during SEI formation can cause a further increase in graphite particle size and an overall electrode dilation as in Figure 34a. Whereas delithiation occurs during charging (in the half cell configuration), and although deformation due to Li$^+$ ion intercalation is recovered as the electrode contracts, the increase in particle sizes due to SEI formation is irreversible [252].

During discharge, at approximately 40 hours, a noticeable dilation was observed. This dilation was not recorded in subsequent graphite dilation experiments, indicating that it was unlikely to be caused by changes in the graphite lattice. It is speculative that this is caused by changes in the SEI structure, as the dilation is minimal (~0.1-0.2%). An in-situ visual diagnostic tool such as X-ray CT, could be used to explore this observation by examining the SEI layer structure at different SOCs.

A high discharge capacity is exhibited at 425 mAh g^{-1} $_{graphite}$ during graphite's first cycle, which is likely attributed to SEI layer formation. The discharge/charge capacities for the graphite/lithium half-cell are not symmetrical (see Figure 34b). The discharge capacity is higher than expected, and the charging capacity is lower than at discharge. Significant overpotentials are evident, and account for lower energy efficiency [253]. Differences in lithiation and delithiation capacities are an indication of continued electrolyte decomposition [252]. E.M.C. Jones *et al.* [252] reported an artificially high specific capacity in the region of 450 mAh g^{-1} $_{graphite}$ during the first graphite lithiation when cycled at an applied C/20 C-rate for three cycles and suggested these irreversible capacities are due to the decomposition of the electrolyte [252] [254].

Much of the discharge capacity is obtained during a plateau (>250 mAh g^{-1} graphite) and very close to 0 V vs. Li/Li$^+$, which could lead to dendrite formation and thus safety issues [167].

Generally, intercalation materials that have high crystallinity can guarantee a low redox overpotential due to the ordered architecture of the lattice and thus result in high energy efficiency. Graphite is an example of an intercalating material that has diffusion channels within the lattice that are relatively open, allowing straightforward intercalating of ions, so that they can reach the redox sites with a negligible energy barrier [255].

4.4.2.2. Applying a constant voltage step

A constant voltage (CV) was applied between discharge/charge in order to investigate the dilation/contraction behaviour of the graphite electrode while it was held at CV (see Figure 35 below).
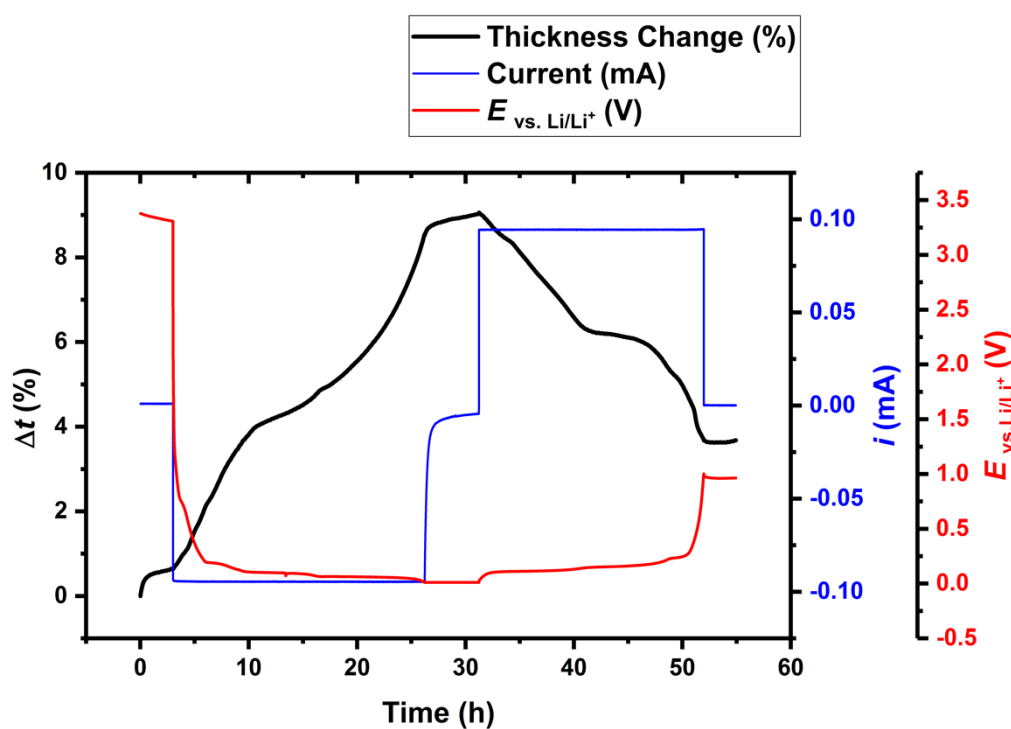
Figure 35: *Potential and current profile and simultaneous dilation record of graphite (NEI) during first discharge/charge and held at constant voltage after discharge.*

When the cell was held at CV (0.01 V) for 5 hours, changes in the electrode thickness were recorded. During CV, the current was allowed to decay to 10% of the current applied during CC discharge. As would be expected, the thickness change recorded for the electrode during a CV is very small compared to the thickness changes exhibited when the electrode is subjected to a CC.

During CC discharge, the Li^+ ions intercalate between the graphite layers, widening the interlayer space and in turn causing the electrode to dilate [256]. The thickness change is approximately 8.75% at the end of discharge and the maximum electrode thickness is recorded just after being held at a CV. A sensible argument for this behaviour is that when held at CV, Li^+ ions cannot deintercalate from between the graphene layers, so one would not expect to see a decrease in electrode thickness. In fact, holding the voltage constant immediately after intercalation ensures any remaining Li^+ ions that have not intercalated during discharge will do so during CV, which would explain a very slight increase in thickness at CV before the electrode is charged (as seen in Figure 35). Tran *et al.* found that using a 2-hour voltage hold at 0.005 V allowed graphite to be fully intercalated and promoted SEI growth. They also found that when adopting a cycling programme with a CV step applied for several hours, the electrode capacity was almost independent of the charge rate when the electrode was fully intercalated [249].

4.4.2.3. Multiple cycle characterisation

In-situ ECD was carried out with the aim of establishing a general trend in volume changes of a graphite electrode over multiple discharge/charge cycles at a higher C-rate (Figure 36). A trend that is different to that exhibited during slow C-rate operation would demonstrate the significance of the chosen C-rate to the dimensional changes of a graphite electrode.
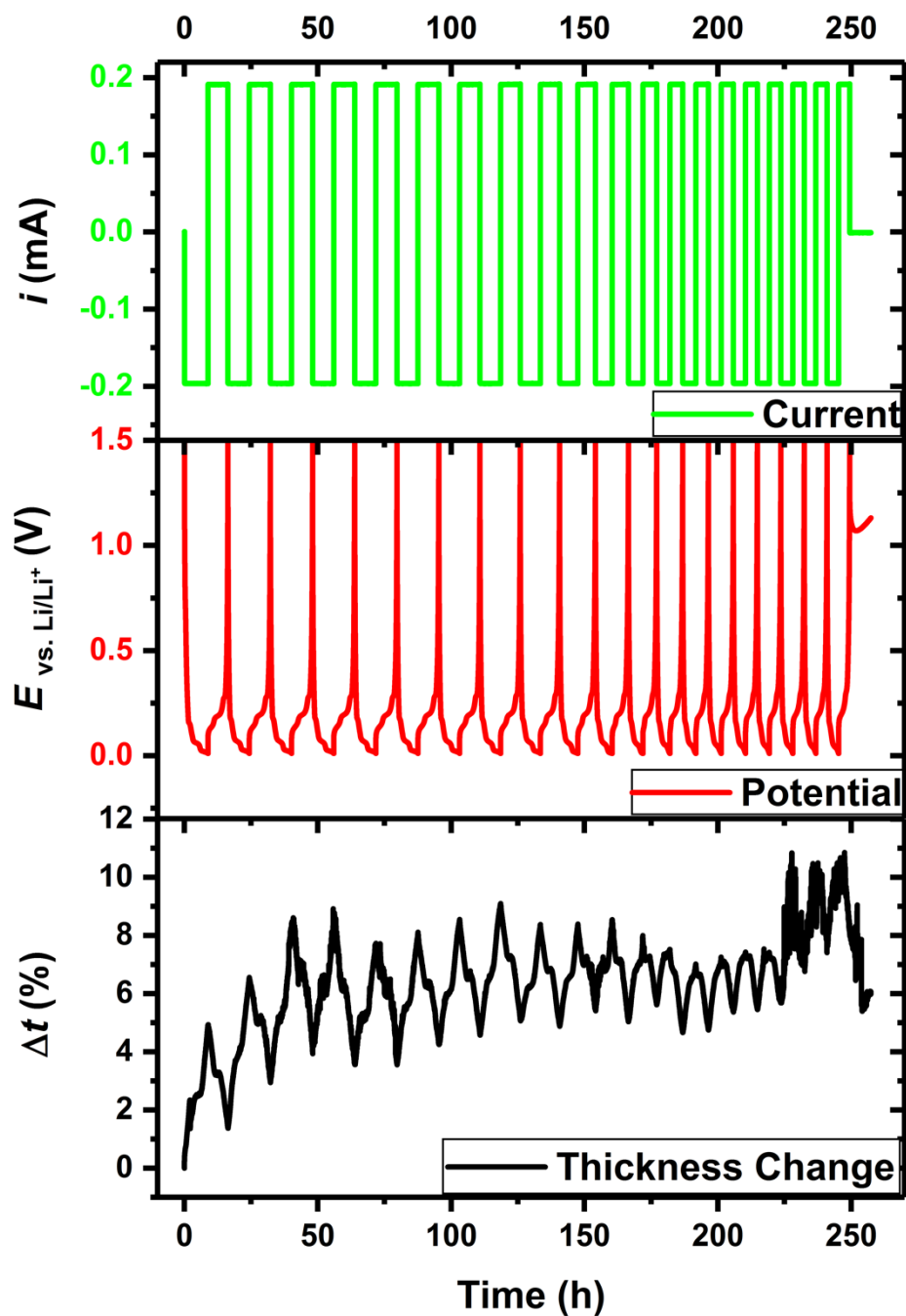
Figure 36: *The potential and current profile and simultaneous dilation record of 20 cycles at C/8 for graphite (NEI).*

An increase in thickness of the electrode across numerous cycles is recorded in Figure 36. The trend in thickness change exhibited is in good agreement with analytical predictions from literature as the graphite electrodes' cumulative irreversible strain increases with additional cycles [252] [257]. The fastest change in thickness occurs during the first three cycles, which can be attributed to morphological changes and continued formation of SEI. The small changes in electrode thickness that occur after the third cycle suggests that graphite particles that dilate during Li$^+$ ion intercalation fill electrode pores. As particles swell to fill the empty voids, there is a hysteresis in the thickness changes recorded, as the changes occur undetected by the dilatometer [258]. It is only when the particles displace vertically away from the electrode, that height changes are detected.

The electrode is shown to periodically "breathe" with each cycle. It has been suggested that this behaviour is due to graphite particles exfoliating to crystalline platelets that do not delaminate from the electrode [259]. Electrode fracture can lead to capacity loss when it causes the active particles to no longer be electrically connected to the current collector, each other, or the binder matrix and arises when the electrode undergoes dilation/contraction during discharge/charge [260]. The highest thickness increase (approx. 11%) is reported during the final cycle (20th cycle).

Graphite's dilation/contraction behaviour is consistent for approximately 14 cycles. The distorted signal in the final 3 cycles could be attributed to electrode delamination (see Figure 37). Graphite phase transitions are significantly more visible in the earlier cycles, and Li$^+$ ion intercalation is affected as the number

of cycles increases and the capacity fades. For instance, stage 1 formation suppresses after approximately 11 cycles, suggesting Li$^+$ ion intercalation into graphite becomes affected. The dilation profiles recorded between cycles 12-17 would suggest full Li$^+$ ion intercalation into graphite no longer occurs and this coincides with the largest fall in electrode capacity occurring between cycle 11 and 12 of 200 mAh g^{-1} $_{graphite}$ down to 160 mAh g^{-1} $_{graphite}$ (see

Figure 38). Subsequent cycling after cycle 12 shows a largely suppressed peak, where stage 1 formation is expected to occur. The inability of Li$^+$ ions to fully intercalate into graphite could be a result of lithium plating, as the cell is cycled to very low voltages. Literature has shown lithium plating can occur when graphite's surface potential falls below 0 V vs Li/Li$^+$ [261]. However, this is an unlikely cause in this scenario and there is no evidence of lithium plating when the electrode is visually inspected during cell disassembly [262].
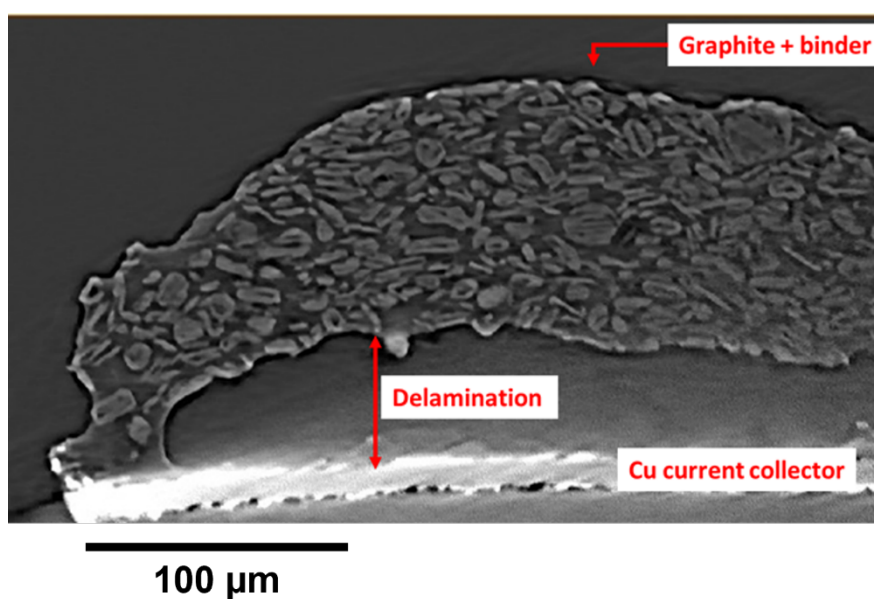
Figure 37: *A 2D virtual slice showing the cross-section of graphite (NEI) post-cycling at rate C/8 for 20 cycles. The image was acquired using X-ray μCT.*

In Figure 37, significant delamination is shown and may be accountable for distorted signal recordings. As the graphite layer delaminates, the sensor records this as height increases that can be mistaken for electrode dilation. Furthermore, the fragility of the graphite may cause it to rise and fall into the empty void between the active material layer (graphite and binder) and Cu current collector, causing height reductions in the recorded data, which can be mistaken for electrode contraction. Thus, details in dimensional changes of graphite may be lost during later cycling. The peak during the discharge/charge transition begins to gradually diminish from the 8th cycle, inferring that electrode delamination began during the 8th cycle.

Post-cycling imaging of graphite shows significant electrode delamination. Electrode delamination is a known issue in LiBs, but its frequency of occurrence can vary depending on a variety of factors, including the electrode materials, cell design and operating conditions. Some studies suggest that the frequency of electrode delamination can be reduced by using optimized electrode coatings, careful cell design, and appropriate stress management during cell assembly and operation [263] [264] [265]. Typical cell operating conditions were chosen for this cell chemistry in this experiment. However, a specialised cell design was used, which could have increased the likelihood of electrode delamination by exposing the electrode to higher levels of mechanical stress.

It is possible that sample preparation ahead of X-ray μCT played a role in electrode damage as graphite is generally fragile post-cycling. However, the gradual diminishing of the discharge/charge transition peak and the distorted signal recordings during the final cycles suggest delamination may have

occurred during cycling and that cycling could have failed had it continued, as the active material is very loosely adhered to the current collector during the final cycle (see Figure 37). Nonetheless, *in-situ* ECD has proven to be a useful tool to elucidate which phase transitions are suppressed during later cycles, by analysing thickness changes during each cycle. Further to electrode delamination, side reactions could be occurring that alter the thickness changes recorded and cause the capacity to fade rapidly. Furthermore, waste products can also form on the surface of the electrode contributing to the overall thickness increase as a result of these side reactions. The practical specific capacity for each cycle is shown in

Figure 38.

154
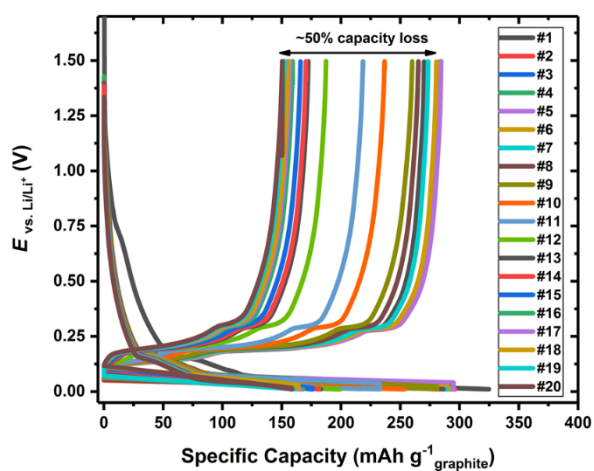
Figure 38: Potential profile and specific capacity record of graphite (NEI) during twenty cycles at C/8.

The practical capacities recorded during ECD measurements fade much faster on cycling compared to equivalent coin cell assemblies during benchmark voltage profiling of the graphite electrodes used in this work (see Section 4.4.1). This finding further suggests that capacity fading is caused by the particular cell configuration which is more complex than conventional coin cells. The difference in capacity values measured for this ECD set-up compared with coin cells is known from previous reports [266] [118] [267]. The highest charge capacity is recorded during the first cycle as approximately 280 mAh g^{-1}$_{graphite}$ at C/8. However, severe capacity fading is observed as the cycle number increases. The specific capacity recorded on the final cycle (cycle 20) is only 140 mAh g^{-1}$_{graphite}$, which is 50% of the initial recorded capacity. In addition, the degree of capacity fading between each cycle is highly random. The high degree of capacity fading could be a result of Li$^+$ ion diffusion limitation playing a major hindering role at cycle rates of C/8.

At C-rates higher than C/20, it is possible that the process becomes diffusion limited due to the dilatometer cell assembly. The large distance that ions must diffuse from one electrode to the other (6.5 mm), via the T-frit and corresponding electrodes, can prove to be a confounding limiting factor which directly affects the electrode capacity. A schematic of the Li$^+$ ion diffusion pathway is shown in

Figure **39**.
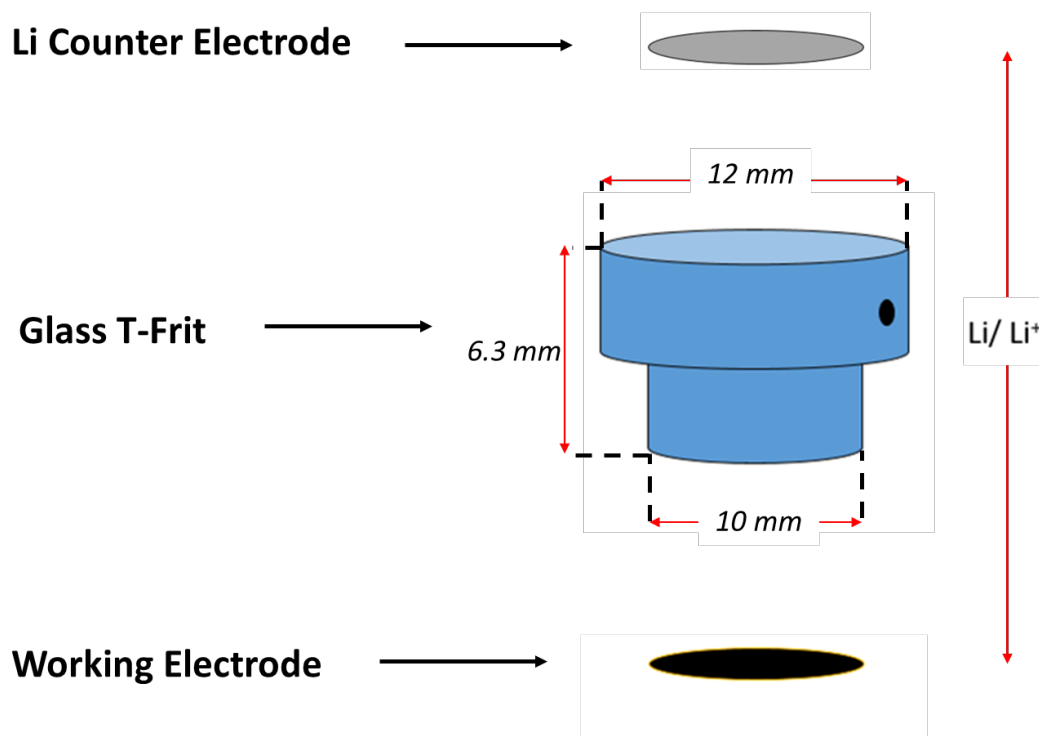
Figure 39: *The components of the dilatometry assembly that contribute to the diffusion limitations of Li/Li⁺.*

In order to achieve sufficient capacity for C-rates faster than C/20 using this *in-situ* dilatometer assembly, it is important to reduce the distance between the WE and CE as much as possible. Reducing the size of the T-frit is not an option since it consists of a delicate glass material and is fixed into position inside the frit flange. Tampering with the T-frit could compromise the cells' hermetically tight assembly against ambient atmosphere.

Two parameters can be used to characterise the thickness changes undergone by the tested electrode over multiple cycles, as shown below. $\Delta\mu$ refers to the thickness change of the graphite electrode between the initial thickness (79 µm) of the electrode and its final thickness after a complete discharge/charge, i.e., $\Delta\mu = \iota_2 - \iota_0$. $\Delta\iota$ refers to the change in electrode thickness within one cycle between a lithiated and delithiated state, i.e., $\Delta\iota = \iota_1 - \iota_2$. Such defined

parameters were applied to the graphite electrode that was cycled at a rate of C/8 for 20 cycles. Changes in $\Delta\mu$ and $\Delta\iota$ are shown in

Figure 40.
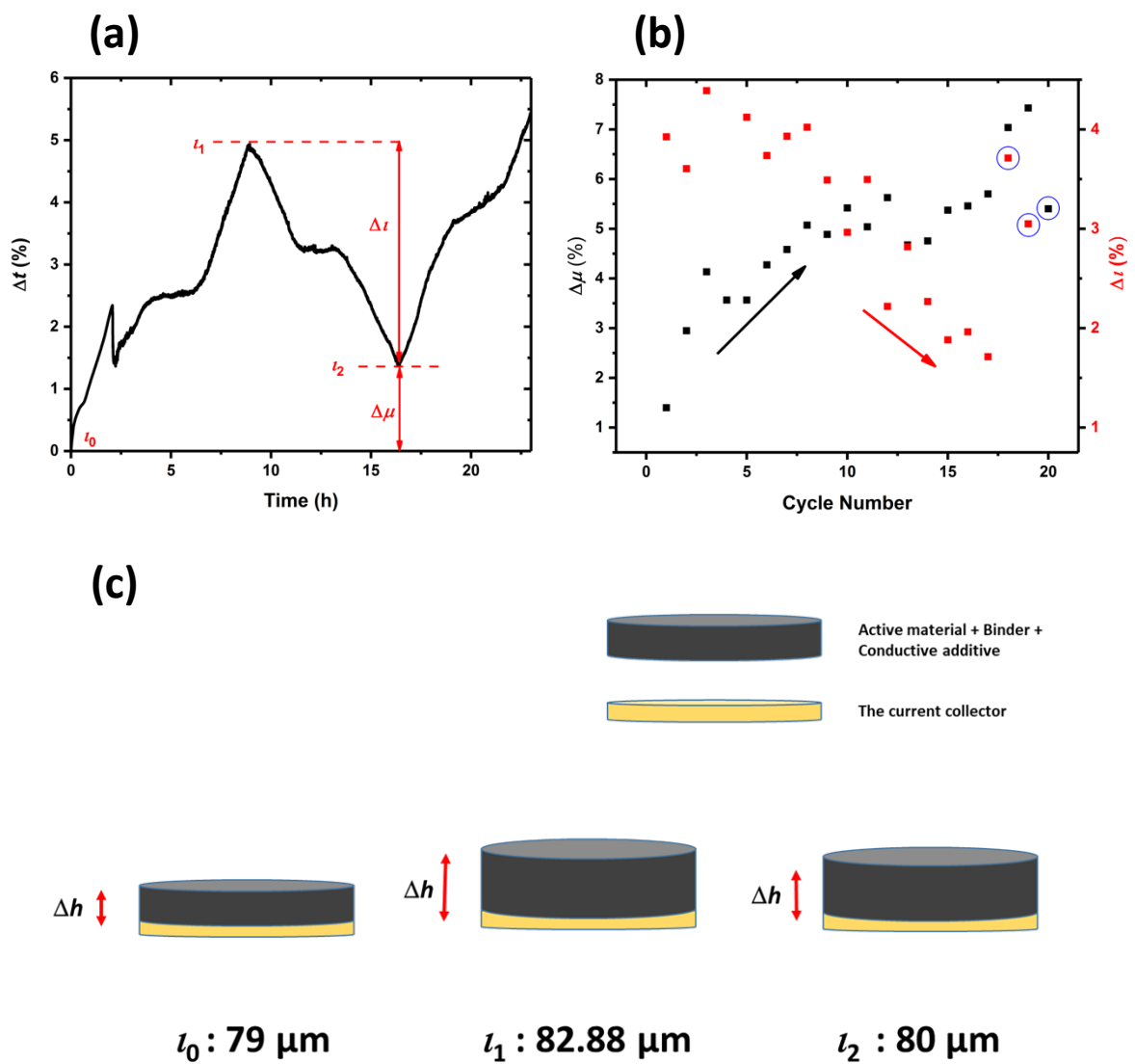
Figure 40: (a) Schematic for calculating $\Delta\mu$ and $\Delta\iota$ and the relationship between the two parameters across one cycle. $\Delta\mu$ refers to the irreversible thickness change of the graphite electrode between the initial thickness (79 µm) of the electrode and its final thickness, i.e., $\Delta\mu = \iota_2-\iota_0$. $\Delta\iota$ refers to the change in thickness within one cycle between a lithiated and delithiated state, i.e., $\Delta\iota = \iota_1-\iota_2$; (b) The change in $\Delta\mu$ and $\Delta\iota$ during 20 cycles at C/8 for the graphite electrode. The circled data points represent anomalous results. (c) shows a sketch of the height changes (Δh) of the electrode as it vertically displaced during one cycle. Height changes (Δh) are used to calculate thickness changes (%).

Numerous processes seem to govern the dilation/contraction behaviour of a graphite electrode. An obvious process observed is general periodic breathing that the electrode undergoes as a result of intercalation/deintercalation. Values for $\Delta\iota$ initially increase during the first few cycles and then decrease upon cycling (see

Figure 40). The values for $\Delta\mu$ are always increasing as cycling progresses. However, the difference between values is largest during the first few cycles. The initial net increase after two cycles is approximately $\Delta\mu$ = 3% and likely related to the exfoliation of the graphite particles. It is unlikely that electrode delamination is accountable for the thickness changes during the first few cycles, as the signal is not highly distorted. Therefore, the first two cycles that lead to an overall thicker electrode, can be seen as "activation cycles". The first cycles are also where the most significant SEI formation is likely to occur,

causing a sharp increase in electrode thickness. However, this change is only temporary as the electrode dilation increases more gradually during subsequent cycling (gradual increase in $\Delta\mu$). It takes around 8 cycles after the initial two cycles for $\Delta\mu$ to increase by 2%. It is possible that the exfoliated particles rearrange themselves during subsequent cycling, though this is speculative relaxation behaviour.

4.4.3. Morphological characterisation of a graphite electrode

4.4.3.1. Scanning electron microscopy

The general increase in $\Delta\mu$ over 20 cycles can be a result of numerous processes as previously discussed. It is possible that side reactions occur as the capacity fades rapidly after 20 cycles. These side reactions can cause electrolyte salts and lithium to form that deposit on the electrode surface contributing to the overall electrode's thickness. Thus, SEM was carried out to investigate the electrode surface and elucidate the possibility of these processes. The tested electrode was compared with an uncycled pristine graphite electrode to allow visualisation of the difference in surface morphology once the electrode is cycled (see Figure 41).
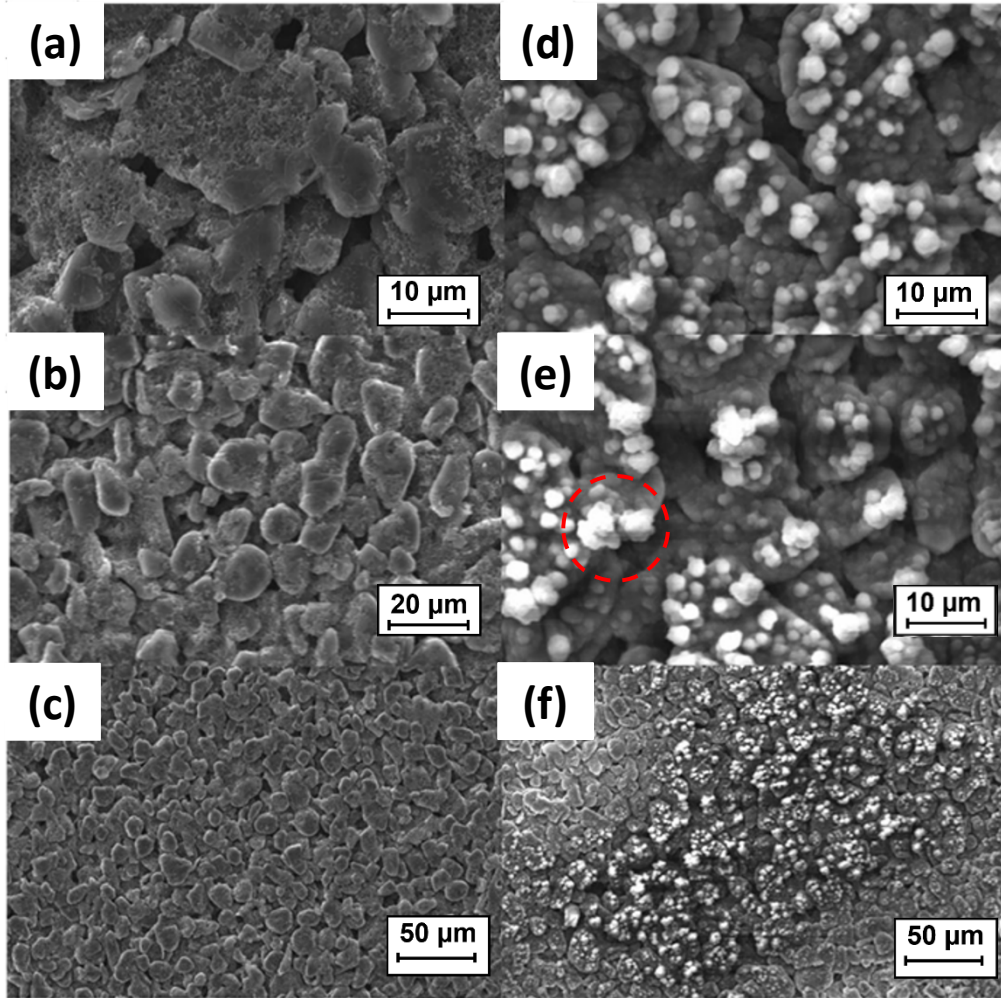
Figure 41: *SEM images of the surface structures of the evaluated pristine (a)-(c) and cycled (d)-(f) graphite electrodes at C/8 rate for twenty cycles: (a), (d) and (e) magnification - 4,800X, (b) magnification - 1,320X, (c) and (f) magnification 1000X. An example of a small fragment on the electrode surface is annotated with a red dashed circle.*

The surface morphology of pristine and cycled graphite is strikingly different as shown in Figure 41, despite the cycled electrodes being rigorously washed to ensure no electrolyte salts would appear during surface evaluation. However, it is possible that lithium deposits and $LiPF_6$ salts were left on the surface from cycling, and not removed entirely during the washing process. Severe degradation had occurred due to the presence of small fragments scattered on the surface of the graphite particles. These small fragments could be graphite

flakes that have delaminated from the electrode as severe electrode delamination is evident in Figure 37. Furthermore, sections of the tested electrode appear elevated at lower magnifications, and it is at these locations where these small fragments seem to reside (Figure 41f).

Elevated sections of the electrode and fragmentation are indicators of severe electrode degradation. The graphite particles are much more homogenous before cell cycling. Gu *et al.* [268] suggest that large changes in the lattice parameters associated with phase changes can lead to the fracture of particles and the loss of contact from the electrode matrix. The graphite particles are highly uniform before cell cycling with no evidence of fragmentation. There is, however, a random distribution and large number of fragments on the electrode surface post-cycling. For instance, a graphite particle in Figure 41e shows a high abundance of fragments on its surface, whereas particles residing further into the bulk appear to have fewer fragments on their surface. There is a possibility that graphite particles that are more elevated have a greater likelihood of these fragments adhering to their surface than particles residing closer to the current collector.

Whilst the micrographs are useful for showing qualitative structural information, their main drawback is that they do not provide quantitative information on inherently three-dimensional structural parameters such as tortuosity and effective diffusion [137]. These parameters directly influence the performance of the electrode in the cell; thus, X-ray CT was also used to evaluate differences in morphology of the fresh and cycled electrode. It should be noted that the accuracy and reproducibility of SEM results can be affected by various sources of errors including sample preparation, imaging conditions and instrument calibration. Furthermore, imaging certain regions of the graphite surface during SEM can result in conclusions being made that are not

indicative of the entire electrode. Nonetheless, elevated sections with small fragments were identified at different parts of the electrode's surface.

4.4.3.2. X-ray μCT image analysis

Electrodes were investigated before and after discharge/charge to examine alterations in the electrode microstructure post-lithiation, which can include particle pulverization and electrode swelling due to solvent uptake. 3D images acquired were used to examine crack propagation, particle size distribution (PSD), and the possibility of electrode delamination. A high accelerating voltage is needed for scanning graphite electrodes in X-ray CT because the active layer of the graphite electrode has low X-ray attenuation, as shown in Figure 42a. In contrast, the copper current collector is highly attenuating to the X-ray beam.
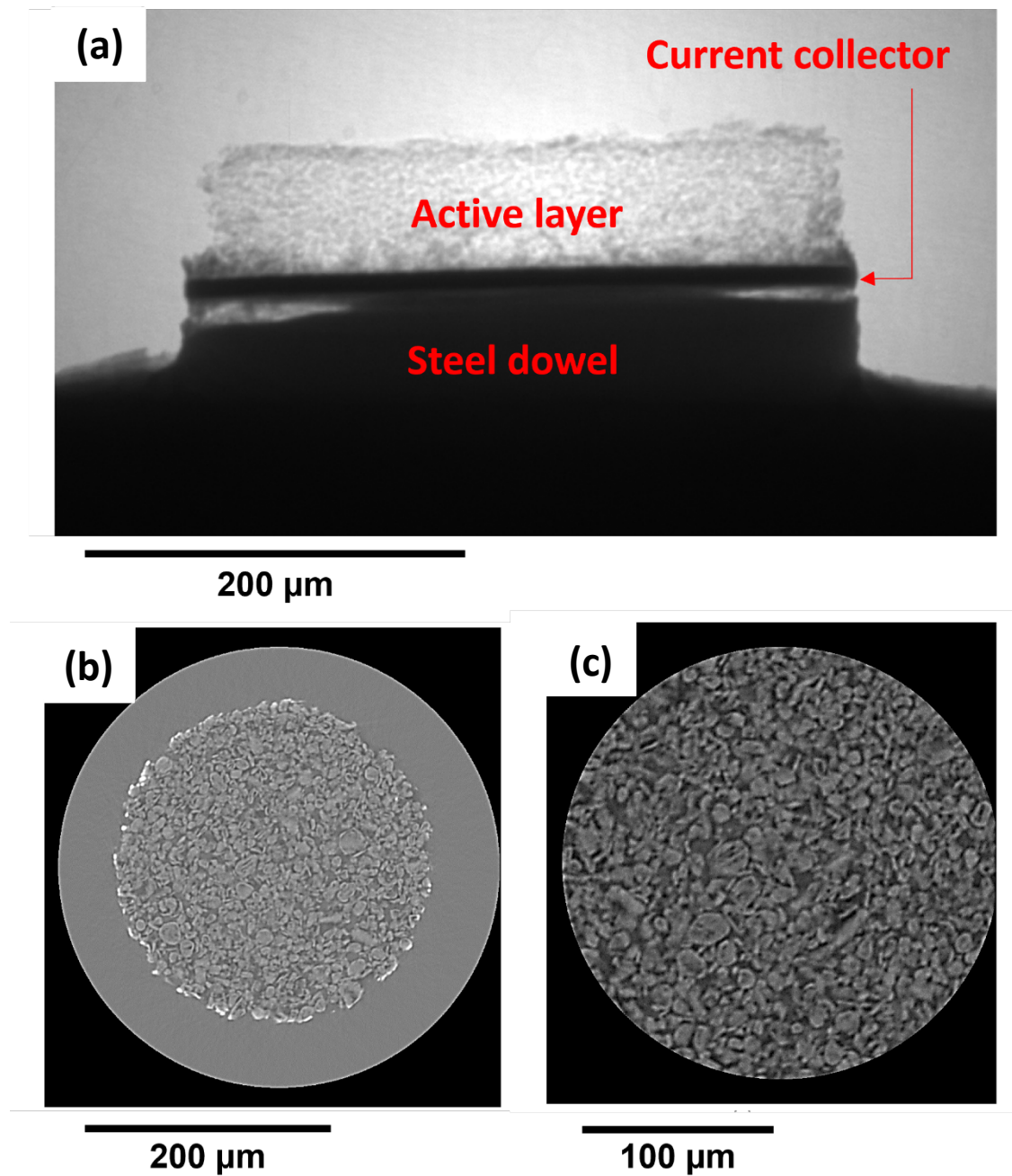
Figure 42: (a) A pristine graphite electrode mounted on a steel dowel and placed on the rotation stage of the X-ray CT instrument. (b) Horizontal cross sections through an X-ray tomography scan of a pristine graphite electrode at 20X magnification and (c) 40X magnification.

Figure 42b and Figure 42c shows horizontal cross-sections through X-ray CT images of the graphite electrode prior to electrochemical testing at two levels

of optical magnification; the horizontal section intersects the active layer region of the graphite electrode detailing the graphite particles and the pore network. The graphite particles have a higher X-ray attenuation than the conductive matrix and electrolyte/pore phases and thus can be identified and isolated via threshold segmentation before rendering in 3D. The X-ray μCT cross-sectional orthoslices shown in Figure **43**a and Figure **43**b were considered reasonably representative of all orthoslices obtained for each electrode and these correspond to approximately middle slice numbers for each electrode.
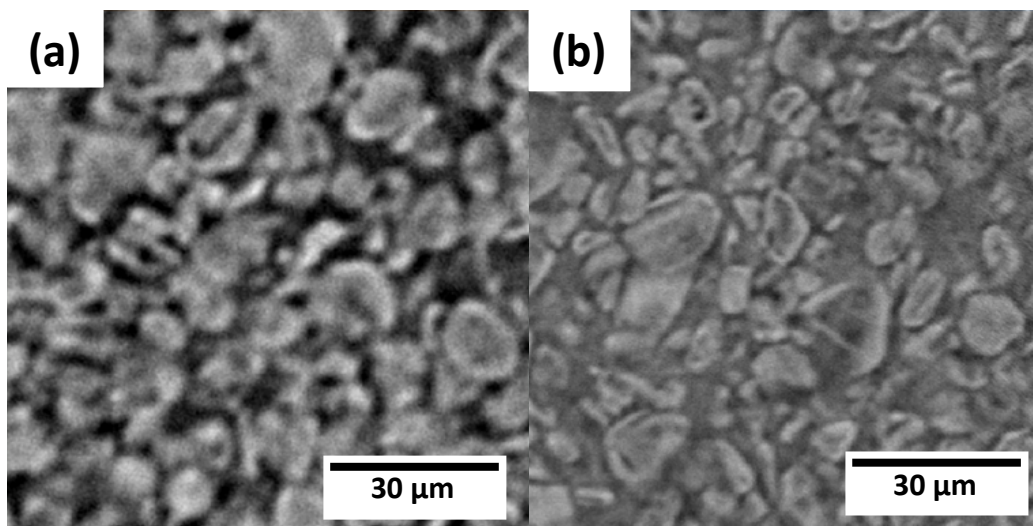
Figure 43: (a) Raw orthoslice of the pristine graphite electrode and (b) cycled electrode at a rate of C/8 for 20 cycles.

The non-uniform shape and size distribution of graphite particles is evident from Figure 43. Their segmentations are shown in Figure **44**a and b respectively for illustrative purposes.
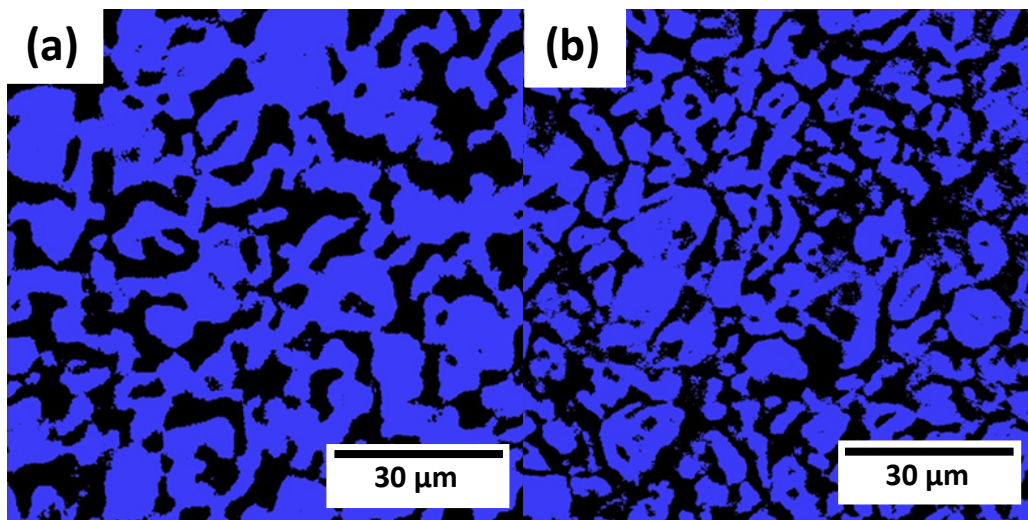
Figure 44: (a) The particle (blue)-pore (black) distribution of the pristine electrode and (b) cycled electrode corresponding to the raw orthoslices in Figure 43.

The electrode is not expected to undergo large changes in PSD after 20 cycles at a relatively slow C-rate of C/8. However, some graphite particles have undergone significant cracking. The particles in Figure **44**b appear smaller compared to particles in Figure **44**a, which is likely to be due to fragmentation. The volume rendering of the solid phase in the pristine and cycled electrode shown in

Figure 45a and

Figure 45b visually demonstrates that the electrode's solid phase volume fraction does not significantly increase as a result of cycling, which is quantified in Table 3. The solid phase can also be referred to as "the active phase" because it is composed of binder, conductive additive, and graphite particles.
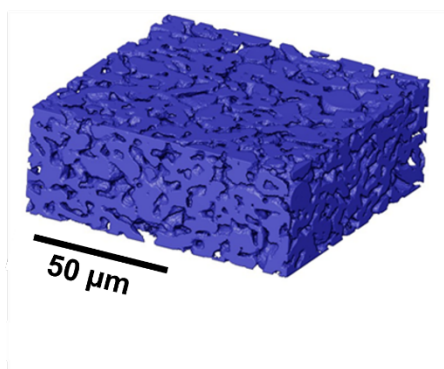
(a)   **(b)**
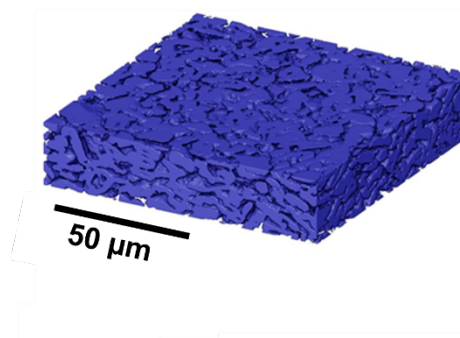
Figure 45: *3D Volume rendering of the particle phase volume fraction of the (a) pristine and (b) cycled graphite electrode.*

The graphite particles of the pristine and cycled electrode are separated and identified, as shown in

Figure **46**a and

Figure **46**b. Random colouring of segmented particles demonstrates the size and shape variation of graphite particles. After the removal of border particles from the volume rendered cycled electrode (

Figure 45b), a high porosity is shown (

Figure **46**b).
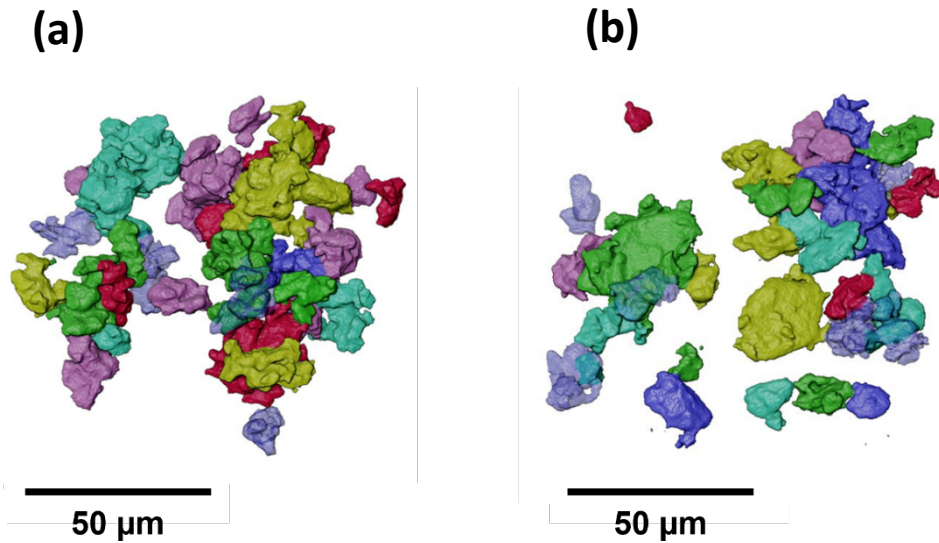
Figure 46: *3D volume rendering of particle network of the (a) pristine and (b) cycled graphite electrode after reconstruction and segmentation and with border kill applied. Particles are randomly coloured to assist in visualisation.*

The rate capability and overall performance of LiBs are highly dependent on the PSD of the battery electrode materials [269]. The PSDs (Figure **47**a and Figure 47b) extracted from the volume renderings of the pristine and cycled graphite electrodes are comparable, providing some validation of the particle sizes in the 2D orthoslice datasets. According to the PSD of particle volumes, most particles in the pristine electrode have a volume between 500 μm^3 to 1000 μm^3. In the case of the cycled electrode, most particles have a volume less than 500 μm^3. In addition, larger particles reside in the pristine electrode compared to the cycled electrode, with some having a particle volume ~5000 μm^3. The largest particles in the cycled electrode are between 2500-3000 μm^3. The presence of larger particles in the pristine electrode suggests smaller pores whereas smaller particles in the cycled electrode suggests larger pores. Electrolyte transport occurs through the electrode pores, carbon and binder

pores [126]. It is likely that the electrolyte can diffuse more readily through larger pores.

(a)   **(b)**
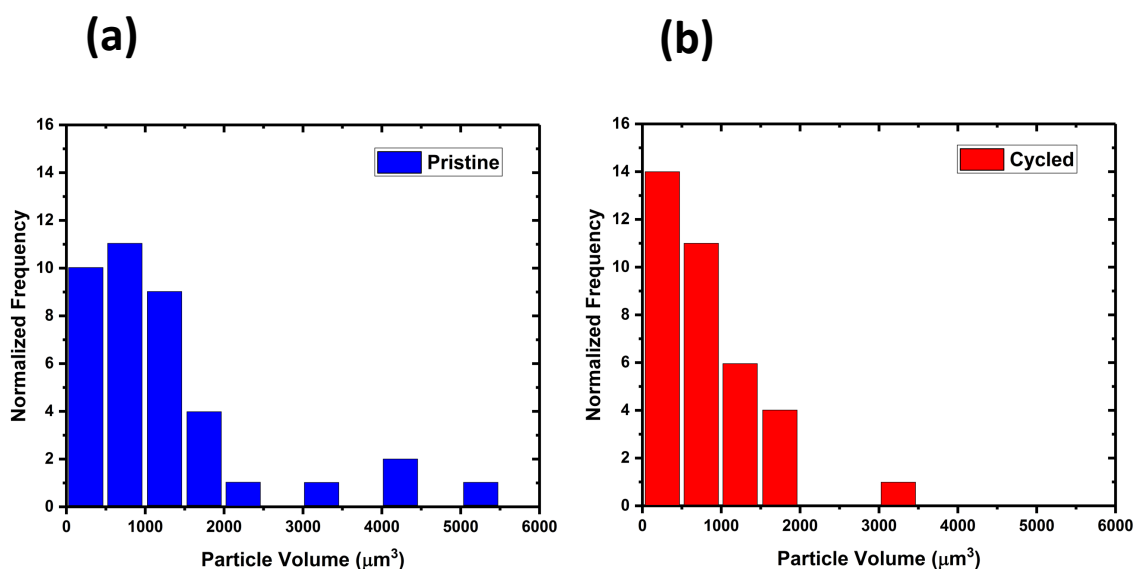
Figure 47: *Volumetric PSD of electrode particles in the (a) pristine electrode and (b) cycled electrode.*

The uncycled electrode in Figure 48a shows how the electrode is expected to look when no delamination is present. The active layer is entirely adhered to the current collector. Whilst the influence of sample preparation cannot be ruled out, it is possible that this electrode delamination contributed to the distorted signal recordings and large thickness changes recorded during later cycling. In contrast, significant electrode delamination is shown in Figure 48b corresponding to the cycled electrode.

(a)   **(b)**

100 µm
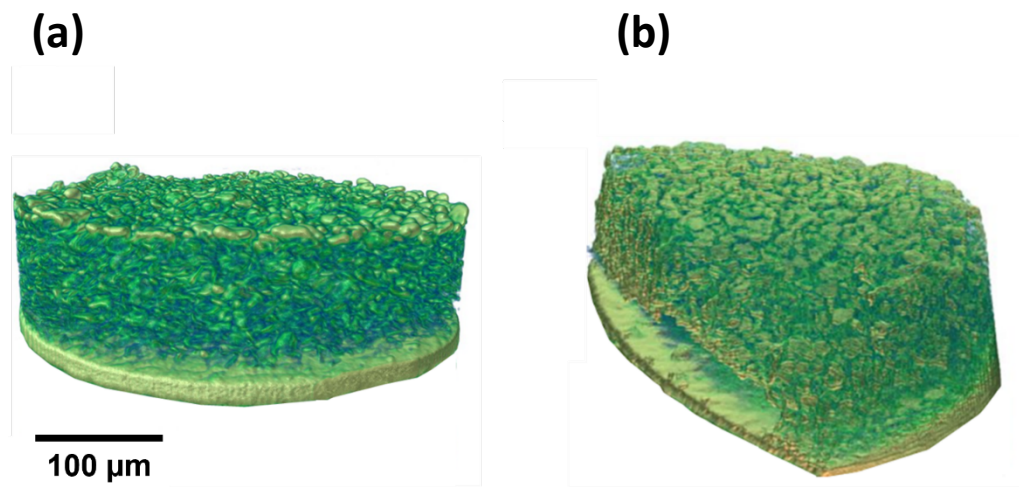
Figure 48: *3D reconstruction of the (a) pristine and (b) cycled electrode show the current collector and active layer, respectively.*

4.4.3.3. Image-based modelling

Table 3: Results of tortuosity factor simulation on the pristine and cycled graphite electrodes. The voxel size (µm) is kept the same for both electrodes (0.203 × 0.203 × 0.203). All simulations were conducted with respect to the pore phase.

Graphite electrode	Solid phase volume fraction (%)	Pore phase volume fraction (%)	Directional percolation (%)	Tortuosity factor (τ), in direction		
				X	Y	Z
Pristine (uncycled)	58.0	42.0	99.1	2.17	2.13	3.02

Tested (cycled)	58.4	41.6	99.4	2.12	1.97	3.28

TauFactor recorded a pore phase volume fraction of 42.0% in the pristine electrode, and a pore phase volume fraction of 41.6% in the cycled electrode. It is generally expected that the pore phase volume fraction would remain very similar after only 20 cycles at a slow C-rate of C/8. Taiwo *et al.* also found a graphite electrode to have a pore phase volume fraction of 42% prior to cycling using TauFactor simulations [127].

Tortuosity factor values are similar for both electrodes in the x-, y- directions of the analysed volume. Interestingly, this is in stark contrast to calculated values in the z- direction which are more tortuous for the cycled electrode despite it having smaller particles than the pristine electrode. It is possible that many of the pores in the cycled electrode are not connected with one another causing a higher tortuosity than the pristine electrode. The highest value of tortuosity factor of 3.28 is recorded in the z-direction in the cycled electrode. The fact that the tortuosity factor is also highest for the pristine electrode in the z-direction suggests that cycling induced degradation is not principally responsible for the high tortuosity value. The z-direction represents the through plane orientation in the electrode and so the tortuosity is expected to be largest here, due to the arrangement of the platelet shape particles. The isotropic recordings for the x- and y-directions are likely due to alignment of the platelet particles within the electrode, caused by packing ordering and calendaring.

Results in Table 3**Error! Reference source not found.** show that the pore phase is less tortuous in the cycled electrode compared to the pristine electrode in the x- and y- directions. Particle cracking could allow for Li^+ ions to diffuse through the electrode with less tortuous diffusion pathways. In addition, empty voids in the pore phase which reduce tortuosity could arise due to cycling.

Directional percolation is slightly higher in the cycled electrode which suggests that more pores are connected and is consistent with a lower tortuosity factor.

4.5. Conclusions

Bulk volume changes of graphite electrodes have been investigated using physical and electrochemical techniques to explore the effect that continuous dilation and contraction has on the overall electrode performance. *In-situ* ECD was successfully used to reveal an irreversible dilation of a graphite electrode during discharge/charge. The tested graphite electrodes were shown to dilate with Li^+ ion intercalation in the standard operating window and by approximately 9% at complete lithiation to LiC_6 during an SEI formation cycle. Cycled electrodes did not return to their original thickness due to severe delamination and changes in the particle-binder matrix which were confirmed with X-ray μCT.

Graphite's dilation/contraction was replicated and consistent across numerous cycles with periodic breathing of the electrode, evident between successive cycles. However, the scale of thickness change was consistently smaller at a faster C-rate. Thus, the findings would suggest that the applied C-rate has an influence on dilatometric measurements. The electrode underwent a thickness change of 3% after a single cycle at C/20 compared to around 7% after 20 cycles at a faster C-rate. At faster C-rates, cycling became diffusion limited, and therefore fewer dimensional changes due to Li^+ ion intercalation and crystal structure changes of the graphite were recorded.

ECD is undoubtedly a powerful technique for measuring the bulk volume changes of a single electrode during cycling. However, using other techniques alongside ECD can shed light on the structural factors which accompany the

volume changes, thus providing a much richer explanation of the complex interplay of degradation mechanisms during cell cycling.

INTENTIONALLY BLANK

Chapter 5

A Dilatometric Investigation of NMC811 Electrodes

5.1. Overview

In this chapter, the bulk volume changes undergone by an NMC811 electrode during cycling are characterised using *in-situ* ECD. Differential electrochemical dilatometry (D-ECD) is used to determine which voltages are associated with the fastest thickness changes in an NMC811 electrode. Correlative X-ray CT is used to reveal vital information about spatial variations in microstructural parameters across the thickness of the NMC811 electrode.

5.2. Introduction

NMC electrode chemistries have been deployed in electric and hybrid-electric vehicles because their layered structures provide high reversible capacities (> 200 mAh g^{-1}) and favourable rate capabilities (electronic conductivity ≈ 2.8 × 10^{-5} S cm^{-1} and Li$^+$ diffusivity of 10^{-8} to 10^{-9} cm^2 s^{-1}) to enable long-range operation and fast-charging [40]. During charge/discharge cycling, reversible Li$^+$ ion transport leads to active materials undergoing alternating volume expansion and contraction which may cause mechanical fracture of the active material resulting in capacity loss [113]. NMC811 electrodes can undergo volume changes as large as 5.1% of the initial thickness when cycled to 4.3 V which can have significant impacts on the structural integrity of the electrode such as micro-crack formation and secondary particle disintegration [270] [271].

Until now, there has been limited work devoted to understanding the bulk thickness changes of nickel-rich cathode materials using *in-situ* ECD. More work has been focused on the anode counterpart such as graphite or graphite-silicon composite anodes because degradation owing to volume changes is known to be more severe in anode materials compared to their cathode counterpart [63] [64] [104] [167] [259] [272]. Although crystallographic changes of NMC particles have been thoroughly examined using XRD measurements [79] [273] and X-ray nano-CT [138] [274], Spingler *et al.* [55] found that NMC electrode expansion (of various stoichiometries) does not entirely correlate with the volume changes of the unit lattice cell of its active materials. Therefore, it is only by measuring the bulk thickness changes of the entire electrode that we can fully understand and predict its behaviour during cycling. The need for a comprehensive approach to understanding the dimensional changes of NMC electrodes cannot be understated as the NMC particles, binder and conductive additive that comprise an NMC electrode can contribute to the bulk transformations of the electrode. In a practical sense, knowledge of bulk thickness changes of cathode materials would be hugely beneficial to battery manufacturing. An

175

understanding of bulk thickness changes of battery components can give new insight on how to manufacture next generation LiBs to accommodate these changes. From an application perspective, a desired property of a practical LiB electrode is that its thickness remains fixed and stable during fast charging and long term operation [118].

The purpose of this work is to evaluate the bulk thickness changes undergone by an NMC811 electrode during cycling and provide new insight into the structural transformations that are undergone during cycling with their consequences on capacity retention. Here, the thickness changes undergone by an NMC811 electrode over a number of cycles are reported using *in-situ* ECD. D-ECD is used to compute at which voltage regions the fastest thickness changes occur in NMC811 electrodes. Pre-existing literature on XRD measurements, NMR spectroscopy [44], mass spectrometry [81] and galvanostatic intermittent titration techniques [273] will be reviewed to explain the findings from *in-situ* ECD and D-ECD respectively. X-ray CT is used for visual inspection of electrode morphology, specifically particle cracking, expansion and porosity that can contribute to electrode dilation/contraction [147] [63].

5.3. Experimental Methodology

5.3.1. Electrode preparation

Commercial NMC811 electrode sheets were obtained directly from suppliers (NEI corporation - NANOMYTE®). The electrode sheets comprised of NMC811 on aluminium foils with 90% NMC, 5% Poly (vinylidene fluoride) (PVDF) and 5% carbon black. An experimental capacity of ≥ 190 mAh g^{-1} is reported in the specification sheet. Prior to electrochemical tests, the NMC811 electrodes were dried at 120 °C under vacuum and inserted into an argon-filled glove box (LABStar, MBraun) with H_2O and O_2 levels kept below 0.5 ppm.

5.3.2. CR2032 Coin cell preparation

NMC811 electrodes provided by NEI corporation (NANOMYTE®) were assembled as NMC811/lithium CR2032 coin cells in an argon-filled glovebox (oxygen and water levels in the glove box were both maintained at <0.5 ppm). The NMC811 electrodes were punched into 15 mm diameter discs for use as the WE, and lithium metal discs (MTI Corp.) were used as the CE (15.6 mm diameter), to ensure an excess of lithium during cycling. Polypropylene film (Celgard 2400, Celgard, LLC) 19 mm diameter discs were used as the separator in each CR2032 coin cell. The coin cells were filled with 100 μL of a standard electrolyte, 1 M $LiPF_6$ dissolved in a mixture of ethylene carbonate. Ethyl methyl carbonate in the ratio 3:7 by volume and with 2% vinylidene carbonate was used as conductive additive.

5.3.3. Cycling of CR2032 cells

NMC811/lithium coin cells were charged and discharged under CC at an applied C/20 C-rate based on NMC811's experimental capacity as quoted by NEI for NMC811 (190 mAh g^{-1} vs Li/Li$^+$) for 10 cycles with a potential window of 2.5 V to 4.3 V. A BCS-805 (BioLogic) battery cycler was used for all NMC811/lithium coin cell cycling experiments.

5.3.4. Dilatometer cell preparation

The dilatometer cell was assembled using the same methodology as discussed in Chapter 4. For these experiments, an NMC811 electrode (10 mm diameter) was used as the WE as opposed to a graphite electrode with a lithium CE.

5.3.5. Cycling of the dilatometer cell

An SP-200 potentiostat (BioLogic, France) was used to cycle the NMC811/lithium dilatometer cells. The current rate was selected based on the active mass of the tested NMC811 electrode. NMC/lithium dilatometer cells were charged and discharged under CC at applied C/20, C/10, C/5 and C/4 C-rates based on the experimental capacity as quoted by NEI for NMC. The NMC811/lithium dilatometer cells were cycled between 2.5 V - 4.3 V under a CC.

5.3.6. Electrode preparation for X-ray micro computed tomography

Ex-situ X-ray μCT experiments involved X-ray imaging of NMC811 electrodes prior to dilatometric experiments (in the pristine state) and following dilatometric measurements (after cycling). As such, *ex-situ* studies were carried out on the bare electrode as opposed to within an assembled electrochemical cell.

The A Series/ Compact Laser Micromachining System (Oxford Lasers, Oxford, UK) with an embedded Class 4, 532 nm wavelength laser was programmed to mill a round NMC811 electrode with a diameter of 2.0 mm. This was judged to be a suitable size for the X-ray μCT instrument field-of-view according to the applied magnification 40X and incident X-ray beam during X-ray imaging.

5.3.7. X-ray micro-computed tomography of NMC811 electrodes

The NMC811 electrode was mounted onto a steel dowel using two-part quick setting epoxy (Araldite Rapid, Huntsman Advanced Materials (Switzerland) GmbH) to be placed into the sample holder of the X-ray tomography instrument. All X-ray imaging was conducted ex situ on lithiated NMC811 electrodes using a ZEISS Xradia 520 Versa (Carl Zeiss Microscopy Inc., Pleasanton, USA) X-ray μCT system. X-ray μCT scans were carried out with an X-ray source tube voltage of 120 kVp- with an exposure time of 30 seconds per projection image. The sample was rotated through 360° with radiographs simultaneously collected at discrete angular intervals, amounting to a total of 2201 projections per scan using 40X magnification. Reconstruction of the radiographic data was achieved using a cone-beam filtered back projection algorithm, implemented in Zeiss Scout and Scan software resulting in a reconstructed voxel size (μm) of 0.187 × 0.187 × 0.187.

5.4. Results and discussion

5.4.1. Benchmark voltage profiling of NMC811 electrodes

As discussed in Chapter 4, benchmark voltage profiling is important to ensure that electrode materials cycle as expected and close to their theoretical capacities, whilst helping to discern capacity issues related to the cell configuration or electrode used. Electrochemical cycling data of the NMC811 electrodes in the NMC811/lithium CR2032 coin cells is presented in Figure **49**.
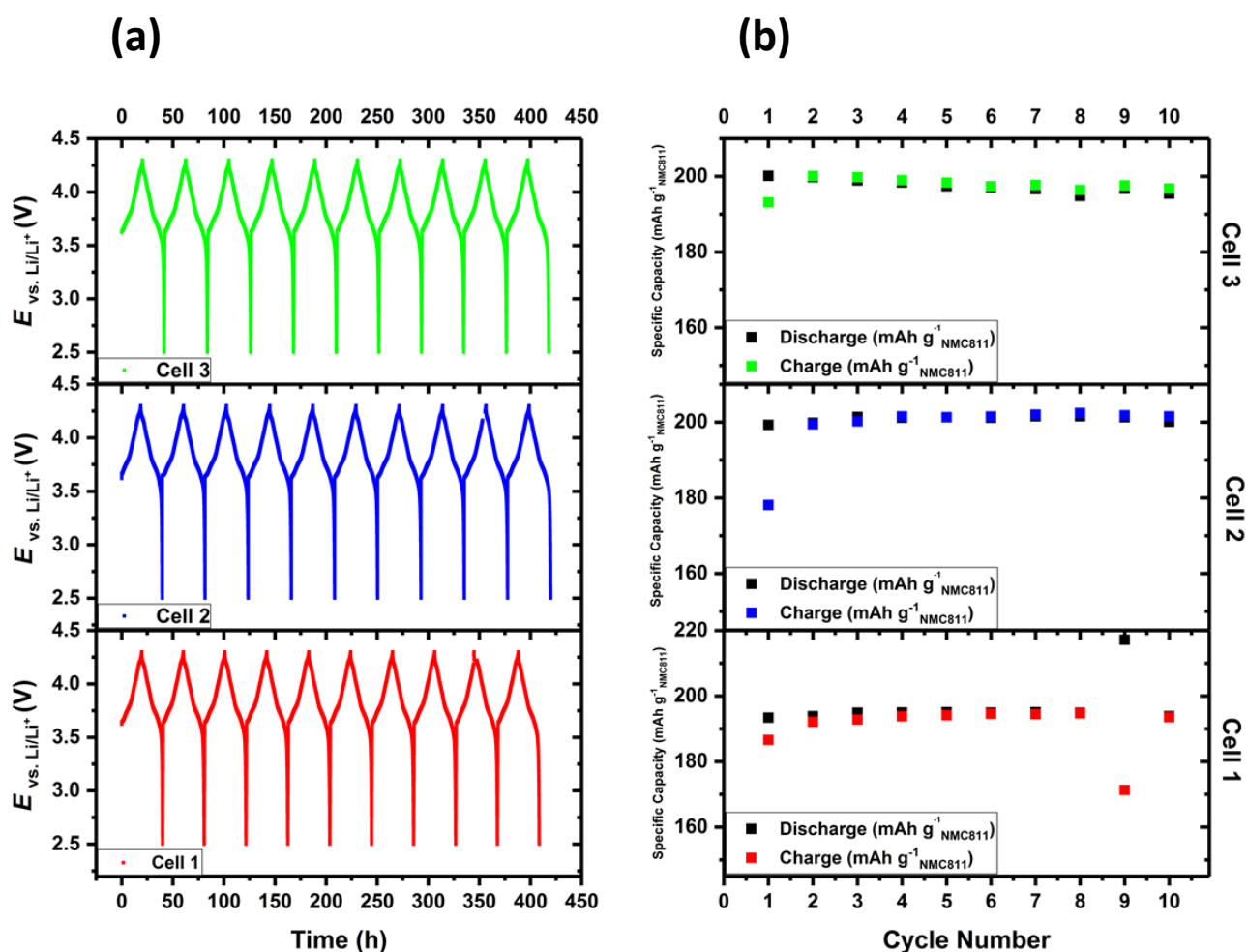
Figure 49: *(a) Potential vs time profile for three NMC811/lithium half cells and (b) specific capacity vs cycle number for the same three cells.*

Charge/discharge capacities of the NMC811/lithium CR2032 coin cells were recorded for 10 cycles between 2.5 V and 4.3 V. This upper voltage limit was chosen as published studies demonstrate that NMC exhibits a surface reconstruction to a rocksalt (Fm3m) structure during high voltage cycling (i.e. 4.3 V and higher) and is responsible for increased cell impedance [275]. No significant overpotentials can be deduced from

Figure **49**a, with each charge/discharge cycle lasting approximately 20 hours by applying a C/20 C-rate under CC.

The specific capacity of each electrode was within range of the theoretical capacity (190 mAh g^{-1} $_{NMC811}$) as shown in

Figure **49**b for each cell. The majority of cycles achieved practical capacities of ~200 mAh g^{-1}$_{NMC811}$. There are minor differences in specific capacity between these NMC811/lithium cells. According to

Figure **49**b, there were minimal changes in charge/discharge capacities from the first cycle to the tenth cycle for each cell. In fact, capacity was retained to a higher extent in the NMC811/lithium cells than the graphite/lithium cells shown in section 4.4.1.

5.4.2. *In-situ* Electrochemical Dilatometry

5.4.2.1. Single cycle characterisation

In Chapter 4, it was found that single cycle characterisation can provide information on volume changes associated with phase transitions in graphite's structure. Furthermore, graphite's dilation profile was reproducible at different C-rates (C/20 and C/8) during discharge/charge despite a noticeable difference in cell capacity. The single cycle characterisation of graphite shown in Chapter 4 was adapted for an NMC811 electrode to investigate its thickness changes during cycling at different applied C-rates during single charge/discharge. As

was discussed in Section 5.2, it is expected that the thickness changes (%) recorded during a single charge/discharge cycle will be far smaller than those recorded for the graphite electrode (max. 8% expansion after discharge) [55].

Figure *50* shows the potential profile and simultaneous thickness changes of two NMC811 electrodes during C/20 and C/5 charge/discharge cycling under CC.
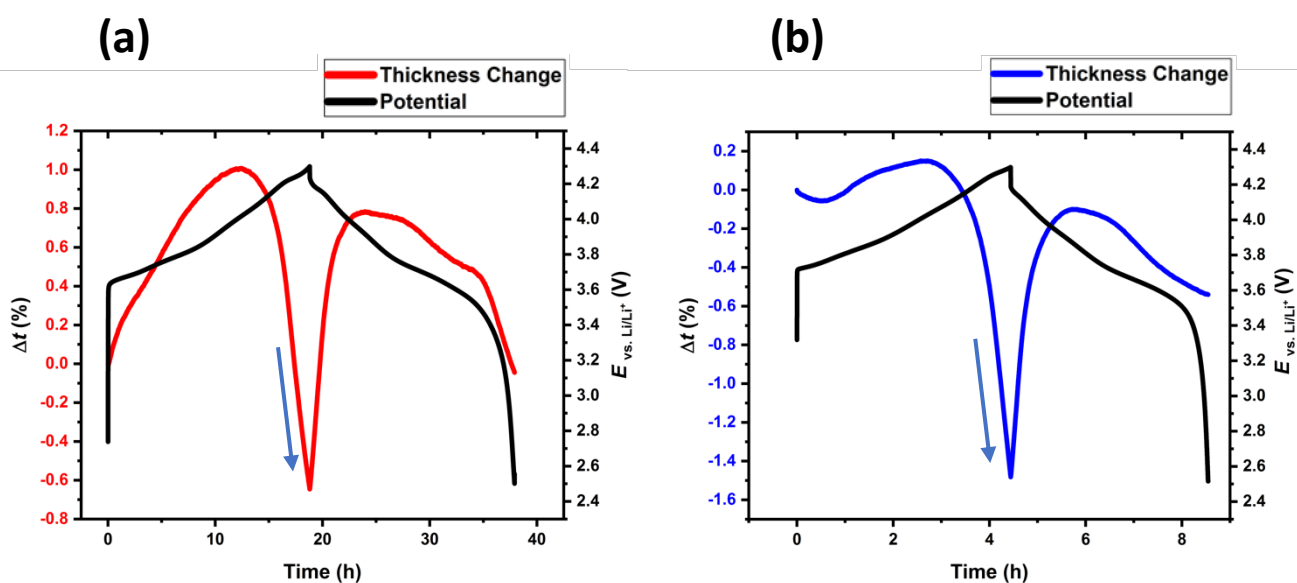
Figure 50: Potential profile and simultaneous thickness changes of an NMC811 electrode during CC cycling at an applied (a) C/20 and (b) C/5 C-rate. The thickness change associated to the c lattice collapse is annotated by a blue arrow in (a) and (b).

According to the detailed view in Figure 50, the thickness of an NMC811 electrode is not highest at the start of charging (2.5 V) when the electrode is fully lithiated. A subtle increase in electrode thickness was reported during the first 2/3 charging at different C-rates. Operando XRD and neutron powder diffraction have been used in research to investigate Li-ion dynamics and structural changes upon electrochemical cycling of NMC811 [273] [276]. According

to neutron diffraction measurements, the NMC811 lattice structure initially contracts because it is dominated by the *a* lattice parameter which gradually decreases until ~4.1 V. Meanwhile, the *c* lattice parameter initially increases until ~4.1 V, which means the interlayer spacing increases. This can be assigned to the brief dilation recorded during the first 2/3 charging shown in Figure 50**Error! Reference source not found.** [277] [278]. Spingler *et al.* [279] also report this subtle increase in thickness during ECD measurements of NMC111 electrodes, indicating that ECD is capable of detecting this bulk microstructural change in different stoichiometries of NMC electrodes. These findings demonstrate that the thickness changes recorded in Spinger et al. study, caused by changes in the *a* lattice and *c* lattice parameter also apply to high-nickel NMC compositions. Additionally, the magnitude of the thickness changes in NMC structures differ with respect to their stoichiometric composition of Ni, Mn and Co.

Above approximately 4.1 V, the *c* lattice parameter rapidly collapses to values smaller than those during full lithiation, hence the rapid contraction of the electrode [81] [273] [276] [280]. This feature also corresponds to the maximum change in electrode thickness (1.7%) during cycling. The transition metal layer spacing decreases owing to the removal of a lithium layer and the overall electrode contracts [81]. Findings from *ex-situ* ^{7}Li solid-state MAS NMR suggest lithium mobility increases as the voltage increases during charging, stimulated by the significant increase in Li-layer spacing and the creation of lithium (di) vacancies, which can also contribute to the electrode rapidly contracting at higher voltages [281].

NMC811 electrodes are known to undergo rapid contraction during the collapse of the *c* lattice parameter at higher states of charge from XRD measurements [273] [278]. Therefore, the rapid decrease in electrode thickness reported during ECD measurements, at the later stages of charge, is ascribed to

the collapse of the *c* lattice parameter. Changes in the *c* lattice parameter are attributed to changes in the interlayer spacing in NMC811's α-NaFeO$_2$ layered oxide structure. This structure is characterized by a close-packed oxygen lattice and alternating layers of Li$^+$ ions and transition metal ions in an octahedral coordination environment (see Figure 4) [273] [282].

It is understandable that the largest thickness changes of the electrode would be associated with changes in the interlayer spacing, as Li$^+$ ions are being inserted and removed during cycling and have direct repercussions on the distance between transition metal layers. Although the porosity/heterogeneity of the electrode morphology will mask these changes to some extent. Other ECD studies have also reported this finding, successfully showing that ECD has a displacement resolution capable of detecting the collapse of the *c* lattice parameter, and that this structural transformation has direct consequences on the bulk dimensional changes of NMC811 electrodes [55]. Jung *et al.* [81] suggest that the collapse of the *c* lattice parameter of NMC811 electrodes at the H2 → H3 phase transition is exacerbated by a decreasing repulsion between the oxygen layers in the NMC811 electrode, caused by oxidation of the oxygen anions (O^{2-} → O$_2$), which ultimately leads to O$_2$ release.
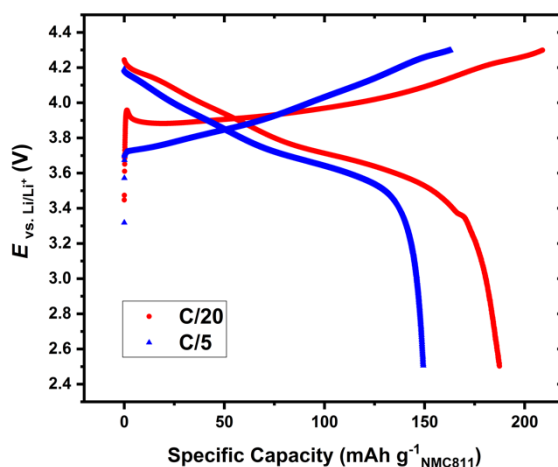
Figure 51: Potential profile and specific capacity record of NMC811/lithium dilatometer cells when cycled at an applied C-rate of C/20 and C/5.

A similar initial charge capacity was recorded for an NMC811/lithium dilatometer cell as an NMC811/lithium CR2032 coin cell at an applied C-rate of C/20 (Figure 49b). The practical discharge capacity was approximately 180 mAh g^{-1} NMC811 and the full-charge capacity was 190 mAh g^{-1} NMC811 during cycling, which correspond to the values of reversible specific capacity in the potential range of 2.5 V- 4.3 V [283] [284]. However, the specific discharge capacity recorded at C/5 was approximately 150 mAh g^{-1} NMC811 (

Figure 51). This decrease in capacity as the C-rate increases further suggests that mass transfer limitations are caused by the large separator in the dilatometer instrument, and that this hinders cycling performance at faster C-rates as this was the case for graphite and NMC811 cell configurations.

The thickness changes undergone by the NMC811 electrode are far less than those recorded for graphite with a maximum of 1% dilation recorded during charging. The dilation profile of an NMC811 electrode displays fewer features in comparison to a graphite electrode that has details in its dilation profile corresponding to phase transitions in its lattice structure. The main feature of the NMC811 electrode's dilation profile is the rapid reduction in electrode thickness that occurs at ~4.1 V. No change in the initial thickness of the

electrode was recorded after the after C/20 charge/discharge cycling which markedly differs from the thickness change recorded after C/5 cycling (~-0.4% contraction). In contrast, irreversible dilation was recorded for graphite after its first cycle (see Figure 34).

Electrode thickness changes appear to be sensitive to the rate of charging in NMC811 electrodes as an overall contraction was recorded after cycling. These findings are consistent with general consensus that NMC811 dilates to a far lesser degree than graphite and thus one can infer that the majority of dilation associated within full cells occurs at the anode, when not accounting for gas evolution [281]. In addition, graphite electrodes underwent an overall increase in electrode thickness after initial cycling due to SEI formation. The fact that NMC811 has no net increase in thickness after initial cycling suggests that the thickness of the cathode SEI layer that is known to form on the surface of NMC811 electrodes is orders of magnitude thinner than the SEI layer formed on graphite, as observed in other studies [285] [286] [287].

5.4.2.2. Applying a constant voltage step

A CV step was applied between charge/discharge to record any further contraction occurring after the cell was charged i.e., cathode delithiations (Figure 52). The current was allowed to decay to 0.01 mA and held at 4.3 V. A voltage region of 3.0-4.3 V was used for these tests.
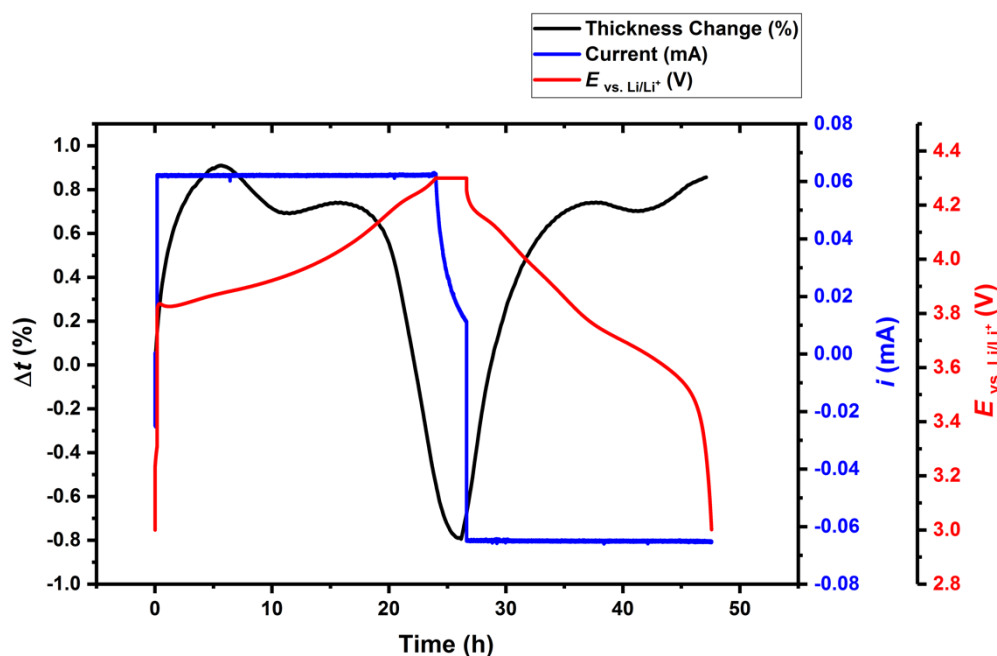
Figure 52: *Potential profile and dilation record of NMC811 (NEI) during charge/discharge at an applied C/20 cycle rate and held at CV between each charging step.*

A slight contraction (<0.2%) of the NMC electrode's thickness was recorded during CV. This follows rapid contraction of the electrode during charging. This slight contraction suggests any Li$^+$ ions that did not deintercalate during charging did so during this step. This is contrary to the slight dilation that was recorded in a graphite electrode during CV cycling that followed discharging. This slight dilation was ascribed to Li$^+$ ions intercalating into the graphite electrode. The findings in Section 4.4.2.2. and this section create a complete perspective of the Li$^+$ ion charge/transfer mechanism expected to occur during CV cycling in a NMC811/graphite cell.

5.4.2.3. Multiple cycle characterisation of an NMC811 electrode

In-situ ECD was applied to an NMC811/lithium dilatometer cell to characterise the thickness changes of an NMC811 electrode across numerous charge/discharge cycles at different cell temperatures as is shown in

Figure 53. A high temperature study was carried out to test whether this could reduce the capacity fading that was reported in Chapter 4 at elevated C-rates by reducing mass transfer limitations. Tests were carried out at 60 °C as most Li-ion manufacturers specify that 50-60 °C is the upper operational temperature range of their batteries [288].

(a)

(b)
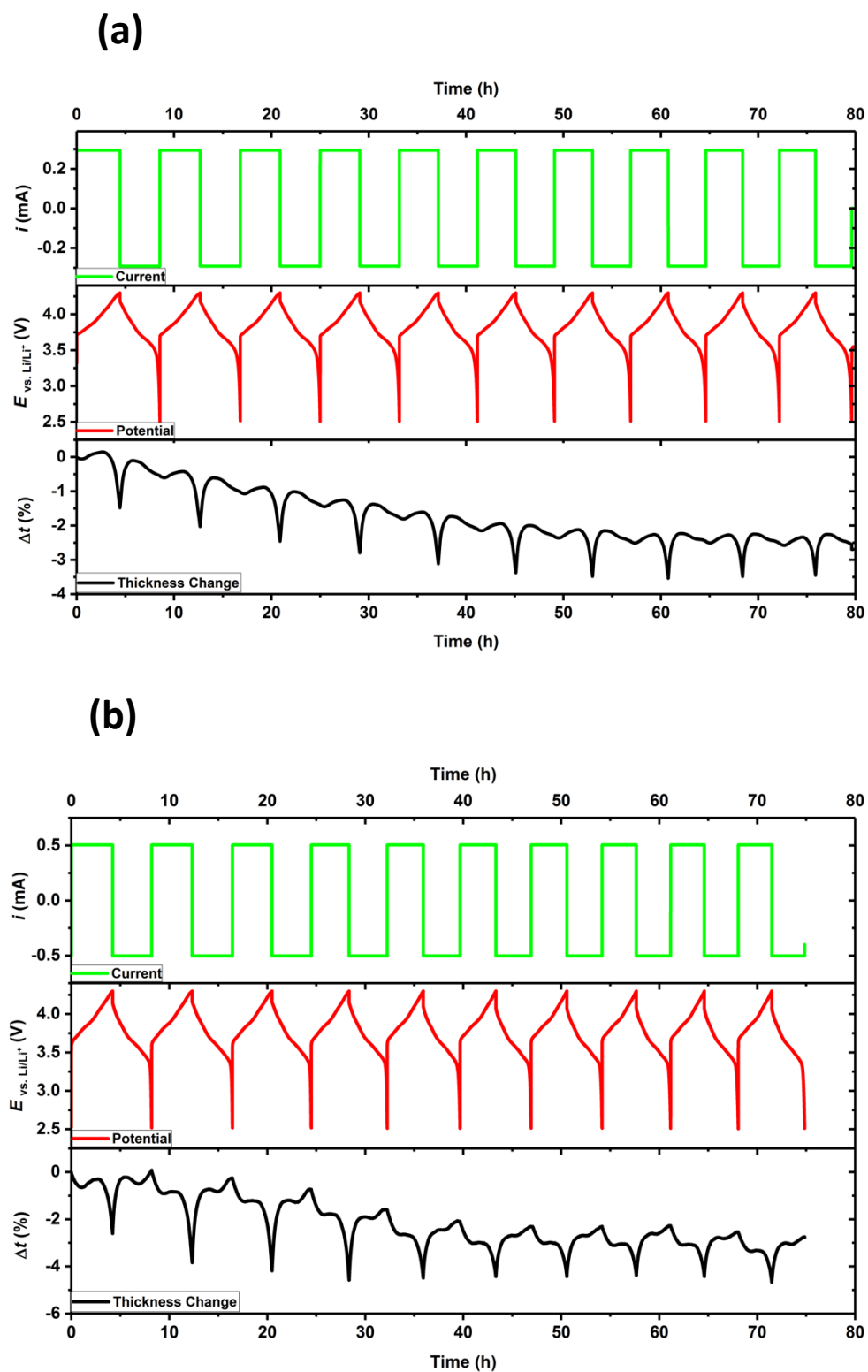
Figure 53: Potential profile and simultaneous dilation record of NMC811 during 10 cycles at C/4 at (a) 25 °C and (b) 60 °C.

At 25 °C, irreversible electrode contraction occurred between cycles 1-5 as the electrode reduced in thickness by 2.0%. After the fifth charge/discharge cycle the NMC811 electrode reversibly expanded and contracted as there did not appear to be a significant net increase/decrease in electrode thickness between these cycles suggesting that a stable NMC811 structure was formed at around ~-2.0% thickness change (electrode contraction). This contraction is in contrast to the widely reported ~2.0% expansion of NMC811 electrodes [289]. However, the dilatometer instrument avoids pressure build-up via gas evolution, which may give rise to differences compared with sealed cells. Furthermore, electrode thickness changes fell as low as -3.5% at the top of charging (4.3 V) during later cycles. The electrode underwent a general contraction throughout cycling and did not return to its initial thickness after 10 cycles; this suggests that NMC811 electrodes undergo irreversible contraction during prolonged charge/discharge cycling. However, the intra-cycle dilation/contraction was consistent during repeated cycling, and thus a reversible and symmetrical 'breathing' behaviour was exhibited as Li$^+$ ions deintercalate/intercalate into the bulk NMC811 electrode.

A similar dilation/contraction profile was observed at 60 °C which suggests the same deintercalation/intercalation mechanism occurs at elevated temperatures. However, the intracycle thickness changes were consistently of a larger magnitude in the cell cycled at 60 °C. Elevated temperature could exacerbate crystal lattice dimensional changes that translate into bulk volume changes of the ensemble electrode [79] [290]. Alternatively, larger intracycle volume changes of the bulk electrode could be due to larger rearrangements of the particle-binder matrix [63]. Nonetheless, the overall thickness change of the NMC811 electrodes after cycling at 25 and 60 °C are similar, indicating that although intracycle thickness changes are slightly higher at a higher temperature, these intracycle volume changes are mostly reversible. An overall contraction of ~2.5% is reported after 10 cycles in both NMC811/lithium dilatometer cells cycled at different temperatures.

It is unclear as to why the electrode thickness decreases most during early cycles. A cathode SEI (cSEI) layer forms during early cycles, but this layer is not expected to cause dramatic changes in electrode thickness, as it is usually less than 50 Å in thickness [291]. Large bulk thickness changes in early cycles are more likely attributed to irreversible rearrangement of active particles in the particle-binder matrix [118]. Electrode degradation during early cycles may cause Li^+ ions to not intercalate/deintercalate to the same extent during later cycles, resulting in smaller electrode thickness changes. In Chapter 4, an irreversible thickness change was also found for graphite electrodes during initial cycling before a reversible thickness change was recorded during later cycles. Irreversible thickness changes in the graphite electrode during early cycling were attributed to SEI formation and rearrangement of graphite particles in the binder-particle matrix. To further quantify the degree of bulk thickness changes in the NMC811 electrode, $\Delta \mu$ and $\Delta \iota$ were calculated for each cycle. In this chapter, ι_1 refers to the thickness change of the electrode at each delithiated state and ι_2 refers to the thickness change of the electrode between each lithiated state.
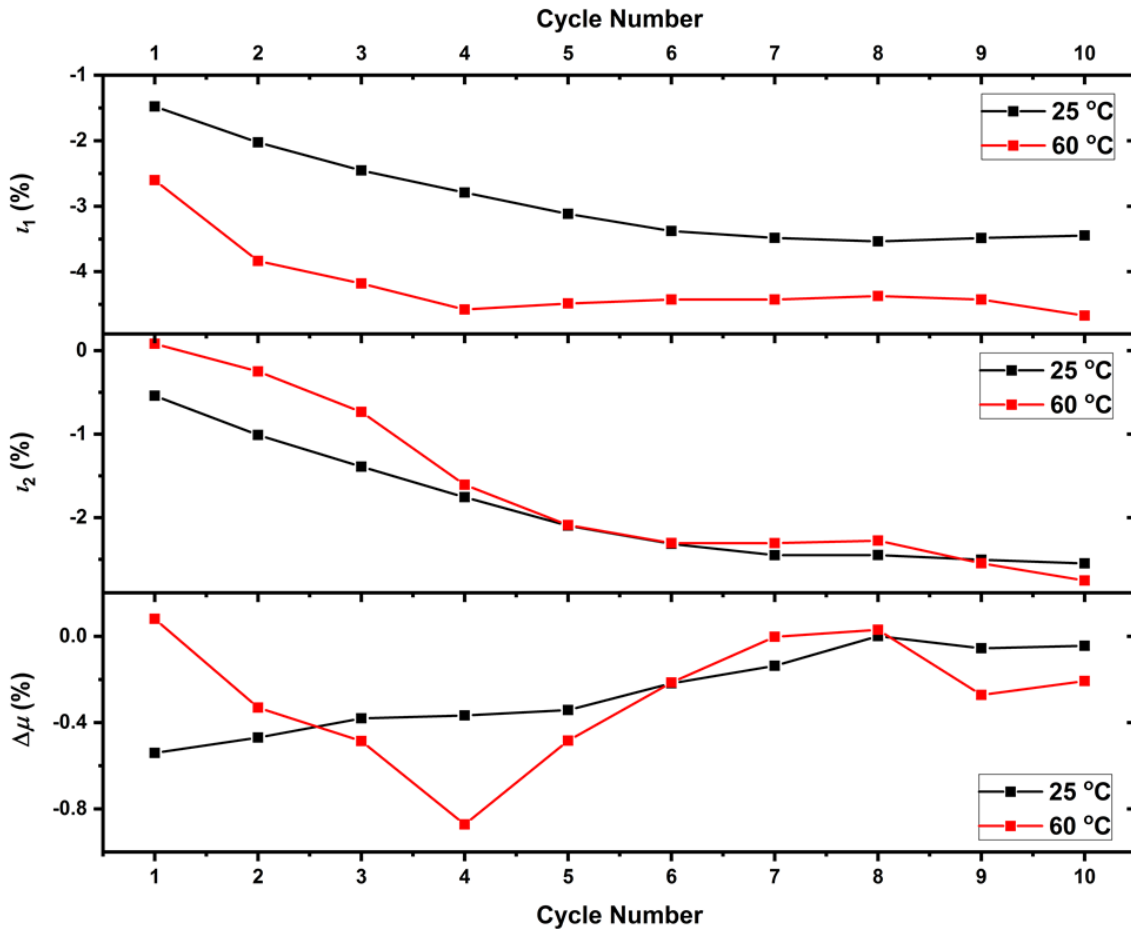
Figure 54: *Calculated values of ι_1 and ι_2 for each cycle during 10 cycles at C/5 for the NMC811 electrode and the change in $\Delta\mu$ during 10 cycles at C/5 for the NMC811 electrode.*

A similar trend in ι_1 and ι_2 was recorded for both electrodes (Figure 54). As cycle number increased, the difference in thickness of the NMC811 electrode between cycles got progressively smaller. Figure 54b shows that once the electrode 'stabilised' during later cycles, close to 0% electrode thickness change was recorded during the final cycles. A negligible electrode thickness change was recorded after the eighth cycle. Nayak *et al.* [118] also report significant relative decreases in electrode thickness during the first few cycles before minimal thickness changes in later cycles and found that the electrode reached a 'more stabilised state' after three cycles. A similar trend can be seen in Figure 54 which shows the difference in thickness between each delithiated state (ι_1)

and lithiated state (ι_2). The difference between ι_1 and ι_2 decreased during the ninth and tenth cycle, which also means that the difference in intracycle electrode thickness between the delithiated and lithiated state was smaller than in previous cycles.

Spingler *et al.*[55] found that numerous electrode materials underwent irreversible thickness changes during early cycles before establishing a 'steady-state' during which minimal inter-cycle thickness changes occur. It is possible that during early cycles, the electrode reverses some of the compaction created by the calendering process. During early electrode dilation and contraction, particle morphology may irreversibly alter in a way that allows particle expansion to be accommodated, leading to an overall thicker electrode. This may be due to the electrode's preference of reducing elastic stress energy [55]. In the literature, the number of cycles it took to reach this state varied depending on the electrode material. For instance, Nickel Cobalt Aluminium (NCA) electrodes were found to require more cycles before undergoing reversible thickness changes between cycles, compared to NMC811. In Chapter 4, a calendered graphite electrode was found to undergo irreversible thickness changes before reversibly 'breathing' during later cycles (from ~7 cycles).

Despite having similar contraction/dilation profiles, lower ι_1 values were recorded when the cell was cycled at 60 °C, meaning larger contractions of the *c* lattice parameter were recorded at 60 °C than at 25 °C. The largest contraction of the NMC811 electrode was recorded during the 4th and final cycle at 60 °C (~-4.6 %). Furthermore, Figure 54 shows that the largest inter-cycle change in thickness ($\Delta\mu$) occurred after the first cycle at 60 °C (-0.5% thickness change), attributed to particle-binder rearrangements. The largest fall in charge capacity also occurred after cycle 1 (

Figure *55*). Larger inter-cycle changes in electrode thickness were recorded between cycles at 60 °C compared to 25 °C and this is exacerbated between

cycles 1-5. The change in electrode thickness reduced after the fourth cycle and reached no change between cycles 7 and 8 indicating the electrode reached a stable state. The larger contractions in the cell cycled at 60 °C could be due to higher levels of oxygen release from the NMC electrode caused by the elevated temperature. Xiong *et al.* [292] found that significant weight loss occurs for NMC electrodes when cycled at higher temperatures due to higher levels of oxygen release. In addition, more oxygen is released with increasing cell voltage, and in this study the largest contractions were recorded at the maximum charge (4.2 V). The onset temperature for oxygen release is around 40 °C [292]. This process, coupled with *c* lattice contraction could exacerbate contraction of NMC electrodes at 60 °C.
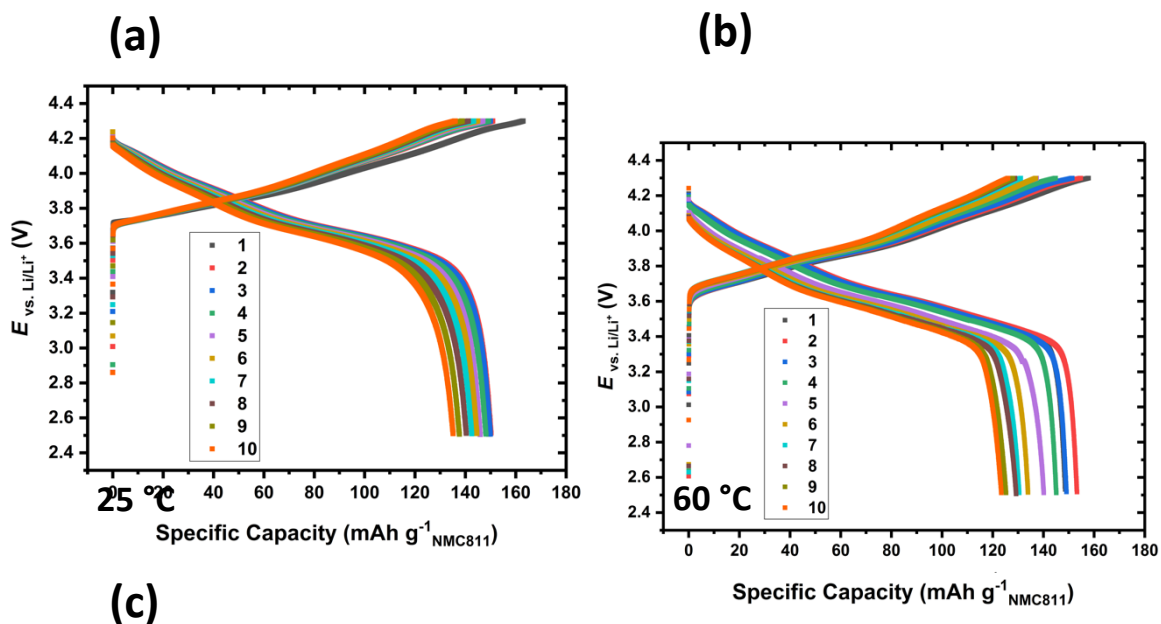
Figure 55: *Potential profile and specific capacity record of NMC811 (NEI) during*

10 cycles at C/4 at (a) 25 °C and (b) 60 °C. (c) Charge and discharge capacity recorded for each cycle during CC cycling.

The specific charge capacity recorded for the first cycle was approximately 163 mAh g^{-1} $_{NMC811}$, and approximately 135 mAh g^{-1} $_{NMC811}$ for the final cycle (~18% capacity loss) (

Figure **55**). The specific charge capacity recorded for the first cycle at 60 °C was approximately 158 mAh g^{-1}$_{NMC811}$ and approximately 123 mAh g^{-1}$_{NMC811}$ during the final cycle (~22% capacity loss). A higher capacity loss was recorded when the cell was cycled at 60 °C (

Figure **55**). Typically, higher capacity fading is reported in higher temperature cells containing NMC (≥ 60 °C) [288]. At elevated temperatures, the kinetics of unwanted side reactions are increased, such as electrolyte decomposition. Deposition of electrolyte reduction products on the electrode can alter its porosity, increase cell impedance and cause capacity fading [293]. However, capacity fading is usually reported over much higher cycle numbers (around 1000-2500 cycles) and for pouch cell and coin cell configurations [294]. Capacity fading is probably exacerbated (particularly at higher temperatures) in the dilatometer set-up due to its design. Studies that use this dilatometer instrument typically cycle less than 100 cycles. Findings suggest that increasing temperature does not improve cell performance by reducing mass transfer limitations across the large separator. The next strategy would be to use a dilatometer instrument that has a smaller separator.

The specific capacity of the NMC811 electrode gradually decreased as cycle number increased. This is expected to occur when a cell is cycled numerous times, however owing to the limitations in this particular dilatometer cell configuration, capacity loss was exacerbated. In fact, specific capacity did not fall to this extent during benchmark voltage profiling of NMC811/lithium CR2032 coin cells. This suggests that the longevity of capacity retention in this particular dilatometer cell is not as effective as in CR2032 coin cell configuration, which may be expected due to the ECD cell complexity. The specific capacity recorded for the first cycle was lower than that recorded

during CR2032 coin cell cycling and lower than the theoretical specific capacity (190 mAh g^{-1}$_{NMC811}$). Consequences of mass transfer limitations are expected to be present in the first cycle and continue throughout cycling and was the case in this study when cycling the cell at an applied C-rate of C/5. Nayak *et al.*[118] also found that capacity values measured using this particular dilatometer apparatus differed from those measured using coin cell arrangements. Nonetheless, cycling can still be reliably carried out using this dilatometer instrument as is demonstrated by the thickness change profile of the electrode.

The potential profile and thickness change profile for each charge/discharge is shown in

Figure 56. This allows examination of the intra-cycle dilation/contraction of the NMC811 electrode during each cycle and the consistency in dimensional changes during each charge/discharge. Marker *et al.* [295] examined the changes in x in Li$_{1-x}$Ni$_{0.8}$Mn$_{0.1}$Co$_{0.1}$O$_2$ during charging using neutron diffraction studies. The stoichiometric changes identified by Marker *et al.* [295] occur at certain voltages and thus the value of x in Li$_{1-x}$Ni$_x$Mn$_y$Co$_z$O$_2$ can be indexed to specific voltages. It can be seen in

Figure 56 that there is no evidence that *in-situ* ECD can detect thickness changes associated to specific "phase transitions" that occur in an NMC811 electrode during charge/discharge cycling. Stoichiometric characterisation of the NMC811 electrode was not possible using this dilatometer apparatus owing to limitations in spatial resolution. This also suggests that specific "phase transitions" that occur at specific voltages do not directly result in measurable bulk dimensional changes of the NMC811 electrode (using this apparatus). This

is in stark contrast to the thickness changes that are reported for graphite electrodes during particular "phase transitions" at specific voltages using ECD [63] [100]. Therefore, "phase transitions" in graphite electrodes have a direct consequence on the bulk structure of the anode, which cannot be said for its often-paired cathode counterpart.

(a)

(b)

(c)

(d)
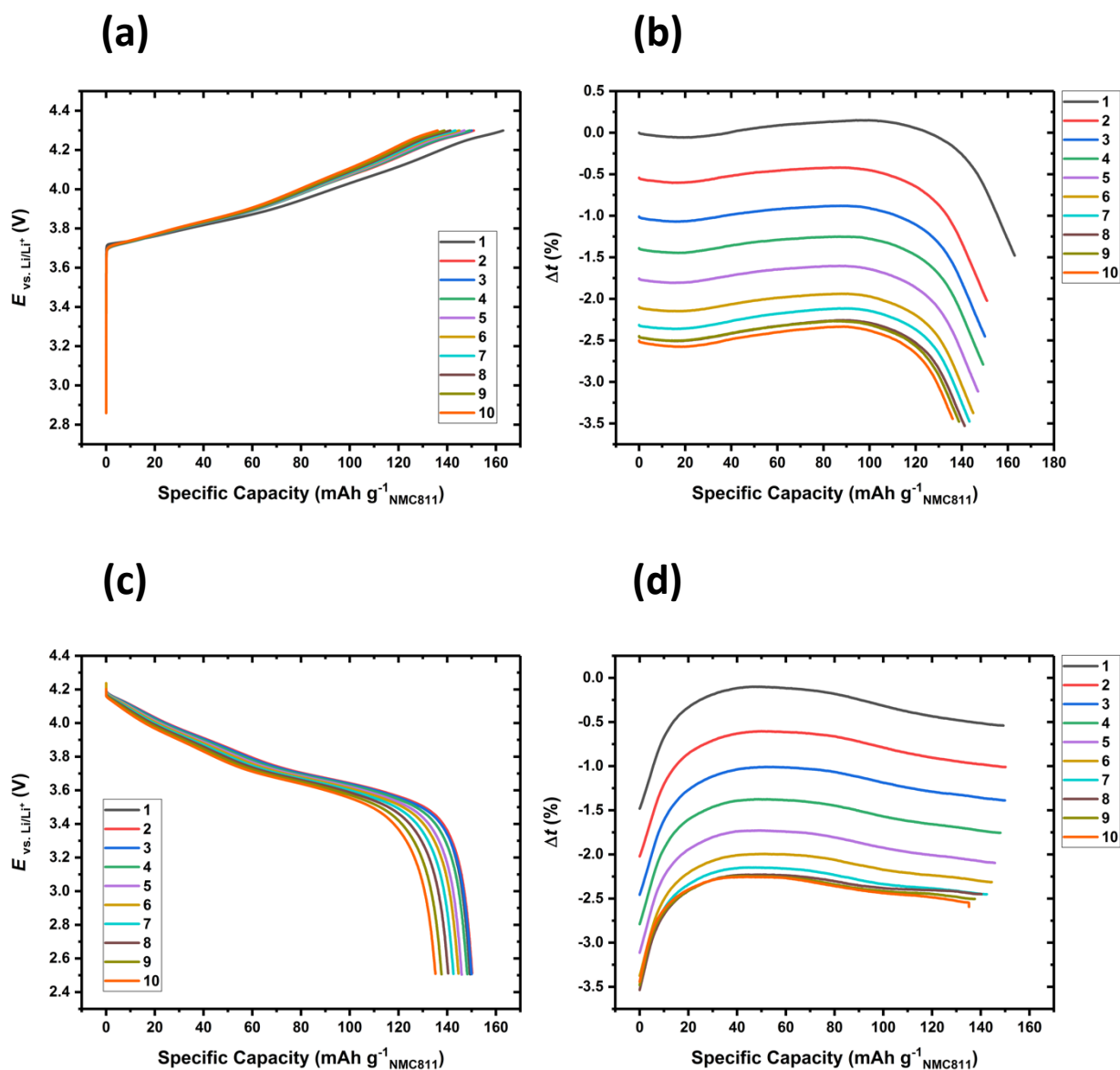
Figure 56: *(a) Potential curve corresponding to each charging stage and (c) discharging state for cycles 1-10 at 25 °C. (b) The associated thickness changes to each charging stage and (d) discharging stage at 25 °C.*

Similar thickness change profiles were recorded for each charge and discharge cycle reflecting the consistency in dilation/contraction behaviour over the course of cycling. However, the intra-cycle thickness changes decreased as cycling progressed owing to the gradual reduction in capacity as less active material was utilised. For instance, thickness change decreased from ~1.5 % during the first cycle to ~1.0% during later cycles. As this contraction at higher capacities is associated to the interlayer spacing of Li$^+$ ions and transition metal ions, this suggests that fewer Li$^+$ ions deintercalated/intercalated into the NMC electrode during later cycles.

5.2.3.4. Differential Capacity Analysis

Differential capacity analysis was carried out to identify capacity changes associated with phases transitions of NMC811. This was carried out to ensure proper intercalation of Li$^+$ ions during charging to inform whether mass transfer limitations impact these transitions and whether these phase transitions cease as cycling increases and capacity fades. It was important to ensure full lithium intercalation as notable capacity issues arise when cycling at elevated C-rates.

Figure *57* shows the resulting dQ/dV plots for the NMC811/lithium dilatometer cell during the first cycle (a) and all cycles (b) at 25 °C, respectively. The formula to calculate dQ/dV is the following:

$$\frac{dQ}{dV} = \frac{Q_n - Q_{n-1}}{V_n - V_{n-1}}$$

(5.1)

Where *Q* refers to capacity and *V* refers to cell voltage for the nth cycle and *n-1* cycle. Most capacity occurred in three regions that are highlighted in

Figure *57*a as regions I, II and III. The maxima of the three peaks were at 3.80, 4.06 and 4.23 V vs. Li^+/Li, respectively (the exception being the first cycle which had a maximum at 3.70 V as opposed to 3.80 V vs. Li^+/Li). Previous reports also suggest that the majority of capacity occurs in these three regions [296] [297].
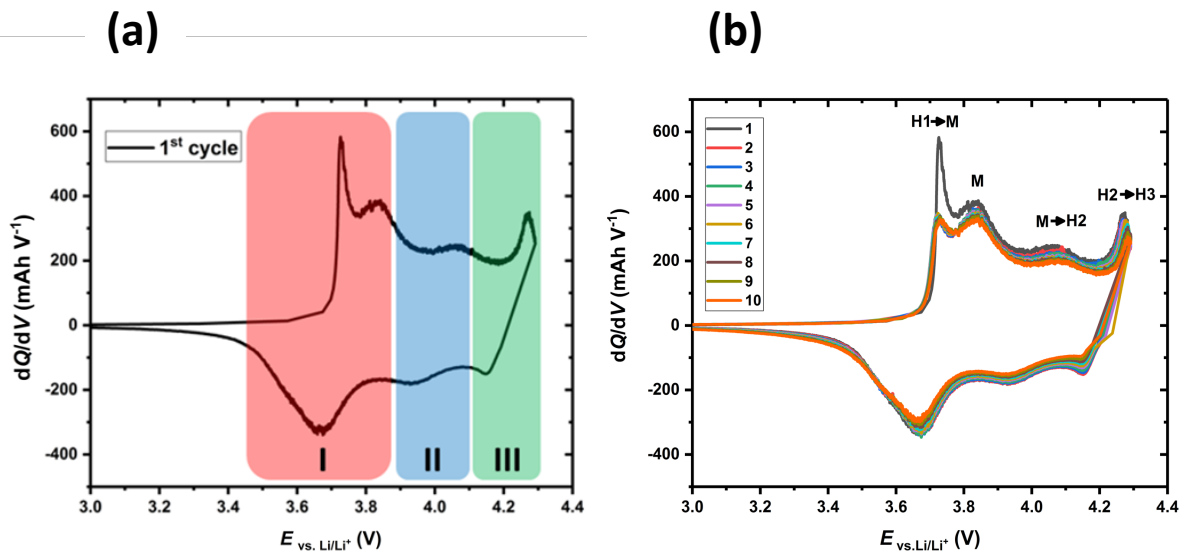
Figure 57: *The differential capacity (dQ/dV) plot for the first charge/discharge cycle at 25 °C (a) and 60 °C (b). The differential capacity (dQ/dV) plots for all 10 charge/discharge cycles at 25 °C (c) and 60 °C (d). Phase transitions of the NMC lattice are annotated in (b) and (d).*

Although the sequence of phases H1 → M → H2 → H3 are presented, it is important

(c)

(d)
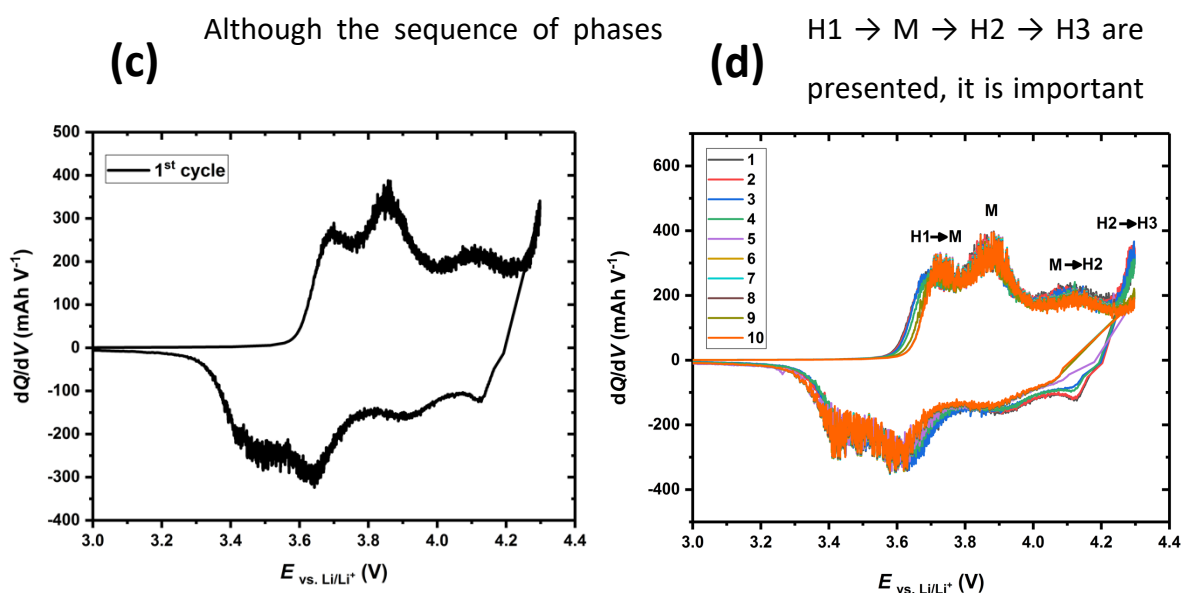
to note that these are qualitative notations and are yet to be fully characterised for NMC811 electrodes. However, the dQ/dV plots for NMC materials have similarities to their parent material LiNiO$_2$, and therefore the peaks in the voltage profile of LiNiO$_2$ are often used to describe features in the dQ/dV plot of Ni-rich materials as well such as NMC and NCA. In the case of LiNiO$_2$, these peaks are coupled with first order phase transitions [273] [298]. The collapse of the *c* lattice parameter, which has been found to have severe consequences on the bulk electrode thickness, is associated with high voltage peaks in the dQ/dV plots, which authors have designated to the H2 → H3 phase transition in the third region in

Figure *57*a [81] [299].

The differential capacity plots for charge/discharge cycling at 60 °C are missing some features that are present at 25 °C. Significant capacity fading was also reported for this experiment, suggesting that capacity fell due to incomplete lithium intercalation into the NMC electrode. Although intra-cycle volume changes were larger at 60 °C (Figure 53b) it may be that Li$^+$ ions that do intercalate have a larger impact on transition metal interlayer spacing and more detrimental particle-binder rearrangements.

5.2.3.5. Differential electrochemical dilatometry analysis

Differential electrochemical dilatometry (D-ECD) was carried out for each charging cycle to examine the rate of thickness changes in the NMC811 electrode during Li$^+$ deintercalation and to determine whether fast/slow electrode thickness changes occurred at specific voltages. As intracycle thickness changes are almost symmetrical, only the charging state was examined. The rate of thickness changes was calculated using the following equation:

$$\frac{d(\Delta t)}{dV} = \frac{(\Delta t)_n - (\Delta t)_{n-1}}{(V)_n - (V)_{n-1}} \tag{5.2}$$

Where Δt refers to thickness change and V refers to voltage at every n^{th} cycle and *n-1* cycle.

(a)

(b)

(c)

(d)
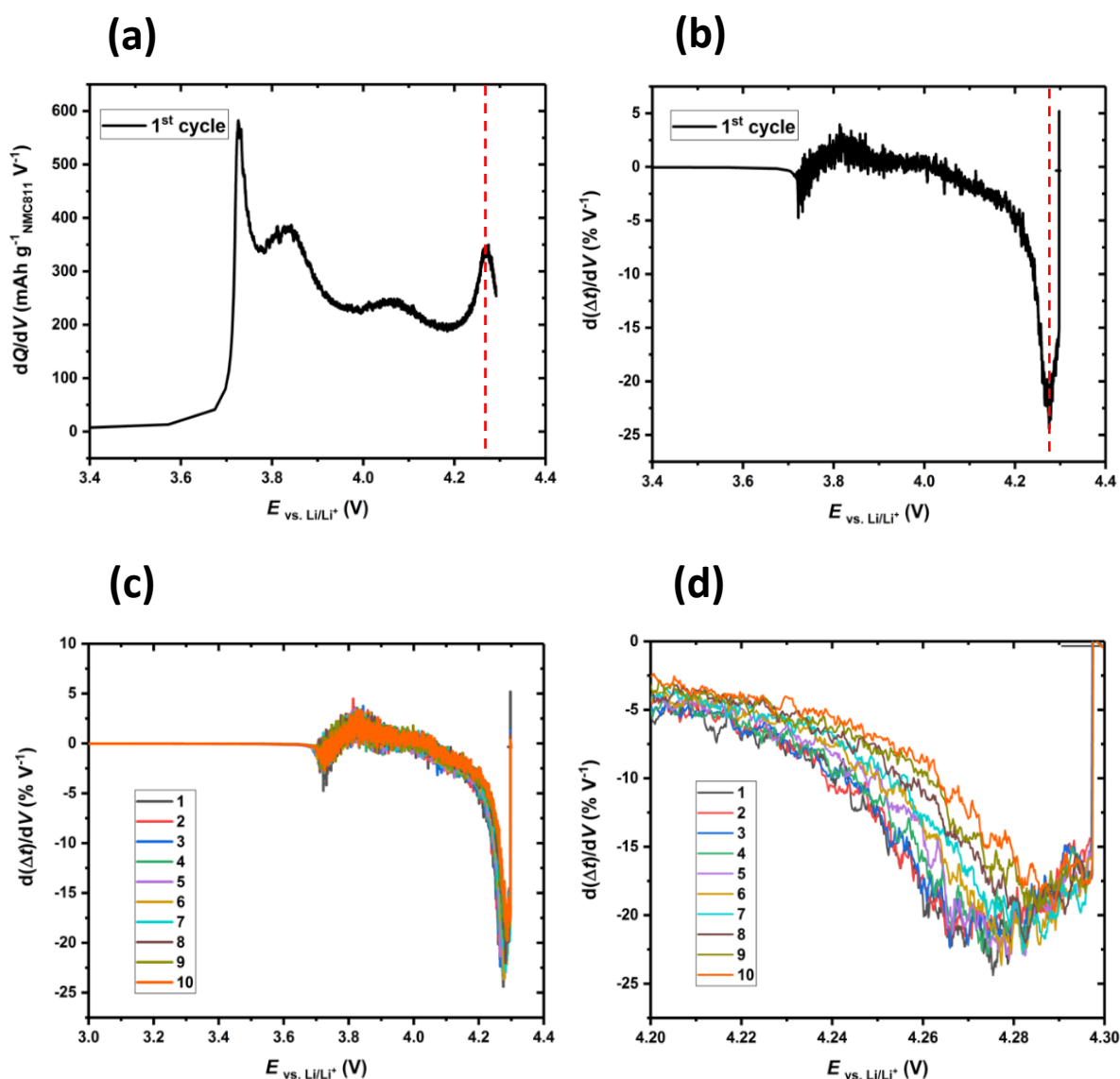
Figure 58 a-d: *dQ/dV charge curve during the first charge cycle at 25 °C with the location of the peak associated to the H2→H3 phase transition annotated (red dashed line) (a) and d(Δt)/dV curve during the first charge cycle at 25 °C with the location of the fastest electrode thickness change annotated (red-dashed line) (b). The differential dilatometry (d(Δt)/dV) plot for cycles 1-10 at 25 °C (c) with magnified scale of the plots between 4.2-4.3 V (d).*

(e)

(f)
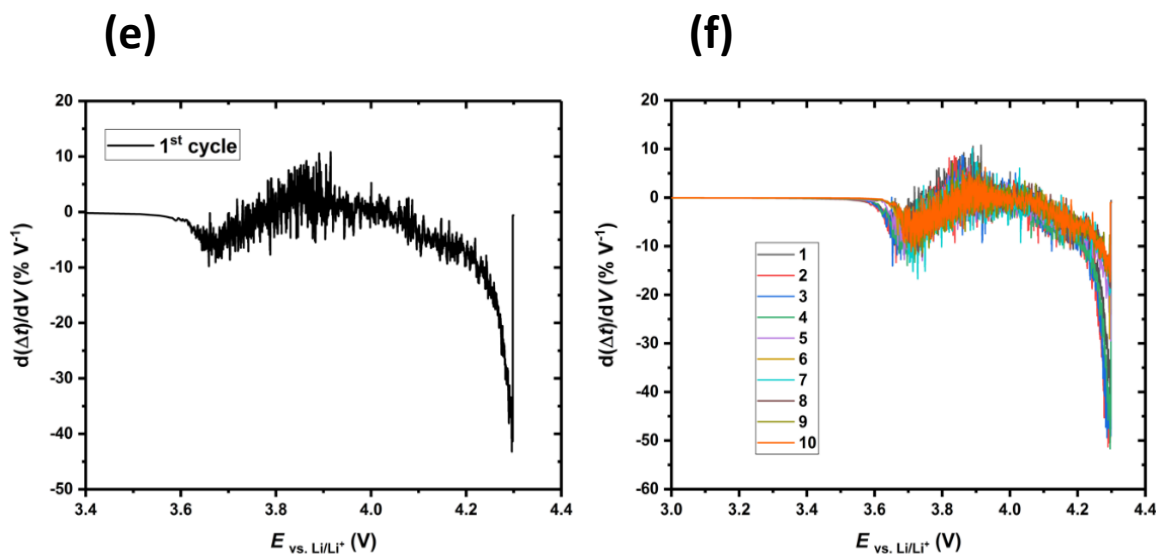
Figure 59 e-f: *(e) The d(Δt)/dV curve during the first charge cycle at 60 °C. (f) The differential dilatometry (d(Δt)/dV) plot for cycles 1-10 at 60 °C.*

An overpotential spike was exhibited in the first cycle by a large H1 → M peak to suggest a surface layer was formed (see

Figure **58**a) [300]. The H1 → M peak corresponds to a phase transition from a hexagonal to a monoclinic lattice of the NMC electrode [81]. The presence of a surface layer composed of electrolytic salts such as Li_2CO_3, $LiHCO_3$ and $NiCO_3$ hinders Li^+ deintercalation and causes a higher open circuit potential and an overpotential spike [300]. One would assume that surface contamination of the NMC811 electrode would cause slower Li^+ deintercalation and thus slow changes in electrode thickness. However, peaks are not present in the d(Δt)/dV plot at voltages at which this H1 → M transition occurs (approximately 3.65 V and 3.8 V vs. Li^+/Li), suggesting negligible thickness change occurred in the bulk NMC811 electrode due to surface contaminants.

A trough (minimum) is present in the d(Δt)/dV plots at approximately the same voltage that the peak associated to H2 → H3 transition is present in the

corresponding dQ/dV plot indicating that the fastest contraction of the NMC811 electrode occurred at the same voltage as the fastest charge transfer. This voltage also aligns with where particular phase transitions are said to occur in LiNO$_2$ materials. The fastest contraction of the NMC811 electrode was present for all cycles in the region of 4.23 V - 4.25 V in accordance with the H2 → H3 phase transition (Figure *58*). Notably, it has also been widely reported in literature that the abruptness of the H2 → H3 phase transition produces a large strain between the two different crystalline domains and consequently leads to significant microcrack generation in NMC811 particles [297] [301]. It is in this particular phase transition that the fastest thickness change occurs, as is shown in Figure *58***Error! Reference source not found.**. The rapid collapse of the c lattice parameter caused a rapid change in the electrode's thickness.

Onset of thickness changes occurred at the same voltage at which charge transfer starts to occur (3.7 V), suggesting that thickness changes are driven by charge transfer reactions. No changes in electrode thickness are therefore expected to occur if the cell is held at open circuit voltage. In addition, no difference in rate of electrode thickness change was found for the first cycle, when compared to the other cycles at 3.7 V, despite cycle 1 having a larger H1 → M peak, which implies that this larger charge transfer exhibited at 3.7 V during the first cycle did not cause any difference in the rate of electrode thickness change.

The voltage at which the H2 → H3 transition peak occurred in the dQ/dV plot and the voltage at which the minimum occurred in the d(Δt)/dV plot were taken for each cycle and plotted in Figure 59. The H2 → H3 peak shifted to higher voltages as cycle number increased which was expected as dQ/dV curves also shifted towards higher voltages with cycling as the electrode degraded. In addition, the minima in the d(Δt)/dV plot shifted towards higher voltages with

each cycle. This may be due to capacity fading, and consequently the NMC811 electrode reaching the same state of charge (SoC) at higher voltages in later cycles. This suggests the collapse of the c lattice parameter still occurred at the same SoC, but at higher voltages. Overpotentials can also be present owing to surface contamination of the NMC811 electrode [299] [82]. One would expect a correlation between the rate of electrode thickness change and Li$^+$ ion mobility, as these charge transfer reactions drive structural changes in LiB electrodes. Marker *et al.* [273] found that the mobility of Li$^+$ ions plateaued when x = 0.6 in Li$_{1-x}$NiMnCoO$_2$ towards 4.0 V. The rate of electrode thickness change plateaued near to 0% V^{-1} between 3.9 V to 4.0 V before the rapid collapse of the c lattice parameter. Li$^+$ ion mobility was found to drop abruptly when x = 0.8 as does the electrode thickness reported in this thesis (

Figure *50*) [273].
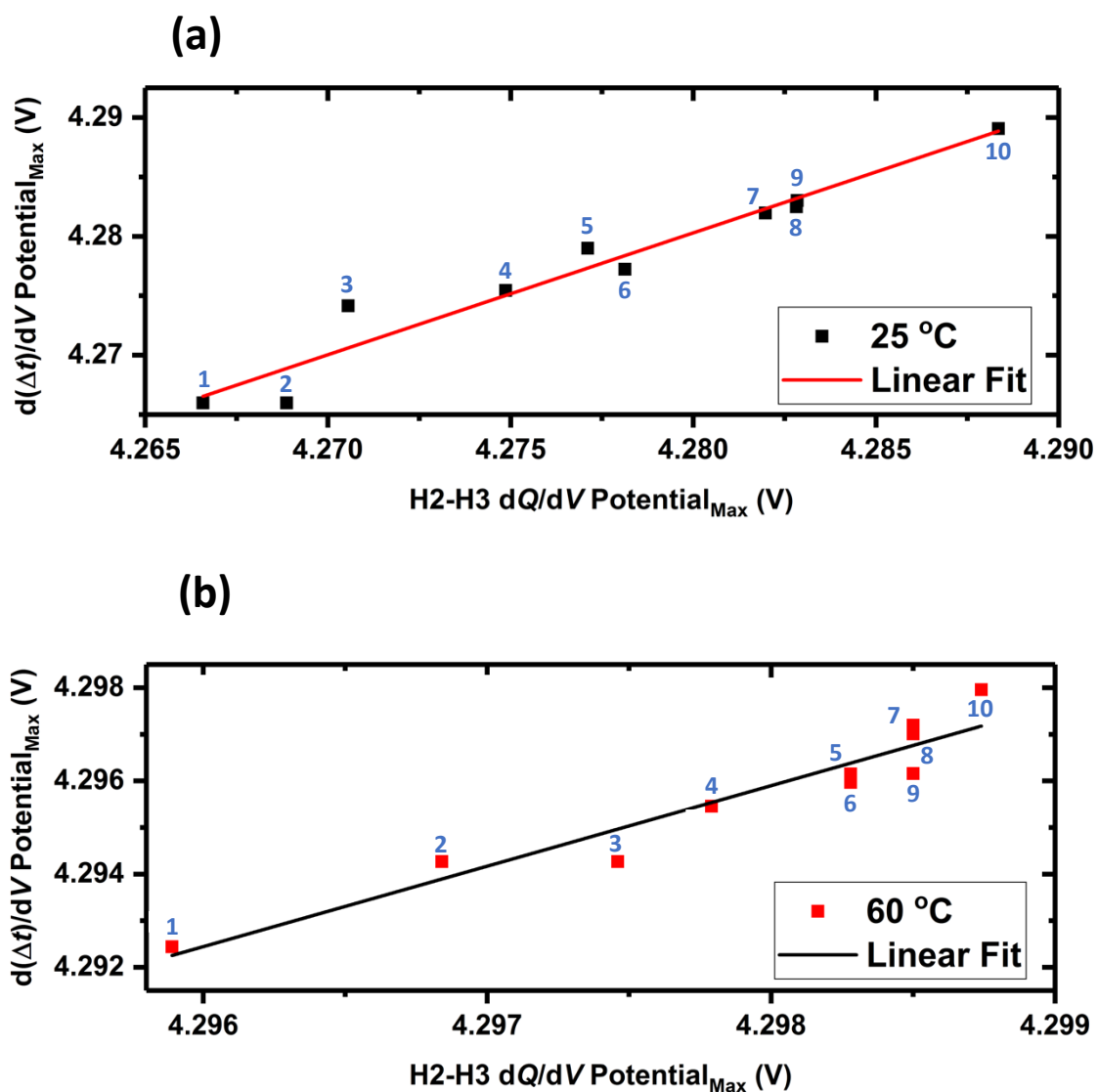
Figure 60: *The maximum potential recorded at the largest trough in d(Δt)/dV plot versus the maximum potential recorded at H2→H3 peak in each dQ/dV plot at 25 °C (a) and 60 °C (b). Each point is annotated with its corresponding cycle number.*

The maximum potential recorded at the H2→H3 peak in each dQ/dV plot for the NMC811 electrode cycled at 60 °C was significantly higher than values recorded at 25 °C which suggests that contraction of the *c* lattice parameter occurred at far higher voltages for the electrode cycled at 60 °C. In addition, the

difference in values between cycles was on a far smaller scale. The largest change in electrode thickness was also recorded at higher potentials in accordance with the rapid collapse of the *c* lattice parameter being the cause of the largest change in thickness of the NMC811 electrode and its effects translating from the crystal structure to the bulk electrode. At 60 °C the maximum potentials recorded were more spread out between cycle 1-4 and then clustered during the final cycles indicating severe capacity fading during later cycles.

5.4.3. Morphological characterisation of an NMC811 electrode

5.4.3.1. Scanning electron microscopy

The tested electrode was compared with an uncycled pristine NMC811 electrode to elucidate whether any changes in surface morphology can occur due to cycling and can contribute to thickness changes measured by *in-situ* ECD (see Figure 61).
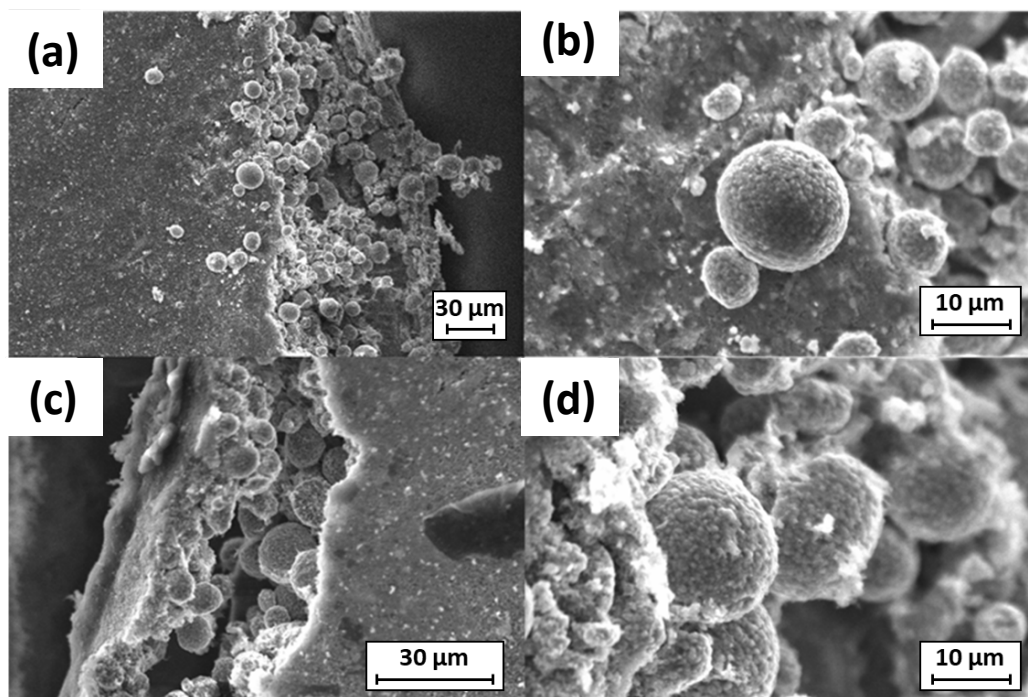
Figure 61: *SEM images of the surface structures of the evaluated pristine (a), (b) and cycled (c), (d) NMC811 electrodes at C/20 rate for ten cycles: (a) magnification - 925X, (b) magnification - 4,440X, (c) magnification - 2,350X and (d) magnification - 5,880X.*

A highly unexpected finding was made using SEM. At lower magnifications, the surface of the NMC811 electrodes was shown to be covered in a carbon black layer (Figure 61a and Figure 61c). This layer was continuous across the entire surface of both the pristine and cycled NMC811 electrodes. However, it did not impact the electrochemical performance of the NMC811 electrodes given the high charge/discharge capacities recorded for these electrodes during benchmark voltage profiling (see Section 5.4.1). It is also likely that this carbon layer did not affect the *in-situ* ECD measurements of thickness changes as particles in the carbon layer should not undergo dilation/contraction with charge/discharge cycling. In addition, the thickness changes measured for the NMC811 electrode were within range of what is expected for this active material [55] [302]. As the carbon layer was present on the surface of the

electrodes prior to cycling, it is highly likely that this carbon layer was deposited on the surface of the electrodes during manufacturing of the electrode sheets.

Regions along the outer edges of the electrodes revealed the NMC811 particles packed underneath the surface layer of carbon. At higher magnifications, the NMC811 secondary particles were seen to be highly spherical and composed of smaller crystal particles (Figure 61b and Figure 61d). These spherical NMC811 particles, are therefore referred to as polycrystalline particles, as they are composed of smaller single crystal particles [303]. Differences in polycrystal and single crystal NMC811 particles, as well as their contribution to thickness changes of LiBs will be explored further in Chapter 6. Finally, the SEM images showed no noticeable differences in particle volume for the pristine and cycled electrodes.

5.4.3.2. X-ray-µCT image analysis

The internal morphology of the cycled NMC811 electrode was compared to a pristine NMC811 electrode to elucidate changes that occur due to cycling. A higher accelerating voltage is needed to scan NMC811 electrodes, compared to graphite electrodes, because the active layer of the NMC811 electrode is more attenuating to the X-ray beam. The X-ray µCT cross-sectional orthoslices shown in Figure 62a and Figure 62b were considered reasonably representative of all orthoslices obtained for each electrode. In addition, these corresponded to approximately middle slice numbers for each electrode.
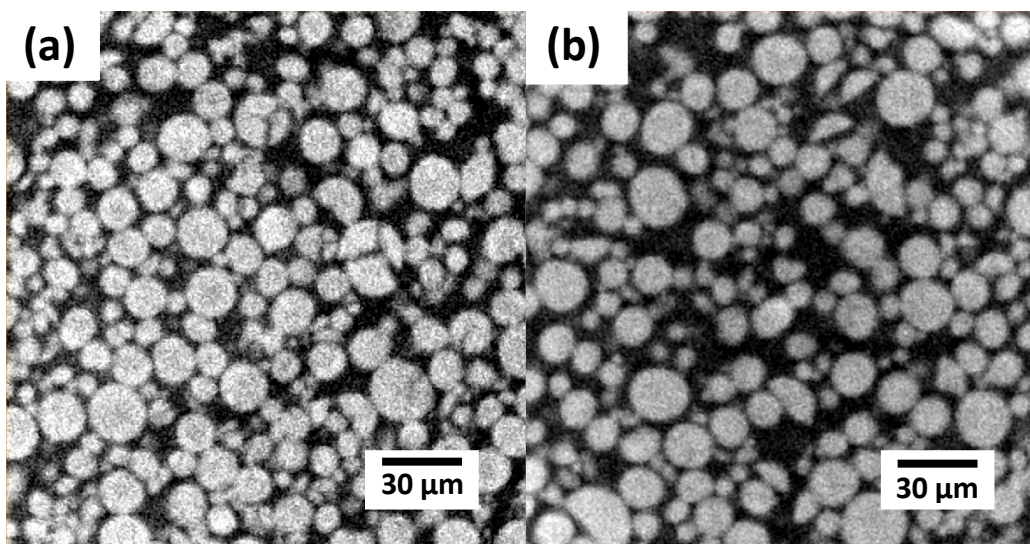
Figure 62: *(a) X-ray µCT image of the pristine NMC811 electrode and (b) cycled electrode showing a cross-sectional orthoslice through the thickness of the sample in the xy phase.*

As was the case for graphite electrodes, the non-uniform shape and size distribution of NMC811 particles is evident from Figure 63. Although, NMC811 particles are more spherical than graphite particles. Numerous particles in the cycled electrode are shown to not be spherical, with "semi-circle" shaped particles present. Semi-circled particles may arise due to two-way particle cracking during the calendering stage of electrode fabrication, and are therefore not necessarily a reflection of cycling [40]. Nonetheless, these non-spherical particles were more abundant in the cycled electrode and spherical particles with three-way and two-way particle cracking were more abundant in the pristine electrode. The intra-particle cracks visualised in the pristine electrode could be a precursor to semi-circle shaped particles accumulating in the electrode after cycling. Cycling could exacerbate the separation of these cracked spherical particles into individual deformed non-spherical particles.
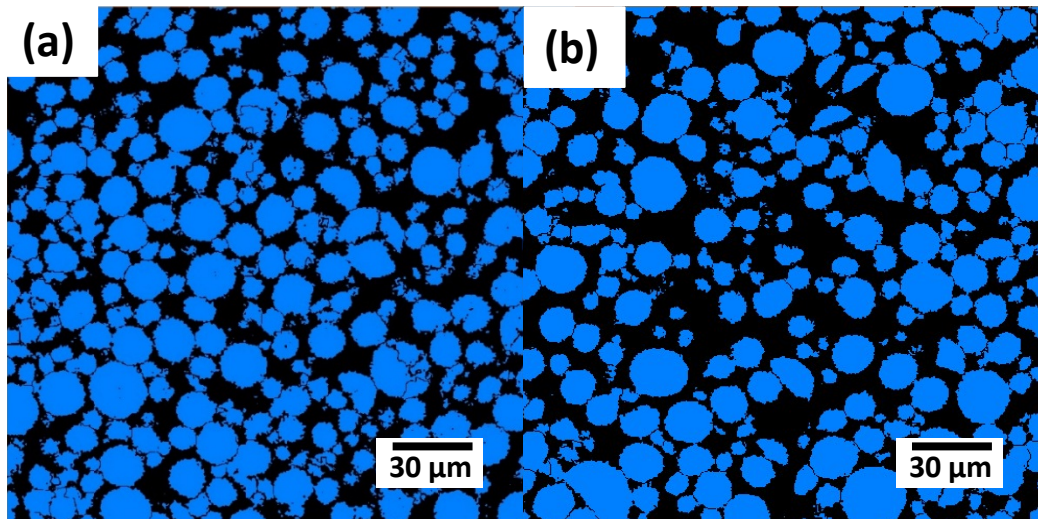
Figure 63: *The particle (blue)-pore (black) distribution of the (a) pristine and (b) cycled electrode after segmentation correspond to the data shown in Figure 62.*

The diverse array of particle shapes and sizes is clearer after particle-pore segmentation. As expected, the more spherical particles are larger than the abnormally shaped particles, as these non-spherical particles are thought to originate from larger spherical particles before particle cracking and fracturing. Particle cracking could occur during cycling and would result in a higher number of smaller particles. This would explain why the cycled electrode had a higher frequency of particles with smaller volumes than the pristine electrode, which had less evidence of non-spherical particles.

(a)

(b)

50 μm

50 μm
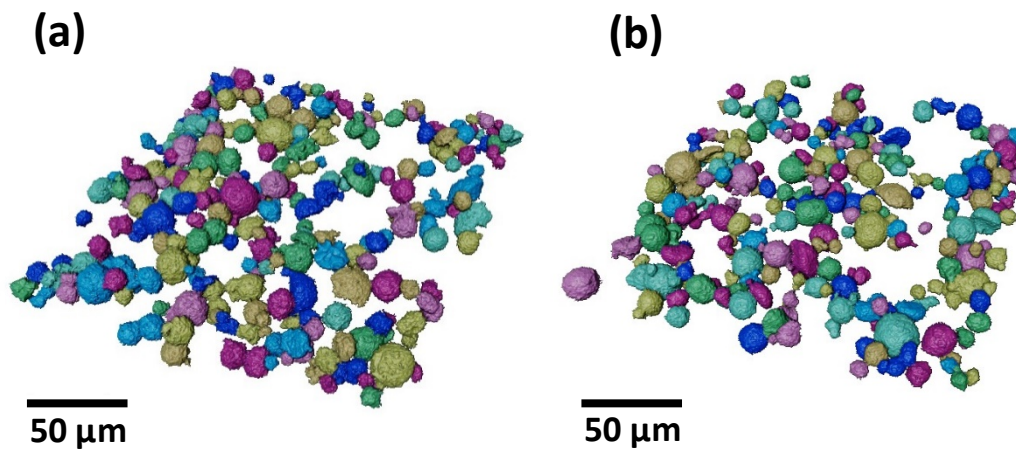
Figure 64: 3D volume rendering of the solid phase (blue) of the (a) pristine NMC811 electrode after reconstruction and segmentation. (b) Cycled electrode particles after algorithmic particle separation and identification.

The Label Analysis tool was used in the Avizo software to label each particle as its own entity. A 3D volume rendering of these particles is shown in

Figure **64**. Random colouring of segmented particles demonstrates the size and shape variation of NMC811 particles. Once the particles had been separated, the PSD was computed for each electrode.

(a)

(b)
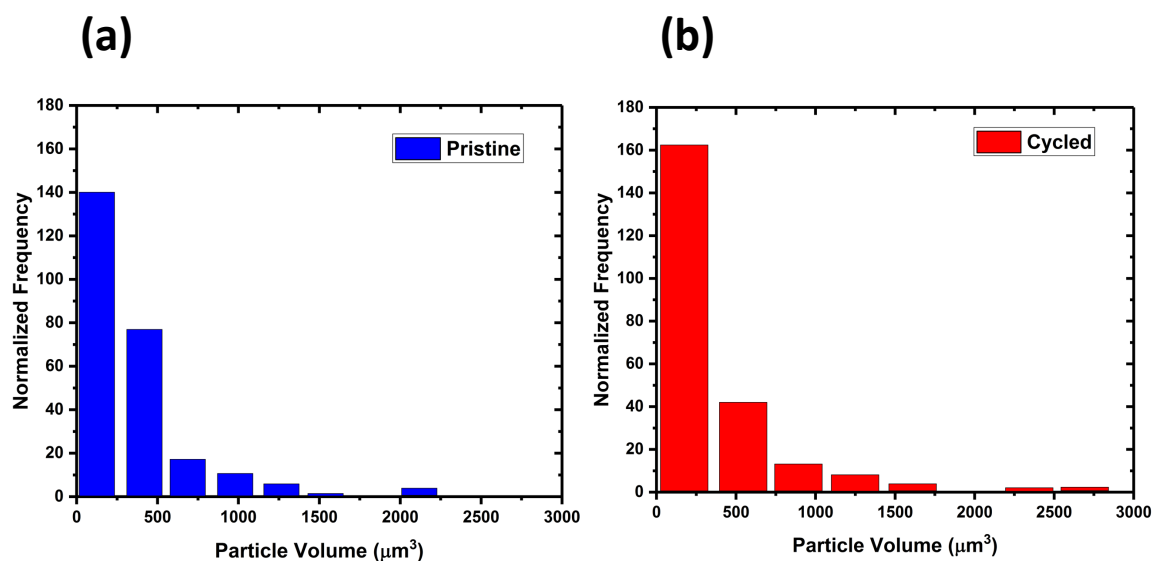
Figure 65: Volumetric PSD of electrode particles in the (a) pristine electrode and (b) cycled electrode.

Similar PSDs were found in both the pristine and cycled electrode, respectively.

Figure **65** shows that particle volumes below 500 μm^3 are most prevalent in both electrodes with a decrease in frequency as the particle volume increases. A similar trend was found for both graphite electrodes suggesting a higher frequency of smaller particles in both electrode materials. More particles that are larger than 2000 μm^3 were found in the pristine electrode compared to the cycled electrode suggesting less "complete" particle fracturing in the pristine electrode. As expected, the cycled electrode had a higher frequency of particles below 500 μm^3 in particle volume, suggesting that larger spherical particles had fractured to form numerous smaller non-spherical particles.

Unlike the graphite electrode that underwent detrimental electrode delamination after cycling, the NMC811 electrode did not necessarily undergo

213

significant degradation after 10 cycles at an applied C/20 C-rate. No distorted signal recordings during ECD measurements indicate no electrode delamination occurred. This is consistent with findings that cathodes are better adhered to the current collector than anodes because anodes generally undergo more drastic volume changes and stress during cycling, which leads to exfoliation of the active material from the current collector [304] [305] [306] [307]. In fact, it appears that more significant, electrode damage can arise during the calendering process of electrode fabrication before the electrode has been cycled. Electrochemical cycling could then aggravate the pre-formed cracks by splitting the damaged spherical particles along the cracked regions to form their own distinct non-spherical particles, and ultimately increasing the surface area of the ensemble electrode. The impact of NMC active particle morphology (such as size and shape) on cell performance will be explored in Chapters 6 and 7.

5.4.3.3. Image-based modelling

Results in Table 4 show that the cycled electrode is more porous than the pristine electrode. TauFactor recorded a pore phase volume fraction of 42.4% in the pristine electrode and a pore phase volume fraction of 45.5% in the cycled electrode. Similarly, to graphite, the cycled NMC811 electrode had a lower tortuosity factor in both the x-, y- directions of the analysed volume and a higher tortuosity factor in the z-direction.

Table 4: Results of tortuosity factor simulation on the pristine and cycled NMC811 electrodes. The voxel size (µm) was kept the same for both electrodes (0.187 × 0.187 × 0.187). All simulations were conducted with respect to the pore phase.

NMC811 electrode	Solid phase volume fraction (%)	Pore phase volume fraction (%)	Directional Percolation (%)	Tortuosity factor (τ), in direction		
				X	Y	Z
Pristine (uncycled)	57.6	42.4	99.6	1.92	1.82	1.79
Tested (cycled)	54.5	45.5	99.9	1.8	1.77	1.83

In general, the pore phase of the cycled electrode was less tortuous than the pristine electrode. A higher evidence of non-spherical particles and thus cracking was present in the cycled electrode, and as such could allow for Li^+ ions to diffuse through the NMC811 electrode more readily with less tortuous pathways as fewer large particles would be obstructing Li^+ ions in the cycled electrode. Similarly to the graphite electrode in Chapter 4, directional percolation was slightly higher for the cycled electrode than the pristine electrode. Once again, this suggests that pores in the cycled electrode were more connected than in the pristine electrode.

5.5. Conclusions

ECD was used to record the bulk volume changes of NMC811 during numerous cycling protocols. The material's dilation/contraction was on a comparably small scale with maximum thickness changes of ~1.7% during charge/discharge at room temperature and different moderate C-rates of C/20 and C/5. The scale of electrode height change appeared to be less influenced by varying the C-rate than in the case of graphite. In addition, a similar intracycle trend in dilation/contraction was exhibited at all tested C-rates. However, the scale of this thickness change reduced during later cycles as the cell capacity also fell which suggested that fewer Li^+ ions were inserted/removed from the electrode during later cycles. Thickness changes of the NMC811 electrode occurred between the range of 3.6 V - 4.3 V. A significant reduction in electrode thickness occurred during the rapid collapse of the *c* lattice parameter at approximately 4.0 V. Irreversible intercycle thickness change during early cycles was recorded during ECD measurements followed by reversible intercycle thickness changes during later cycles once an electrochemical steady-state had been achieved.

For the time known to the author, D-ECD was used to examine the rate of thickness changes of the NMC811 electrode during CC cycling. The fastest change in electrode thickness occurred at voltages circa. 4.2 V vs. Li^+/Li, and shifted to higher voltages as cycling progresses, in accordance with the H2 → H3 phase transition peak also shifting to higher voltages with cycling. X-ray CT showed more cracked particles in a cycled NMC811 electrode compared to a pristine electrode. Furthermore, cycled electrodes were found to have lower porosity and higher directional percolation than a pristine electrode, which was also found for the cycled graphite electrode in Chapter 4.

D-ECD could be used to record the rate of electrode thickness changes when the cell is subjected to harsh cycling conditions. For example. the rate of thickness change could be measured when the cell is cycled beyond a stable voltage range or used to measure the rate of thickness change with respect to

varying interior cell temperature. Findings could unveil the structural changes occurring in cells prior to battery failure and be used to improve battery safety.

Future studies should use dilatometric apparatus capable of measuring bulk thickness changes at high C-rates (e.g., 1C and faster) to assess NMC811 electrodes durability to fast charging. NMC electrodes in electric vehicles need to be durable to fast charging and retain high capacities for long range operation. This study suggests that more severe bulk thickness changes would be recorded when the LiB is cycled at higher C-rates. Lithium plating may also contribute to thickness changes of the electrode at these higher C-rates.

Chapter 6

Three-Dimensional Characterisation of Lithium-ion Batteries

6.1. Overview

Herein, degradation mechanisms of LiBs composed of the same electrode chemistries reported in earlier chapters are explored using correlative X-ray CT and acoustic techniques. X-ray µCT was used at the cell length-scale to ascertain the cell assembly parameters and arrangement, to inform the acoustic interpretation. In addition, X-ray nCT was used to examine differences in morphology between electrodes that can cause differing acoustic signal interactions and thus influence the acoustic signature of Li-ion cells. The results in this chapter form part of a paper under review by the author in Journal of Power Sources.

6.2. Introduction

Most $LiNi_xMn_yCo_zO_2$ (NMC) electrodes consist of anisotropic single crystal primary particles aggregated to form polycrystalline secondary particles [308] [309]. Electrodes composed of polycrystalline NMC particles have large gravimetric capacity and good rate capabilities but do not perform as well as single crystal equivalents in terms of volumetric energy density and cycling stability [40]. This has prompted research into well-dispersed single-crystalline NMC products as an alternative solution for high-energy-density batteries [310] [311].

The NMC particles' crystallinity and morphology has a large influence on the energy density, cycling stability, and rate capability of the electrode in practical applications. For instance, the evolution of micro-cracks in NMC811 (where x ≈ 0.8) is far more prevalent in polycrystalline NMC811 (PC-NMC811) particles compared to single crystal NMC811 (SC-NMC811) particles, due to an isotropic lattice volume dilation/contraction in SC-NMC811 particles which lowers the risk of intergranular microcrack formation [40] [312]. Though both materials are composed of crystallites of the same material (NMC811 with R3m symmetry), the morphology of these crystallites, and the particles they form, are significantly different. The PC-NMC811 electrode is made up of large (~10 μm), spherical agglomerates of multiple small crystallites of around ~300-500 nm, each of which tends to have an anisotropic morphology. In contrast, the SC-NMC811 electrode is made up of individual particles of ostensibly single crystallites that are larger than the primary particles, but smaller than their agglomerates in the PC-NMC811 electrode. These particles are of the order of

1-5 μm in size, less oblong in shape and are composed of one, or only a few, crystal grains [309].

The Li-ion cells studied in this chapter will contain electrodes composed of either SC-NMC811 particles, or PC-NMC811 particles. The commercial NMC811 sheets evaluated in chapter 5 had a polycrystalline particle structure. Before evaluating the degradation of LiBs during cycling, it is imperative to characterise their entire morphology using X-ray CT to identify intrinsic physical and chemical properties that may impact acoustic measurements (Chapter 7). Intrinsic physical properties such as particle size, electrode density, local electrode composition and tortuosity, provide significant challenges to directly measure thicknesses in LiBs as these factors can vary considerably between different whole-cells and influence their acoustic behaviour. In this chapter, various X-ray CT instruments are used to facilitate multi-length-scale X-ray CT experiments in order to reveal information on the entire commercial LiBs.

6.3. Experimental Methodology

6.3.1. Sample preparation

LiBs comprising NMC811 and graphite electrodes (NMC/Gr) were supplied by LiFUN Technology Ltd (Zhuzhou City, China) in a 5-layer wounded pouch cell configuration with dimensions of 25 mm × 18 mm. The NMC811 and graphite electrodes were fabricated at LiFUN Technology Ltd, and the cells were obtained dry. The cells were transferred to a vacuum oven and dried under vacuum at 100 °C overnight (approx. 12 hours) to remove any air and moisture from the cell before transferring to an argon-filled glovebox. Pouch cells were filled with 0.8 mL of 1.0 M $LiPF_6$ dissolved in a mixture of ethylene carbonate: ethyl methyl carbonate in the ratio 3:7 by volume with 2% (by weight) vinylene

carbonate additive (Soulbrain MI) and then sealed at -70 kPa gauge pressure using a vacuum chamber (Audionvac VMS 53, Audion Elektro). A small vacuum is needed to account for vapour pressure of the EMC electrolyte additive. Within 30 mins of sealing, cells were held at 1.5 V overnight using a multi-channel battery cycler (BCS-805, Biologic). This avoids dissolution of the copper current collector and gives sufficient time for wetting of the electrodes and separator.

Table 5: Properties of the single-crystalline NMC811/graphite pouch cell provided by LiFUN Technology Ltd.

	Item	Single-Crystal
Cathode	Material	NMC811
	Tap density (g cm^{-3})	3.3
	Active mass loading	95.5%
	Coating weight (mg cm^{-2})	16.7
Anode	Material	Graphite
	Tap density (g cm^{-3})	1.5
	Active mass loading	94.8%
	Coating weight (mg cm^{-2})	11.3

Table 6: Properties of the polycrystalline NMC811/graphite pouch cell provided by LiFUN Technology Ltd.

	Item	Polycrystal
Cathode	Material	NMC811
	Tap density (g cm^{-3})	3.3
	Active mass loading	96.4%
	Coating weight (mg cm^{-2})	18
Anode	Material	Graphite

Tap density (g cm^{-3})	1.5
Active mass loading	94.8%
Coating weight (mg cm^{-2})	13

6.3.2. Entire cell characterisation using X-ray µCT

A Nikon XTH 225 ST laboratory X-ray microscope was used to probe the internal cell structure of each SC-NMC811/Gr and PC-NMC811/Gr pouch cell before electrochemical cycling. These scans were obtained at an accelerating voltage of 180 kV and an incident beam power of 18.5 W, using a W target and a 0.5 mm Cu filter. 3176 projections were obtained for each scan with the geometric magnification of the system resulting in a pixel size of approximately 24.5 µm. "Nikon CT Agent" software was used to reconstruct all radiographic images using a cone beam filtered back projection algorithm. Visualisation of all reconstructed X-ray imaging scans was performed using Avizo software (FEI, France). The software allows for visualisation of all the electrode layers and current collection tabs inside the cell.

6.3.3. Cell disassembly and preparation for X-ray CT

Once discharged, cycled pouch cells were transferred to a controlled environment so that they could be opened safely, because some chemicals inside the battery can react with water and with oxygen. Due to the hazardous nature of the battery components this process was done in an argon-filled glove box (LABStar, MBraun). Ceramic scissors were used to remove the tabs and then to make incisions along the top and sides of the cell. The wound cell was then removed from the aluminium casing and unwound. The electrodes were left to dry for 24 hours inside the glovebox once they had been fully separated. The electrodes were then washed with dimethyl carbonate (Sigma Aldrich). If the electrolyte is not removed from the electrodes, hazardous materials can be

released from them at a later stage in the process. Once the electrodes had dried, they were lasered down and mounted on a steel dowel for X-ray CT using the same method discussed in Section 4. 4. 3. 8. The rest of the pouch cells were discarded, such as the separator and outer casing. X-ray μCT was carried out on the SC-NMC811 and PC-NMC811 electrodes using a Zeiss Versa 620 system with the method discussed in Section 4. 4. 3. 9 resulting in a reconstructed voxel size (μm) of 0.192 × 0.192 × 0.192.

6.3.4. Scanning electron microscopy of NMC811 electrodes

SEM was used to examine differences in morphology between SC-NMC811 and PC-NMC811 electrodes prior to galvanostatic cycling. As discussed in Chapter 4, pristine electrodes were mounted onto conductive stubs without any prior washing as these were harvested from dry cells with no electrolyte. Electrode samples were prepared in a glovebox and transferred to the SEM in a vacuum-sealed transfer vial to avoid any air or moisture contamination.

6.3.5. Identification of internal cell characteristics using X-ray nCT

To provide electrode morphology information, X-ray nCT was performed on pristine (uncycled) samples of SC-NMC811 and PC-NMC811 electrodes. An A Series/Compact Laser Micromachining System (Oxford Lasers, Oxford, UK) with a 532 nm wavelength laser was used to prepare samples for X-ray nCT [313]. Tomographic scans were performed using an Ultra 810 X-ray instrument (Zeiss Xradia 810 Ultra, Carl Zeiss., CA, USA) equipped with a rotating Cr anode source producing a quasi-monochromatic beam with a characteristic emission peak at 5.4 KeV (Cr-Kα). X-ray CT scans were carried out with an X-ray source tube voltage of 30 kV$_p$ with exposure time of 60 seconds per projection image, and a total of 1001 projection images were collected. All radiographic data reported

have isotropic voxel lengths of 126 nm with the detector set to 2 × 2 pixel binning. All reconstructions were achieved using commercial software employing parallel-beam filtered-back-projection algorithms ("Reconstructor Scout-and-Scan", Carl Zeiss., CA, USA). 3D visualizations of reconstructed tomograms were processed using Avizo software (FEI, France) which allows particles to be separated and identified. A thresholding algorithm derived from Otsu's method [314] was adopted for segmentation of the NMC particles using the Auto-Threshold module in Avizo [315]. Neighbouring particles that were in contact with one another were separated using the Separate Objects Avizo module which identifies boundaries (lines) between objects and separates them along these boundaries using a 3D watershed algorithm on the segmented binarized image stack [315]. This module also assigns a unique label to each separated object. The Label Analysis Avizo module, was then used to extract volumetric PSD, particle sphericity and surface area. Histograms were plotted for each data range using 24 bins and fitted with Gaussian curves to determine cumulative frequency. The standard deviation and mean values were tabulated for each plotted histogram and correspond to the peak of the Gaussian curves. Border particles were effectively removed from the 3D volume rendering of electrodes using "border kill" function for volumetric PSD analysis, ensuring any subsequent analysis was conducted only on particles that were wholly within the field of view of the imaging. The Volume Fraction module was used to determine the volume fraction of active material, carbon binder domain (CBD) and pores of each NMC811 electrode.

6.4. Results and discussion

6.4.1. Cell characterisation

X-ray CT was used to provide information pertaining to the layered structure of the pouch cells prior to electrochemical cycling. The internal architecture of

each SC-NMC811/Gr and PC-NMC811/Gr pouch cell was examined before electrochemical cycling to identify whether differences in acoustic response between these cells could be attributed to differences in cell build rather than the microstructure of the NMC811 electrode.
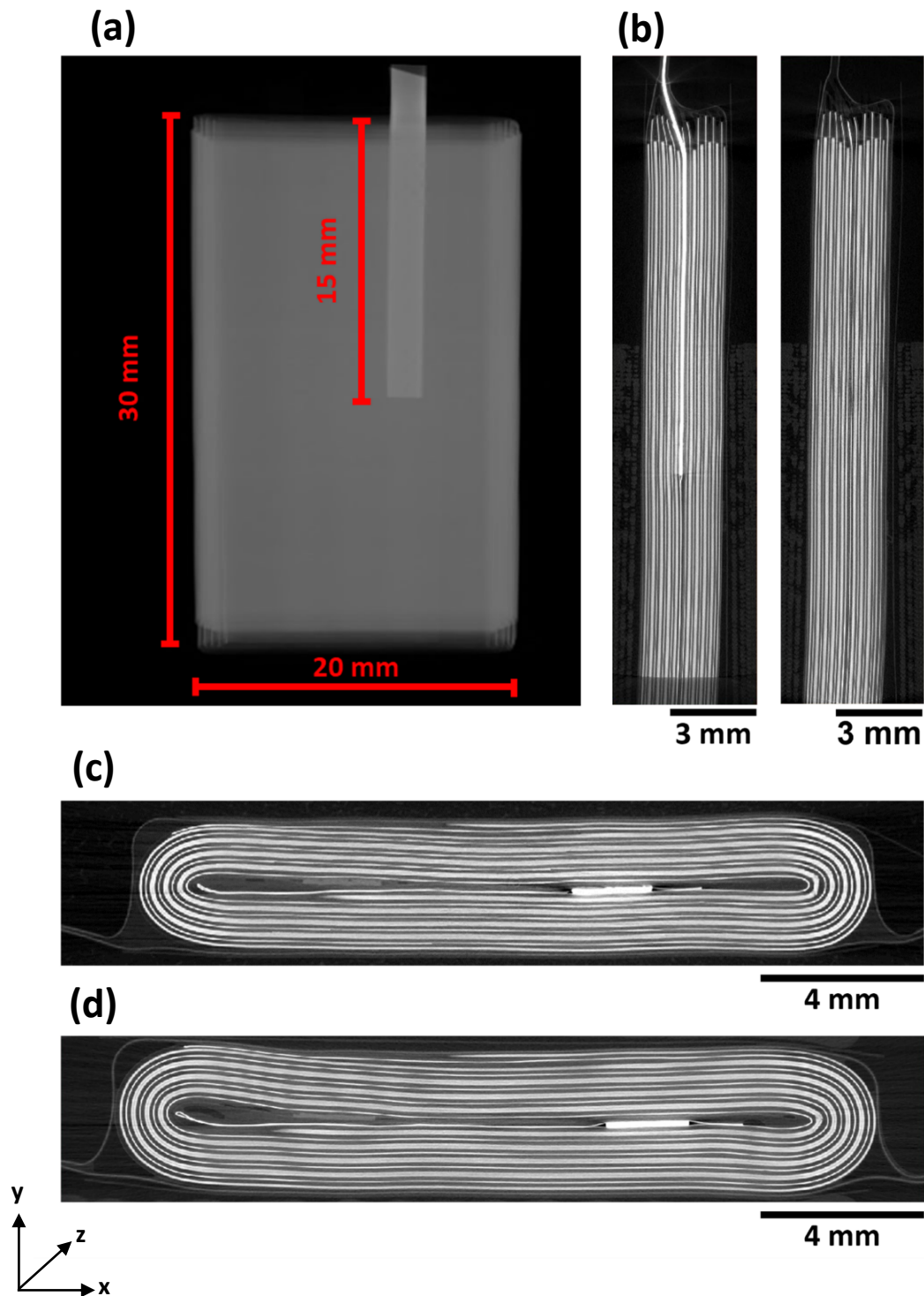
Figure 66: *X-ray CT images of the SC-NMC811/Gr pouch cell showing (a) the volume rendering of the entire cell in the XY plane with the anode current*

collecting tab, (b) X-ray CT orthogonal slices taken in the XZ plane with the anode current collecting tab present and after the anode current collector tab. X-ray CT renderings of a pristine SC-NMC811/Gr cell (c) and a pristine PC-NMC811/Gr cell (d).

The X-ray CT datasets shown in Figure 66 demonstrate the similarity in internal architecture between the SC and PC cells examined in this work. The SC-NMC811/Gr and PC-NMC811/Gr cells each have the same number of wound active layers [cathode-separator-anode-separator] which result in an equal number of internal interfaces at which acoustic reflections can occur in both cell types (Figure 66(c) and Figure 66(d)) [161]. There are also no detectable differences in the internal architecture or defects present in either of the SC-NMC811/Gr cell and PC-NMC811/Gr cells, suggesting that differences in acoustic response between the SC-NMC811/Gr cell and PC-NMC811/Gr cell principally arise as a result of differences in the transmission characteristics of the SC-NMC811 and PC-NMC811 cathodes (as the anodes in both instances are the same), caused by the material properties of the NMC811 electrodes. The graphite anode in the SC-NMC811/Gr and PC-NMC811/Gr cells have the same active mass loading (94.8%) and tap density (1.5 g cm^{-3}). Therefore, acoustic signals are not expected to vary between the cells due to differences in these electrodes.

The nickel current collector tab is clearly visible in Figure 66; possible complications can be caused in the acoustic response of pouch cells by the current collector tabs running through the length of the cell for approximately 15 mm as the transducer is placed at the centre of the cell, and thus the acoustic signal would have to propagate through the respective tabs in both SC-NMC811/Gr and PC-NMC811/Gr cells (Figure 66(a) and Figure 66(b)) [151].

In addition, differences in the physical structure of the two pouch cells can be visualised in .

Figure 66. Differences include gas bubbles (variable electrolyte distribution) and differences in the origin of the wounded electrode layers. Inhomogeneities between different NMC811/Gr pouch cells may play a confounding role in acoustic experiments in Chapter 7 as varied intrinsic physical attributes, belonging to the cell can be present prior to experimentation.

6.4.2. Surface characterisation of a SC-NMC811 and PC-NMC811 electrode

SC-NMC811 and PC-NMC811 electrodes were harvested from disassembled NMC811/Gr cells to capture scanning electron micrographs of the two cathode electrode surfaces. SEM images are presented in Figure 67.
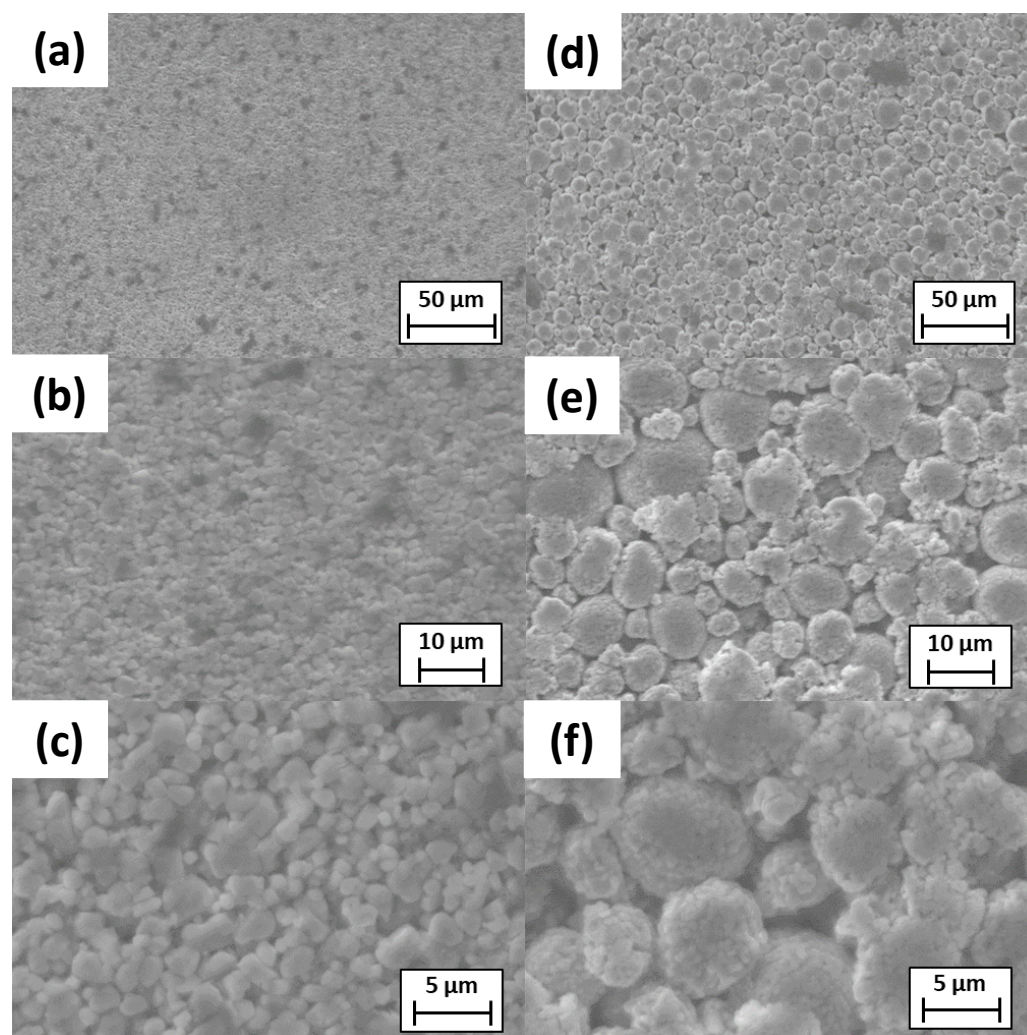
Figure 67: *SEM images of the surface structures of the evaluated SC-NMC811 (a)-(c) and PC-NMC811 (d)-(f) electrodes, (a) and (d) magnification - 1,000X, (b) and (e) magnification - 3,670X, (c) and (f) magnification 8090X.*

The surface of the SC-NMC811 and PC-NMC811 electrodes appear to have NMC811 particles packed closely together. At lower magnifications of 1000X the single crystal particles are not clear owing to their small size whereas polycrystalline particles appear much larger. At a magnification of 8090X, the PC-NMC811 particles are clearly visible as is how they are composed of numerous primary particles (assume to be single crystallites) agglomerated into larger PC-NMC811 particles (secondary particles) [316]. The SC-NMC811 particles

appear to agglomerate into spherical secondary particles in the PC-NMC811 electrode, whereas the shape of SC-NMC811 particles is more diverse in the SC-NMC811 electrode, with no particular shape appearing to be dominant. The largest particle in the SC-NMC811 electrode still appears to be smaller than any of the particles in the PC-NMC811 electrode. The PC-NMC811 particles are not identical, and there are some secondary particles that appear to pack primary particles more uniformly than others. Some PC-NMC811 particles also appear to have cavities present between the agglomerated single crystal particles.

6.4.3. Electrode characterisation using X-ray μCT

It is widely reported that electrodes with densely packed particles are expected to have better electrochemical performance [30] [317] [318] [319]. Therefore, the reconstructed microstructures need to be investigated with geometric characteristics such as PSD, particle sphericity, electrode surface area and tortuosity that describe the heterogenous electrodes [320]. SC-NMC811 and PC-NMC811 electrodes were also harvested from the NMC811/Gr cells to examine differences in bulk electrode morphology that can influence the interaction of the ultrasonic sound pulse with the electrode interface. 3D images were acquired to examine crack propagation, PSD, and electrode porosity.
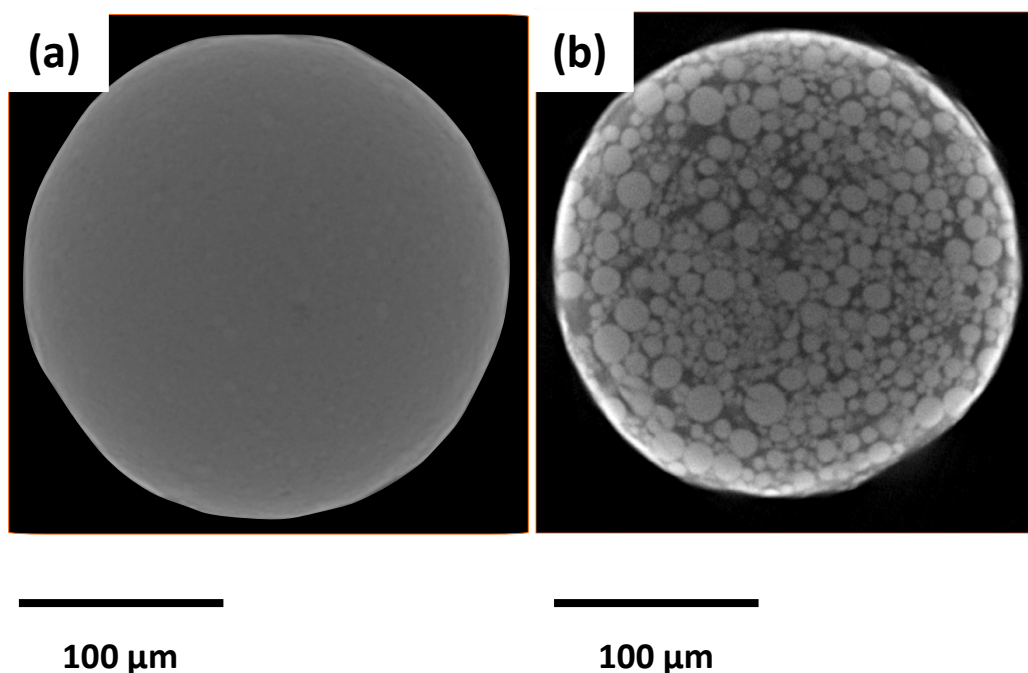
Figure 68: *Horizontal cross sections through an X-ray tomography scan of an SC-NMC811 electrode (a) and PC-NMC811 electrode (b). Optical magnification 40X magnification.*

The particles of the PC-NMC811 electrode are more visible than the particles of the SC-NMC811 electrode using X-ray μCT at 40X optical magnification due to the difference in size of single crystal and polycrystalline particles. X-ray μCT does not provide a feasible measure of the SC-NMC811 electrode as the single crystal particles are too small to be visualised and separated at this magnification.

6.4.4. Electrode characterisation using X-ray nCT

X-ray nCT imaging was carried out to visualise differences in morphology between pristine SC-NMC811 and PC-NMC811 electrodes and quantitatively analyse whether these differences could influence the acoustic response of the SC-NMC811/Gr and PC-NMC811/Gr cells.

(a)　　　　　　　　**(b)**

30 µm　　　　　　　30 µm
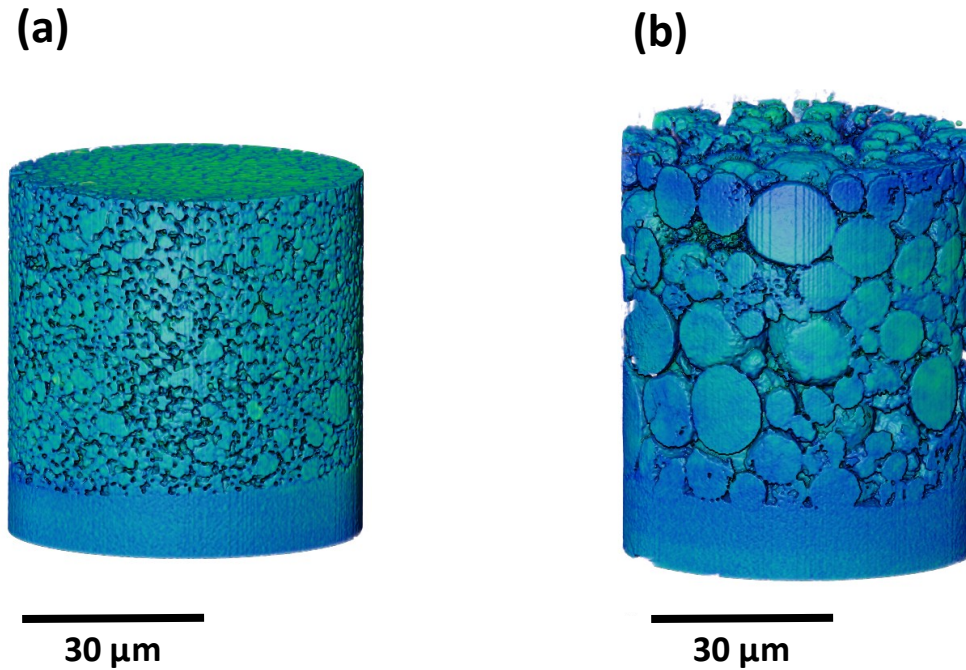
Figure 69: *3D reconstruction of the laser-milled pristine SC-NMC811 electrode pillar (a) and pristine PC-NMC811 electrode pillar (b) showing the current collector and active layer, respectively.*

The cylindrical shape of the SC-NMC811 and PC-NMC811 electrode specimens is evident in

Figure *69* during X-ray nCT scanning. Laser milling LiB electrodes as a pillar is effective in providing undamaged electrode specimens for X-ray CT imaging. This further suggests that the large delamination shown in the cycled graphite electrode in Chapter 4 is likely caused during cell testing as a variety of laser-milled pillars have been prepared in this work without any significant damage. Larger particles and larger pores can be seen in the PC-NMC811 electrode pillar (

Figure *69*).

(a)

(b)

10 μm   **10 μm**
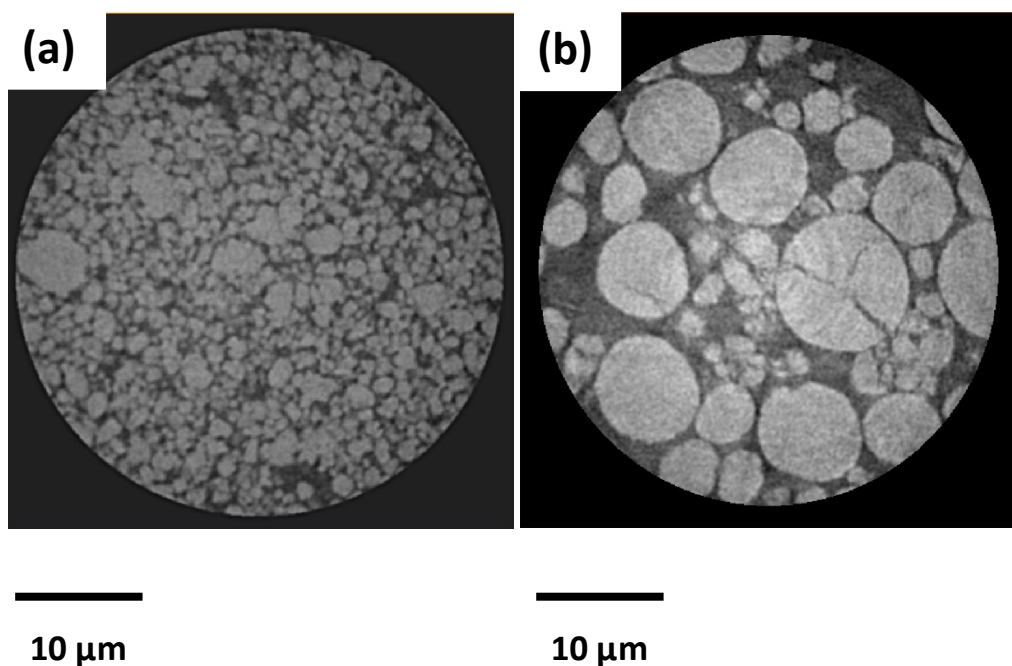
Figure 70: Horizontal cross sections through an X-ray CT scan of an SC-NMC811 electrode (a) and PC-NMC811 electrode (b).

From first observation, the SC-NMC811 particles and PC-NMC811 particles can be visualised along with the pore network in the respective electrodes. Other morphological features can also be visualised from the horizontal cross sections such as the two-way and three-way cracking on various PC-NMC811 particles. Furthermore, the complete separation of a particle due to a crack running through the entire length of a PC-NMC811 particle resulting in two separate particles. As the electrode is uncycled (pristine), it is likely that this particle cracking mechanism is caused during the calendering process of electrode manufacturing [78] [84]. Similar, to X-ray μCT discussed in previous chapters, an orthoslice representative of the entire electrode volume was chosen for further image processing from X-ray nCT using Avizo software. Particle and pore phase

volume fractions were segmented using the separate object tools and the subsequent 3D Tiff stack was used for TauFactor simulations.

10 µm   10 µm
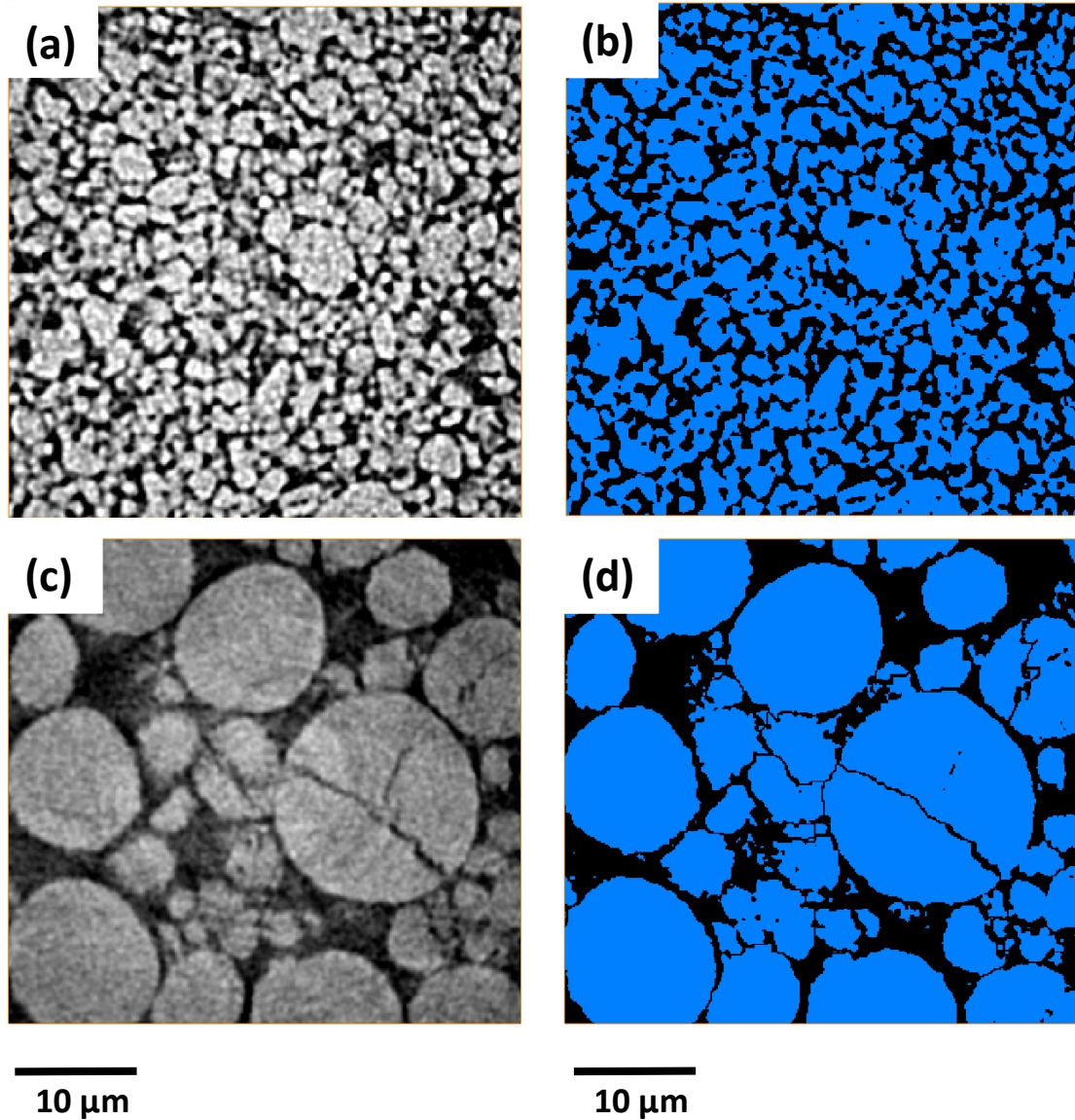
Figure 71: (a) Orthoslice of the SC-NMC811 electrode with its (b) corresponding particle (blue)-pore (black) distribution and (c) an orthoslice of the PC-NMC811 electrode with (d) its corresponding particle (blue)-pore (black) distribution after segmentation.

The SC-NMC811 particles appear more tightly packed with shorter distances between the respective particles. The smaller gap between particles provides higher possibility of electrical connection between the particles. In addition, the PC-NMC811 electrode has larger pores, the relatively larger pore radii of this electrode demonstrate a high possibility of isolated particles. Electrically isolated particles cause capacity loss, which suggests the SC-NMC811 electrode will have better capacity retention as it is more densely packed. Zheng *et al.*[321] state that electrodes with high packing density have higher breaking strength, which can avoid the shedding of active materials during battery processing and electrochemical cycling. This is another reason to suggest that SC-NMC811 electrodes will have higher specific capacities and rate capabilities than PC-NMC811 electrodes.
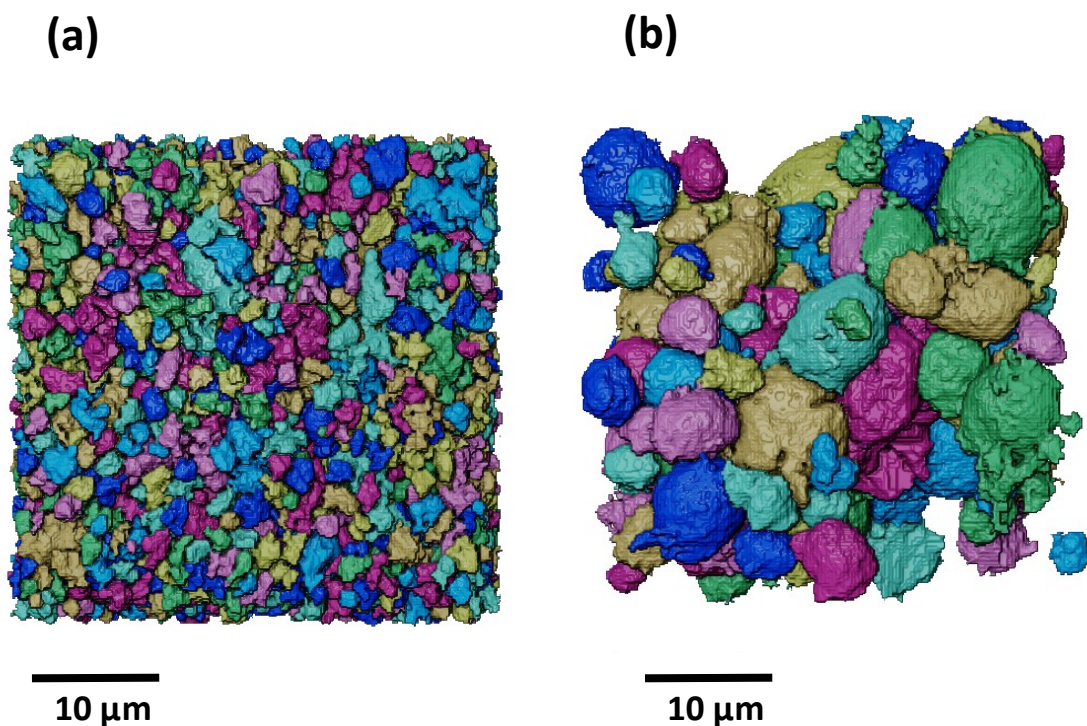
Figure 72: *3D volume rendering of the active material particle network of the SC-NMC811 electrode (a) and PC-NMC811 electrode (b) after reconstruction and segmentation and with a border kill operation applied. Particles are randomly coloured to assist in visualisation.*

As expected, the polycrystalline particles of the PC-NMC811 electrode are far larger than the single crystal particles of the SC-NMC811 electrode (shown in Figure 72a and Figure 72b. As single crystal particles are smaller than agglomerated PC-NMC811 particles, optimising the size is critical for the single-crystalline particles to maintain rate capabilities similar to those of polycrystalline particles. Research has suggested a median size of 1-4 μm is sufficient to ensure rate capabilities are maintained in SC systems [322]. The equivalent diameter of particles and pores was extracted from the volume rendering of the SC-NMC811 and PC-NMC811 electrodes to better understand the transmitted acoustic signal propagation through the cell during cycling.

Particles in the SC-NMC811 electrode range between 0.1-3.0 μm in diameter and particles in the PC-NMC811 electrode range between 1-13 μm in diameter (Figure 73a and Figure 73b). Furthermore, larger pore diameters are recorded between active material particles in the PC-NMC811 electrode (1.0-7.5 μm) compared to the SC-NMC811 electrode (around 0.1-1.2 μm) (Figure 73c and Figure 73d). This may be because single crystal particles can be more tightly packed into the electrode than the polycrystalline particles due to their smaller size. As a result, a higher solid phase volume fraction and a lower porosity is recorded for the SC-NMC811 electrode (see Table 7).

Table 7: Active material and pore and CBD volume fraction recorded for each electrode determined using the Volume Fraction module in Avizo.

Electrode	Active material (vol. %)	Pore and CBD (vol. %)
SC-NMC811	73.2	26.8
PC-NMC811	68.8	31.2

Consequently, different acoustic amplitudes are recorded for the active layers between these cells. The PC-NMC811/Gr cell showed more attenuation than the SC-NMC811/Gr during cycling and displayed lower acoustic amplitude peaks corresponding to the active layers that are also present in the SC-NMC811/Gr cell. It is expected that the SC-NMC811 electrodes will have a higher Young's modulus than PC-NMC811 electrodes owing to the higher solid phase volume fraction and smaller interstitial distances between particle grains in the SC-NMC811 electrode, which should result in an overall stiffer electrode with higher signal reflectance and therefore higher acoustic amplitude recordings. It is also possible that PC-NMC811 particles themselves have a lower Young's modulus than SC-NMC811 particles due to SC-NMC811 particles having larger grains compared to smaller, more loosely bound agglomerated grains in the PC-NMC811 particle.

(a)

(b)

(c)

(d)
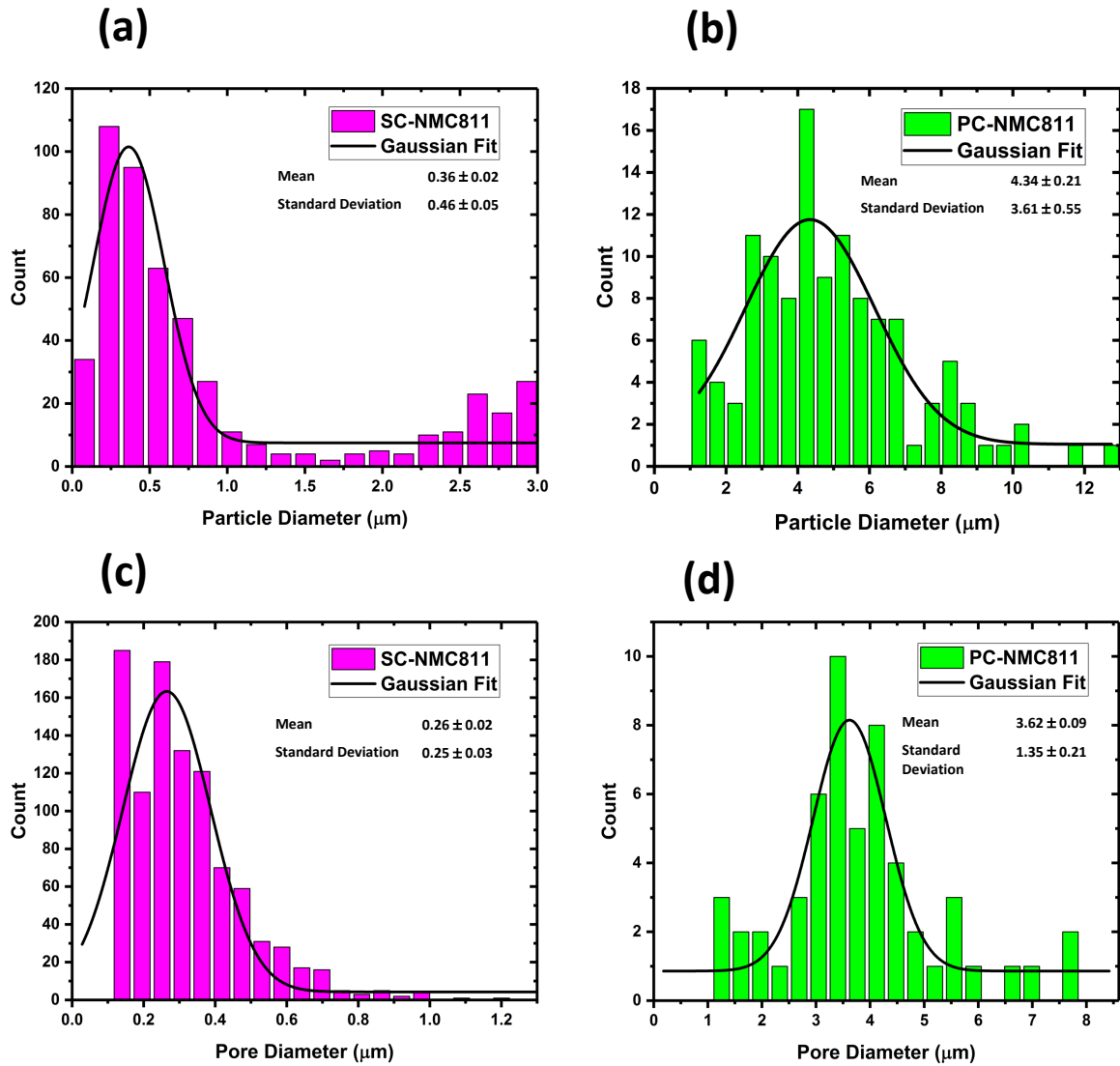
Figure 73: *Equivalent particle diameter of the (a) SC-NM811 and (b) PC-NMC811 electrode. Equivalent pore diameter for the (c) SC-NMC811 electrode and (d) PC-NMC811 electrode.*

The volumetric PSDs (Figure 73(a) and Figure 73(b)) extracted from the volume renderings of the SC-NMC811 and PC-NMC811 electrodes are very different, correlating with the particle sizes in the horizontal cross sections through the X-ray CT scans shown in Figure 70(a) Figure 70(b). The single crystal particles range in volume between 0.5-600 μm^3 and the polycrystalline (secondary) particles range in volume between 10-1000 μm^3. In addition, a higher number

of particles is recorded in the SC-NMC811 electrode ROI compared to the number of particles in the PC-NMC811 electrode ROI. Based on these findings, it is expected that acoustic signals will propagate through the SC-NMC811 electrode in a more facile manner than the PC-NMC811 electrode as acoustic signals propagate through solid media with less attenuation than liquid media (electrolyte), which will fill the interstitial sites in a working cell [323].
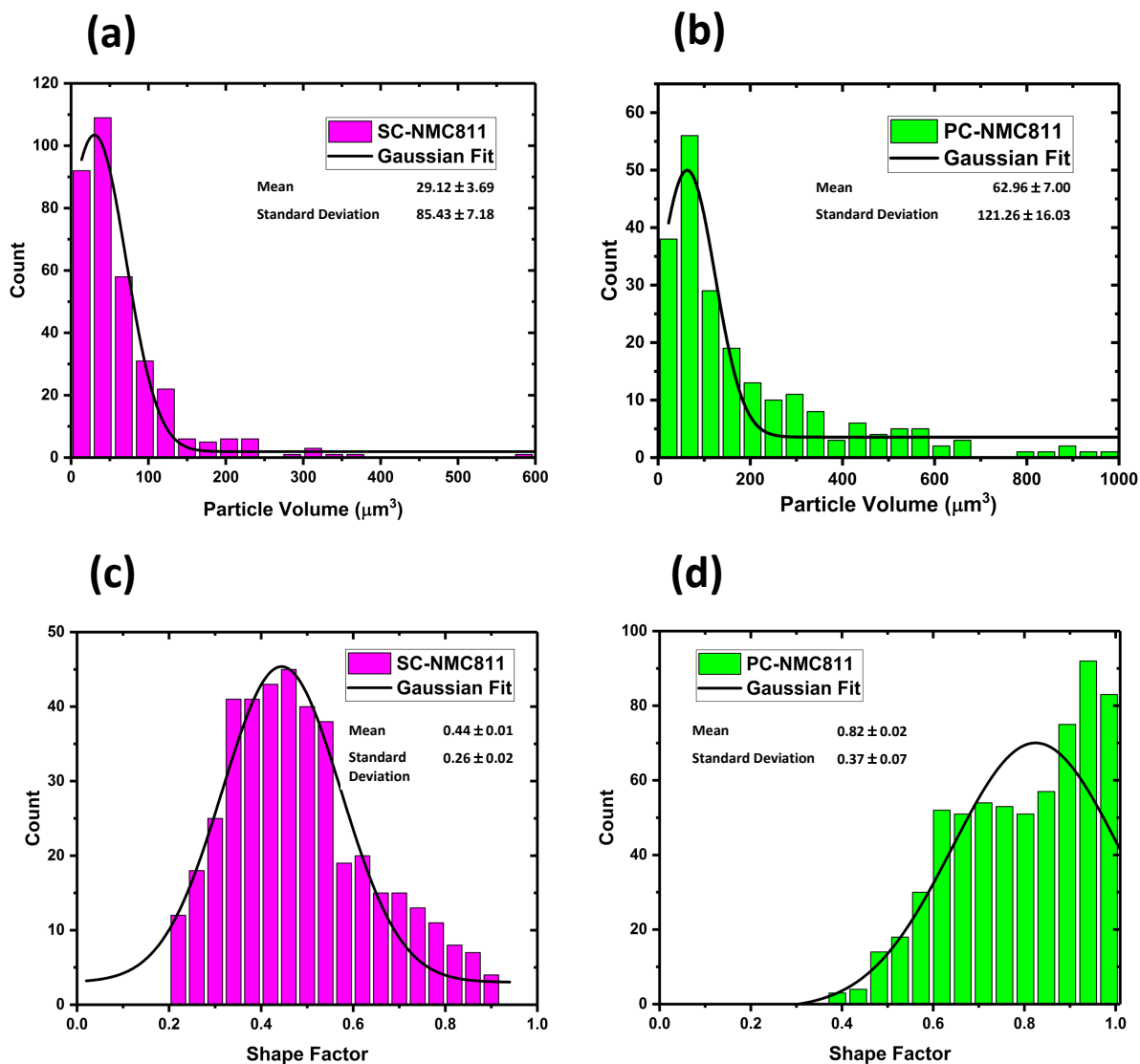
Figure 74: *Volumetric PSD of electrode particles in the (a) SC-NMC811 electrode and (b) PC-NMC811 electrode. Shape factor (or sphericity) of particles in the SC-NMC811 electrode (c) and PC-NMC811 electrode (d).*

The shape factor (or sphericity) characterises how closely a particle resembles a sphere. A particle that has a shape factor of 1 is perfectly spherical with smaller values indicating less sphericity [324]. The shape factor, S, of a particle with a volume of V and surface area of A can be calculated from Eq. 6.1:

$$S = 6\sqrt{\pi}\,\frac{V}{\sqrt{A^3}} \qquad (6.1)$$

The polycrystalline particles of the PC-NMC811 electrode consist of numerous SC-NMC811 particles agglomerated into larger spherical secondary particles (see Figure 67) [316]. The SC-NMC811 electrode features a more diverse array of particle shapes and sizes than the PC-NMC811 electrode (Figure 74(c) and Figure 74(d)). Nonetheless, the differences in particle shapes between the SC-NMC811 electrodes and PC-NMC811 electrodes are not expected to influence the degree of reflection of the incident acoustic signal because the particles are smaller than the incident acoustic signal wavelength [235]. For instance, when passing through air λ = 70 μm, aluminium λ = 1200 μm and copper λ = 452 μm. The acoustic signal wavelength changes according to the material interface it passes through due to differences in material density and Young's modulus. Therefore, differences in density/morphology between the PC-NMC811 and SC-NMC811 electrodes will cause a difference in acoustic signal wavelength as it passes through these electrodes. Particle size and shape affect material properties of the electrode layer such as electrode density, which alters the signal's wavelength, affect ToF and signal attenuation [325]. Theoretically speaking, it is possible to detect morphological changes such as particle cracking by increasing the frequency of the acoustic signal and thereby shortening its wavelength. The signal can also be localised to a ROI by adjusting the position of the sensor. However, there is a trade-off as lower ultrasonic frequencies provide better wave penetration through an entire LiB cell, whereas higher frequency provides higher resolution and focal sharpness [57].

The particle surface area and particle volume specific surface area (VSSA) were obtained from the reconstructed microstructure of each NMC811 electrode (Figure 75). VSSA can provide both structural and cycling performance-related information for LiB electrodes, as the particle-pore interface is where charge transfer reactions occur during battery cycling between the active material and the electrolyte. There are large differences in VSSA between particles in the SC-NMC811 electrode and PC-NMC811 electrode. The SC-NMC811 particles have a larger VSSA despite particles in the PC-NMC811 electrode having surface areas ~7 times larger than the largest surface areas in the SC-NMC811 electrode. However, the majority of SC-NMC811 and PC-NMC811 particles have surface areas below 100 μm^2. On average, the SC NMC particles have a smaller surface area than the PC NMC particles. However, polycrystalline particles have been found to crack extensively during cycling, which increases the surface area of the ensemble electrode and provides more sites for Li intercalation/deintercalation [40]. In contrast, singe crystal particles do not undergo cracking during cycling [312] [326] [327]. Therefore, more gas formation and capacity fading occurs in the PC-NMC811/Gr cell during repeated cycling [144] [310] [328] [311] [329].
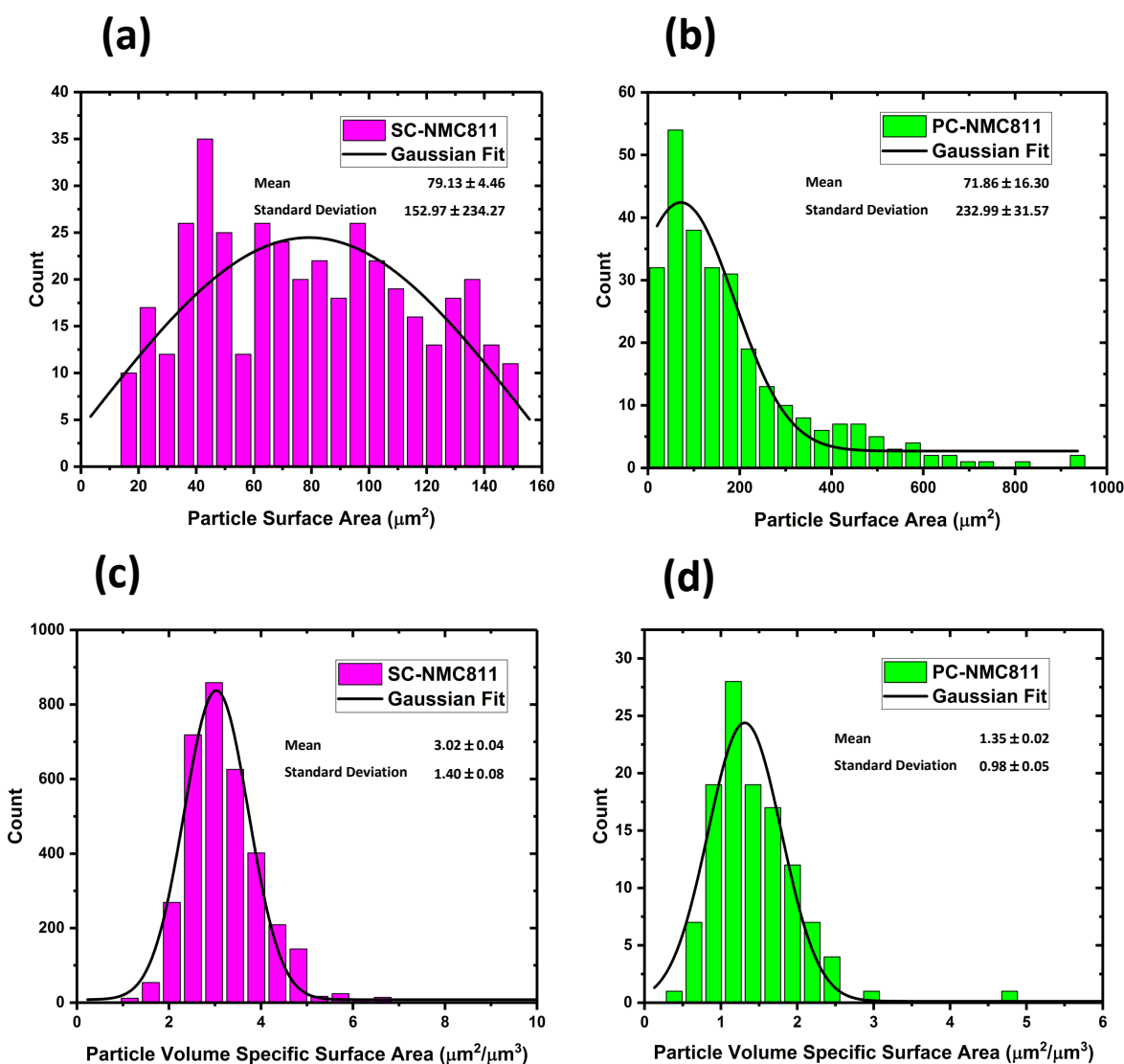
Figure 75: *The surface area of particles in the SC-NMC811 electrode (a) and PC-NMC811 electrode (b). The VSSA of particles in the SC-NMC811 electrode (c) and the PC-NMC811 electrode (d).*

Heenan *et al.*[40] report that various polycrystalline NMC811 particles undergo cracking prior to cycling owing to calendering of the electrode during electrode processing stages. This gives rise to various individual smaller secondary particles that originate from larger particles. These findings suggest that the wider variety of particle surface areas that exist in the PC-NMC811 electrode

may be caused by particle cracking which occurred during calendering (see Figure 75(b)). Both SC-NMC811 and PC-NMC811 electrodes were calendered, which would further suggest that calendering is more detrimental for polycrystalline electrodes. Particle cracking is not expected to occur in the SC-NMC811 electrode to the same degree as the PC-NMC811 electrode owing to their initial size and lack of internal grains (Figure 74(a)). Larger particles are also more prone to cracking during expansion/contraction of the electrode after repeated charge/discharge cycling leading to various degradation mechanisms such as phase transformation [278], cathode-electrolyte parasitic reactions [79] [81] [296] and transition metal dissolution [86] [330]. Therefore, from these findings, we can assume that the PC-NMC811 electrode will have poorer capacity retention and overall cycling performance than the SC-NMC811 electrode. Manganese dissolution from NMC electrodes has been reported to induce elevated rates of electrolyte reduction at the graphite electrode, causing further SEI formation reactions [70]. The gas evolution caused by these reactions would exacerbate signal attenuation.

According to Eastwood *et al*. [135] a nano-structured material with a high VSSA can facilitate rapid de/intercalation of Li^+ ions which accommodates rapid charge/discharge cycling [135]. The SC-NMC811 electrode has a far higher VSSA than the PC-NMC811 electrode to suggest this electrode would have a better cycling performance at higher C-rates. Nonetheless, rate capability may come at the expense of overall LiB capacity, as large particles are required to maximise the amount of Li^+ ions that can intercalate into the bulk electrode [331]. The SC-NMC811 electrode has far smaller particle volumes than the PC-NMC811 electrode.

6.5. Conclusions

X-ray CT and SEM has been used to confirm significant differences in morphology between SC-NMC811 electrodes and PC-NMC811 electrodes. Multiple length-scale X-ray CT experiments were carried out to image the entire interior architecture of a LiB as well as the microstructure of the NMC811 electrode. The need for a multi-length-scale approach was evidenced during X-ray µCT experiments of the SC-NMC811 electrode as the resolution used could not provide a suitable image of the SC-NMC811 electrode for further image processing yet the polydispersity of SC-NMC811 particles was evidenced when using an X-ray nCT resolution. The resolution required for 3D microstructural characterisation is specific to the physical parameters of the material under investigation.

Use of X-ray CT revealed some interesting aspects of the interior cell architecture of the tested LiBs. For instance, the elongated tabs that run through around half the length of the cell may affect acoustic signal propagation through the cell. Numerous geometrical parameters such as particle sphericity, equivalent particle/pore diameter and volumetric PSD were assessed for each NMC811 electrode. The PC-NMC811 electrode was largely characterised as having much larger particles with larger interstitial distances between active particles. The SC-NMC811 electrode had far smaller particles, with smaller interstitial distances between them. These differences were hypothesised to influence electrode density and Young's modulus, both critical physical properties that can alter acoustic recordings for either material.

INTENTIONALLY BLANK

Chapter 7

Electrochemical Acoustic ToF Spectroscopy as a Diagnostic Tool for Degradation Mechanisms of Lithium-ion Batteries

7.1. Overview

The primary purpose of using acoustic spectroscopy was to evaluate its capability in detecting degradation mechanisms of Li-ion cells during cycling. In previous chapters, ECD has been demonstrated as a powerful technique to reveal degradative dimensional changes that occur to single electrodes during cycling; herein, acoustic spectroscopy is used to measure the degradation of whole-cell assemblies in order to facilitate a multi scale approach to evaluating the degradation of LiBs during similar cycling protocols. The aim is to integrate the information obtained from ECD and X-ray CT with acoustic spectroscopy to reveal degradation mechanisms that can be detected across these techniques at different length-scales. The results in this chapter form part of a paper under review by the author in Journal of Power Sources.

7.2. Introduction

During prolonged cycling, EA-ToF spectroscopy measurements of whole cell assemblies can be complicated by various phenomena including gas formation, material stress changes and thermal expansion. In addition, intrinsic physical properties such as particle size, electrode density and local electrode composition provide significant challenges to directly measuring thicknesses in LiBs, as these factors can vary considerably between different cells and influence their acoustic behaviour. Therefore, some familiarity with the acoustic signature of different full cells is beneficial for discerning changes in acoustic signatures due to intrinsic physical properties and structural changes during cycling.

To the authors' knowledge, this is the first time EA-ToF spectroscopy has been carried out on LiBs composed of SC-NMC811 cathodes, to explore whether EA-ToF spectroscopy can provide sensitivity capable of detecting the intrinsic difference in bulk electrode properties caused by the different particle morphology of the tested NMC811 electrodes. EA-ToF spectroscopy was also used to evaluate changes in the acoustic signal's ToF between LiBs composed of either SC-NMC811 electrodes or PC-NMC811 electrodes during cycling and whether these ToF changes correlated with changes in exterior cell temperature.

7.3. Experimental methodology

7.3.1. Single point EA-ToF spectroscopy

EA-ToF measurements were carried out using an Olympus Epoch 650 ultrasonic flaw detector (Olympus Corp, Japan) with a pulse-echo contact transducer (M110-RM, Olympus Corp, Japan). A frequency of 2.25 MHz was chosen for all EA-ToF measurements using a piezoelectric transducer element (6 mm diameter), capable of frequencies of up to 5 MHz. Ultrasonic couplant (H-2, Olympus Corp, Japan) was applied to maintain interfacial contact between the cell and transducer to facilitate propagation of the ultrasonic pulse into the pouch cell. Constant pressure was applied behind the transducer with a 200 g weight placed on top of the sensor (Figure 76). It was ensured that the transducer was placed directly in the centre of each cell during EA-ToF spectroscopy to avoid any possible differences in acoustic response between cells caused by the transducer's location along the length of the current collector inside the cell. A uniform weight is placed on the transducer to ensure a consistent signal is obtained throughout the measurements. The magnitude of this weight was determined based on the experimental setup to optimise the signal amplitude through the LiB. However, a lower value may be used with a higher initial gain in the acoustic signal to achieve the same results (and vice versa) throughout the measurements, by ensuring consistent contact between the transducer and the cell.

(a)

Thermocouples

Pouch cell

Heat resistant tile

(b)

Weight (200 g)

To potentiostat

Transmitting transducer

X

Y

Z
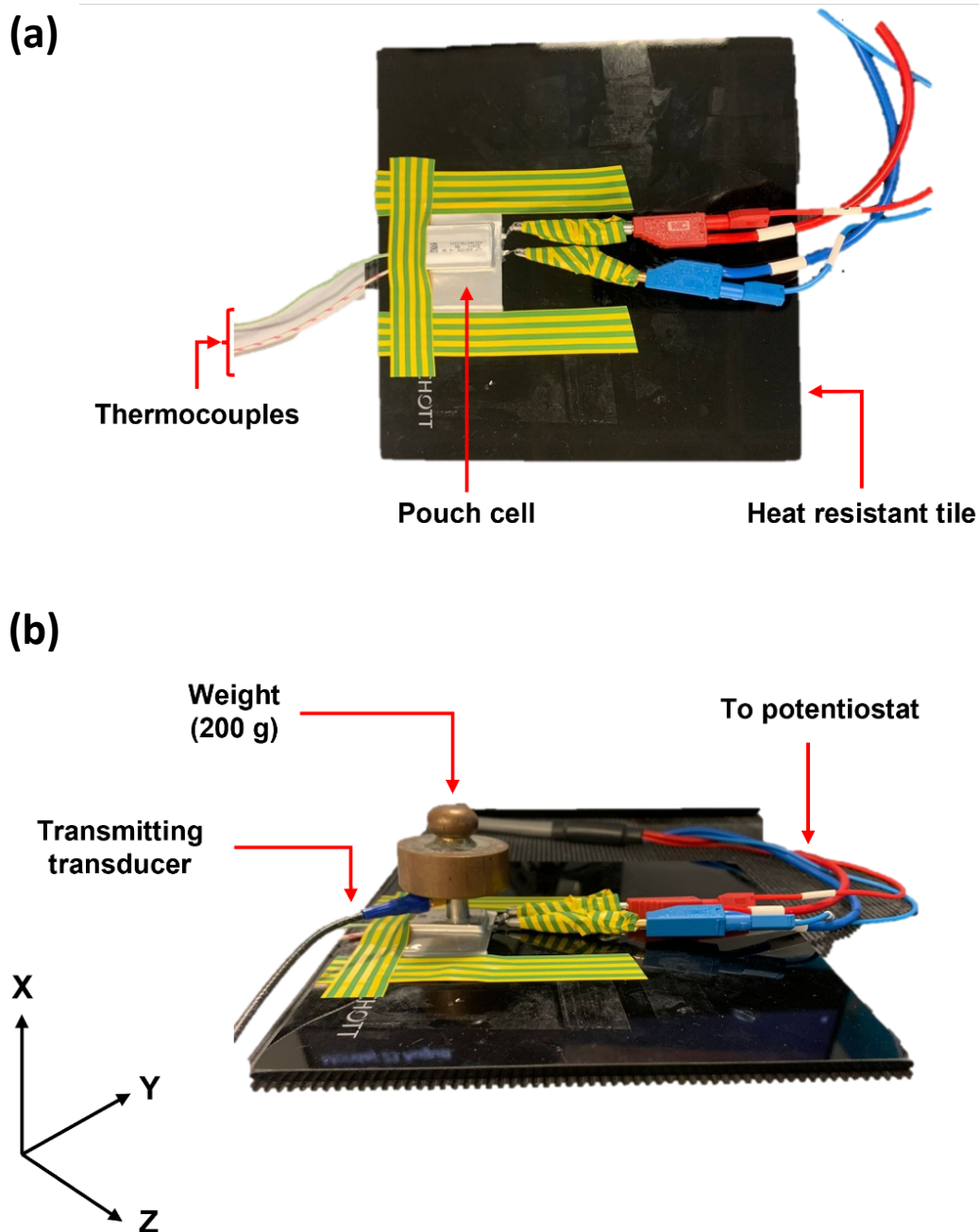
Figure 76: A photograph of an EA-ToF spectroscopy test set up with a pouch cell (a) top-view and (b) side-view with an ultrasound transducer and weight.

The magnitude of the measured acoustic response by the transducer is in part determined by the gain, which was set at 58 dB to optimise the magnitude of

the received signal over the time range of interest. The voltage applied to the piezoelectric transducer was 200 V. The resolution of each waveform data sample, with 8000 discrete mapping points equally spaced across the range of 20 μs, provides a ToF resolution of 20.2 ns for each data point.

7.3.2. Acoustic data acquisition and data processing

Acoustic data acquisition was carried out in parallel with electrochemical cycling. The ultrasound waveform data was transferred from the Epoch 650 through an RS232 connection and output files acquired by a custom python code. All acoustic recordings made during EA-ToF measurements were saved as .txt files in a single directory and auto-generated every 60 seconds. Each .txt file corresponded to a single sound pulse. 8000 data points were saved in each .txt file for every 20 μs sound pulse. All acoustic data collected was analysed using Python 3.7.

7.3.3. Temperature measurements during EA-ToF spectroscopy

A K-type thermocouple was placed onto the underside of the NMC811/Gr cell during galvanostatic cycling and connected to an input channel on a Pico Technology TC-08 data logger. PicoLog 6 data logging software was used to record the exterior temperature of the NMC811/Gr cell. Recordings were taken in 10 second intervals. Temperature data was saved as a picolog file and exported as CSV.

7.3.4. Battery cycling during EA-ToF spectroscopy

Electrochemical testing was carried out using an SP-200 potentiostat (BioLogic, France). Pouch cells were initially put through a formation cycle using a constant current protocol with an applied rate of C/20 and a potential window of 2.5 V-4.3 V for one cycle. The applied current was based on the nominal capacity of the cells (210 mAh). After initial cycling, NMC811/Gr cells were disconnected and returned to the glovebox. A small incision was made along the edge of the NMC811/Gr pouch cell casing to allow for gas to be mitigated before resealing. The NMC811/Gr cells were then resealed for long-term cycling.

7.4. Results and discussion

7.4.1 Signal response during EA-ToF measurements of the NMC811/Gr cells

Naturally, the acoustic signal response received by the ultrasonic flaw detector can vary considerably depending on the sample under investigation. This is to be expected due to the variation in material interfaces across different tested samples. In this work, all EA-ToF experiments were conducted on the same pouch cell geometry to minimise variations between the tested pouch cells. Figure 77 explains the acoustic response received by the ultrasonic flaw detector-receiver from a SC-NMC811/Gr pouch cell.
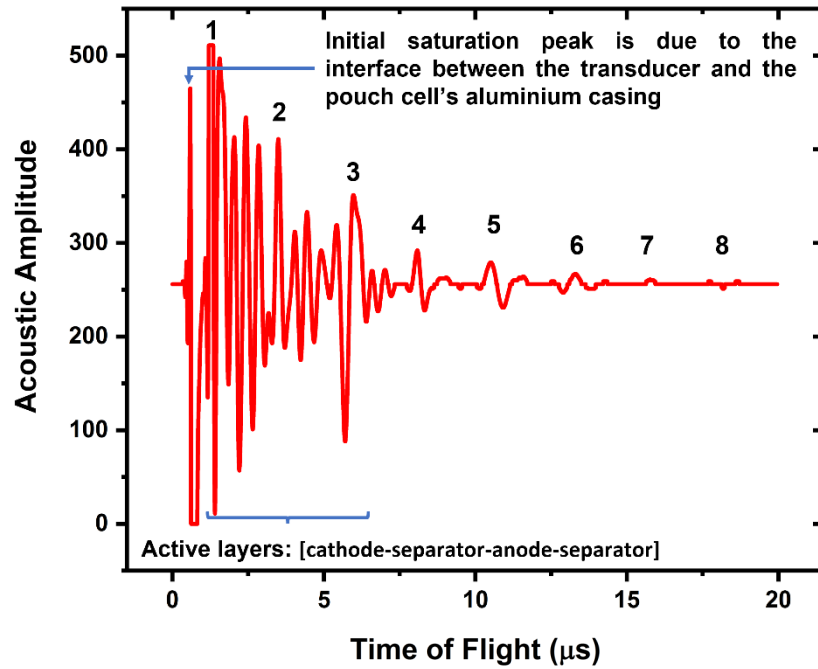
Figure 77: *The initial acoustic waveform generated by pulsing through the layers of a SC-NMC811/Gr pouch cell. Eight 'echo' peaks are identified and annotated as well as the active layers and initial saturation peak due the transducer-pouch cell interface.*

The acoustic amplitude of the reflected peaks in an EA-ToF response are in part determined by the reflection coefficient (R). This coefficient describes the amount of reflection of an incident acoustic wave and is highly influenced by the relative acoustic impedance (Z) of the two materials at a given interface [153]. Signal attenuation from the cell will also play a role in the amplitude of the peaks; the deeper the acoustic signal propagates into a cell, the more material the signal has to pass through, so the more attenuated it is and the lower the amplitude of the peak caused at each material interface [161]. The acoustic impedance and reflection coefficient can be calculated as shown in Eqs. 7.1 and 7.2 [153]:

$$Z = \rho c \qquad\qquad\qquad (7.1)$$

$$R = \left(\frac{Z_2 - Z_1}{Z_1 - Z_2}\right)^2 \qquad\qquad\qquad (7.2)$$

Typically, numerous material flaws such as inter- and intra-particle cracking are expected to alter the ensemble electrode morphology and thus appear on the EA-ToF spectrogram within the peaks associated with the active layers (where an active layer consists of the combination of cathode-separator-anode-separator), for example dampening in acoustic amplitude or intermittent loss of acoustic signal. Gas/SEI formation can cause non discriminative signal attenuation for numerous active layers in the cell simultaneously.

The initial acoustic ToF response (Figure 77) contains several key features that are present throughout all acoustic experiments presented in this work. Firstly, a sharp peak is present at approximately 0.63 µs. This peak is associated with the generation of an ultrasonic pulse. This peak was in the same location for all SC-NMC811/Gr and PC-NMC811/Gr pouch cells measured and was thus treated as an artefact of the signal response [125] [151] [161]. The following peaks are indicative of the internal structure of the cell. Each peak indicates an interface in the sample, in this case an active layer in the pouch cell [161]. As the ultrasonic sound waveform penetrates deeper through the pouch cell, the amplitude of the signal decreases. This decay in acoustic signal is expected as a result of numerous physical phenomena acting on the sound waveform including wave spreading, signal attenuation and acoustic waves interfering with each other as they pass through the battery medium [151] [161]. A portion of the ultrasound propagates through the entire length of the pouch cell and reaches the back wall [332]. This signal is mostly reflected, as opposed to transmitted. This is due

to the large difference in acoustic impedance of the air and the pouch cell packaging which results in equally spaced 'echo' peaks that generally have higher acoustic amplitude than other peaks with similar ToF [151] [237]. Eight 'echo' peaks can be identified in Figure 77. The first 'echo' peak (labelled as 1 in Figure 77) occurs at ~1.5 µs and the final 'echo' peak (labelled as 8 in Figure 77) occurs at ~18.0 µs. By the time the sound pulse has passed through the active layers and towards the back wall of the pouch cell the signal has dissipated significantly.

7.4.2. Gassing during first cycle SEI formation

The acoustic response of PC-NMC811/Gr and SC-NMC811 cells was monitored for gas formation during their formation cycle because significant gas accumulation is expected as an SEI layer forms on the anode surface [152] [333]. EA-ToF measurements were carried out to determine whether the accumulated gas affects the acoustic signal propagating through the cell and in turn effect the EA-ToF response. The cells were then degassed and resealed before continuing acoustic measurements with cell cycling.

The EA-ToF spectrograms plotted with respect to time for the SC-NMC811/Gr and PC-NMC811/Gr cells during formation cycles are shown in Figure 78 with the red regions representing high amplitude peaks and the blue regions representing low amplitude troughs. White regions correspond to regions where no change in amplitude of the initial generated acoustic pulse is recorded. The first horizonal line at approximately 0.6 µs corresponds to the initial saturation of the transducer and is present in all EA-ToF spectrograms evaluated in this work. The subsequent lines in the EA-ToF spectrograms represent each active layer interface.
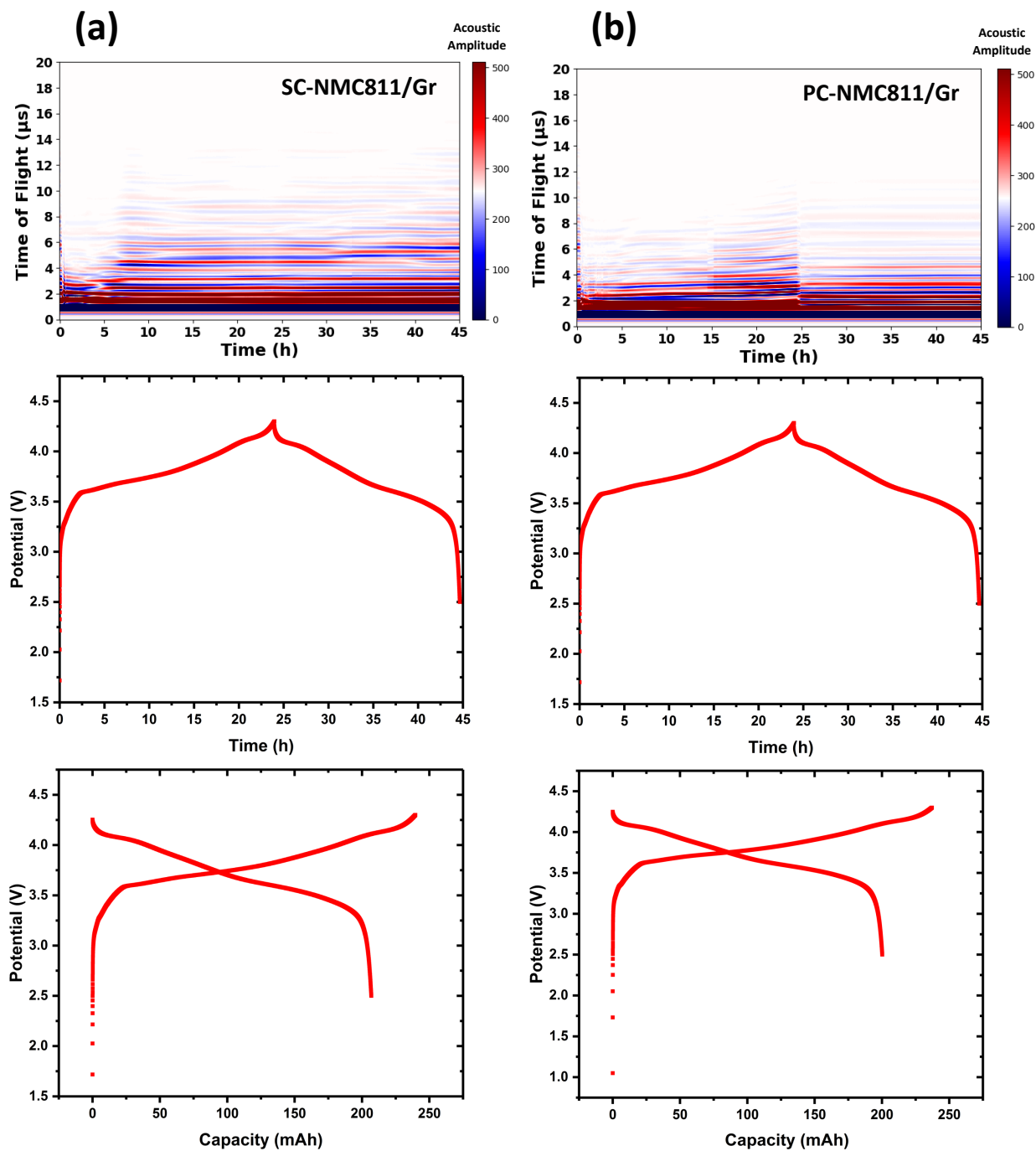
Figure 78: *EA-ToF spectrogram plotted with respect to time with the region where most signal attenuation occurs in white(top); potential profile of the first cycle at a current rate of 0.0105 A (C/20) (middle); and potential profile versus capacity (bottom) of SC NMC811/Gr cell (a, left column) and PC-NMC811/Gr cell (b, right column).*

Significant acoustic signal attenuation was observed during the first 6 hours of cycling of the SC-NMC811/Gr cell and PC-NMC811/Gr cell (see Figure 78). The gas that forms during SEI formation significantly attenuates the acoustic signal because the impedance mismatch between transducer/gas is higher than for transducer/liquid. A loss of acoustic signal was evident throughout the entire formation cycle; however, most significant signal attenuation occurs during charging, as most electrolyte decomposition occurs at these potentials [334]. The gas that forms on the electrode during SEI formation then diffuses out into other regions of the pouch cell which causes the reappearance of the acoustic signal. The EA-ToF spectrograms collected for the PC-NMC811/Gr cells would suggest that more gas forms during SEI formation in these cells compared to the SC-NMC811/Gr cells (Figure 78). Signal attenuation due to gas formation perseveres throughout the entire duration of the first charge/discharge cycle to a greater extent than was observed for SC-NMC811/Gr cells.

Thus, acoustic signals can indicate which voltages significant gas formation occurs at during SEI formation. Despite, acoustic signals returning after the early part of charging, it is still possible that minimal gassing occurs, that is not enough to attenuate the acoustic signals. Once a stable SEI layer has formed, it is expected that cell degradation will occur due to gradual anode passivation, as opposed to the significant gassing that is recorded during the first cycle at C/20 and that LiBs with different anode compositions will exhibit different levels of first cycle signal attenuation [152]. Bommier *et al.* [152] found that significant gas formation occurs during the first 20 hours of a C/20 formation cycle for cells containing silicon-graphite anodes. Therefore, gaseous by-products that arise during SEI formation in silicon anodes are likely to cause acoustic signals to be attenuated differently to silicon-graphite anodes and graphite anodes, respectively. However, these cells have the same anode composition but differing cathode compositions, which implies that differences in first cycle gas evolution caused by different cathode compositions can also be detected with EA-ToF measurements. As was previously mentioned, SC-

NMC811 particles are less likely to have intra-particle cracks compared to PC-NMC811 particles [40]. As in the case of intra-particle cracks, inter-particle cracks are associated with additional electrolyte decomposition, new cathodic SEI layer formation, gas evolution and aggravated electrochemical resistance [335]. There are various reports that suggest more gas evolution occurs in cells that contain PC-NMC811 electrodes compared to SC-NMC811 electrodes [336] [310]. Li et al.[310] carried out a detailed *in-situ* gas evolution comparison between SC-NMC811 and aluminium-coated PC-NMC811 electrodes. The results revealed that PC-NMC811 electrodes release more gas than SC-NMC811 electrodes. In fact, SC-NMC811 electrodes were also found to release negligible gas at 4.6 V. In addition, whilst O_2 release from NMC was expected to be higher with increasing voltage, SC-NMC811 electrodes showed lower oxygen intensity indicating that less oxygen release occurs in SC-NMC811 compared with aluminium-coated PC-NMC811 and uncoated PC-NMC811 electrodes at each voltage.

7.4.3. C-rate dependency test

A C-rate dependency test was carried out on both of the NMC811/Gr cells to determine how EA-ToF measurements are affected by changing the current rate and for determining ToF shift patterns during different C-rates. After the SC-NMC811/Gr cells and PC-NMC811/Gr cells had been formed at C/20, they were tested at constant current rates of C/10, C/5, C/2.5 and 1C. The C-rate was brought back to the initial C-rate (C/10) at the end of the experiment to see whether the cells had incurred any capacity loss caused by faster charging. Differences in acoustic behaviour between the two different cell configurations could be attributed to the difference in morphology between single-crystalline NMC811 electrodes and polycrystalline NMC811 electrodes respectively.

EA-ToF signals are highly affected by the SoC of the LiB as lithiation can affect the density and Young's modulus of electrodes [238] [337]. The effect of SoC on electrode properties such as the Young's modulus (E_{mod}), density (ρ) and Poisson ratio (υ) which directly affect the speed of sound (c) are shown in Eq. 7.3, K and G are the bulk and shear moduli respectively (Eqs. 7.4 and 7.5) [235].

$$c = \sqrt{\frac{K+\frac{4}{3}G}{\rho}} \qquad (7.3)$$

$$K = \frac{E_{mod}}{3(1-2\upsilon)} \qquad (7.4)$$

$$G = \frac{E_{mod}}{2(1+\upsilon)} \qquad (7.5)$$
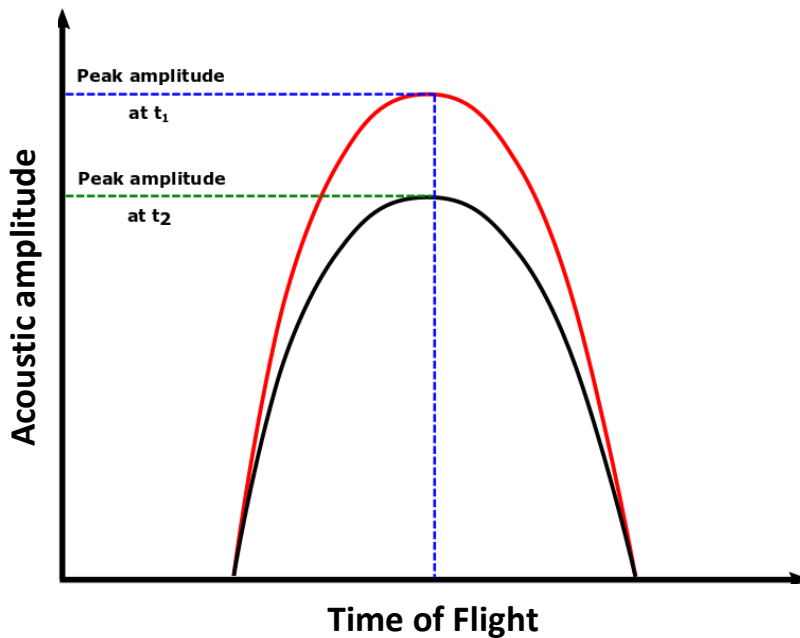
Figure 79: A change in measured amplitude at a given material interface due to a change in the ratio of acoustic impedances.

Acoustic signals change in their maximum amplitude with respect to time, indicating physical change in the corresponding electrode layers. For example, a highly lithiated anode will have a lower material density and be less dense than the same anode with less lithiation [338]. Graphite (C_6) has a density of 2.26 g cm^{-3}, whereas lithiated graphite (LiC_6) has a density of 2.20 g cm^{-3}. Materials with a higher density are expected to be associated with lower acoustic signal amplitudes than materials with lower density. However, graphite's (C_6) Young's modulus increases from 32 GPa to 109 GPa when it is fully lithiated (LiC_6) [337] [235]. A higher Young's modulus causes a higher acoustic signal amplitude. Therefore, properties can have complicated effects on the acoustic signal, and therefore the implications of the EA-ToF measurements require care in interpretation. The EA-ToF spectrograms obtained for the SC-NMC811/Gr and PC-NMC811/Gr cells during the C-rate dependency test are shown in Figure 80.

(a)

(b)

(c)
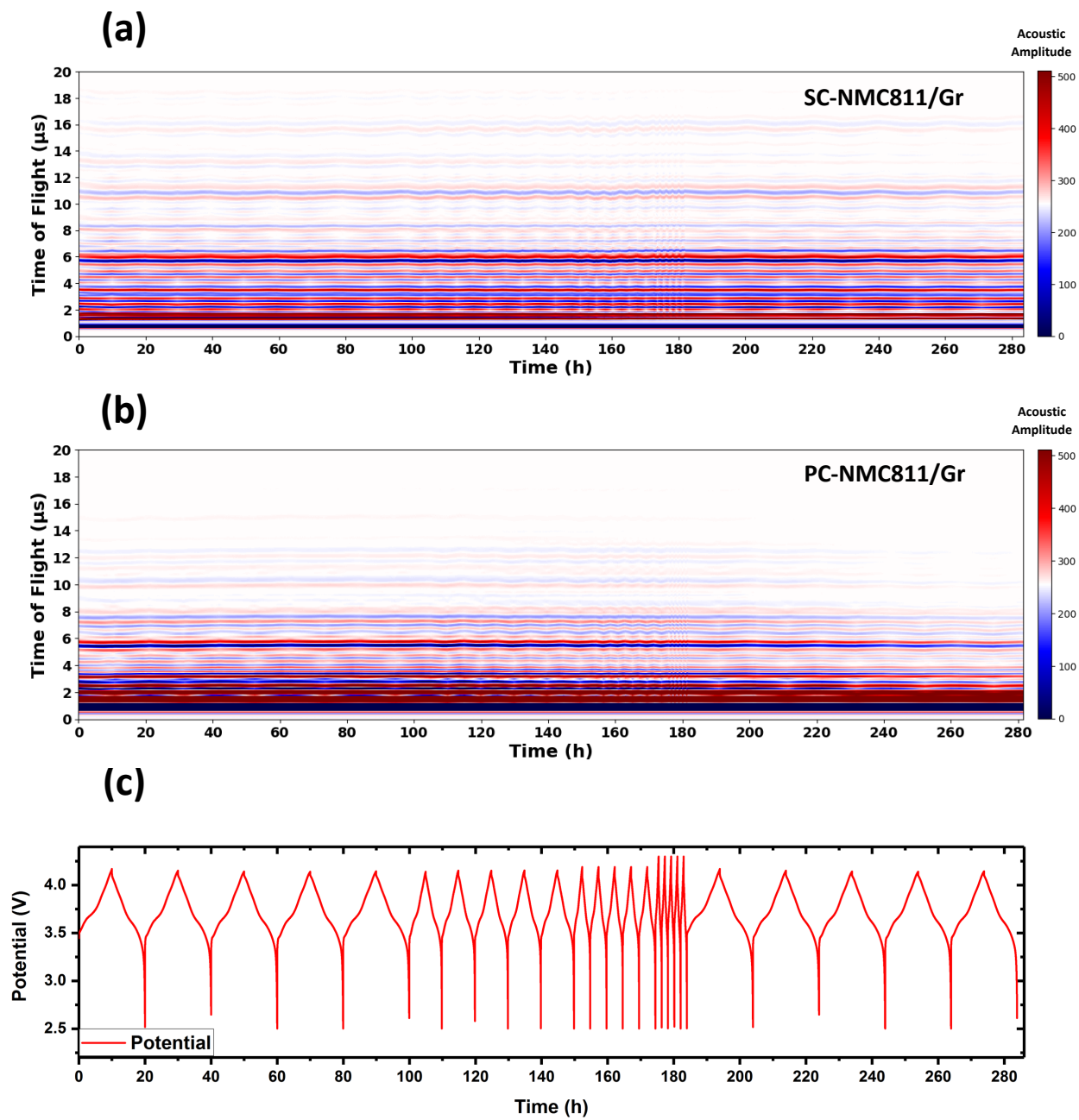
Figure 80 a-c: *EA-ToF spectrograms plotted with respect to time for the SC-NMC811/Gr cell (a) and the PC-NMC811/Gr cell (b) during the C-rate dependency test. The potential profile (c).*

(d)

(e)   **(f)**
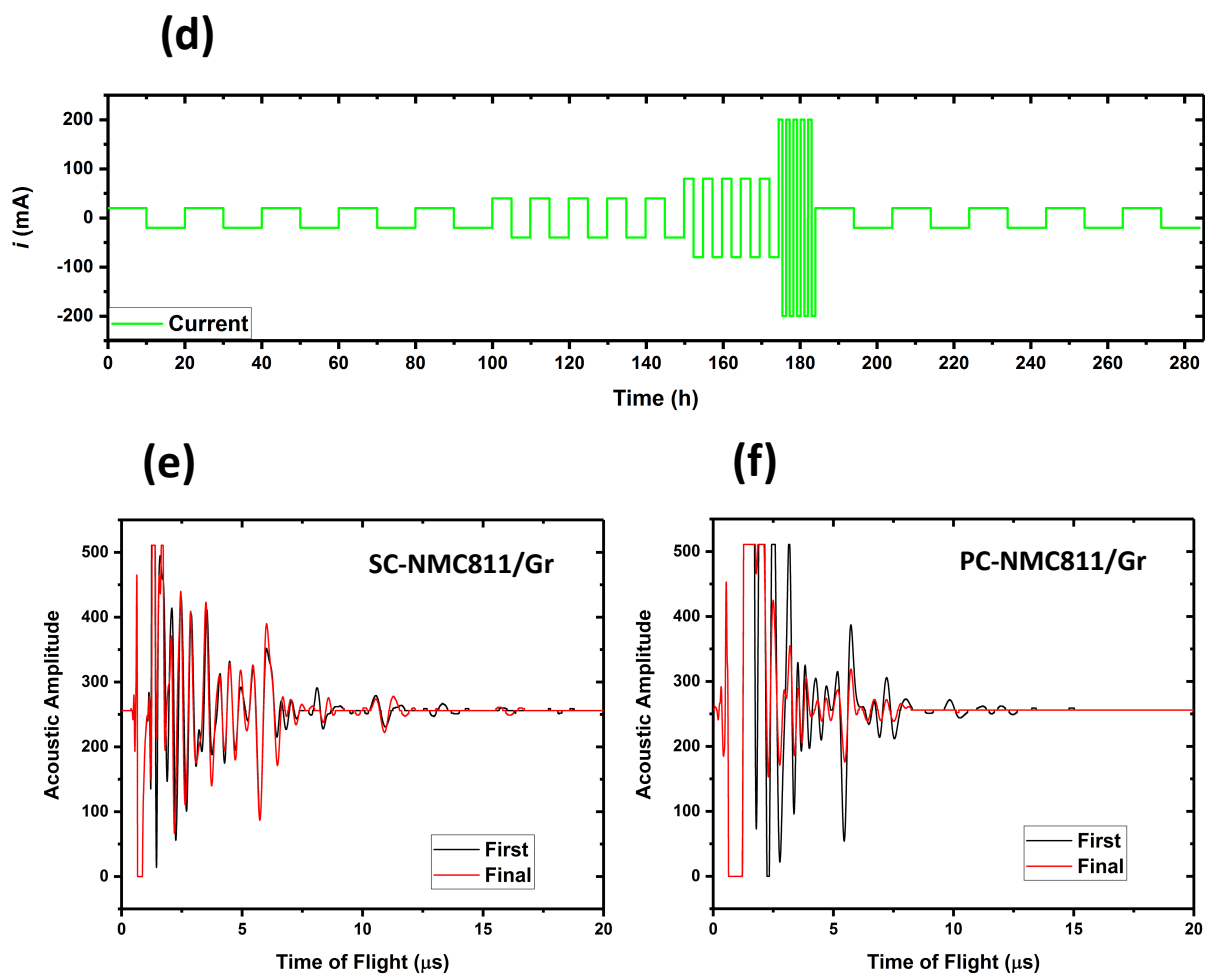
Figure 81 d-f: *(d) Current profile plotted with respect to time for the SC-NMC811/Gr cell and the PC-NMC811/Gr cell during the C-rate dependency test. First and final acoustic waveforms received by the ultrasonic flaw detector for the (e) SC-NMC811/Gr cell and (f) PC-NMC811/Gr cell.*

Lower signal attenuation is present in the EA-ToF spectrogram of the SC-NMC811/Gr cell during the C-rate dependency test than during formation (Figure 80). EA-ToF signals are more distinct for each active layer in the SC-NMC811/Gr cells. This suggests that most gas formation occurred during the initial SEI formation cycle and that a stable SEI layer had been formed before these experiments. It also confirms that gases formed during the formation cycle were effectively evacuated by the cells' degassing after formation, and before conducting the C-rate dependency test. Nonetheless, there are stark

differences between the EA-ToF spectrograms of the SC-NMC811/Gr cell and the PC-NMC811/Gr cell. The acoustic amplitude of the active layers reduces significantly after cycling at 1C in the EA-ToF spectrogram of the PC-NMC811/Gr cell, indicating the formation of gas during the C-rate dependency test in the PC-NMC811/Gr, even after the initial formation cycle was completed.

A significant difference is shown in acoustic amplitude in the peaks between the first and final waveform for the PC-NMC811/Gr cell. More gas may have formed in the PC-NMC811/Gr cell due to higher oxygen release from the PC-NMC811 particles or further electrolyte decomposition [310]. There are large differences in amplitude of acoustic signals for each active layer between the SC-NMC811/Gr and PC-NMC811/Gr cell. This can occur due to the difference in morphology of the electrode compositions, in particular due to electrode density and Young's modulus. Differences in acoustic intensity measured at active layer interfaces arise from differences in the physical properties of the materials at those interfaces [238]. Although the bulk moduli of the anode and cathode change during cycling, the anode composition is the same in both cells and therefore differences in amplitude are considered to be primarily attributed to differences in the cathode layer. Higher amplitude EA-ToF signals are present in the EA-ToF spectrogram for the SC-NMC811/Gr cell compared to the PC-NMC811/Gr cell. This demonstrates the capability of using EA-ToF spectroscopy to identify differences in cells that vary only in the morphology of the cathode. The difference in morphology between SC-NMC811 electrodes and PC-NMC811 electrodes can have direct consequences on the EA-ToF measurements of the NMC811/Gr cells.

The PC-NMC811/Gr cell showed more attenuation than the SC-NMC811/Gr during cycling and displayed lower acoustic amplitude peaks corresponding to the active layers that are also present in the SC-NMC811/Gr cell. It is expected that the SC-NMC811 electrodes will have a higher Young's modulus than PC-

NMC811 electrodes owing to the smaller interstitial distances between particle grains in the SC-NMC811 electrode, which should result in an overall stiffer electrode with higher signal reflectance and therefore higher acoustic amplitude recordings. It is also possible that PC-NMC811 particles themselves have a lower Young's modulus than SC-NMC811 particles due to SC-NMC811 particles having larger grains compared to smaller, more loosely bound agglomerated grains in the PC-NMC811 particle.

7.4.4. Electrochemical characterisation

Figure 80a indicates that the SC-NMC811/Gr cell underwent minimal capacity loss during the C-rate dependency test. Its highest capacity (225 mAh) was achieved at the slowest C-rate (C/10) and its capacity decreased with increasing current rate, until the lowest capacity (182 mAh) was recorded during the highest C-rate (1C), as would be expected for CC cycling. The capacity falls by 8 mAh between the applied C/10 and C/5 C-rates and then falls by 10 mAh between C/5 and C/2.5. The largest capacity drop occurs between C/2.5 and 1C of ca. 20 mAh. Capacities around of 225 mAh are retained when returned to initial C-rate (C/10). According to Figure 80d, the highest dQ/dV peak occurs for the slowest charge/discharge cycle (C/10). The height of this peak is similar for all subsequent C-rates including for the cycle that returns to C/10. The dQ/dV curve at 1C is significantly more shifted to higher voltages than the dQ/dV curves for the other C-rates. Charging at increasing C-rates produces the same information, as evidenced by the same shape of the dQ/dV curve; however, the IR-drop is higher at faster C-rates and thus the peak positions appear more shifted [339]. Shifting of dQ/dV curves is also evidence of capacity fade, which agrees with the fall in capacity shown in Figure 80b. However, the cell voltage is largely determined by the cathode potential, as opposed to the anode potential. This presents a drawback in using a dQ/dV plot for full cell systems because peaks are caused by changes in the overall cell voltage, which is the difference between the anode and cathode potentials. Therefore, processes that occur at the anode are more difficult to discern [340] [341].
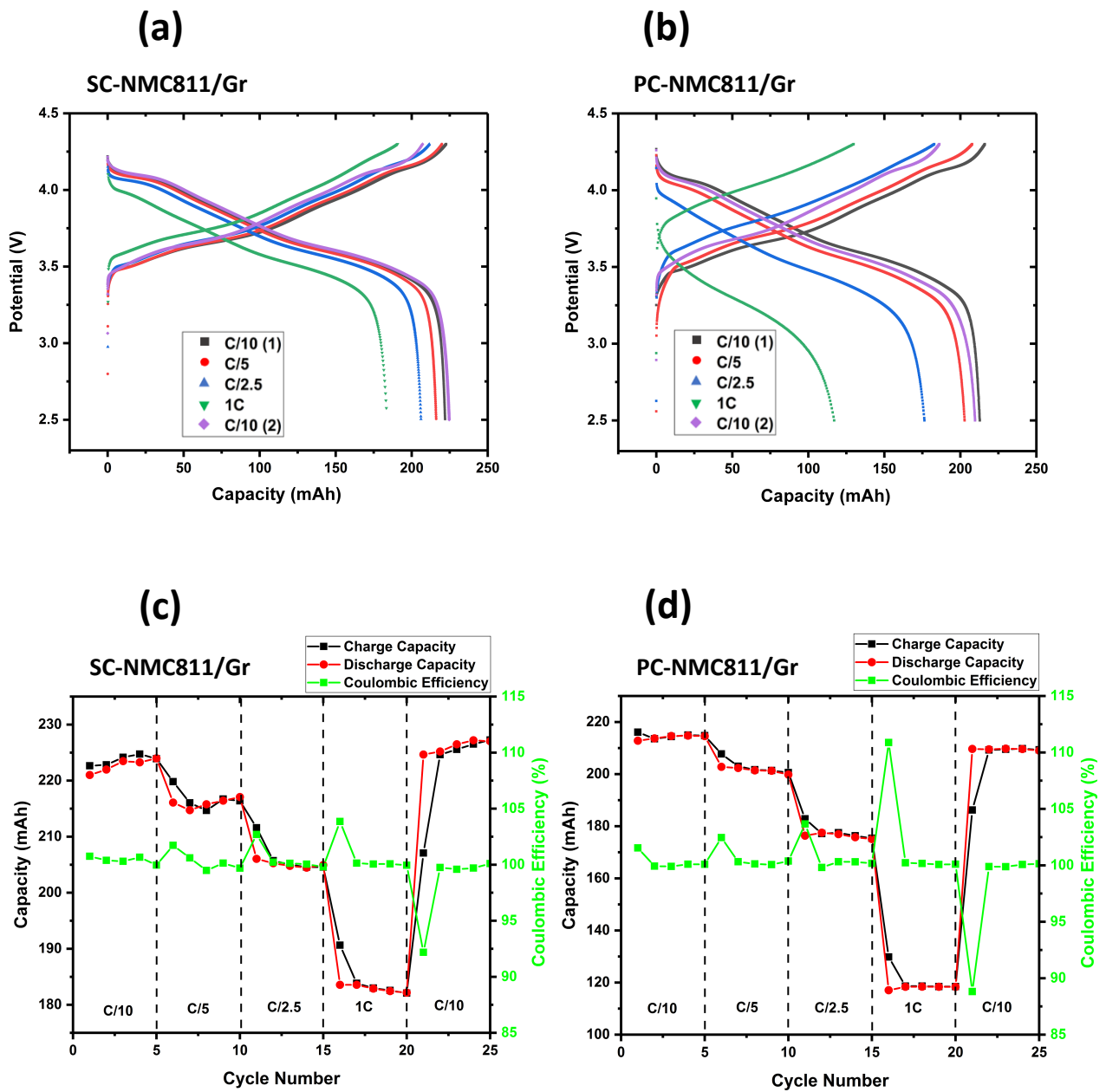
Figure 82 a-d: *Electrochemical characterisation for each cell during the C-rate dependency testing: Potential vs capacity plot at each C-rate for the SC-NMC811/Gr cell (a) and PC-NMC811/Gr cell (b), Charge, discharge capacity and coulombic efficiency vs cycle number for all C-rates for the SC-NMC811/Gr cell (c) and the PC-NMC811/Gr cell (d)*

(e)

SC-NMC811/Gr

(f)
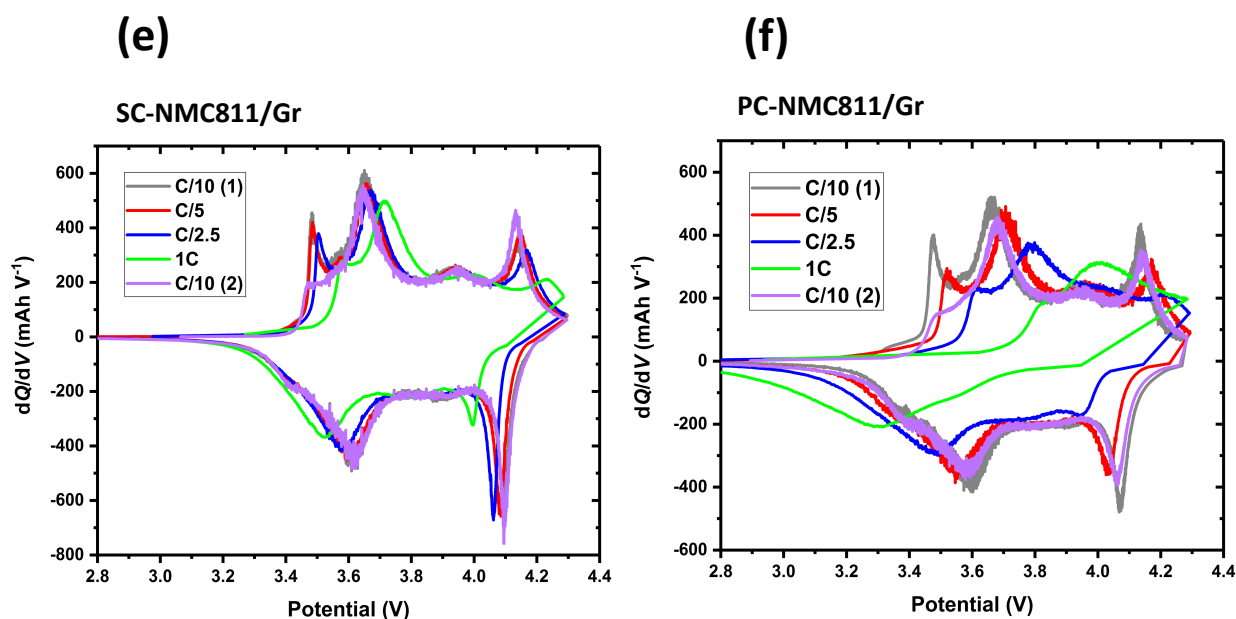
PC-NMC811/Gr

Figure 83 e-f: *Differential capacity vs cell potential curves for the first cycle at each C-rate for the SC-NMC811/Gr cell (e) and PC-NMC811/Gr cell (f).*

More capacity fading occurs in PC-NMC811/Gr cells compared to SC-NMC811/Gr cells as C-rate is increased (Figure 80c and Figure 80d). Decreases in capacity occur with every increase in the current rate, with capacity falling as low as 118 mAh during 1C (46% capacity drop from C/10). However, 96% of the initial capacity appears to be retained when the cell is cycled again at C/10 with capacities around 210 mAh being recorded. Capacity fading is usually indicative of cell degradation processes. However, no changes in the acoustic amplitude of the active layers are recorded when the cells are cycled at different C-rates, suggesting there is no severe cell degradation. In fact, the acoustic amplitude measured for each respective electrode layer remains fairly consistent throughout cycling in the NMC811/Gr cells. Measured amplitude is governed by physical changes in the electrode interfaces and intrinsic physical properties. Therefore, it is likely that the different microstructural properties of the SC-NMC811 and PC-NMC811 cathodes cause different degrees of cell polarisation in the tested cells and therefore ionic resistance. The PC-NMC811/Gr cells

appear to have higher polarisation than the SC-NMC811/Gr cell as lower capacities are measured at higher C-rates for the PC-NMC811/Gr cell. The fact that both cells retain their capacity when returned to slower C-rates also suggests that no deleterious degradation processes are incurred due to higher C-rate cycling for the relatively low number of cycles conducted (and modest C-rates) in this experiment. In addition, vast changes in the morphology are not expected to occur after only 20 cycles. It should be noted that the manufacturer recommends a maximum C-rate of C/3 for these cells, based on the high loading of the electrodes; 1C would appear to be excessive for the cells, particularly the PC-NMC811/Gr cell.

Upon cycling, the differential capacity for all cells revealed a significant peak shift related to phase transformation towards higher voltage for the process of delithiation and towards lower voltage for lithiation (Figure 80e and Figure 80f). Xia et al. found that the degree of cracking in NMC811 particles is positively correlated with the charging/discharging rate using nano resolution X-ray CT [301] [342]. PC-NMC811 electrodes are prone to more cracking than SC-NMC811 electrodes and the random orientation of the crystal grains within the PC secondary particles causes inter-primary-cracking. Primary particles are often assumed to be single crystals but are much smaller than the single crystals in the SC-NMC811 material so have a higher surface area/volume ratio. Each time a polycrystalline particle cracks it exposes more surface allowing side reactions and capacity loss, as well as potentially electrically disconnecting the particles from the system increasing impedance and creating barriers for lithium diffusion within the solid state of the agglomerate [84].

7.4.5. ToF shift measurements of a SC-NMC811/Gr cell and a PC-NMC811/Gr Cell

According to Eq. 3.5, ToF is determined by the path length travelled of the acoustic signal, Young's modulus, and density of material interfaces the signal passes through. During operation, a LiB undergoes changes in these physical properties and in turn altering the acoustic signal ToF. The 1-dimensional displacement of a material interface causes the acoustic signal to pass through the material at a different time during its flight, causing an apparent ToF shift. A negative ToF shift means the acoustic signal travels faster through the cell i.e., a shorter duration of time elapses before the acoustic signal encounters the material interface in question. A positive ToF shift means the acoustic signal takes longer to travel through the cell. This method can be used to track changes in density and Young's modulus during cycling [57].
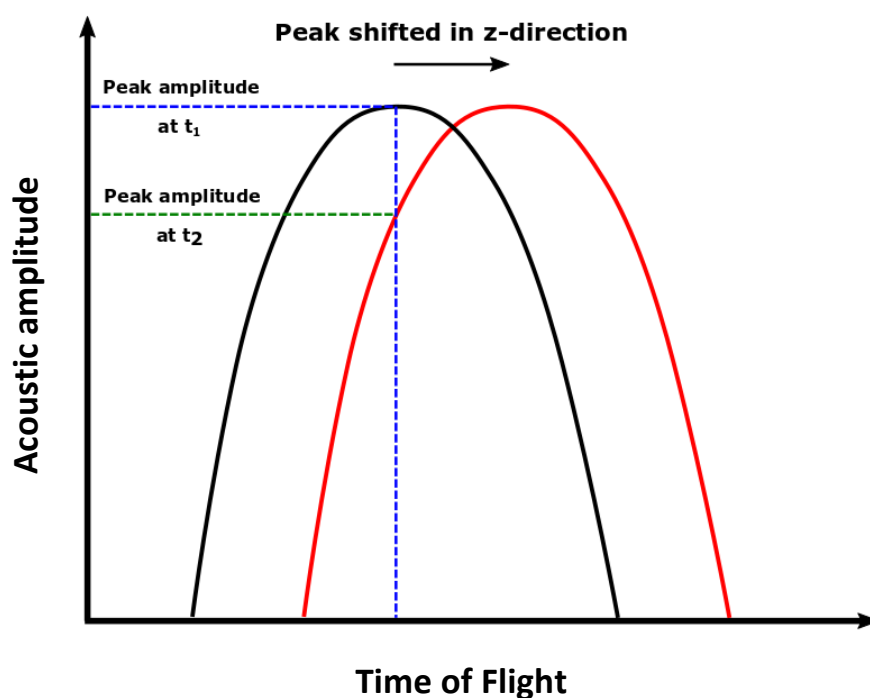
Figure 84: *Illustration of how a peak is shifted in the z-direction during EA-ToF spectroscopy towards higher ToF values.*

Figure **84** shows that both phenomena cause a change in measured amplitude due to the material interface physically moving in z-direction. When the material properties remain constant, a positive ToF shift can correspond to cell expansion, as a thicker cell would ultimately lead to a greater distance through which the ultrasonic wave has to travel. Conversely, a negative ToF shift can be attributed to cell contraction [57] [152] [235]. Figure 85 shows the ToF shift recorded for the third echo peak of the SC-NMC811/Gr cell and PC-NMC811/Gr cell during the C-rate dependency test and the associated exterior cell temperature profiles. ToF shift is normalised to zero at the start of charge/discharge cycling. The third echo peak was chosen because it is easily identifiable in the acoustic waveform for both SC-NMC811/Gr and PC-NMC811/Gr cells and has a high acoustic amplitude throughout cycling. The first and second echo peaks also have a high acoustic amplitude but have ToF values that are similar to the active layers in the cell, making it more difficult to isolate during data processing. Nonetheless, all echo peaks represent the signal that has travelled through the entire cell and is reflected back. Therefore, these echo peaks give the same information as each other about the cumulative properties of all the layers within the cell. Other peaks are related to reflections from active layers within the cell and thus will only show changes occurring in those respective layers before the reflection occurs from the back wall of the cell.
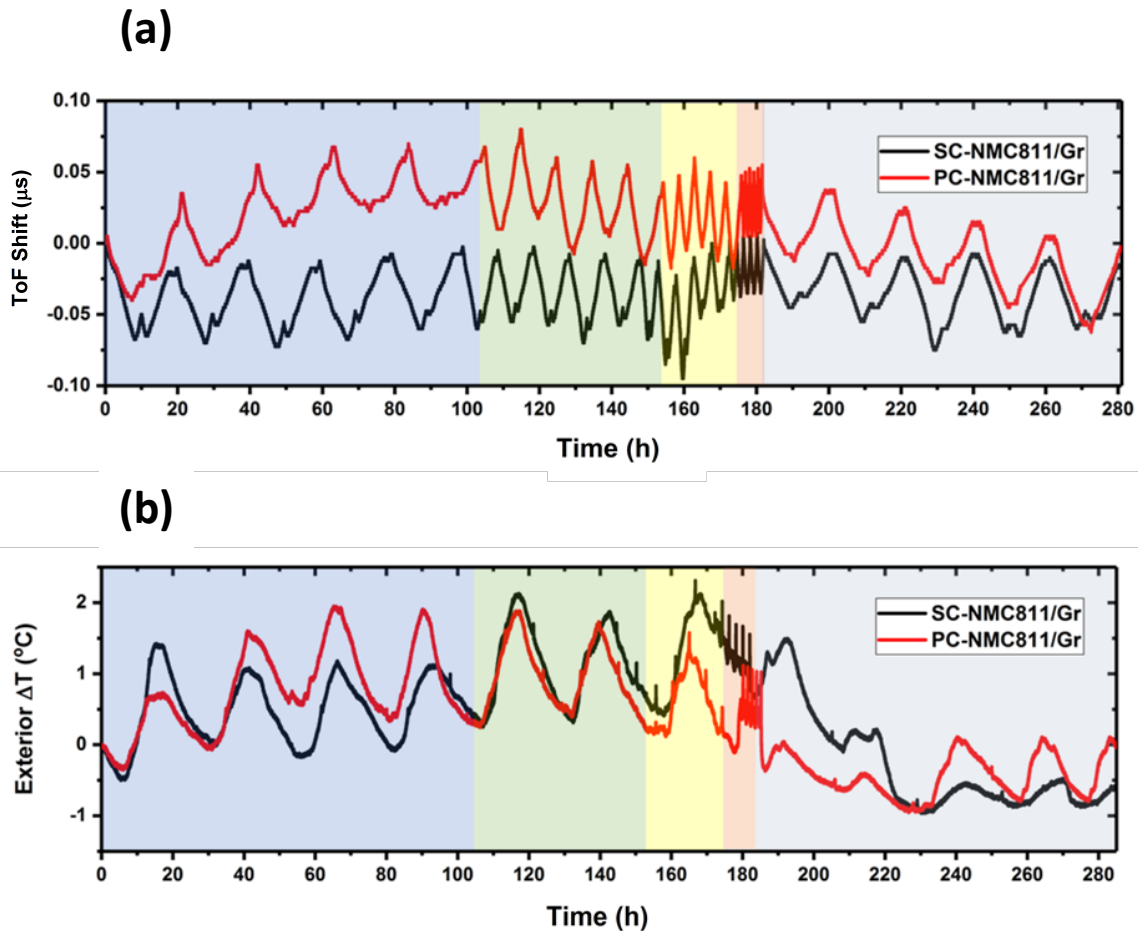
Figure 85: (a) ToF shift obtained at current rates of C/10, C/5, C/2.5 and 1C for the SC-NMC811/Gr (black) and PC-NMC811/Gr cell (red). (b) The change in exterior cell temperature (ΔT) during C-rate dependency testing for the SC-NMC811/Gr cell (black) and PC-NMC811/Gr cell (red). Shaded areas in each graph indicate each C-rate: C/10 (blue), C/5 (green), C/2.5 (yellow), 1C (red) and the second C/10 cycling stage (grey).

ToF shift and acoustic amplitude of peaks are highly influenced by thickness changes of the cell, as well as the interaction between material properties such as electrode density, Young's modulus and electrolyte viscosity, which can also impact ToF shift and acoustic amplitude, resulting in a complex decoupling process of the acoustic signal interaction with the cell [343] [344]. For instance, in Figure 85, during charging a negative ToF shift is observed; if ToF shift was solely attributed to thickness changes, a positive ToF shift would be expected during

the first charge at C/10, as lithiation of the graphite anode would cause these electrodes to get thicker. This trend in ToF shift during first charging is due to other material properties playing a confounding role on the ToF shift. Stage 1 corresponds to fully lithiated graphite (LiC_6 stoichiometry) which results in an increase in the Young's modulus of graphite which in turn causes a negative ToF shift according to Eq. 3.5 [152] [235]. In this case, graphite expands ~8% when charging, but the modulus changes by *ca.* ~300%, as such material property changes are dominant [63] [345]. NMC811 electrodes only undergo ~2% volume expansion [63] [55] [64]. This increase in Young's modulus of the graphite electrode increases wave propagation speed and ultimately causes a negative ToF shift. Similar results were reported in acoustic studies conducted by Bommier *et al.*[152], Ladpli *et al.*[162] and Knehr *et al.*[346]. Rong Xu *et al.* [347] reported that NMC electrodes undergo a decrease in Young's modulus and stiffness during lithium extraction from the layered crystalline particles due to Jahn-Teller distortion, depletion of electrostatic interactions of Li-O, and charge localization cumulatively weakening ionic transition metal-oxide bonding. To our knowledge, quantitative information on the Young's modulus of PC-NMC811 and SC-NMC811 electrodes has not yet been reported. During charging, lithium extraction and the accompanying decrease in Young's modulus of the NMC811 electrode occur during lithium intercalation of graphite and the associated increase in Young's modulus of the graphite electrode. Given that a negative ToF shift is recorded during charging, it is evident that changes in Young's modulus of the graphite electrode are larger than changes in the NMC811 electrode.

The PC-NMC811/Gr cell undergoes a positive ToF shift during C/10 cycling, as ToF shift increases above 0 µs and reaches nearly 0.08 µs after the first charge/discharge during C/5 cycling (see Figure 85a). Both cell capacity and ToF shift then decline with increasing C-rate over time [152]. These changes in ToF shift can arise from cumulative changes in stress and strain of the active layers of the cell during repeated cycling. The largest negative ToF shift occurs during the second C/10 cycling stage, as the cell cools despite PC-NMC811/Gr cell

capacity returning to 210 mAh which suggests cell cooling plays a confounding role in ToF shift patterns (see Figure 85b). As mentioned in Section 6.4.4, the PC-NMC811 electrodes has larger interstitial voids than the SC-NMC811 electrode. These interstitial voids can aid in rapid cooling of the PC-NMC811 electrode despite the higher overpotential and ohmic heating, which would explain why cell cooling is more evident in the PC-NMC811/Gr at faster C-rates and the second C/10 cycling stage than the SC-NMC811/Gr cell. It should be noted that although changes in ToF shift occur between cycles, the magnitude of these ToF shifts are very small which suggest that no severe cell degradation or damage have occurred throughout cycling.

The SC-NMC811/Gr cell is largely characterised by a negative ToF shift pattern throughout the entire C-rate dependency test with a maximum ToF shift of 0 µs at 1C. This is most apparent when a C/2.5 C-rate is applied with ToF shift reaching nearly -0.10 µs. The SC-NMC811/Gr cell stays relatively stable around a centre line (~ -0.04 µs ToF shift) whereas the PC-NMC811/Gr cell moves away from a stable ToF, potentially indicating expansion, fracture or dislocation of the reflective interfaces inside the PC-NMC811/Gr cell [125]. As both NMC811/Gr cells contain the same anode composition, the significantly positive ToF shift recorded for the PC-NMC811/Gr cell throughout cycling can be attributed to the PC-NMC811 electrodes. The ToF shift patterns for the SC-NMC811/Gr cell suggests that it undergoes less changes in stress and strain of the active layers between cycles compared to the PC-NMC811/Gr cell. The ToF shift pattern of the SC-NMC811/Gr cell then increases during 1C cycling towards 0 µs ToF shift. It is the general consensus that higher C-rate operation can lead to thermal expansion in LiBs [348] [349]. However, as this increase in ToF shift is not also recorded for the PC-NMC811/Gr cell during 1C operation, it is likely that this trend is attributed to other physical changes in the NMC811 electrodes. The most negative ToF shift value recorded (-0.10 µs) for the SC-NMC811/Gr cell is not correlated with the lowest cell temperature, implying that other physical properties influence the ToF shift pattern recorded for the SC-NMC811/Gr cell.

It has been reported that particles in a SC-NMC electrode undergo less cracking and reduced lattice strains compared to particles in a PC-NMC electrode during repeated cycling, resulting in a more ordered, higher density electrode [350] [351]. Increased electrode density, higher electrolyte viscosity, and reduced cell thickness would exacerbate a negative ToF shift as the cell is cooled [344] [352] [353].

ToF shift maxima do not correlate entirely with exterior cell temperature maxima at slower C-rates. This is expected given the ohmic heating of Li-ion cells during slower CC cycling (slower heating of the cell at slower C-rates), except for at 1C when the ohmic heating is high enough to heat up the cell. This means that the fluctuations/peaks and troughs of the ToF measurements at slower C-rates are more attributable to the ambient room temperature than the electrochemistry of the cell and subsequent changes in material properties.

After the C-rate dependency test, both cells return to their original ToF (i.e., 0 µs) suggesting there is no change in cell thickness after cycling and that the thickness changes that occur during cycling are reversible. The trend in ToF shift during each cycle is consistent throughout charge/discharge cycling with a negative ToF shift during graphite lithiation and positive ToF shift with graphite delithiation. There is no evidence of any further degradation mechanisms occurring during cycling that contribute to the ToF shift measurements of the cell at this length-scale. As expected, the intracycle trends in magnitude of ToF shift are similar for both NMC811/Gr cells given that intracycle ToF shift patterns are dominated by the graphite electrodes, present in both cells. Throughout charge/discharge cycling, the cell periodically expands and contracts as the graphite electrode undergoes lithium intercalation/deintercalation [64]. The cell could be said to periodically breathe with charge/discharge cycling. During these reversible processes, simultaneous changes in electrode stress and strain occur at the active layers and effect the

speed at which the signal passes through the active layers [354]. This demonstrates the usefulness of ToF shift measurements for gathering information on numerous physical changes that occur during cycling LiBs compared to devices such as push-piston dilatometers, thickness gauges and micrometers that are solely designed to measure cell thickness changes [355] [356]. However, the use of these devices in tandem with EA-ToF spectroscopy could be useful to discern which ToF measurements can be attributed to thickness changes of the cell, rather than other functional parameters such as Young's modulus and electrode density.

These two cell chemistries are composed of the same graphite electrode, but different NMC811 electrodes. The difference in ToF shift patterns between the SC-NMC811/Gr and PC-NMC811/Gr cells is therefore most likely to be due to the different physical properties of the NMC811 electrodes which directly cause a variation in the Young's modulus of these respective electrodes. However, there are numerous physical processes that can alter the cell's ToF shift, such as external temperature, cell gassing and material properties. The SC-NMC811 and PC-NMC811 electrodes also have different C-rate dependencies, so at a given C-rate the state of lithiation will be different in the two materials - this may also cause some differences in the ToF as the assumed SOC is different for a given point in the cycle. As the SC-NMC811 and PC-NMC811 electrodes have different Young's modulus and density, the acoustic signal will inevitably vary in its interaction with them (refer to Eqs. 4, 5 and 6). Difference in density and Young's modulus of these electrodes has a direct influence on the ToF shift.

7.5. Conclusion

For the first time known to the author, EA-ToF spectroscopy has successfully been used to distinguish between LiBs composed of either SC-NMC811 or PC-NMC811 electrodes. It has been demonstrated that the acoustic behaviour of LiBs is influenced by the morphology of the NMC811 electrodes, with the different particle sizes influencing density and Young's modulus of the cathode. Consequently, acoustic signals propagate through these respective materials with varying reflectance and transmission. Furthermore, differences in acoustic signal attenuation were recorded during formation cycling of the SC-NMC811/Gr and PC-NMC811/Gr cells which was attributed to gas evolution and SEI layer formation. EA-ToF spectrograms indicated that more gas formed throughout the formation cycle in the PC-NMC811/Gr than the SC-NMC811/Gr cell, despite the SC-NMC811/Gr cell having more gas formation at the beginning of first charging and both cells containing the same anode composition. This was likely attributed to additional electrolyte decomposition, new cathodic SEI layers formation, gas evolution and aggravated electrochemical resistance in the PC-NMC811 electrodes. Furthermore, differences in acoustic amplitude of the active layers were recorded for the PC-NMC811/Gr cell and SC-NMC811/Gr during the C-rate dependency test with gas formation present in the PC-NMC811/Gr cell during later cycles. Generally, a lower acoustic amplitude was detected for the majority of active layers in the PC-NMC811/Gr cell compared to the SC-NMC811/Gr cell which was attributed to differences in particle morphology of the NMC811 electrodes.

Finally, ToF shift patterns revealed differences between cells that vary in particle morphology of the NMC811 cathode. For instance, the PC-NMC811/Gr cell largely underwent positive ToF shifts during C-rate testing whilst the SC-NMC811/Gr cell predominately underwent negative ToF shift during cycling. Nonetheless, an interchanging positive/negative ToF shift was recorded between charge/discharge for the SC-NMC811/Gr cell and PC-NMC811/Gr cells

before both returned to their original ToF. Whilst there are numerous physical processes that can affect EA-ToF spectroscopy measurements, it is a powerful technique for measuring physical changes in ostensibly similar cells and using other techniques such as X-ray CT alongside EA-ToF spectroscopy can improve our understanding of cell architecture, and electrode morphology by revealing intrinsic physical attributes that can directly impact EA-ToF measurements.

Chapter 8

Conclusions and Future Perspectives

8.1. Conclusions and Summary

Improving LiB technology remains at the forefront of scientific research to achieve global electrification and replace non-renewable energy technologies. Battery properties that are a primary focus for improvement are durability and cycle life. The literature review in Chapter 2 showed that numerous degradation mechanisms contribute to reducing these properties. The work carried out in this thesis has focused primarily on specific degradation mechanisms of LiBs, such as volume changes and particle cracking during operation, at various length-scales that collectively hinder battery performance. However, as demonstrated by correlative X-ray CT and EA-ToF spectroscopy, a focus on any single degradation mechanism cannot be considered comprehensive as multiple degradation processes occur simultaneously. Therefore, imaging and characterisation techniques at multiple length-scales are used to understand which degradation processes may contribute to, or result in, dimensional changes of LiBs. In chapter 3, the working principles of different cell configurations and electrochemical techniques were discussed. The advantages of supplementing in-situ dilatometry with techniques such as SEM, X-ray CT and acoustic spectroscopy to provide a richer understanding of degradation processes in battery electrodes was explored.

In Chapter 4, the bulk thickness changes of commercially available graphite electrodes were recorded using *in-situ* ECD during multiple cycling protocols. These experiments provided an understanding of the magnitude of dilation/contraction that a commonly used LiB anode undergoes during cycling and how applying different cycling parameters, for example a CV step, affects the dimensional changes undergone by the electrode. As this chapter included the first works in this thesis using the three-electrode dilatometer cell, a knowledge of important considerations for good cell performance was established. The most notable consideration is the impact that a large separator has on the performance of a Li-ion cell at fast C-rate cycling protocols. Numerous features were recorded on the dilation profile of graphite electrodes during discharge/charge that were directly caused by phase transitions in graphite's crystal lattice structure. This demonstrated that direct effects caused by microstructural processes undergone in a graphite electrode can be detected when measuring the bulk dilation/contraction of the electrode.

In Chapter 5, ECD testing was also carried out using NMC811 electrodes, to identify that fast C-rates also present limitations when cycling different electrode materials. *In-situ* ECD testing of NMC811 electrodes confirmed that bulk thickness changes in a graphite electrode are significantly higher than the commonly paired cathode material, supporting the general consensus that the majority of thickness change undergone by an NMC811/Gr LiB is caused by the anode. These two materials are commonly paired together in LiBs that are manufactured and marketed today. Furthermore, a relatively featureless dilation profile was recorded for NMC811 electrodes in comparison to graphite electrodes, with a gradual expansion before a rapid contraction associated to the collapse of the c lattice parameter. Both dilation profiles for graphite and NMC811 electrodes were relatively symmetrical during discharge/charge and vice versa, demonstrating the reversibility of microstructural processes during a single cycle.

It would be beneficial in future research to explore the bulk thickness changes of these electrodes, when an alternative CE to lithium metal is used during dilatometric testing. The thickness changes may be affected by the material chosen as the counter electrode. A CE that better reflects real world LiB chemistries such as Si/graphite, or graphite electrodes could be paired with cathode chemistries such as NMC or NCA at the WE.

In Chapter 6, X-ray μCT was used to probe the interior architecture of NMC811/Gr LiBs and combined with X-ray nCT to characterise the individual NMC811 electrodes that varied in particle morphology. These techniques facilitated a multi-scale approach to understanding the cell microstructure and electrode morphology. From this, various geometrical parameters were quantified such as particle sphericity, surface area and particle size distribution to elucidate differences between the electrodes that can influence EA-ToF spectroscopy measurements. Most notably, polycrystalline NMC particles were larger and more spherical than single crystal NMC particles. These differences are hypothesised to have direct repercussions on the ensemble electrode's density and Young's modulus which affect EA-ToF measurements. X-ray CT is undoubtedly a powerful all-round technique that allows unmatched visual interpretation of LiBs. It is therefore unsurprising that it is being widely adopted as the chosen visual interrogation technique in conjunction with other diagnostic techniques, to provide a complete perspective of degradation events in LiBs.

In Chapter 7, EA-ToF spectroscopy was used to evaluate the physical changes of NMC811/Gr pouch cells. Numerous physical parameters, such as Young's modulus, electrode density and gas formation, influenced ToF shift differently. An understanding of how these physical factors influence acoustic signal propagation is required in order to interpret correctly the impacts on different physical properties. For instance, the Young's modulus of graphite electrodes

increased by 300% during charging, which caused ToF shift to decrease. Therefore, any ToF shift increases that occurred due to graphite expansion were masked by the effects of changes in Young's modulus during cell charging. By using X-ray CT to provide a visual diagnosis of the LiBs, findings from EA-ToF spectrometry were effectively assigned to different physical attributes of the LiB. In theory, X-ray CT could be used to corroborate physical changes that were identified using EA-ToF spectroscopy, such as gas formation and thermal expansion. However, using X-ray CT over long time-periods during prolonged cycling is extremely expensive. Hence, this study demonstrates how different experimental techniques can be combined based on their features to effectively measure certain properties of a LiB.

In the following section, a future perspective will be provided on the outlook for ECD and acoustic analysis of LiBs. Future work for these techniques will be suggested based on current literature. The experiments carried out in this thesis can augment understanding of bulk thickness changes of LiBs applied to real-life applications.

8.2. Future Perspectives

8.2.1. ECD measurements at various external temperatures

LiBs in modules and battery packs often have to perform at different external temperatures. For instance, battery packs in an EV are exposed to various external temperatures throughout the year [357]. In the USA, cell temperatures can commonly reach below -5 °C in the winter and high above 35 °C in the summer [358] [359]. The optimum temperature range of a LiB is between 35 - 40 °C for maintaining battery health. The temperature of a LiB should not exceed 50 °C because this can accelerate degradation [360]. In laboratory studies,

external temperatures can be altered during ECD testing to improve understanding of how external temperature affects the bulk thickness changes undergone by LiB electrodes during charging. Findings from ECD measurements can demonstrate the degradative bulk thickness changes that can occur in LiB systems in EVs.

8.2.2. Integrating ECD devices into real-world applications

ECD is well suited for laboratory applications, but less suited to real-world applications since the integration of a dilatometer in a battery system is difficult and potentially destructive. Strain gauges measure volume expansion and show more promise for real-world application, given that they have been used in a laboratory setting to evaluate a matrix of cylindrical LiBs on battery ageing during operation [168] [361]. These devices measure volume changes between 3 - 10 % for cylindrical LiBs [168]. The most desirable attribute of ECD devices which sets them apart from other techniques, is that they can often measure bulk volume changes of single electrodes at a very fine spatial resolution whilst mitigating gas evolution effects. Whilst strain gauges are more suited to real-world devices, they cannot provide the spatial resolution that ECD devices can, because they cannot mitigate gas evolution effects and are not currently capable of measuring volume changes of single electrodes.

In order for an ECD device to be compatible with cell modules and battery packs, each ECD device would need to be designed to measure bulk volume changes of the whole cylindrical LiBs (Figure 86). In addition, this device would ideally be compatible with the onboard battery management system or a data logging system that stores volume change recordings. Furthermore, the ECD device would have to be designed in a way that it does not obstruct neighbouring LiBs in the ensemble battery pack and does not compromise the electrical conductivity of the system, for instance, by contributing any further

impedance or electrical resistance to the entire LiB system. Furthermore, if used in an EV, the ECD system would have to be lightweight, as any significant increases in the weight of the EV would require more power to operate it. Undoubtedly, the major challenges in realising this would be the size and location of the ECD device with respect to each LiB. It is likely that dimensional change measurements would take place on the longer sides of the cylindrical Li-ion cells. This would necessitate an increased distance between each cylindrical cell to allow for ECD devices to be fitted between them. This would also result in more extensive electrical wiring between each Li-ion cell to connect the ECD device to any data logging system.
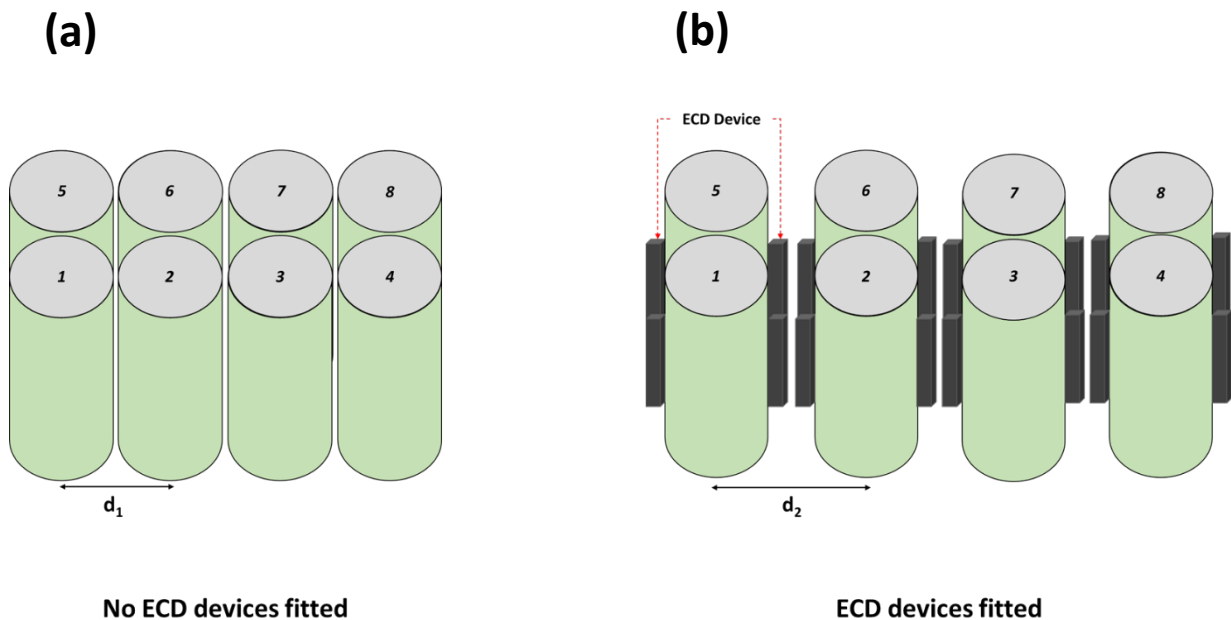
Figure 86: A schematic illustrations of two battery packs composed of 8 equidistant cylindrical LiBs. The first battery pack (a) contains no ECD devices, and the second battery pack (b) contains an ECD device for each cylindrical cell. The distance (d_2) between the centre of two cylindrical cells in the second battery pack (b) is significantly larger than the distance (d_1) between the centre of two cylindrical cells in the first battery pack (a).

8.2.3. ECD measurements during fast charging

Most dilatometric studies reviewed in this work investigate thickness variations during Li-ion cell cycling with moderately slow C-rates. There is a lack of dilatometric studies at high C-rates, or on ageing, safety, and abusive conditions apart from lithium plating. Addressing this noticeable gap in the literature would provide valuable information about the performance of batteries under more realistic cycling and ageing regimes. This is likely to be associated with limitations in design in the current state-of-the-art commercial push-piston dilatometers and challenges with in-house constructed dilatometers. As was found in this thesis, the large bespoke separator of the ECD instrument caused mass transfer limitations and therefore the dilatometer cell did not perform in accordance with experimental capacities measured using coin-cells. Therefore, moderate C-rates were used in this thesis to ensure optimum cell performance. Future ECD devices should feature a smaller separator to resemble those used in LiB devices, and to avoid severe mass transfer limitations. X-ray CT does not have this limitation and thus can be used to evaluate LiB dimensional changes, as well as cell failure, at extreme conditions [125]. However, conducting long-term X-ray CT experiments is extremely expensive.

8.2.4. Acoustic interrogation of cell modules and battery packs

Currently, there is limited evidence in literature of acoustic interrogation of LiB modules and packs. Most published reports are focused on understanding acoustic signal interactions with a single LiB [152] [57] [362]. In real life application, LiBs tend to be integrated into battery modules and packs, housing numerous LiBs to increase power output in a range of devices such as EVs and grid-scale energy storage systems. Therefore, it is imperative to improve understanding of how acoustic spectroscopy can be used to examine systems housing numerous adjacent LiBs.

Acoustic studies of single LiBs have been carried out in laboratory practices for monitoring gas formation, SoC and SoH [57]. Acoustic interrogation is also a tool capable of detecting battery off-gassing prior to thermal runaway [125]. Therefore, its potential to be applied to real-world battery systems to make them safer, by detecting the onset of thermal runaway, is appealing. Currently, laboratory studies mostly use piezoelectric transducers as ultrasound flaw detectors, as used in this work [362] [153]. However, this apparatus may be more suited to laboratory practice as opposed to real-life application, due to the size and number of necessary transducers for acoustic monitoring and data logging of battery packs. These factors could pose engineering challenges on battery pack integration.

Devices that have the potential to carry out acoustic monitoring of LiB modules and packs are fibre optic sensors. Zhang *et al*. [363] demonstrated the possibility of using fibre optic sensors to detect acoustic emission of Li-ion cells [364]. These sensors can achieve an enhanced signal-to-noise ratio when compared to piezoelectric transducers commonly used for EA-ToF spectroscopy measurements [365]. However, research on using fibre optic sensors as a means for acoustic analysis of Li-ion cells is limited. Currently, fibre optic sensors are used to measure battery parameters, such as SoC and cell temperature, in various battery packs with battery management systems.

8.2.5. EA-ToF spectroscopy measurements of different Li-ion cell configurations

This work has demonstrated that acoustic signals can vary according to minor physical differences between LiBs. Acoustic interrogation of LiBs can become even more complicated by cell-type i.e., coin, cylindrical or pouch cell configuration. In the case of cylindrical LiBs, mathematical modelling would be

required to account for angular reflections at every active layer, including the cell casing, with more physical factors complicating the acoustic signals than for pouch cells. These complications may be a reason why cylindrical cells are rarely investigated using EA-ToF spectroscopy (Figure 87). However, given that LiBs used in EVs are commonly cylindrical, there is potential for useful information on this cell architecture [366].
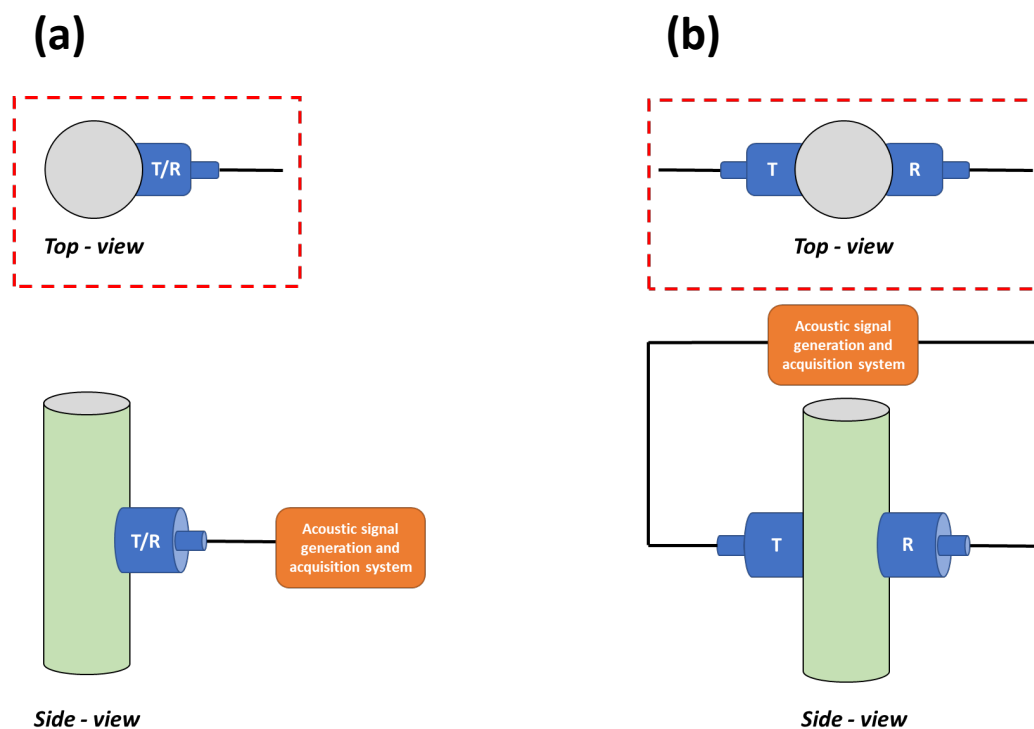
Figure 87: *Schematic illustrations of two EA-ToF spectroscopy experimental design with a single cylindrical cell (green) that has a piezoelectric transducer/receiver (T/R) (a) and an individual piezoelectric transducer (T) and receiver (R) (b), connected to an acoustic signal generation and acquisition system.*

Another consideration that has to be made for EA-ToF spectroscopy of cylindrical LiBs is the acoustic transducer device that is used. For instance, if a flat-faced acoustic transducer is employed, an uneven distance between transducer and cell occurs across the transducer-cell interface. This transducer

is widely commercially available and is the chosen transducer for many EA-ToF spectroscopy studies. However, R&D should be focussed on designing an acoustic transducer to facilitate accurate acoustic measurements of cylindrical cells. For instance, a single acoustic transducer placed on the surface of a cylindrical cell may have a concave design that curves around the exterior of the cell, so that an equal distance between the cell and transducer is maintained across the length of the transducer-cell interface. This would mitigate acoustic signal propagation artefacts caused by variations in distance between the acoustic transducer and cylindrical cell casing.

8.3 General Outlook

Further adoption of LiBs looks likely in the short term, particularly in the transport sector, as this is critical to efforts to achieve carbon neutrality and sustainability. With more LiBs adopted in real-life applications, it is inevitable that there will be more opportunities to couple diagnostic techniques with these devices. Findings from these diagnostic devices will be crucial for optimising battery performance and ultimately achieving climate targets.

The future landscape of battery diagnostics could feature passive, non-destructive fibre optic and acoustic sensing devices being coupled together to measure battery performance [367]. This thesis has demonstrated the synergy of using visualisation techniques such as X-ray CT imaging with acoustic techniques, demonstrating the potential to optimise a technique for battery diagnostics that features both acoustic and visual measurements, a so called "photoacoustic" diagnosis. The optical attributes together with the acoustic features of the technique would provide a detailed perspective on battery properties and be able to detect physical changes such as deleterious volume changes during operation.

8.4. Dissemination

The work discussed in this thesis has been disseminated in the form of research articles and presentations at both national and international conferences. A list of publications focused on gaining new insights into the degradation and failure of Li-ion batteries are presented below.

First Author Publications

- Michael, H. *et al.* A Dilatometric Study of Graphite Electrodes during Cycling with X-ray Computed Tomography. *J. Electrochem. Soc.* **168**, 010507 (2021).

- Michael, H., Jervis, R., Brett, D. J. L. & Shearing, P. R. Developments in Dilatometry for Characterisation of Electrochemical Devices. *Batter. Supercaps* 1–20 (2021).

- Michael, H. *et al.* Correlative Electrochemical Acoustic Time-of-Flight Spectroscopy and X-ray Imaging to Monitor the Performance of Single-Crystal and Polycrystalline NMC811/Gr Lithium-Ion Batteries. *J. Power Sources.* **542**, 231775 (2022).

Other Publications

- Sharp *et al*. Thermal Runaway of Li-Ion Cells: How Internal Dynamics, Mass Ejection, and Heat Vary with Cell Geometry and Abuse Type. *J. Electrochem. Soc. Accepted Manuscript.*
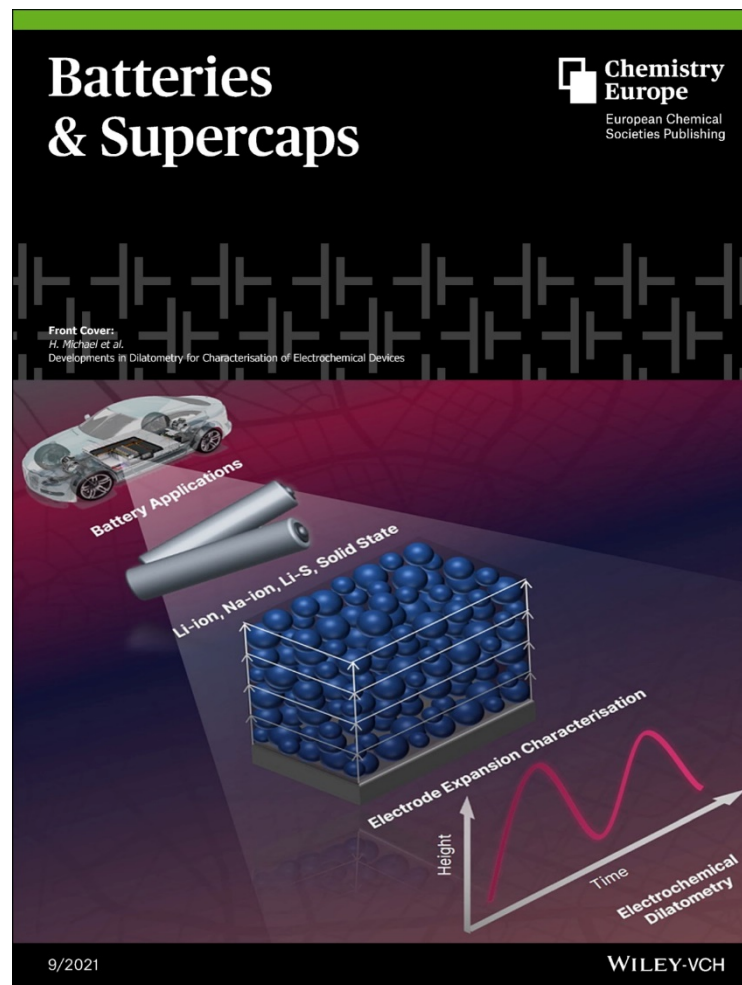
Figure 88: Journal cover published by the author

Technical presentations

- ECS Meeting, 2020. *Title: A Dilatometric Study of Graphite Electrodes during Cycling with X-ray Computed Tomography.*

- STFC Batteries conference, 2019. *Title: A Dilatometric Study of Li-ion Battery Electrodes during Cycling with X-ray Computed Tomography.*

- LEMD conference, University College London, 2019. *Title: A Dilatometric Study of Graphite Electrodes during Cycling with X-ray Computed Tomography.*

- Electrochem conference, University of Strathclyde, 2019. *Title: A Dilatometric Study of Graphite Electrodes during Cycling with X-ray Computed Tomography.*

- MRS Spring Meeting & Exhibit, Honolulu, 2022. *Title: Correlative Electrochemical Acoustic Time-of-Flight Spectroscopy and X-ray Imaging to Monitor the Performance of Single-Crystal and Polycrystalline NMC811/Gr Lithium-Ion Batteries.*

INTENTIONALLY BLANK

References

[1]   J. Rogelj, M. Den Elzen, N. Höhne, T. Fransen, H. Fekete, H. Winkler, R. Schaeffer, F. Sha, K. Riahi, M. Meinshausen, *Nature* **2016**, *534*, 631–639.

[2]   S. Yoda, K. Ishihara, *J. Power Sources* **1997**, *68*, 3–7.

[3]   H. Lund, W. Kempton, *Energy Policy* **2008**, *36*, 3578–3587.

[4]   T. Kåberger, *Glob. Energy Interconnect.* **2018**, *1*, 48–52.

[5]   D. D. Sarma, A. K. Shukla, *ACS Energy Lett.* **2018**, *3*, 2841–2845.

[6]   Y. Nishi, *J. Power Sources* **2001**, *100*, 101–106.

[7]   D. Di Lecce, R. Verrelli, J. Hassoun, *Green Chem.* **2017**, *19*, 3442–3467.

[8]   A. Yoshino, *Angew. Chemie - Int. Ed.* **2012**, *51*, 5798–5800.

[9]   K. J. Stevenson, *J. Solid State Electrochem.* **2012**, *16*, 2017–2018.

[10]   T. E. Society, **2016**.

[11]   C. S. Johnson, S. D. Korte, J. T. Vaughey, M. M. Thackeray, T. E. Bofinger, Y. Shao-Horn, S. A. Hackney, *J. Power Sources* **1999**, *81–82*, 491–495.

[12]   F. C. Godoi, S. Prakash, B. R. Bhandari, *Rev. 3D Print. potential red meat Appl.* **2021**, 1–61.

[13]   J. Frazelle, *Commun. ACM* **2021**, *64*, 52–59.

[14]   S. Megahed, W. Ebner, *J. Power Sources* **1995**, *54*, 155–162.

[15]   H. Löbberding, S. Wessel, C. Offermanns, M. Kehrer, J. Rother, H. Heimes, A. Kampker, *World Electr. Veh. J.* **2020**, *11*, 1–15.

[16]   K. Chayambuka, G. Mulder, D. L. Danilov, P. H. L. Notten, *Adv. Energy Mater.* **2020**, *10*, DOI 10.1002/aenm.202001310.

[17]   F. Duffner, N. Kronemeyer, J. Tübke, J. Leker, M. Winter, R. Schmuch, *Nat. Energy* **2021**, *6*, 123–134.

[18]   D. Linden, T. B. Reddy, *HANDBOOK OF BATTERIES*, **n.d.**

[19]   Y. Mekonnen, A. Sundararajan, A. I. Sarwat, *Conf. Proc. - IEEE SOUTHEASTCON* **2016**, *2016-July*, 2–7.

[20]   D. Bresser, J. Asenbauer, M. Kuenzel, T. Eisenmann, A. Birrozzi, J. K. Chang, S. Passerini, *J. Phys. Chem. Lett.* **2020**, *11*, 8238–8245.

[21]   W. Zhao, J. Yi, P. He, H. Zhou, *Electrochem. Energy Rev.* **2019**, *2*, 574–605.

[22]   K. Xu, *Chem. Rev.* **2004**, *104*, 4303–4417.

[23]   M. Park, X. Zhang, M. Chung, G. B. Less, A. M. Sastry, *J. Power Sources* **2010**, *195*, 7904–7929.

[24]   S. Goriparti, E. Miele, F. De Angelis, E. Di Fabrizio, R. Proietti Zaccaria, C. Capiglia, *J. Power Sources* **2014**, *257*, 421–443.

[25]   X. Xiao, W. Zhou, Y. Kim, I. Ryu, M. Gu, C. Wang, G. Liu, Z. Liu, H. Gao, *Adv. Funct. Mater.* **2015**, *25*, 1426–1433.

[26]   D. J. Pereira, J. W. Weidner, T. R. Garrick, *J. Electrochem. Soc.* **2019**, *166*, A1251–A1256.

[27]   X. Song, K. Kinoshita, *J. Electrochem. Soc.* **1995**, *142*, 3297–3302.

[28]   T. Tran, K. Kinoshita, *J. Electroanal. Chem.* **1995**, *386*, 221–224.

[29]   L. Zhang, C. Chen, *Prog. Chem.* **2011**, *23*, 275–283.

[30]   J. S. Gnanaraj, Y. S. Cohen, M. D. Levi, D. Aurbach, *J. Electroanal. Chem.* **2001**, *516*, 89–102.

[31]   N. Takami, *J. Electrochem. Soc.* **1995**, *142*, 371.

[32]   S. Flandrois, B. Simon, *Carbon N. Y.* **1999**, *37*, 165–180.

[33]   X. Y. Song, K. Kinoshita, *J. Electrochem. Soc.* **1996**, *143*, L120–L123.

[34] G. V Zhuang, P. N. Ross, A. Augustsson, M. Herstedt, K. Edstro, J. Nordgren, A. L. Source, L. Berkeley, M. S. Division, L. Berkeley, *Phys. Chem. Chem. Phys.* **2004**, *6*, 4185–4189.

[35] T. Ohzuku, N. Matoba, K. Sawai, *J. Power Sources* **2001**, *97–98*, 73–77.

[36] J. Asenbauer, T. Eisenmann, M. Kuenzel, A. Kazzazi, Z. Chen, D. Bresser, *Sustain. Energy Fuels* **2020**, *4*, 5387–5416.

[37] A. Mukhopadhyay, B. W. Sheldon, *Prog. Mater. Sci.* **2014**, *63*, 58–116.

[38] A. Ito, K. Shoda, Y. Sato, M. Hatano, H. Horie, Y. Ohsawa, *J. Power Sources* **2011**, *196*, 4785–4790.

[39] J. Hong, D. H. Seo, S. W. Kim, H. Gwon, S. T. Oh, K. Kang, *J. Mater. Chem.* **2010**, *20*, 10179–10186.

[40] T. M. M. Heenan, A. Wade, C. Tan, J. E. Parker, D. Matras, A. S. Leach, J. B. Robinson, A. Llewellyn, A. Dimitrijevic, R. Jervis, P. D. Quinn, D. J. L. Brett, P. R. Shearing, *Adv. Energy Mater.* **2020**, *10*, 2002655.

[41] L. Batteries, M. Gu, I. Belharouak, J. Zheng, H. Wu, J. Xiao, A. Genc, K. Amine, S. Thevuthasan, D. R. Baer, J. Zhang, N. D. Browning, J. Liu, C. Wang, **2013**, 760–767.

[42] E. A. Olivetti, G. Ceder, G. G. Gaustad, X. Fu, *Joule* **2017**, *1*, 229–243.

[43] X. L. Wang, K. An, L. Cai, Z. Feng, S. E. Nagler, C. Daniel, K. J. Rhodes, A. D. Stoica, H. D. Skorpenske, C. Liang, W. Zhang, J. Kim, Y. Qi, S. J. Harris, *Sci. Rep.* **2012**, *2*, DOI 10.1038/srep00747.

[44] C. Xu, K. Märker, J. Lee, A. Mahadevegowda, P. J. Reeves, S. J. Day, M. F. Groh, S. P. Emge, C. Ducati, B. Layla Mehdi, C. C. Tang, C. P. Grey, *Nat. Mater.* **2021**, *20*, 84–92.

[45] J. Kasnatscheew, S. Röser, M. Börner, M. Winter, *ACS Appl. Energy Mater.* **2019**, *2*, 7733–7737.

[46] M. M. Thackeray, J. R. Croy, E. Lee, A. Gutierrez, M. He, J. S. Park, B. T.

Yonemoto, B. R. Long, J. D. Blauwkamp, C. S. Johnson, Y. Shin, W. I. F. David, *Sustain. Energy Fuels* **2018**, *2*, 1375–1397.

[47]   B. Jache, J. O. Binder, T. Abe, P. Adelhelm, *Phys. Chem. Chem. Phys.* **2016**, *18*, 14299–14316.

[48]   J. Li, L. E. Downie, L. Ma, W. Qiu, J. R. Dahn, **2015**, *162*, 1401–1408.

[49]   Y. K. Ahn, Y. N. Jo, W. Cho, J. S. Yu, K. J. Kim, *Energies* **2019**, *12*, 1–10.

[50]   R. Jung, M. Metzger, F. Maglia, C. Stinner, H. A. Gasteiger, *J. Phys. Chem. Lett.* **2017**, *8*, 4820–4825.

[51]   T. Or, S. W. D. Gourley, K. Kaliyappan, A. Yu, Z. Chen, *Carbon Energy* **2020**, *2*, 6–43.

[52]   M. G. Boebinger, J. A. Lewis, S. E. Sandoval, M. T. McDowell, *ACS Energy Lett.* **2020**, *5*, 335–345.

[53]   C. Wang, A. J. Appleby, F. E. Little, *J. Electroanal. Chem.* **2002**, *519*, 9–17.

[54]   J. P. Pender, G. Jha, D. H. Youn, J. M. Ziegler, I. Andoni, E. J. Choi, A. Heller, B. S. Dunn, P. S. Weiss, R. M. Penner, C. B. Mullins, *ACS Nano* **2020**, *14*, 1243–1295.

[55]   F. B. Spingler, S. Kücher, R. Phillips, E. Moyassari, A. Jossen, *J. Electrochem. Soc.* **2021**, *168*, 040515.

[56]   D. S. Eastwood, V. Yufit, J. Gelb, A. Gu, R. S. Bradley, S. J. Harris, D. J. L. Brett, N. P. Brandon, P. D. Lee, P. J. Withers, P. R. Shearing, *Adv. Energy Mater.* **2014**, *4*, 1–7.

[57]   J. O. Majasan, J. B. Robinson, R. E. Owen, M. Maier, A. N. P. Radhakrishnan, M. Pham, T. G. Tranter, Y. Zhang, P. R. Shearing, D. J. L. Brett, *J. Phys. Energy* **2021**, *3*, 032011.

[58]   W. J. Zhang, *J. Power Sources* **2011**, *196*, 877–885.

[59]   S. Choi, T. Kwon, A. Coskun, *Science (80-.).* **2017**, *283*, 279–283.

[60]   A. Magasinski, B. Zdyrko, I. Kovalenko, B. Hertzberg, R. Burtovyy, C. F. Huebner, T. F. Fuller, I. Luzinov, G. Yushin, *ACS Appl. Mater. Interfaces* **2010**, *2*, 3004–3010.

[61]   E. J. Berg, C. Villevieille, D. Streich, S. Trabesinger, P. Novák, *J. Electrochem. Soc.* **2015**, *162*, A2468–A2475.

[62]   S. Martinet, *Nanosci. Technol.* **2016**, 471–512.

[63]   H. Michael, F. Iacoviello, T. Heenan, A. Llewellyn, J. Weaving, R. Jervis, D. Brett, P. R. Shearing, *J. Electrochem. Soc.* **2021**, *168*, 010507.

[64]   M. Bauer, J. V Persson, M. A. Danzer, M. Wachtler, H. Stowe, *J. Power Sources* **2016**, *317*, 93–102.

[65]   S. Schweidler, L. De Biasi, A. Schiele, P. Hartmann, T. Brezesinski, J. Janek, *J. Phys. Chem. C* **2018**, *122*, 8829–8835.

[66]   J. Vetter, M. E. Spahr, F. Krumeich, P. Nov, **2006**, *153*, 385–390.

[67]   J. B. Siegel, A. G. Stefanopoulou, P. Hagans, Y. Ding, D. Gorsich, *J. Electrochem. Soc.* **2013**, *160*, A1031–A1038.

[68]   M. Winter, J. O. Besenhard, M. E. Spahr, P. Novák, *Adv. Mater.* **1998**, *10*, 725–763.

[69]   V. A. Agubra, J. W. Fergus, *J. Power Sources* **2014**, *268*, 153–162.

[70]   B. Rowden, N. Garcia-Araez, *Energy Reports* **2020**, *6*, 10–18.

[71]   K. Edström, M. Herstedt, D. P. Abraham, *J. Power Sources* **2006**, *153*, 380–384.

[72]   Y.-H. Chen, C.-W. Wang, G. Liu, X.-Y. Song, V. S. Battaglia, A. M. Sastry, *J. Electrochem. Soc.* **2007**, *154*, A978.

[73]   K. Tasaki, A. Goldberg, J.-J. Lian, M. Walker, A. Timmons, S. J. Harris, *J. Electrochem. Soc.* **2009**, *156*, A1019.

[74]   P. Verma, P. Maire, P. Novák, *Electrochim. Acta* **2010**, *55*, 6332–6341.

[75] M. B. Pinsona, M. Z. Bazant, *J. Electrochem. Soc.* **2013**, *160*, DOI 10.1149/2.044302jes.

[76] M. Herstedt, H. Rensmo, H. Siegbahn, K. Edström, *Electrochim. Acta* **2004**, *49*, 2351–2359.

[77] O. V. Bushkova, T. V. Yaroslavtseva, Y. A. Dobrovolsky, *Russ. J. Electrochem.* **2017**, *53*, 677–699.

[78] A. K. C. Estandarte, J. Diao, A. V. Llewellyn, A. Jnawali, T. M. M. Heenan, S. R. Daemi, J. J. Bailey, S. Cipiccia, D. Batey, X. Shi, C. Rau, D. J. L. Brett, R. Jervis, I. K. Robinson, P. R. Shearing, *ACS Nano* **2021**, *15*, 1321–1330.

[79] S. Bak, E. Hu, Y. Zhou, X. Yu, S. D. Senanayake, S. Cho, K. Kim, K. Y. Chung, X. Yang, K. Nam, *Appl. Mater. Interfaces* **2014**, *6*, 22594–22601.

[80] K. Min, K. Kim, C. Jung, S. W. Seo, Y. Y. Song, H. S. Lee, J. Shin, E. Cho, *J. Power Sources* **2016**, *315*, 111–119.

[81] R. Jung, M. Metzger, F. Maglia, C. Stinner, H. A. Gasteiger, *J. Electrochem. Soc.* **2017**, *164*, A1361–A1377.

[82] R. Jung, R. Morasch, P. Karayaylali, K. Phillips, F. Maglia, C. Stinner, Y. Shao-Horn, H. A. Gasteiger, *J. Electrochem. Soc.* **2018**, *165*, A132–A141.

[83] T. Li, X.-Z. Yuan, L. Zhang, D. Song, K. Shi, C. Bock, *Degradation Mechanisms and Mitigation Strategies of Nickel-Rich NMC-Based Lithium-Ion Batteries*, Springer Singapore, **2020**.

[84] T. M. M. Heenan, A. Wade, C. Tan, J. E. Parker, D. Matras, A. S. Leach, J. B. Robinson, A. Llewellyn, A. Dimitrijevic, R. Jervis, P. D. Quinn, D. J. L. Brett, P. R. Shearing, *Adv. Energy Mater.* **2020**, *10*, DOI 10.1002/aenm.202002655.

[85] Y. Shao-Horn, in (Eds.: G.-A. Nazri, G. Pistoia), Springer US, Boston, MA, **2003**, pp. 478–506.

[86] M. D. Radin, S. Hy, M. Sina, C. Fang, H. Liu, J. Vinckeviciute, M. Zhang, M. S. Whittingham, Y. S. Meng, A. Van der Ven, *Adv. Energy Mater.*

2017, *7*, DOI 10.1002/aenm.201602888.

[87]   W. Li, S. Lee, A. Manthiram, *Adv. Mater.* **2020**, *32*, 1–6.

[88]   J. Kim, H. Lee, H. Cha, M. Yoon, M. Park, J. Cho, *Adv. Energy Mater.*
       2018, *8*, 1870023.

[89]   E. Rossen, C. D. W. Jones, J. R. Dahn, *Solid State Ionics* **1992**, *57*, 311–
       318.

[90]   Y. Park, N. S. Choi, S. Park, S. H. Woo, S. Sim, B. Y. Jang, S. M. Oh, S.
       Park, J. Cho, K. T. Lee, *Adv. Energy Mater.* **2013**, *3*, 206–212.

[91]   X. He, J. Ren, L. Wang, W. Pu, C. Jiang, C. Wan, *J. Power Sources* **2009**,
       190, 154–156.

[92]   T. Hupfer, E. C. Bucharskydr, K. G. Schelldr, M. J. Hoffmannprof, *Solid
       State Ionics* **2017**, *302*, 49–53.

[93]   R. A. Jonson, P. J. McGinn, *Solid State Ionics* **2018**, *323*, 49–55.

[94]   B. Davaasuren, F. Tietz, *Solid State Ionics* **2019**, *338*, 144–152.

[95]   W. Biberacher, A. Lerf, J. O. Besenhard, H. Mohwald, T. Butz, *Mat. Res.
       Bull.* **1982**, *17*, 1385–1392.

[96]   J. O. Besenhard, J. Yang, M. Winter, *J. Power Sources* **1997**, *68*, 87–90.

[97]   J. Yang, M. Winter, J. O. Besenhard, *Solid State Ionics* **1996**, *90*, 281–
       287.

[98]   J. O. Besenhard, M. Winter, J. Yang, W. Biberacher, *J. Power Sources*
       1995, *54*, 228–231.

[99]   M. Hahn, O. Barbieri, R. Gallay, R. Kötz, *Carbon N. Y.* **2006**, *44*, 2523–
       2533.

[100] M. Hahn, H. Buqa, P. W. Ruch, D. Goers, M. E. Spahr, J. Ufheil, P. Novák,
       R. Kötz, *Electrochem. Solid-State Lett.* **2008**, *11*, A151.

[101] M. M. Hantel, R. Nesper, A. Wokaun, R. Kötz, *Electrochim. Acta* **2014**,

134, 459–470.

[102] M. Hahn, O. Barbieri, F. P. Campana, R. Kotz, R. Gallay, *Appl. Phys* **2006**, *82*, 633–638.

[103] W. Brehm, A. L. Santhosha, Z. Zhang, C. Neumann, A. Turchanin, M. Seyring, M. Rettenmayr, J. R. Buchheim, P. Adelhelm, *J. Power Sources Adv.* **2020**, *6*, 100031.

[104] S. Ivanov, D. Sauerteig, A. Dimitrova, S. Krischok, A. Bund, *J. Power Sources* **2020**, *457*, 228020.

[105] D. Sauerteig, S. Ivanov, H. Reinshagen, A. Bund, *J. Power Sources* **2017**, *342*, 939–946.

[106] J. B. Siegel, A. G. Stefanopoulou, P. Hagans, Y. Ding, D. Gorsich, *J. Electrochem. Soc.* **2013**, *160*, A1031–A1038.

[107] M. Winter, G. H. Wrodnigg, J. O. Besenhard, W. Biberacher, P. Novák, *J. Electrochem. Soc.* **2000**, *147*, 2427.

[108] J. Huesker, L. Froböse, A. Kwade, M. Winter, T. Placke, *Electrochim. Acta* **2017**, *257*, 423–435.

[109] M. R. Wagner, P. R. Raimann, A. Trifonova, K. C. Möller, J. O. Besenhard, M. Winter, *Anal. Bioanal. Chem.* **2004**, *379*, 272–276.

[110] H.-D. Yoo, J.-H. Ryu, S.-H. Park, Y.-W. Park, B.-H. Ka, S.-M. Oh, *J. Electrochem. Sci. Technol.* **2011**, *2*, 45–50.

[111] F. Grimsmann, F. Brauchle, T. Gerbert, A. Gruhle, M. Knipper, J. Parisi, *J. Energy Storage* **2017**, *12*, 132–137.

[112] M. Kerlau, M. Marcinek, R. Kostecki, *J. Power Sources* **2007**, *174*, 1046–1051.

[113] Y. Qi, S. J. Harris, *J. Electrochem. Soc.* **2010**, *157*, A741.

[114] A. C. Ngandjong, T. Lombardo, E. N. Primo, M. Chouchane, A. Shodiev, O. Arcelus, A. A. Franco, *J. Power Sources* **2021**, *485*, 229320.

[115] B. Rieger, S. Schlueter, S. V Erhard, J. Schmalz, G. Reinhart, A. Jossen, *J. Energy Storage* **2016**, *6*, 213–221.

[116] D. Y. W. Yu, M. Zhao, H. E. Hoster, *ChemElectroChem* **2015**, *2*, 1090–1095.

[117] O. Dolotko, A. Senyshyn, M. J. Mühlbauer, K. Nikolowski, H. Ehrenberg, *J. Power Sources* **2014**, *255*, 197–203.

[118] P. K. Nayak, L. Yang, K. Pollok, F. Langenhorst, *ChemElectroChem* **2019**, *6*, 2812–2819.

[119] R. A. House, G. J. Rees, M. A. Pérez-Osorio, J. J. Marie, E. Boivin, A. W. Robertson, A. Nag, M. Garcia-Fernandez, K. J. Zhou, P. G. Bruce, *Nat. Energy* **2020**, *5*, 777–785.

[120] K. Ariyoshi, H. Yamamoto, Y. Yamada, *Electrochim. Acta* **2018**, *260*, 498–503.

[121] M. Nagayama, K. Ariyoshi, Y. Yamamoto, T. Ohzuku, *J. Electrochem. Soc.* **2014**, *161*, A1388–A1393.

[122] J. Barker, *Electrochim. Acta* **1999**, *45*, 235–242.

[123] Z. J. Schiffer, J. Cannarella, C. B. Arnold, *J. Electrochem. Soc.* **2016**, *163*, A427–A433.

[124] C. Chen, Y. Wei, Z. Zhao, Y. Zou, D. Luo, *Electrochim. Acta* **2019**, *305*, 65–71.

[125] M. T. M. Pham, J. J. Darst, D. P. Finegan, J. B. Robinson, T. M. M. Heenan, M. D. R. Kok, F. Iacoviello, R. Owen, W. Q. Walker, O. V. Magdysyuk, T. Connolley, E. Darcy, G. Hinds, D. J. L. Brett, P. R. Shearing, *J. Power Sources* **2020**, *470*, 228039.

[126] S. R. Daemi, C. Tan, T. Volkenandt, S. J. Cooper, A. Palacios-Padros, J. Cookson, D. J. L. Brett, P. R. Shearing, *ACS Appl. Energy Mater.* **2018**, *1*, 3702–3710.

[127] O. O. Taiwo, D. P. Finegan, J. Gelb, C. Holzner, D. J. L. Brett, P. R. Shearing, *Chem. Eng. Sci.* **2016**, *154*, 27–33.

[128] V. Yufit, P. Shearing, R. W. Hamilton, P. D. Lee, M. Wu, N. P. Brandon, *Electrochem. commun.* **2011**, *13*, 608–610.

[129] C. Tan, S. Daemi, O. Taiwo, T. Heenan, D. Brett, P. Shearing, *Materials (Basel).* **2018**, *11*, 2157.

[130] S. C. Chao, Y. F. Song, C. C. Wang, H. S. Sheu, H. C. Wu, N. L. Wu, *J. Phys. Chem. C* **2011**, *115*, 22040–22047.

[131] P. R. Shearing, L. E. Howard, P. S. Jørgensen, N. P. Brandon, S. J. Harris, *Electrochem. commun.* **2010**, *12*, 374–377.

[132] S. Frisco, A. Kumar, J. F. Whitacre, S. Litster, *J. Electrochem. Soc.* **2016**, *163*, A2636–A2640.

[133] A. Tkachuk, F. Duewer, H. Cui, M. Feser, S. Wang, W. Yun, *Zeitschrift fur Krist.* **2007**, *222*, 650–655.

[134] M. Feser, J. Gelb, H. Chang, H. Cui, F. Duewer, S. H. Lau, A. Tkachuk, W. Yun, *Meas. Sci. Technol.* **2008**, *19*, DOI 10.1088/0957-0233/19/9/094001.

[135] D. S. Eastwood, R. S. Bradley, F. Tariq, S. J. Cooper, O. O. Taiwo, J. Gelb, A. Merkle, D. J. L. Brett, N. P. Brandon, P. J. Withers, P. D. Lee, P. R. Shearing, *Nucl. Instruments Methods Phys. Res. Sect. B Beam Interact. with Mater. Atoms* **2014**, *324*, 118–123.

[136] T. Otaki, *Opt. Rev.* **2000**, *7*, 119–122.

[137] O. O. Taiwo, D. P. Finegan, J. Gelb, C. Holzner, D. J. L. Brett, P. R. Shearing, *Chem. Eng. Sci.* **2016**, *154*, 27–33.

[138] S. R. Daemi, C. Tan, A. Vamvakeros, T. M. M. Heenan, D. P. Finegan, M. Di Michiel, A. M. Beale, J. Cookson, E. Petrucco, J. S. Weaving, S. Jacques, R. Jervis, D. J. L. Brett, P. R. Shearing, *Phys. Chem. Chem. Phys.* **2020**, *22*, 17814–17823.

[139] Z. Xu, M. M. Rahman, L. Mu, Y. Liu, F. Lin, *J. Mater. Chem. A* **2018**, *6*, 21859–21884.

[140] M. D. R. Kok, J. B. Robinson, J. S. Weaving, A. Jnawali, M. Pham, F. Iacoviello, D. J. L. Brett, P. R. Shearing, *Sustain. Energy Fuels* **2019**, *3*, 2972–2976.

[141] R. F. Ziesche, T. Arlt, D. P. Finegan, T. M. M. Heenan, A. Tengattini, D. Baum, N. Kardjilov, H. Markötter, I. Manke, W. Kockelmann, D. J. L. Brett, P. R. Shearing, *Nat. Commun.* **2020**, *11*, 1–11.

[142] Y. Wu, S. Saxena, Y. Xing, Y. Wang, C. Li, W. K. C. Yung, M. Pecht, *Energies* **2018**, *11*, DOI 10.3390/en11040925.

[143] Samsung, "Galaxy Note7: What we discovered," **2017**.

[144] T. Bond, R. Gauthier, A. Eldesoky, J. Harlow, J. R. Dahn, *J. Electrochem. Soc.* **2022**, *169*, 020501.

[145] L. Körner, S. Lawes, D. Bate, L. Newton, N. Senin, R. Leach, *Meas. Sci. Technol.* **2019**, *30*, DOI 10.1088/1361-6501/ab37e5.

[146] X. Lu, A. Bertei, D. P. Finegan, C. Tan, S. R. Daemi, J. S. Weaving, K. B. O'Regan, T. M. M. Heenan, G. Hinds, E. Kendrick, D. J. L. Brett, P. R. Shearing, *Nat. Commun.* **2020**, *11*, 1–13.

[147] A. Yermukhambetova, C. Tan, S. R. Daemi, Z. Bakenov, J. A. Darr, D. J. L. Brett, P. R. Shearing, *Sci. Rep.* **2016**, *6*, 1–9.

[148] D. Patel, J. B. Robinson, S. Ball, D. J. L. Brett, P. R. Shearing, *J. Electrochem. Soc.* **2020**, *167*, 090511.

[149] C. Tan, A. S. Leach, T. M. M. Heenan, R. Jervis, D. J. L. Brett, P. R. Shearing, in *Adv. Sustain. Energy Policy, Mater. Devices* (Eds.: Y. Gao, W. Song, J.L. Liu, S. Bashir), Springer International Publishing, Cham, **2021**, pp. 513–544.

[150] Y. He, M. Li, Z. Meng, S. Chen, S. Huang, Y. Hu, X. Zou, *Mech. Syst. Signal Process.* **2021**, *148*, DOI 10.1016/j.ymssp.2020.107146.

[151] J. B. Robinson, M. Maier, G. Alster, T. Compton, D. J. L. Brett, P. R. Shearing, *Phys. Chem. Chem. Phys.* **2018**, DOI 10.1039/C8CP07098A.

[152] C. Bommier, W. Chang, J. Li, S. Biswas, G. Davies, J. Nanda, D. Steingart, *J. Electrochem. Soc.* **2020**, *167*, 020517.

[153] J. B. Robinson, R. E. Owen, M. D. R. Kok, M. Maier, J. Majasan, M. Braglia, R. Stocker, T. Amietszajew, A. J. Roberts, R. Bhagat, D. Billsson, J. Z. Olson, J. Park, G. Hinds, A. Ahlberg Tidblad, D. J. L. Brett, P. R. Shearing, *J. Electrochem. Soc.* **2020**, *167*, 120530.

[154] H. Inoue, R. Tsuzuki, S. Nohara, C. Iwakura, *Electrochem. Solid-State Lett.* **2006**, *9*, 504–507.

[155] S. Didier-Laurent, H. Idrissi, L. Roué, *J. Power Sources* **2008**, *179*, 412–416.

[156] H. Inoue, R. Tsuzuki, S. Nohara, C. Iwakura, *J. Alloys Compd.* **2007**, *446–447*, 681–686.

[157] K. Azumi, S. Ishiguro, T. Mizuno, M. Seo, *J. Electroanal. Chem.* **1993**, *347*, 111–121.

[158] M. Maier, Q. Meyer, J. Majasan, R. E. Owen, J. B. Robinson, J. Dodwell, Y. Wu, L. Castanheira, G. Hinds, P. R. Shearing, D. J. L. Brett, *Front. Energy Res.* **2020**, *8*, 1–6.

[159] M. Maier, Q. Meyer, J. Majasan, C. Tan, I. Dedigama, J. Robinson, J. Dodwell, Y. Wu, L. Castanheira, G. Hinds, P. R. Shearing, D. J. L. Brett, *J. Power Sources* **2019**, *424*, 138–149.

[160] K. Rhodes, N. Dudney, E. Lara-Curzio, C. Daniel, *J. Electrochem. Soc.* **2010**, *157*, A1354.

[161] R. J. Copley, D. Cumming, Y. Wu, R. S. Dwyer-Joyce, *J. Energy Storage* **2021**, *36*, DOI 10.1016/j.est.2021.102406.

[162] P. Ladpli, F. Kopsaftopoulos, F. K. Chang, *J. Power Sources* **2018**, *384*, 342–354.

[163] A. Tranchot, H. Idrissi, *J. Power Sources* **2016**, *330*, 253–260.

[164] M. Hahn, H. Buqa, P. W. Ruch, D. Goers, M. E. Spahr, J. Ufheil, P. Novák, R. Kötz, *Electrochem. Solid-State Lett.* **2008**, *11*, A151.

[165] A. Tranchot, A. Etiemble, H. Idrissi, **2015**, *279*, DOI 10.1016/j.jpowsour.2014.12.126.

[166] T. Kim, J. E. Soc, T. Kim, S. Park, S. M. Oh, *J. Electrochem. Soc* **2007**, *154*, A1112–A1117.

[167] T. Palaniselvam, M. Goktas, B. Anothumakkool, Y. N. Sun, R. Schmuch, L. Zhao, B. H. Han, M. Winter, P. Adelhelm, *Adv. Funct. Mater.* **2019**, *29*, 1–12.

[168] L. K. Willenberg, P. Dechent, G. Fuchs, D. U. Sauer, E. Figgemeier, *Sustain.* **2020**, *12*, 557.

[169] B. Karmakar, P. Kundu, S. Jana, R. N. Dwivedi, *J. Am. Ceram. Soc* **2002**, *85*, 2572–2574.

[170] A. Abdelmonem, M. Soliman, H. Palkowski, A. Elsabbagh, *Metals (Basel).* **2021**, *11*, 1–17.

[171] https://www.tainstruments.com/dil-806/, Accessed **2023**.

[172] R. Küchler, T. Bauer, M. Brando, F. Steglich, *Rev. Sci. Instrum.* **2012**, *83*, 095102.

[173] M. O. Steinitz, J. Genossar, W. Schnepf, D. A. Tindall, *Rev. Sci. Instrum.* **1986**, *57*, 297–298.

[174] G. M. Schmiedeshoff, A. W. Lounsbury, D. J. Luna, S. J. Tracy, A. J. Schramm, S. W. Tozer, V. F. Correa, S. T. Hannahs, T. P. Murphy, E. C. Palm, A. H. Lacerda, S. L. Bud'Ko, P. C. Canfield, J. L. Smith, J. C. Lashley, J. C. Cooley, *Rev. Sci. Instrum.* **2006**, *77*, 123907.

[175] J. J. Neumeier, R. K. Bollinger, G. E. Timmins, C. R. Lane, R. D. Krogstad, J. Macaluso, *Rev. Sci. Instrum.* **2008**, *79*, 1–8.

[176] S. Jun, Y. J. Nam, H. Kwak, K. T. Kim, D. Y. Oh, Y. S. Jung, *Adv. Funct. Mater.* **2020**, *30*, 1–8.

[177] S. H. Jung, U. H. Kim, J. H. Kim, S. Jun, C. S. Yoon, Y. S. Jung, Y. K. Sun, *Adv. Energy Mater.* **2020**, *10*, 1–12.

[178] K. V. Santhosh, B. K. Roy, *Procedia Technol.* **2012**, *4*, 854–861.

[179] G. Prit, P. Goyal, T. Islam, *2019 IEEE 16th India Counc. Int. Conf. INDICON 2019 - Symp. Proc.* **2019**.

[180] M. Winter, G. H. Wrodnigg, J. O. Besenhard, W. Biberacher, P. Novák, *J. Electrochem. Soc.* **2000**, *147*, 2427.

[181] D. Sauerteig, S. Ivanov, H. Reinshagen, A. Bund, *J. Power Sources* **2017**, *342*, 939–946.

[182] G. Jeong, S. Min, N. Soon, Y. Kim, C. Kyoung, *Electrochim. Acta* **2011**, *56*, 5095–5101.

[183] R. Fu, M. Xiao, S. Y. Choe, *J. Power Sources* **2013**, *224*, 211–224.

[184] M. Bauer, B. Rieger, S. Schindler, P. Keil, M. Wachtler, M. A. Danzer, A. Jossen, *J. Energy Storage* **2017**, *10*, 1–10.

[185] W. Zhang, D. Schröder, T. Arlt, I. Manke, R. Koerver, R. Pinedo, D. A. Weber, J. Sann, W. G. Zeier, J. Janek, *J. Mater. Chem. A* **2017**, *5*, 9929–9936.

[186] F. J. Vidal-Iglesias, J. Solla-Gullón, A. Rodes, E. Herrero, A. Aldaz, *J. Chem. Educ.* **2012**, *89*, 936–939.

[187] K. D. Vernon-Parry, *III-Vs Rev.* **2000**, *13*, 40–44.

[188] S. L. Flegler, J. W. Heckman, K. L. Klomparens, **n.d.**

[189] Y. S. Susiapan, A. R. Ruzairi, C. L. Goh, F. R. Hafiz, A. R. Herlina, *Int. J. Integr. Eng.* **2017**, *9*, 31–43.

[190] W. A. Kalender, *Phys. Med. Biol.* **2006**, *51*, DOI 10.1088/0031-

9155/51/13/R03.

[191] S. C. Garcea, Y. Wang, P. J. Withers, *Compos. Sci. Technol.* **2018**, *156*, 305–319.

[192] P. Education, **2001**.

[193] I. Palo, P. E. C. Ho, P. P. Data, **2007**, *2*.

[194] O. O. Taiwo, **2016**.

[195] P. Hermanek, J. S. Rathore, V. Aloisi, S. Carmignato, in *Ind. X-Ray Comput. Tomogr.* (Eds.: S. Carmignato, W. Dewulf, R. Leach), Springer International Publishing, Cham, **2018**, pp. 25–67.

[196] V. Busignies, B. Leclerc, P. Porion, P. Evesque, G. Couarraze, P. Tchoreloff, **2006**, *64*, 38–50.

[197] J. Hinebaugh, P. R. Challa, A. Bazylak, **2012**, 994–1000.

[198] P. Pietsch, V. Wood, **2017**, 451–481.

[199] P. J. Withers, D. Grimaldi, C. K. Hagen, E. Maire, M. Manley, A. Du Plessis, *Nat. Rev. Methods Prim.* **n.d.**, DOI 10.1038/s43586-021-00015-4.

[200] L. Salvo, P. Cloetens, E. Maire, S. Zabler, J. J. Blandin, J. Y. Buffière, W. Ludwig, E. Boller, D. Bellet, C. Josserond, *Nucl. Instruments Methods Phys. Res. Sect. B Beam Interact. with Mater. Atoms* **2003**, *200*, 273–286.

[201] **N.d.**

[202] J. R. Izzo, A. S. Joshi, K. N. Grew, W. K. S. Chiu, A. Tkachuk, S. H. Wang, W. Yun, *J. Electrochem. Soc.* **2010**, *157*, S5.

[203] Carl Zeiss Microscopy GmbH, **2018**, 11.

[204] C. Holzner, M. Feser, S. Vogt, B. Hornberger, S. B. Baines, C. Jacobsen, *Nat. Phys.* **2010**, *6*, 883–887.

[205]   G. Schneider, **1998**, *75*, 85–104.

[206]   P. J. Withers, *Mater. Today* **2007**, *10*, 26–34.

[207]   Z. Xradia, U. Family, **n.d.**

[208]   K. M. Hanson, *Radiol. Skull Brain* **1981**, *5*, 3941–3955.

[209]   P. M. Shikhaliev, P. M. Shikhaliev, P. M. Shikhaliev, **2005**, DOI 10.1088/0031-9155/50/24/004.

[210]   Y. Kyriakou, D. Prell, C. T. Badea, S. M. Johnston, W. Zbijewski, M. Defrise, **2004**, DOI 10.1088/0031-9155/49/14/N06.

[211]   E. Pessis, R. Campagna, J. M. Sverzut, F. Bach, M. Rodallec, H. Guerini, A. Feydy, J. L. Drapé, *Radiographics* **2013**, *33*, 573–583.

[212]   J. A. Meganck, K. M. Kozloff, M. M. Thornton, S. M. Broski, S. A. Goldstein, *Bone* **2009**, *45*, 1104–1116.

[213]   M. L. Bouxsein, S. K. Boyd, B. A. Christiansen, R. E. Guldberg, K. J. Jepsen, R. Müller, *J. Bone Miner. Res.* **2010**, *25*, 1468–1486.

[214]   O. M. H. Ahmed, Y. Song, *Sains Malaysiana* **2018**, *47*, 1883–1890.

[215]   B. De Man, J. Nuyts, P. Dupont, G. Marchai, P. Suetens, *IEEE Trans. Nucl. Sci.* **2000**, *47*, 977–981.

[216]   M. Bazalova, L. Beaulieu, S. Palefsky, F. Verhaegen, *Med. Phys.* **2007**, *34*, 2119–2132.

[217]   E. Meyer, R. Raupach, M. Lell, B. Schmidt, M. Kachelrieß, *Med. Phys.* **2010**, *37*, 5482–5493.

[218]   M. Bal, L. Spies, *Med. Phys.* **2006**, *33*, 2852–2859.

[219]   J. Gu, L. Zhang, G. Yu, Y. Xing, Z. Chen, in *Med. Imaging 2006 Image Process.* (Eds.: J.M. Reinhardt, J.P.W. Pluim), SPIE, **2006**, pp. 1965–1972.

[220]   G. Wang, D. L. Snyder, J. A. O'Sullivan, M. W. Vannier, *IEEE Trans. Med. Imaging* **1996**, *15*, 657–664.

[221] H. S. Park, Y. E. Chung, J. K. Seo, *Philos. Trans. R. Soc. A Math. Phys. Eng. Sci.* **2015**, *373*, 1–11.

[222] X. Pan, E. Y. Sidky, M. Vannier, *Inverse Probl.* **2009**, *25*, DOI 10.1088/0266-5611/25/12/123009.

[223] S. J. Cooper, A. Bertei, P. R. Shearing, J. A. Kilner, N. P. Brandon, *SoftwareX* **2016**, *5*, 203–210.

[224] J. Banhart , **2008**.

[225] H. Zhang, D. Zeng, H. Zhang, J. Wang, Z. Liang, J. Ma, *Med. Phys.* **2017**, *44*, 1168–1185.

[226] B. R. Jennings, K. Parslow, **1988**, *419*, 137–149.

[227] W. E. Lorensen, H. E. Cline, *Proc. 14th Annu. Conf. Comput. Graph. Interact. Tech. SIGGRAPH 1987* **1987**, *21*, 163–169.

[228] Y. K. Chen-wiegart, R. Demike, C. Erdonmez, K. Thornton, S. A. Barnett, J. Wang, *J. Power Sources* **2014**, *249*, 349–356.

[229] S. J. Cooper, A. Bertei, P. R. Shearing, J. A. Kilner, N. P. Brandon, *SoftwareX* **2016**, *5*, 203–210.

[230] S. R. Daemi, C. Tan, T. Volkenandt, S. J. Cooper, A. Palacios-padros, J. Cookson, D. J. L. Brett, P. R. Shearing, **2018**, DOI 10.1021/acsaem.8b00501.

[231] H. N. G. Wadley, *Rev. Prog. Quant. Nondestruct. Eval.* **1986**, *5 A*, 271–293.

[232] J. Dziewierz, A. Gachagan, *IEEE Trans. Ultrason. Ferroelectr. Freq. Control* **2013**, *60*, 1256–1259.

[233] D. G. Eitzen, H. N. G. Wadley, *J. Res. Natl. Bur. Stand. (United States)* **1984**, *89*, 75–100.

[234] M. F. Shehadeh, A. H. E. Ahmed, M. J. A. Steel, *J. Nondestruct. Eval.* **2019**, *38*, 1–15.

[235] G. Davies, K. W. Knehr, B. Van Tassell, T. Hodson, S. Biswas, A. G. Hsieh, D. A. Steingart, *J. Electrochem. Soc.* **2017**, *164*, A2746–A2755.

[236] W. Sachse, K. Y. Kim, **1986**, *25*, 195–203.

[237] C. B. Scruby, K. A. Stacey, G. R. Baldwin, C. B. Scruby, H. N. G. Wadley, J. J. Hill, C. B. Scruby, J. C. Collingwood, **1987**.

[238] A. G. Hsieh, S. Bhadra, B. J. Hertzberg, P. J. Gjeltema, A. Goy, J. W. Fleischer, D. A. Steingart, *Energy Environ. Sci.* **2015**, *8*, 1569–1577.

[239] T. M. Proctor, **1997**, *1163*, DOI 10.1121/1.387763.

[240] R. Kažys, A. Voleišis, B. Voleišienė, *Ultrasound* **2008**, *63*, 7–17.

[241] B. Shivamurthy, H. K. Sachidanada, **2018**, *02016*, 1–7.

[242] Y. H. Kim, S. Song, S.-S. Lee, J.-K. Lee, S.-S. Hong, H. S. Eom, *J. Korean Soc. Nondestruct. Test.* **2002**, *22*.

[243] C. Bommier, W. Chang, Y. Lu, J. Yeung, G. Davies, R. Mohr, M. Williams, D. Steingart, *Cell Reports Phys. Sci.* **2020**, *1*, 100035.

[244] A. Etiemble, J. Adrien, E. Maire, H. Idrissi, D. Reyter, L. Roué, *Mater. Sci. Eng. B* **2014**, *187*, 1–8.

[245] S. H. Ng, C. Vix-Guterl, P. Bernardo, N. Tran, J. Ufheil, H. Buqa, J. Dentzer, R. Gadiou, M. E. Spahr, D. Goers, P. Novák, *Carbon N. Y.* **2009**, *47*, 705–712.

[246] M. Wissler, *J. Power Sources* **2006**, *156*, 142–150.

[247] M. Inaba, H. Yoshida, Z. Ogumi, S. Rod, **1995**, *142*.

[248] N. A. W. Holzwarth, S. G. Louie, S. Rabii, *Phys. Rev. B* **1983**, *28*, 1013–1025.

[249] T. D. Tran, J. H. Feikert, R. W. Pekala, K. Kinoshita, *J. Appl. Electrochem.* **1996**, *26*, 1161–1167.

[250] J. R. Dahn, *Phys. Rev. B* **1991**, *44*, 9170–9177.

[251] Z. Peng, T. W. Yang, Z. J. Li, Z. H. Li, Q. L. Jin, R. Zhou, *Zhongguo Youse Jinshu Xuebao/Chinese J. Nonferrous Met.* **2011**, *21*, 1045–1051.

[252] E. M. C. Jones, Çapraz, S. R. White, N. R. Sottos, *J. Electrochem. Soc.* **2016**, *163*, A1965–A1974.

[253] K. R. Tallman, B. Zhang, L. Wang, S. Yan, K. Thompson, X. Tong, A. Kiss, A. C. Marschilok, K. J. Takeuchi, D. Bock, E. S. Takeuchi, **2019**, DOI 10.1021/acsami.9b16794.

[254] P. Verma, P. Maire, P. Novák, *Electrochim. Acta* **2010**, *55*, 6332–6341.

[255] A. Eftekhari, *Sustain. Energy Fuels* **2017**, *1*, 2053–2060.

[256] P. Press, N. York, **1995**, *142*, 1746–1752.

[257] E. M. C. Jones, M. N. Silberstein, S. R. White, N. R. Sottos, *Exp. Mech.* **2014**, *54*, 971–985.

[258] J. Gonzalez, K. Sun, M. Huang, J. Lambros, S. Dillon, *J. Power Sources* **2014**, *269*, 334–343.

[259] M. Goktas, C. Bolli, E. J. Berg, P. Novák, K. Pollok, F. Langenhorst, M. v. Roeder, O. Lenchuk, D. Mollenhauer, P. Adelhelm, *Adv. Energy Mater.* **2018**, *8*, 1702724.

[260] B. Key, M. Morcrette, J. M. Tarascon, C. P. Grey, *J. Am. Chem. Soc.* **2011**, *133*, 503–512.

[261] C. Uhlmann, J. Illig, M. Ender, R. Schuster, E. Ivers-Tiffée, *J. Power Sources* **2015**, *279*, 428–438.

[262] N. Legrand, B. Knosp, P. Desprez, F. Lapicque, S. Raël, *J. Power Sources* **2014**, *245*, 208–216.

[263] F. Tariq, V. Yufit, D. S. Eastwood, Y. Merla, M. Biton, B. Wu, Z. Chen, K. Freedman, G. Offer, E. Peled, P. D. Lee, D. Golodnitsky, N. Brandon, *ECS Electrochem. Lett.* **2014**, *3*.

[264] M. Baunach, S. Jaiser, S. Schmelzle, H. Nirschl, P. Scharfer, W. Schabel,

Dry. Technol. **2016**, *34*, 462–473.

[265] Y. Qian, B. Lu, Y. Bao, Y. Zhao, Y. Song, J. Zhang, *Appl. Math. Mech. (English Ed.* **2021**, *42*, 1703–1716.

[266] M. Goktas, C. Bolli, E. J. Berg, P. Novák, K. Pollok, F. Langenhorst, M. Roeder, O. Lenchuk, D. Mollenhauer, *Adv. Energy Mater.* **2018**, *1702724*, 1–11.

[267] C. Chen, C. Pan, W. Su, J. Rick, C. Wang, **2015**, *2*, 8613–8626.

[268] W. Gu, Z. Sun, X. Wei, H. Dai, *Electrochim. Acta* **2014**, *133*, 107–116.

[269] P. R. Shearing, N. P. Brandon, J. Gelb, R. Bradley, P. J. Withers, A. J. Marquis, S. Cooper, S. J. Harris, *J. Electrochem. Soc.* **2012**, *159*, A1023–A1027.

[270] J. P. Pender, G. Jha, D. H. Youn, J. M. Ziegler, I. Andoni, E. J. Choi, A. Heller, B. S. Dunn, P. S. Weiss, R. M. Penner, C. B. Mullins, *ACS Nano* **2020**, *14*, 1243–1295.

[271] A. O. Kondrakov, A. Schmidt, J. Xu, H. Geßwein, R. Mönig, P. Hartmann, H. Sommer, T. Brezesinski, J. Janek, *J. Phys. Chem. C* **2017**, *121*, 3286–3294.

[272] T. Palaniselvam, C. Mukundan, I. Hasa, A. L. Santhosha, M. Goktas, H. Moon, M. Ruttert, R. Schmuch, K. Pollok, F. Langenhorst, M. Winter, S. Passerini, P. Adelhelm, *Adv. Funct. Mater.* **2020**, *2004798*, 1–12.

[273] K. Märker, P. J. Reeves, C. Xu, K. J. Griffith, C. P. Grey, *Chem. Mater.* **2019**, *31*, 2545–2554.

[274] S. Li, Z. Jiang, J. Han, Z. Xu, C. Wang, H. Huang, C. Yu, S. J. Lee, P. Pianetta, H. Ohldag, J. Qiu, J. S. Lee, F. Lin, K. Zhao, Y. Liu, *Nat. Commun.* **2020**, *11*, 1–9.

[275] J. Li, H. Liu, J. Xia, A. R. Cameron, M. Nie, G. A. Botton, J. R. Dahn, **2017**, *164*, DOI 10.1149/2.0651704jes.

[276] D. Goonetilleke, N. Sharma, W. K. Pang, V. K. Peterson, R. Petibon, J. Li, J. R. Dahn, *Chem. Mater.* **2018**, *31*, 376–386.

[277] N. Yabuuchi, Y. Makimura, T. Ohzuku, *J. Electrochem. Soc.* **2007**, *154*, A314.

[278] J. Li, R. Shunmugasundaram, R. Doig, J. R. Dahn, *Chem. Mater.* **2016**, *28*, 162–171.

[279] F. B. Spingler, W. Wittmann, J. Sturm, B. Rieger, A. Jossen, *J. Power Sources* **2018**, *393*, 152–160.

[280] Y. Koyama, N. Yabuuchi, I. Tanaka, H. Adachi, T. Ohzuku, *J. Electrochem. Soc.* **2004**, *151*, A1545.

[281] M. N. Obrovac, L. Christensen, D. B. Le, J. R. Dahn, **2007**, 849–855.

[282] Y. Liu, H. Wu, K. Li, H. Li, D. Ouyang, P. P. Arab, N. Phattharasupakun, D. Rathore, M. Johnson, Y. Wang, S. Yin, J. R. Dahn, *J. Electrochem. Soc.* **2020**, *167*, 120533.

[283] C. Tian, F. Lin, **2018**, *2*, DOI 10.1021/acs.accounts.7b00520.

[284] C. Julien, A. Mauger, K. Zaghib, H. Groult, *Materials (Basel).* **2016**, *9*, DOI 10.3390/MA9070595.

[285] Z. Zhang, J. Yang, W. Huang, H. Wang, W. Zhou, Y. Li, Y. Li, J. Xu, W. Huang, W. Chiu, Y. Cui, *Matter* **2021**, *4*, 302–312.

[286] B. Heidrich, L. Pritzlaff, M. Börner, M. Winter, P. Niehoff, *J. Electrochem. Soc.* **2022**, *169*, 030533.

[287] Y. Qian, C. Schultz, P. Niehoff, T. Schwieters, S. Nowak, F. M. Schappacher, M. Winter, *J. Power Sources* **2016**, *332*, 60–71.

[288] R. Genieser, S. Ferrari, M. Loveridge, S. D. Beattie, R. Beanland, H. Amari, G. West, R. Bhagat, *J. Power Sources* **2018**, *373*, 172–183.

[289] P. Mohtat, S. Lee, V. Sulzer, J. B. Siegel, A. G. Stefanopoulou, *J. Electrochem. Soc.* **2020**, *167*, 110561.

[290] J. Alvarado, C. Wei, D. Nordlund, T. Kroll, D. Sokaras, Y. Tian, Y. Liu, M. M. Doeff, *Mater. Today* **2020**, *35*, 87–98.

[291] K. Edström, T. Gustafsson, J. O. Thomas, *Electrochim. Acta* **2004**, *50*, 397–403.

[292] D. J. Xiong, L. D. Ellis, J. Li, H. Li, T. Hynes, J. P. Allen, J. Xia, D. S. Hall, I. G. Hill, J. R. Dahn, *J. Electrochem. Soc.* **2017**, *164*, A3025–A3037.

[293] M. M. Kabir, D. E. Demirocak, *Int. J. Energy Res.* **2017**, *41*, 1963–1986.

[294] K. Jalkanen, J. Karppinen, L. Skogström, T. Laurila, M. Nisula, K. Vuorilehto, *Appl. Energy* **2015**, *154*, 160–172.

[295] K. Märker, P. J. Reeves, C. Xu, K. J. Griffith, C. P. Grey, *Chem. Mater.* **2019**, *31*, 2545–2554.

[296] J. Li, L. E. Downie, L. Ma, W. Qiu, J. R. Dahn, *J. Electrochem. Soc.* **2015**, *162*, A1401–A1408.

[297] H. H. Ryu, K. J. Park, C. S. Yoon, Y. K. Sun, *Chem. Mater.* **2018**, *30*, 1155–1163.

[298] H. Li, N. Zhang, J. Li, J. R. Dahn, *J. Electrochem. Soc.* **2018**, *165*, A2985–A2993.

[299] C. Xu, P. J. Reeves, Q. Jacquet, C. P. Grey, *Adv. Energy Mater.* **2020**, *2003404*, 1–12.

[300] J. Sicklinger, H. Beyer, L. Hartmann, F. Riewald, C. Sedlmeier, H. A. Gasteiger, *J. Electrochem. Soc.* **2020**, *167*, 130507.

[301] S. Yin, W. Deng, J. Chen, X. Gao, G. Zou, H. Hou, X. Ji, *Nano Energy* **2021**, *83*, 105854.

[302] P. K. Nayak, L. Yang, K. Pollok, F. Langenhorst, *ChemElectroChem* **2019**, *6*, 2812–2819.

[303] E. R. Logan, H. Hebecker, X. Ma, J. Quinn, Y. HyeJeong, S. Kumakura, J. Paulsen, J. R. Dahn, *J. Electrochem. Soc.* **2020**, *167*, 060530.

[304] Y. Yang, W. Yuan, X. Zhang, Y. Ke, Z. Qiu, J. Luo, Y. Tang, C. Wang, Y.
        Yuan, Y. Huang, *Appl. Energy* **2020**, *276*, 115464.

[305] J. Li, K. Adewuyi, N. Lotfi, R. G. Landers, J. Park, *Appl. Energy* **2018**, *212*,
        1178–1190.

[306] M. Yamada, T. Watanabe, T. Gunji, J. Wu, F. Matsumoto, *Electrochem*
        2020, *1*, 124–159.

[307] P. Zhu, D. Gastol, J. Marshall, R. Sommerville, V. Goodship, E. Kendrick,
        J. Power Sources **2021**, *485*, 229321.

[308] J. Zhu, G. Chen, *J. Mater. Chem. A* **2019**, *7*, 5463–5474.

[309] R. Weber, C. R. Fell, J. R. Dahn, S. Hy, *J. Electrochem. Soc.* **2017**, *164*,
        A2992–A2999.

[310] J. Li, A. R. Cameron, H. Li, S. Glazier, D. Xiong, M. Chatzidakis, J. Allen, G.
        A. Botton, J. R. Dahn, *J. Electrochem. Soc.* **2017**, *164*, A1534–A1544.

[311] J. Langdon, A. Manthiram, *Energy Storage Mater.* **2021**, *37*, 143–160.

[312] G. Liu, M. Li, N. Wu, L. Cui, X. Huang, X. Liu, Y. Zhao, H. Chen, W. Yuan,
        Y. Bai, *J. Electrochem. Soc.* **2018**, *165*, A3040–A3047.

[313] J. J. Bailey, T. M. M. Heenan, D. P. Finegan, X. Lu, S. R. Daemi, F.
        Iacoviello, N. R. Backeberg, O. O. Taiwo, D. J. L. Brett, A. Atkinson, P. R.
        Shearing, *J. Microsc.* **2017**, *267*, 384–396.

[314] C. Tan, A. S. Leach, T. M. M. Heenan, H. Parks, R. Jervis, J. N. Weker, D.
        J. L. Brett, P. R. Shearing, *Cell Reports Phys. Sci.* **2021**, 100647.

[315] N. Otsu, P. L. Smith, D. B. Reid, C. Environment, L. Palo, P. Alto, P. L.
        Smith, *IEEE Trans. Syst. Man. Cybern.* **1979**, *C*, 62–66.

[316] T. Wang, K. Ren, M. He, W. Dong, W. Xiao, H. Pan, J. Yang, Y. Yang, P.
        Liu, Z. Cao, X. Ma, H. Wang, *Front. Chem.* **2020**, *8*, 1–8.

[317] H. Zheng, L. Tan, G. Liu, X. Song, V. S. Battaglia, *J. Power Sources* **2012**,
        208, 52–57.

[318] M. Ebner, F. Geldmacher, F. Marone, M. Stampanoni, V. Wood, **2013**, 845–850.

[319] J. Shim, K. A. Striebel, *J. Power Sources* **2003**, *119–121*, 955–958.

[320] O. Sinica, **2016**, *18*, 33–37.

[321] H. Zheng, L. Tan, G. Liu, X. Song, V. S. Battaglia, *J. Power Sources* **2012**, *208*, 52–57.

[322] T. Kimijima, N. Zettsu, K. Teshima, *Cryst. Growth Des.* **2016**, *16*, 2618–2623.

[323] V. V Kadam, R. Nayak, in *Acoust. Text.* (Eds.: R. Padhye, R. Nayak), Springer Singapore, Singapore, **2016**, pp. 33–42.

[324] A. Haibel, I. Manke, A. Melzer, J. Banhart, *J. Electrochem. Soc.* **2010**, *157*, A387.

[325] M. Musiak, Z. S. Li, **2021**, 1–5.

[326] G. Qian, Y. Zhang, L. Li, R. Zhang, J. Xu, Z. Cheng, S. Xie, H. Wang, Q. Rao, Y. He, Y. Shen, L. Chen, M. Tang, Z. F. Ma, *Energy Storage Mater.* **2020**, *27*, 140–149.

[327] M. Ge, S. Wi, X. Liu, J. Bai, S. Ehrlich, D. Lu, W. K. Lee, Z. Chen, F. Wang, *Angew. Chemie - Int. Ed.* **2021**, *60*, 17350–17355.

[328] J. Hu, L. Li, Y. Bi, J. Tao, J. Lochala, D. Liu, B. Wu, X. Cao, S. Chae, C. Wang, J. Xiao, *Energy Storage Mater.* **2022**, *47*, 195–202.

[329] Y. Lu, T. Zhu, E. McShane, B. D. McCloskey, G. Chen, *Small* **2022**, *2105833*, 1–10.

[330] L. Romano Brandt, J. J. Marie, T. Moxham, D. P. Förstermann, E. Salvati, C. Besnard, C. Papadaki, Z. Wang, P. G. Bruce, A. M. Korsunsky, *Energy Environ. Sci.* **2020**, *13*, 3556–3566.

[331] D. Kehrwald, P. R. Shearing, N. P. Brandon, P. K. Sinha, S. J. Harris, *J. Electrochem. Soc.* **2011**, *158*, A1393.

[332] Y. Wu, Y. Wang, W. K. C. Yung, M. Pecht, *Electron.* **2019**, *8*, DOI 10.3390/electronics8070751.

[333] R. Bernhard, M. Metzger, H. A. Gasteiger, *J. Electrochem. Soc.* **2015**, *162*, A1984–A1989.

[334] S. J. An, J. Li, C. Daniel, D. Mohanty, S. Nagpure, D. L. Wood, *Carbon N. Y.* **2016**, *105*, 52–76.

[335] B. You, Z. Wang, F. Shen, Y. Chang, W. Peng, X. Li, H. Guo, Q. Hu, C. Deng, S. Yang, G. Yan, J. Wang, *Small Methods* **2021**, *5*, 1–28.

[336] Y. Kim, *ACS Appl. Mater. Interfaces* **2012**, *4*, 2329–2333.

[337] Y. Qi, L. G. Hector, C. James, K. J. Kim, *J. Electrochem. Soc.* **2014**, *161*, F3010–F3018.

[338] R. Mo, X. Tan, F. Li, R. Tao, J. Xu, D. Kong, Z. Wang, B. Xu, X. Wang, C. Wang, J. Li, Y. Peng, Y. Lu, *Nat. Commun.* **2020**, *11*, 1–11.

[339] B. Wu, V. Yufit, Y. Merla, R. F. Martinez-Botas, N. P. Brandon, G. J. Offer, *J. Power Sources* **2015**, *273*, 495–501.

[340] M. Dubarry, V. Svoboda, R. Hwu, B. Y. Liaw, *Electrochem. Solid-State Lett.* **2006**, *9*, DOI 10.1149/1.2221767.

[341] W. M. Dose, C. Xu, P. Grey, M. F. L. De Volder, W. M. Dose, C. Xu, C. P. Grey, M. F. L. De Volder, *Cell Reports Phys. Sci.* **n.d.**, *1*, 100253.

[342] S. Xia, L. Mu, Z. Xu, J. Wang, C. Wei, L. Liu, P. Pianetta, K. Zhao, X. Yu, F. Lin, Y. Liu, *Nano Energy* **2018**, *53*, 753–762.

[343] M. Yi, F. Jiang, L. Lu, J. Ren, M. Jin, Y. Yuan, Y. Xiang, X. Geng, X. Zhang, X. Han, M. Ouyang, *Int. J. Energy Res.* **2021**, 1–22.

[344] B. Semburg, *Nucl. Instruments Methods Phys. Res. Sect. A Accel. Spectrometers, Detect. Assoc. Equip.* **2009**, *604*, 215–218.

[345] Y. Qi, H. Guo, L. G. Hector, A. Timmons, *J. Electrochem. Soc.* **2010**, *157*, A558.

[346] K. W. Knehr, T. Hodson, C. Bommier, G. Davies, A. Kim, D. A. Steingart, *Joule* **2018**, *2*, 1146–1159.

[347] R. Xu, H. Sun, L. S. de Vasconcelos, K. Zhao, *J. Electrochem. Soc.* **2017**, *164*, A3333–A3341.

[348] K. Y. Oh, J. B. Siegel, L. Secondo, S. U. Kim, N. A. Samad, J. Qin, D. Anderson, K. Garikipati, A. Knobloch, B. I. Epureanu, C. W. Monroe, A. Stefanopoulou, *J. Power Sources* **2014**, *267*, 197–202.

[349] P. Mohtat, J. B. Siegel, A. G. Stefanopoulou, *ECS Meet. Abstr.* **2019**, 1–21.

[350] G. Li, Y. Wen, B. Bin Chu, L. You, L. Xue, X. Chen, T. Huang, A. Yu, *ACS Sustain. Chem. Eng.* **2021**, *9*, 11748–11757.

[351] Y. Liu, J. Harlow, J. Dahn, *J. Electrochem. Soc.* **2020**, *167*, 020512.

[352] P. A. Oliveira, R. M. B. Silva, G. C. Morais, A. V. Alvarenga, R. P. B. Costa-Félix, *J. Phys. Conf. Ser.* **2016**, *733*, DOI 10.1088/1742-6596/733/1/012040.

[353] K. Nowacki, W. Kasprzyk, *Int. J. Thermophys.* **2010**, *31*, 103–112.

[354] J. B. Robinson, M. Pham, M. D. R. Kok, T. M. M. Heenan, D. J. L. Brett, P. R. Shearing, *J. Power Sources* **2019**, *444*, 227318.

[355] H. Popp, M. Koller, M. Jahn, A. Bergmann, *J. Energy Storage* **2020**, *32*, 101859.

[356] H. Michael, R. Jervis, D. J. L. Brett, P. R. Shearing, *Batter. Supercaps* **2021**, 1–20.

[357] K. Qian, C. Zhou, Y. Yuan, M. Allan, *2010 China Int. Conf. Electr. Distrib. CICED 2010* **2010**, 1–6.

[358] Ehsan Samadani, Mehrdad Mastali, Siamak Farhad, Roydon A. Fraser, Michael Fowler, *Int. J. Energy Res.* **2015**, *40*, 379–392.

[359] R. Suarez-Bertoa, J. Pavlovic, G. Trentadue, M. Otura-Garcia, A. Tansini,

B. Ciuffo, C. Astorga, *ACS Omega* **2019**, *4*, 3159–3168.

[360] T. H. Tran, S. Harmand, B. Sahut, *J. Power Sources* **2014**, *265*, 262–272.

[361] S. Zhu, L. Yang, J. Wen, X. Feng, P. Zhou, F. Xie, J. Zhou, Y. N. Wang, *J. Power Sources* **2021**, *516*, 230669.

[362] J. B. Robinson, D. P. Finegan, T. M. M. Heenan, K. Smith, E. Kendrick, D. J. L. Brett, P. R. Shearing, *J. Electrochem. Energy Convers. Storage* **2018**, *15*, 1–9.

[363] Q. Zhang, Y. Zhu, X. Luo, G. Liu, M. Han, *Opt. Lett.* **2017**, *42*, 631.

[364] Y. D. Su, Y. Preger, H. Burroughs, C. Sun, P. R. Ohodnicki, *Sensors (Switzerland)* **2021**, *21*, 1–36.

[365] L. Hu, G. Liu, Y. Zhu, X. Luo, M. Han, *IEEE Photonics J.* **2016**, *8*, DOI 10.1109/JPHOT.2016.2527018.

[366] P. N. Halimah, S. Rahardian, B. A. Budiman, *Int. J. Sustain. Transp. Technol.* **2019**, *2*, 54–57.

[367] J. Huang, S. T. Boles, J. M. Tarascon, *Nat. Sustain.* **2022**, *5*, DOI 10.1038/s41893-022-00859-y.